



Loughborough University
SCHOOL OF AERONAUTICAL, AUTOMOTIVE, CHEMICAL
AND MATERIALS ENGINEERING
DEPARTMENT OF CHEMICAL ENGINEERING

PhD Thesis

**MODEL BASED OPTIMIZATION OF BATCH AND
CONTINUOUS CRYSTALLIZATION PROCESSES**

Dimitrios Fysikopoulos

A Doctoral Thesis submitted in partial fulfilment of the
requirements for the award of the degree of Doctor of
Philosophy in Chemical Engineering

March 2018



Loughborough University
SCHOOL OF AERONAUTICAL, AUTOMOTIVE, CHEMICAL
AND MATERIALS ENGINEERING
DEPARTMENT OF CHEMICAL ENGINEERING

PhD Thesis

**MODEL BASED OPTIMIZATION OF BATCH AND
CONTINUOUS CRYSTALLIZATION PROCESSES**

Dimitrios Fysikopoulos

A Doctoral Thesis submitted in partial fulfilment of the
requirements for the award of the degree of Doctor of
Philosophy in Chemical Engineering

March 2018

To my family

Acknowledgements

I would like to take the opportunity and express my deepest gratitude to those who have contributed to this thesis and without them this PhD wouldn't be possible.

First of all, I would like to thank my academic supervisors, Professor Chris Rielly, Professor Zoltan Nagy and Dr. Brahim Benyahia for granting me the opportunity to work with them. Thank you for your guidance, support and devotion during the project. Since the time I joined the crystallization group, they gave me the opportunity to collaborate with several researchers from Loughborough and other Universities, to participate in national and international conferences and to collaborate with several industrial partners. Thank you for giving me the chance to experience all of these during my PhD.

I would also like to deeply thank all colleagues at Loughborough University and the wider CMAC community past and present. The PhD wouldn't have been completed without the support from Akos, Aniruddha, Qinglin, Wei, Elena, Iyke, Louisa and Ravi. Thank you for all the useful discussions and suggestions.

Special thanks to my friends, Emmanuel, Vaggelis, Ilias, Anargyros, Keddon, Apostolos, George, Rajesh, Stephanie, Maria, Stathis, Konstantinos and Zhuang for the good times we had in Loughborough and elsewhere. Life in Loughborough wouldn't be so great if you guys were not around.

I would also like to thank EPSRC and the Doctoral Training Centre in Continuous Manufacturing and Crystallization (CMAC) for funding this work (Grant ref: EP/K503289/1).

Last but not least, I would like to thank my family, my parents Ioannis and Stavroula and my brother Apostolos. They believed in me from the beginning of my career and they keep supporting me in all possible ways, selflessly and without hesitation. They are by far the most important reason for the accomplishment of this PhD, which I dedicate to them.

Dimitris I. Fysikopoulos
Loughborough, March 2018

Abstract

Crystallization is an important separation process, extensively used in most chemical industries and especially in pharmaceutical manufacturing, either as a method of production or as a method of purification or recovery of solids. Typically, crystallization can have a considerable impact on tuning the critical quality attributes (CQAs), such as crystal size and shape distribution (CSSD), purity and polymorphic form, that impact the final product quality performance indicators and inherent end-use properties, along with the downstream processability. Therefore, one of the critical targets in controlled crystallization processes, is to engineer specific properties of the final product.

The purpose of this research is to develop systematic computer-aided methodologies for the design of batch and continuous mixed suspension mixed product removal (MSMPR) crystallization processes through the implementation of simulation models and optimization frameworks. By manipulating the critical process parameters (CPPs), the achievable range of CQAs and the feasible design space (FDS) can be identified. Paracetamol in water and potassium dihydrogen phosphate (KDP) in water are considered as the model chemical systems. The studied systems are modelled utilizing single and multi-dimensional population balance models (PBMs). For the batch crystallization systems, single and multi-objective optimization was carried out for the determination of optimal operating trajectories by considering mean crystal size, the distribution's standard deviation and the aspect ratio of the population of crystals, as the CQAs represented in the objective functions. For the continuous crystallization systems, the attainable region theory is employed to identify the performance of multi-stage MSMPRs for various operating conditions and configurations. Multi-objective optimization is also applied to determine a Pareto optimal attainable region with respect to multiple CQAs. By identifying the FDS of a crystallization system, the manufacturing capabilities of the process can be explored, in terms of mode of operation, CPPs, and equipment configurations, that would lead to the selection of optimum operation strategies for the manufacturing of products with desired CQAs under certain manufacturing and supply chain constraints.

Nevertheless, developing reliable first principle mathematical models for crystallization processes can be very challenging due to the complexity of the underlying phenomena, inherent to population balance models (PBMs). Therefore, a novel framework for parameter estimability

for guaranteed optimal model reliability is also proposed and implemented. Two estimability methods are combined and compared: the first is based on a sequential orthogonalization of the local sensitivity matrix and the second is Sobol, a variance-based global sensitivities technic. The framework provides a systematic way to assess the quality of two nominal sets of parameters: one obtained from prior knowledge and the second obtained by simultaneous identification using global optimization. A multi-dimensional population balance model that accounts for the combined effects of different crystal growth modifiers/ impurities on the crystal size and shape distribution of needle-like crystals was used to validate the methodology. A cut-off value is identified from an incremental least square optimization procedure for both estimability methods, providing the required optimal subset of model parameters. In addition, a model-based design of experiments (MBDoe) methodology approach is also reported to determine the optimal experimental conditions yielding the most informative process data. The implemented methodology showed that, although noisy aspect ratio data were used, the eight most influential and least correlated parameters could be reliably identified out of twenty-three, leading to a crystallization model with enhanced prediction capability.

A systematic model-based optimization methodology for the design of crystallization processes under the presence of multiple impurities is also investigated. Supersaturation control and impurity inclusion is combined to evaluate the effect on the product's CQAs. To this end, a morphological PBM is developed for the modelling of the cooling crystallization of pure KDP in aqueous solution, as a model system, under the presence of two competitive crystal growth modifiers/ additives: aluminum sulfate and sodium hexametaphosphate. The effect of the optimal temperature control with and without the additives on the CQAs is presented via utilizing multi-objective optimization. The results indicate that the attainable size and shape attributes, can be considerably enhanced due to advanced operation flexibility. Especially it is shown that the shape of the KDP crystals can be affected even by the presence of small quantity of additives and their morphology can be modified from needle-like to spherical, which is more favourable for processing. In addition, the multi-impurity PBM model is extended by the utilization of a high-resolution finite volume (HR-FV) scheme, instead of the standard method of moments (SMOM), in order for the full reconstruction and dynamic modelling of the crystal size and shape distribution to be enabled. The implemented methodology illustrated the capabilities of utilizing high-fidelity computational models for the investigation of crystallization processes in impure media for process and product design and optimization purposes.

Table of Contents

THESIS ACCESS CONDITIONS AND DEPOSIT AGREEMENT	III
LIST OF FIGURES.....	XV
LIST OF TABLES.....	XXI
1 INTRODUCTION	1
1.1 BACKGROUND.....	1
1.2 RESEARCH AIMS AND OBJECTIVES.....	5
1.3 RESEARCH CONTRIBUTION	6
1.4 THESIS ROADMAP	8
2 LITERATURE REVIEW.....	10
2.1 INTRODUCTION	11
2.2 FUNDAMENTALS OF CRYSTALLIZATION.....	12
2.3 MECHANISMS OF CRYSTALLIZATION	15
2.3.1 Nucleation	16
2.3.2 Crystal Growth and Dissolution	26
2.3.3 Breakage and Agglomeration	29
2.4 POPULATION BALANCE MODELLING (PBM).....	31
2.5 NUMERICAL TECHNIQUES FOR THE SOLUTION OF POPULATION BALANCE EQUATIONS (PBEs).....	33
2.6 CONCLUSIONS	37
NOMENCLATURE	38
GREEK LETTERS	39
3 SYSTEMATIC MODEL – BASED DESIGN AND OPTIMIZATION OF BATCH AND CONTINUOUS COOLING CRYSTALLIZATION PROCESSES.....	41
3.1 INTRODUCTION	42
3.2 PROCESS MODELS	47
3.2.1 Unseeded Batch & Continuous Cooling Crystallization of Paracetamol	49
3.2.2 Unseeded Batch & Continuous Cooling Crystallization of KDP	53
3.3 OPTIMIZATION PROBLEM FORMULATION.....	58
3.4 RESULTS AND DISCUSSION.....	66
3.4.1 Case Study 1: Unseeded Batch & Continuous Cooling Crystallization of Paracetamol	68
3.4.2 Case Study 2: Unseeded Batch & Continuous Cooling Crystallization of KDP	85
3.5 CONCLUSIONS	96
NOMENCLATURE	98
GREEK LETTERS	99
SUBSCRIPTS	99

SUPERSCRIPTS	99
4 MODEL REALIABILITY AND ESTIMABILITY ANALYSIS OF A MULTI – IMPURITY POPULATION BALANCE MODEL FOR CRYSTALLIZATION PROCESSES.....	101
4.1 INTRODUCTION	102
4.2 METHOD	105
4.3 PROCESS MODEL.....	108
4.4 ESTIMABILITY ANALYSIS	113
4.4.1 Ranking the Model Parameters – Orthogonalization Method	113
4.4.2 Global Sensitivity Analysis	117
4.5 OPTIMAL EXPERIMENTAL DESIGN (OED).....	119
4.6 RESULTS AND DISCUSSION.....	122
4.6.1 Parameter Estimability Analysis	122
4.6.2 Local Estimability Analysis: LSA and Orthogonalization Algorithm.....	124
4.6.3 Global Sensitivity Analysis (GSA).....	131
4.6.4 Optimal Experimental Design (OED)	139
4.7 CONCLUSIONS	145
NOMENCLATURE	148
GREEK LETTERS	150
SUBSCRIPTS	150
5 OPTIMAL CONTROL STRATEGIES OF CSSD BASED ON THE COMBINATION OF SUPERSATURATION CONTROL AND ADDITION OF CGMS	153
5.1 INTRODUCTION	154
5.2 PROCESS MODEL.....	157
5.3 OPTIMIZATION PROBLEM FORMULATION.....	163
5.4 RESULTS AND DISCUSSION.....	164
5.4.1 Simulation – based analysis of MIAM model	165
5.4.2 Multi – objective Optimization Problem of MIAM	172
5.5 CONCLUSIONS	177
NOMENCLATURE	178
GREEK LETTERS	179
SUBSCRIPTS	180
6 CONCLUSIONS AND FUTURE WORK.....	181
6.1 SUMMARY AND CONCLUSIONS.....	181
6.2 FUTURE WORK.....	183
7 REFERENCES	187
8 APPENDIX A: PUBLICATIONS.....	213

LIST OF FIGURES

Figure 1.1. Schematic of the integrated crystallization and product formulation process chain to enable end-to-end precision manufacturing.	2
Figure 2.1. Solubility - Supersolubility diagram.	14
Figure 2.2. Nucleation mechanisms.	17
Figure 2.3. Free energy diagram for primary nucleation illustrating the existence of a critical radius, r_c .	19
Figure 2.4. Schematic illustrating the two-step nucleation mechanism: Dense liquid cluster forms followed by the formation of nucleus inside the cluster. (a) Macroscopic viewpoint in the plane, (b) Macroscopic viewpoint of events along dashed line in (a) and (c) The free energy ΔG along two possible pathways for nucleation of crystals from solution.	20
Figure 2.5. Arrays of interfacial tension between the three phases: liquid (<i>l</i>) Solid (<i>s</i>) and Crystal deposit (<i>c</i>).	22
Figure 2.6. Two-step crystal growth theory: Growing crystal-solution interface.	28
Figure 3.1. Graphical representation of the morphology of the KDP crystal.	54
Figure 3.2. (a) A continuous stirred tank reactor (CSTR) configuration that approximates a plug flow reactor (PFR) (b) Example of a reactor superstructure.	59
Figure 3.3. Graphical representation of possible combinations of different types of crystallizers, including potential recycle loops, feed and outflow streams.	60

Figure 3.4. Construction of the attainable region of particle size for a cascade of 3 MSMPR crystallizers for the cooling crystallization of paracetamol in water. The optimization problems solved for the determination of the FR are indicated by the equations and the arrows respectively.	64
Figure 3.5. (a) Temperature, (b) solute concentration and (c) phase diagram trajectories obtained from the implementation of different cooling strategies: Natural, Linear, Cubic and Optimal cooling.	69
Figure 3.6. (a) Nucleation rate, (b) growth rate and (c) supersaturation trajectories obtained from the implementation of different cooling strategies: Natural, Linear, Cubic and Optimal cooling.	69
Figure 3.7. (a) μ_0 , (b) μ_1 , (c) μ_2 and (d) μ_3 trajectories obtained from the implementation of different cooling strategies: Natural, Linear, Cubic and Optimal cooling.	70
Figure 3.8. (a) Number, (b) Sauter and (c) weight mean size trajectories obtained from the implementation of different cooling strategies: Natural, Linear, Cubic and Optimal cooling.	71
Figure 3.9. Standard deviation (S_d) trajectories obtained from the implementation of different cooling strategies: Natural, Linear, Cubic and Optimal cooling.	72
Figure 3.10. Attainable region of particle size with respect to time for the cooling batch crystallization of paracetamol in water.	73
Figure 3.11. Solute concentration profiles obtained corresponding to the attained states for the determination of the FR.	73
Figure 3.12. Attainable regions of (a) number mean size (L_{10}), (b) Sauter mean size (L_{32}) and (c) standard deviation (S_d) with respect to time.	74
Figure 3.13. Attainable regions of (a) μ_0 , (b) μ_1 , (c) μ_2 and (d) μ_3 with respect to time.	74
Figure 3.14. Pareto optimal-front obtained for the multi-objective optimization problem of maximizing the number mean size and minimizing the standard deviation of the distribution with respect to t_{batch} .	77
Figure 3.15. (a) Temperature and (b) solute concentration trajectories obtained from the implementation of two different cooling strategies corresponding to the boundaries of the Pareto front for $t_{batch} = 300$ mins: Upper and Lower boundary.	78
Figure 3.16. (a) Nucleation rate, (b) growth rate and (c) supersaturation trajectories obtained from the implementation of two different cooling strategies corresponding to the boundaries of the Pareto front for $t_{batch} = 300$ mins: Upper and Lower boundary.	78
Figure 3.17. Standard deviation (S_d) trajectories obtained from the implementation of two different cooling strategies corresponding to the boundaries of the Pareto front for $t_{batch} = 300$ mins: Upper and Lower boundary.	79

- Figure 3.18.** Attainable regions of particle size with respect to total residence time for a cascade of: 2, 3 and 4 MSMPR crystallizers. 80
- Figure 3.19.** Determination of the attainable region of particle size for a cascade of 2 crystallizers through optimization (— •) and excessive simulation (•). 81
- Figure 3.20.** Operating policy for *minimum* point marked in figure 3.16 (— •) for total residence time $\tau = 60$ mins. 82
- Figure 3.21.** Operating policy for *maximum* point marked in figure 3.16 (— •) for total residence time $\tau = 60$ mins. 84
- Figure 3.22.** Pareto optimal-front obtained for the multi-objective optimization problem of maximizing the number mean size and minimizing the standard deviation of the distribution with respect to different residence times. 84
- Figure 3.23.** 3D Pareto optimal-front obtained for the multi-objective optimization problem of maximizing the number mean size ($\bar{x}_1 = \frac{\mu_{0,1}}{\mu_{0,0}}$), minimizing the mean aspect ratio (AR) and minimizing the standard deviation of the distribution in x_1 direction ($S_{d,1}$) with respect to different batch time (t_{batch}). 87
- Figure 3.24.** XY cartesian plane of the 3D Pareto optimal-front obtained for the multi-objective optimization problem of maximizing the number mean size ($\bar{x}_1 = \frac{\mu_{0,1}}{\mu_{0,0}}$), minimizing the mean aspect ratio (AR) and minimizing the standard deviation of the distribution in x_1 direction ($S_{d,1}$) with respect to different batch time (t_{batch}). 87
- Figure 3.25.** XZ cartesian plane of the 3D Pareto optimal-front obtained for the multi-objective optimization problem of maximizing the number mean size ($\bar{x}_1 = \frac{\mu_{0,1}}{\mu_{0,0}}$), minimizing the mean aspect ratio (AR) and minimizing the standard deviation of the distribution in x_1 direction ($S_{d,1}$) with respect to different batch time (t_{batch}). 88
- Figure 3.26.** YZ cartesian plane of the 3D Pareto optimal-front obtained for the multi-objective optimization problem of maximizing the number mean size ($\bar{x}_1 = \frac{\mu_{0,1}}{\mu_{0,0}}$), minimizing the mean aspect ratio (AR) and minimizing the standard deviation of the distribution in x_1 direction ($S_{d,1}$) with respect to different batch time (t_{batch}). 89
- Figure 3.27.** Implementation of two different cooling strategies corresponding to the boundaries of the Pareto front for $t_{batch} = 180$ mins: Upper (—) and Lower boundary (—). 90
- Figure 3.28.** Relative supersaturation (σ) trajectories obtained from the implementation of two different cooling strategies corresponding to the boundaries of the Pareto front for $t_{batch} = 180$ mins: Upper (—) and Lower boundary (—). 90
- Figure 3.29.** Phase diagram trajectories obtained from the implementation of two different cooling strategies corresponding to the boundaries of the Pareto front for $t_{batch} = 180$ mins: Upper (—) and Lower boundary (—). 91

Figure 3.30. (a) Aspect ratio (AR), (b) Solute concentration, (c) mean crystal width size ($L_{n,2}$) and (d) Mean crystal length size ($L_{n,1}$) trajectories obtained from the implementation of two different cooling strategies corresponding to the boundaries of the Pareto front for $t_{batch} = 180 mins$: Upper (—) and Lower boundary (—).	92
Figure 3.31. Determination of the 3D attainable region via stochastic simulation analysis of the: mean particle size ($L_n = \mu_{0,1} / \mu_{0,0}$) and mean aspect ratio (AR).	94
Figure 3.32. Determination of the attainable region of the mean crystal length size ($L_n = \mu_{0,1} / \mu_{0,0}$) via stochastic simulation analysis.	95
Figure 3.33. Determination of the attainable region of the aspect ratio (AR) via stochastic simulation analysis.	95
Figure 3.34. Determination of the attainable region for the standard deviation of the distribution in x_1 direction ($S_{d,1}$) via stochastic simulation analysis.	96
Figure 4.1. Schematic of the parameter identification and estimability analysis framework.	106
Figure 4.2. Causal loop diagram illustrating the interaction between the moments in the two-dimensional case.	110
Figure 4.3. Graphical representation of how the optimal design criteria can be related to the parameter uncertainty and can be utilized to minimize the parameter error by identifying the optimum operating trajectory.	120
Figure 4.4. Comparison of the dynamic sensitivity of selected model parameters: (a) g_1 (b) $K_{e,CGM2}$ (c) $k_{p,0}$ (d) $k_{CGM1,m,0}$.	125
Figure 4.5. Comparison of the sensitivity profiles of selected model parameters: (a) $p_1 : k_{ads,0,CGM1}$ & $p_2 : k_{des,0,CGM1}$ and (b) $p_7 : \Delta G_{des,1}$ & $p_9 : k_{ads,0,CGM2}$.	126
Figure 4.6. Box plot illustrating the variation of the sensitivity of the estimated model parameters.	127
Figure 4.7. Correlation matrix for the estimated nominal parameter set.	128
Figure 4.8. Maximum likelihood error vs the number of selected parameters for: (a) nominal set of parameters estimated by Borsos et al. (2016) – sequential approach and (b) nominal set of parameters estimated in this work – simultaneous approach.	130
Figure 4.9. Sobol analysis for the 1 st case scenario: (a) first order sensitivity indices of the 23 parameters in descending order (b) total order sensitivity indices in descending order (c) first order sensitivity indices for a sample of randomly generated sets of parameters (d) total order sensitivity indices for a sample of randomly generated sets of parameters.	132

Figure 4.10. Sobol analysis for the 2nd case scenario: (a) first order sensitivity indices of the 23 parameters in descending order (b) total order indices in descending order (c) first order sensitivity indices for a sample of randomly generated sets of parameters (d) total order sensitivity indices for a sample of randomly generated sets of parameters.	133
Figure 4.11. Maximum likelihood error vs the number of selected parameters for both Sobol scenarios.	135
Figure 4.12. Comparison between the experimental and simulated mean aspect ratio dynamic evolution: (a) Experiment 1 (400 g H ₂ O ; 150 gr KDP; 12.5 ppm CGM1; 0.0 ppm CGM2), (b) experiment 2 (400 g H ₂ O ; 150 gr KDP; 12.5 ppm CGM1; 7.5 ppm CGM2) and (c) experiment 3 (400 g H ₂ O ; 150 gr KDP; 0.0 ppm CGM1; 5.0 ppm CGM2).	137
Figure 4.13. Comparison between the experimental and simulated mean aspect ratio dynamic evolution: Experiment 1 (400 g H ₂ O ; 150 gr KDP; 12.5 ppm CGM1; 0.0 ppm CGM2) and experiment 2 (400 g H ₂ O ; 150 gr KDP; 12.5 ppm CGM1; 7.5 ppm CGM2) by considering 8 and 23 parameters.	138
Figure 4.14. Optimal operating temperature trajectories for experimental design based on D-Optimal criterion.	141
Figure 4.15. Optimal operating concentration trajectories for experimental design based on D-Optimal criterion.	142
Figure 4.16. Optimal operating temperature trajectories for experimental design based on A-Optimal criterion.	142
Figure 4.17. Optimal operating concentration trajectories for experimental design based on A-Optimal criterion.	143
Figure 4.18. Relative supersaturation trajectories: Linear and D-Optimal cooling design with $C_{CGM1} = C_{CGM2} = 5 \text{ ppm}$.	144
Figure 4.19. Crystal growth rates along the x_1 axis: Linear and D-Optimal cooling profiles with $C_{CGM1} = C_{CGM2} = 5 \text{ ppm}$.	144
Figure 4.20. Crystal growth rates along the x_2 axis: Linear and D-Optimal cooling profiles with $C_{CGM1} = C_{CGM2} = 5 \text{ ppm}$.	145
Figure 5.1. Representation of the finite volume discretization of a two-dimensional CSD considering a uniform 2D grid.	159
Figure 5.2. Linear cooling profile is utilized for all the simulations.	166
Figure 5.3. Dynamic evolution of the: (a) solute concentration trajectory under the presence of different amounts of CGMs, (b) CGM1 impurity concentration and (c) CGM1 impurity concentration.	168
Figure 5.4. Effect of the CGMs concentration on (a) relative supersaturation (σ), (b) crystal growth along the characteristic length x_1 (G_{x_1}) and (c) crystal growth along the characteristic width x_2 (G_{x_2}).	169

- Figure 5.5.** Effect of the *CGMs* concentration on the (a) evolution of the mean crystal size of population along the characteristic length x_1 ($\mu_{0,1}/\mu_{0,0}$) and (b) evolution of the mean crystal size of population along the characteristic length x_2 ($\mu_{1,0}/\mu_{0,0}$). 170
- Figure 5.6.** Effect of the *CGMs* concentration on the evolution of the mean aspect ratio. 171
- Figure 5.7.** Effect of the *CGMs* concentration on the evolution crystal size and shape distribution (CSSD) for: (a) view 1 and (b) view 2. 172
- Figure 5.8.** 3D Pareto optimal-front obtained for the multi-objective optimization problem of maximizing the number mean size ($\bar{x}_1 = \frac{\mu_{0,1}}{\mu_{0,0}}$), minimizing the mean aspect ratio (AR) and minimizing the standard deviation of the distribution in x_1 direction ($S_{d,1}$) with respect to different additives' (C_{CGMi}) concentration. 174
- Figure 5.9.** Pareto optimal-front obtained for the multi-objective optimization problem of maximizing the number mean size ($\bar{x}_1 = \frac{\mu_{0,1}}{\mu_{0,0}}$), minimizing the mean aspect ratio (AR) and minimizing the standard deviation of the distribution in x_1 direction ($S_{d,1}$) with respect to different additives' (C_{CGMi}) concentration.: (a) XY cartesian plane, (b) XZ cartesian plane and (c) YZ cartesian plane. 176

LIST OF TABLES

Table 3.1. Crystallization model parameters with 95% confidence intervals (C.I.), variables and physical properties utilized for modelling the system Paracetamol in Water (Nagy et al., 2008).	53
Table 3.2. Crystallization model parameters, variables and physical properties utilized for modelling the system potassium dihydrogen-phosphate (KDP) in Water (Togkalidou et al., 2001 ; Gunawan et al., 2004 ; Majumder et al., 2013b ; Szilágyi et al., 2015 ; Borsos et al., 2016).	57
Table 4.1. Complete set of differential-algebraic equations (DAEs) that represent the Multi-Impurity Adsorption Model (MIAM).	112
Table 4.2. Orthogonalization algorithm for estimability analysis.	115
Table 4.3. Nominal vector of the model parameters and their confidence intervals (C.I.).	123
Table 4.4. Ranking of parameters with the highest estimability potential.	129
Table 4.5. Summary of the parameter ranking based on Orthogonalization algorithm and the Sobol analysis.	136
Table 4.6. Parameter precision design using D-optimal and A-optimal criteria with respect to different initial impurities concentration.	140
Table 5.1. Process variables and physical properties.	165

1 INTRODUCTION

1.1 Background

The pharmaceutical industry has undergone through an unprecedented change over the past few years. Imminent patent expirations, low productivity, new regulatory incentives and the constantly increasing costs that outpace the development of new pharmaceuticals have increased the need for more efficient manufacturing processes ([DiMasi et al, 2003](#); [Basu et al., 2008](#); [Suresh et al., 2008](#); [Price, 2014](#)). Currently, the development of a drug can take from 10 – 15 years with the cost of bringing the drug to market ranging between \$0.8 and \$2 billion, while it has only 20% chance of FDA approval ([Kessel et al., 2011](#); [Aksu et al., 2012](#); [Benyahia et al., 2012](#)). To this end, continuous manufacturing, process intensification and process systems engineering tools, such as model-based design, optimization and advanced process control, can be utilized in conjunction, or individually, to improve the efficiency of the manufacturing processes and the quality attributes of the product itself.

Crystallization is an important separation process, extensively used in most chemical industries and especially in pharmaceutical manufacturing, either as a method of production or as a method of purification or recovery of solids ([Mersmann, 2001](#)). It can be utilized in challenging separations such as ultrapure powders or heat sensitive compounds combining particle

formation and purification in a single operation. Also, crystallization has proven to be more energy efficient than other separation processes, such as distillation since the heat of crystallization can be significantly lower – ranging from $1/5^{\text{th}}$ to $1/10^{\text{th}}$ – comparing to the heat of evaporation. Many substances of scientific, technological, and commercial importance are in crystalline form, ranging from large-tonnage commodity materials to high-value specialty chemicals, such as active pharmaceutical ingredients (APIs).

In fact, the pharmaceutical industry relies heavily on crystallization as 70% of all the pharmaceuticals formulation and 90% of APIs involve at least one crystallization step during the manufacturing process (Alvarez et al., 2010; Pena and Nagy, 2015). Besides, crystallization is one of the key steps in the production of pharmaceutical tablets which are the most popular dosage form (see **Figure 1.1**). Hence, the crystallization step has a considerable impact on tuning the critical quality attributes (CQAs), such as crystal size and shape distribution (CSSD), purity and polymorphic form, that impact the final product quality performance indicators and inherent end-use properties (e.g. bioavailability, tablet stability, dissolution, dosage form etc.), along with the downstream processability (e.g. filtration, drying etc.) (Rawlings et al., 1993; Wibowo and Ng, 2001; Nagy et al., 2013; Rawlings et al., 1993). Therefore, one of the critical targets in controlled crystallization processes, is to engineer specific properties of the final product. Narrow and uniform crystal size distribution (CSD), high yield of the process, maximum crystal purity, acceptable crystal morphology, specific polymorphic form and consistent product are in most cases desirable, subjected to certain economic and operational constraints (Mersmann, 2001). Consequently, designing a process, which satisfies all the target specifications is a major challenge in industrial crystallization.

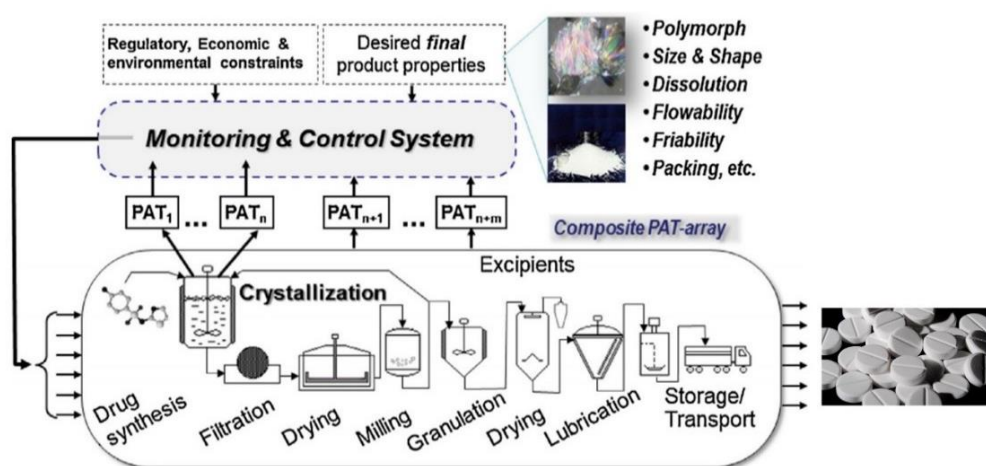


Figure 1.1. Schematic of the integrated crystallization and product formulation process chain to enable end-to-end precision manufacturing (Adapted from Nagy et al. (2013)).

With the recent advances in online process analytical technology (PAT) tools, more reliable and real-time data can be made available for process understanding and manipulation (Nagy et al., 2013; Yu et al., 2004). Hence, improved monitoring in combination with systematic design and effective control of the crystallization processes can lead to more robust and efficient manufacturing processes and consequently to higher product quality (Nagy et al., 2009; Mesbah et al., 2012; Kwon et al., 2014; Brown et al., 2018). Therefore, developing high fidelity models and model-based approaches have received considerable attention in many different areas, such as process design, control, real time optimization and Quality-by-Design (Mascia et al., 2013; Lakerveld et al., 2013; Su et al., 2015; Su et al., 2016).

A prerequisite to apply process design and model-based control strategies, however, is the availability of a high fidelity mathematical model. The most fundamental approach for modelling particulate processes, such as crystallization, is the population balance model (PBM) framework (Randolph and Larson, 1988; Ramkrishna et al., 2000) coupled with kinetic expressions, mass and energy balances, which yields a set of nonlinear integro-partial differential equations. The set provides a rigorous approach to model the dynamic evolution of the dispersed phase system's properties, such as CSSD (Sato et al., 2008; Borsos, et al., 2014; Borsos et al., 2016). Although the PBM framework is based on first principles, a general theoretical mathematical expression for the determination of the crystallization kinetics doesn't exist and hence, empirical or semi-empirical expressions (e.g. power-law etc.) are used, that in most of the cases account for the supersaturation as the key variable (Rawlings et al., 1993; Cao et al., 2012).

Estimating the kinetic parameters for these expressions, however is a non-trivial process. In general, the full characterization of the process requires large amounts of information, which, however, are not always available (Rawlings et al., 1993). Also, the quality and the information content of the available experimental data can be affected by many factors such as noisy measurements, limited number of data points, poor design of experiments (DoE) and limited range of operating conditions, which inadequately cover the design and operating space (Perregaard et al., 1993; Chu et al., 2011; Brown et al., 2018). Additionally, strong influence of a parameter on one or more of the measured responses, high correlation between the parameter effects and/or the effects of a parameter on model predictions can also lead to unreliable and inaccurate identification of the unknown parameter values, which in turn degrades the prediction capability of the mathematical model (Kravaris et al., 2013; Benyahia et al., 2013).

Apart from the experimental errors, challenges could also arise based on the model structure itself. Several assumptions are typically made during the model development to simplify the numerical complexity of the system with the risk, however, to affect the predictability of the model leading to under/over-estimation of essential variables (Su et al., 2015). However, it should be highlighted that there is a considerable trade-off between complexity and computational cost, which should be considered during decision-making. In general, models utilized for advanced control and complex optimization purposes should be simple due to computational time constraints. Therefore, appropriate numerical methods and solvers should be used based on the application of the model. Also, simplified lumped models are typically employed instead of distributed systems. Of course, the assumption of uniform mixing is not always valid and consequently the hydrodynamics should be evaluated as well especially when large scale processes are considered (Kougoulos et al., 2006). Furthermore, the hydrodynamics can affect the kinetic parameters, as well as the homogeneity of the system. The former may have a greater impact since in many cases the time scales for crystallization are longer comparing to the ones for mixing.

Another assumption which is typically made, to simplify the PBM framework is the consideration that crystals have a constant shape (Randolph and Larson, 1988; Ramkrishna et al., 2000). Consequently, only one characteristic size is required for modelling the crystallization phenomena. Nevertheless, this hypothesis is not valid for most of the cases, since crystals exhibit more complicated morphologies, e.g. with varying aspect ratios. In this case, multi-dimensional models can be utilized to model the evolution of the CSSD (Acevedo et al., 2015; Hemalatha and Rani, 2017). Although significant research has been already conducted for the design and optimization purposes using 1D crystallization models (i.e. CSD) a systematic design methodology for multi-dimensional PBMs (i.e. CSSD) is still missing.

Although modelling the CSSD could be computationally complex and intensive, developing a systematic design methodology to control the size and shape attributes could be even more challenging. There are several approaches that have been implemented to modify the CSSD, such as supersaturation control, temperature cycling, mechanical post-processing (e.g. wet-milling) or use of additives (Acevedo and Nagy, 2014; Eisenschmidt et al., 2016; Yang et al., 2017). However, combination of the methods, such as supersaturation control and additives inclusion, which could form promising hybrid approaches resulting in enhanced attainable and size attributes due to the increased operation window, has gone unstudied.

1.2 Research Aims and Objectives

The overall aim of this thesis is to develop robust population balance model-based tools for design, parameter estimation and optimization of crystallization processes considering multiple internal coordinates for CSSD design in pure/impure medium. Based on that, the following objectives were identified:

- To develop one-dimensional and multi-dimensional lumped models for modelling and optimization purposes.
- To develop a systematic model-based methodology for the design of batch and continuous crystallization processes through the implementation of optimization frameworks. In this way the achievable crystal quality attributes (CQAs) can be evaluated by manipulating the critical process parameters (CPPs).
- To utilize both single-objective and multi-objective optimization methods to determine optimal operating recipes and identify the feasible ATRs by considering single/multiple CQAs, different modes of operation, and different configurations.
- To perform parameter estimation on the studied crystallization systems with the scope to model the processes more reliably.
- To develop a systematic approach for parameter estimation for problems considering a large number of model parameters and limited amount of data (or data with low information content).
- To perform local and global sensitivity analysis to determine how the variations of the outputs could be related to certain variations of the input variables.
- To develop algorithms which can be applied for estimability analysis to assess whether optimal model reliability has been implemented. That also requires the development of a systematic methodology – via incremental optimization in this case – to determine the optimal subset of model parameters.

- To perform model-based design of experiments (MBDoE) to determine the optimal experimental conditions yielding the most informative process data, which can be used for the accurate identification of the nucleation, crystal growth and pinning mechanism parameters.
- To identify and propose a new hybrid methodology for designing the CSSD. That requires the utilization of a systematic multi-objective optimization approach to explore the feasible range of the size and shape attributes.
- To apply an advanced numerical scheme for modelling the multi-impurity PBM. That requires the implementation of high-resolution finite volume (HR-FV) scheme, instead of the standard method of moments (SMOM), so that full reconstruction and dynamic modelling of the crystal size and shape distribution can be enabled.

1.3 Research Contribution

The main contributions of this thesis are summarized below:

- The development of a generic and systematic model-based design methodology for a wide range of crystallization processes for the identification of the attainable regions by incorporating single- and multi-objective optimization algorithms. This is the first time that a systematic study is conducted for the identification of the attainable regions by considering multi-dimensional PBMs. Also, it is the first that multi-objective optimization is presented as a robust way of determining the ATRs for both 1D and 2D PBMs, generating high dimensional attainable regions. The validity of the process is evaluated by a stochastic simulation approach as well.
- The development of a new framework for parameter estimability for guaranteed optimal model reliability. Two estimability methods are combined and compared: the first is based on a sequential orthogonalization of the local sensitivity matrix and the second is Sobol, a variance-based global sensitivities technic. This is the first time that the modified Gram Schmidt Orthogonalization algorithm and Sobol analysis are combined and applied in crystallization and equally the first time that the estimability

analysis in general has been applied to assess the model reliability of a multi-dimensional PBM in crystallization. The application of the framework can enhance the development of more reliable and high-fidelity models for the pharmaceutical industry for process design, optimization and advanced control.

- The integration of a model-based design of experiments (MBCoE) approach into the proposed framework. As a result, the experimental operation is optimised to maximize the information content and reduce the cost inherent to redundant experimental information with the scope of improving the model predictability.
- The potential application of the proposed framework to evaluate the information content of the data measured by process analytical tools (PAT). In the case of systems utilizing different sensors, the information content of each sensor can be assessed and consequently the number of parameters that can be estimated from each individual PAT or from their combination (e.g. sensors providing different outputs) can be determined, which helps select the most appropriate PAT depending on the targeted level of prediction capability and application (e.g. process control).
- The utilization of a high-resolution finite volume technique (HR-FV), which arises from combining a semi-discrete FV method with the robust upwind Van Leer flux limiter, to solve the novel multi-impurity adsorption model (MIAM). By implementing the latter numerical method, the MIAM can be employed for modelling the CSSD evolution under the presence of multiple growth modifiers (aka growth additives). Therefore, the model can be used for process design, optimization and control of crystallization processes in impure medium.
- Comprehensive model-based study to evaluate the effect of additives inclusion, with and without supersaturation control, on the product's CQAs. Multi-objective optimization was applied for the identification of high dimensional attainable regions. The implemented methodology can be used to predict the feasible attainable regions (ATRs) of systems under the presence of additives/impurities.

1.4 Thesis Roadmap

The thesis comprises of six chapters and is structured as follows:

Chapter 2: Literature Review: This chapter presents an overview with respect to the fundamentals of crystallization, such as solubility, supersaturation and metastable zone width. The phenomena occurring during crystallization are discussed and their mechanisms are explained in detail. Modelling of crystallization processes by utilizing the population balance equations framework is also introduced. By reviewing the existing theories and modelling approaches, challenges, opportunities and gaps towards the implementation of these theories in industrial crystallization are identified and presented.

Chapter 3: Systematic Model – Based Design and Optimization of Batch and Continuous Cooling Crystallization Processes: In this chapter a systematic methodology is presented for the design of batch and continuous crystallization processes through the implementation of optimization frameworks. It is shown how via utilizing optimization the achievable attained states of the CQAs can be identified. After a comprehensive literature review is reported with respect to the design of batch and continuous crystallization processes, the methodology is comprehensively described. The results of the analysis are demonstrated into the results section, which is divided in two different parts since single and multi-dimensional population balance models (PBMs) are utilized for different case studies. The advantages and the limitations of utilizing optimization to identify feasible regions are highlighted.

Chapter 4: Model Reliability and Estimability Analysis of a Multi-Impurity Population Balance Model for Crystallization Processes: This chapter forms the core of this thesis and is divided to into three sections. The novel framework for parameter estimability for guaranteed optimal model reliability is presented and implemented. Then, the estimability analysis and optimal experimental design concepts are presented, followed by the results. In the last section the enhanced capabilities of the framework are demonstrated over the conventional approach for parameter estimation.

Chapter 5: Optimal Control Strategies of CSSD based on the Combination of Supersaturation Control and Addition of CGMs: In this chapter the effect of additives inclusion, with and without supersaturation control, is evaluated for the design of crystal product with targeted size and shape attributes. A morphological population balance model

(PBM) is utilized for the modelling of the cooling crystallization under the presence of two competitive crystal growth modifiers (additives). The effect of the optimal temperature control with and without the additives on the attainable region is presented utilizing multi-objective optimization. In addition, the multi-impurity PBM model is extended by the utilization of a high-resolution finite volume (HR-FV) scheme, instead of the standard method of moments (SMOM), in order for the full reconstruction and dynamic modelling of the crystal size and shape distribution to be enabled. The implemented methodology illustrated the capabilities of utilizing high-fidelity computational models for the investigation of crystallization processes in impure media for process design and optimization purposes.

Chapter 6: Conclusions and Recommendations for Future Work: In this final chapter the dissertation's conclusions are presented along with recommendations for future work.

2 LITERATURE REVIEW

Crystallization has been utilized extensively in several chemical industries as an essential unit operation. As a result, extensive research has been conducted for the development of the scientific basis defining the process. In this Chapter, an overview is presented with respect to the fundamentals of crystallization. The phenomena occurring during crystallization are discussed and their mechanisms are explained in detail. Modelling of crystallization processes by utilizing the population balance equations framework is also introduced. By reviewing the existing theories and modelling approaches, challenges, opportunities and gaps towards the implementation of these theories in industrial crystallization are identified and presented. The literature review reveals that although crystallization has been extensively applied, the phenomena describing crystallization have not been fully understood due to their inherent complexity.

2.1 Introduction

Crystallization, which is conceptually a way to isolate chemical substances in the solid form for long-term storage and/or downstream processing, includes a series of processes resulting in the formation of a new heterogeneous phase from a solution (Mullin, 2001; Mersmann, 2001). Moreover, during crystallization, randomly organized solute molecules, ions or atoms are arranged in a certain manner forming an ordered and systematic three-dimensional structure which is called crystal. The imposed driving force resulting in the formation of this new phase is attributed to the change in Gibbs free energy (overall excess free energy), ΔG , during the transition from a thermodynamically metastable to a stable state. Therefore, the energy barrier that is required to be overcome for the formation of the first tiny crystallites of the new phase corresponds to ΔG . These clusters, also known as embryos or nuclei (Mullin, 2001), may be either re-suspended in the solution, or by overcoming an energy barrier they may grow generating crystals. Therefore, crystallization conceptually proceeds in two steps: nucleation and crystal growth, which typically occur almost simultaneously. Other processes also may occur within a system, that could affect several crystal attributes, namely breakage and agglomeration. All the aforementioned phenomena have a stochastic nature since they could be affected by numerous factors, such as solution thermal history, utilized cooling rate, hydrodynamics, mass and heat transfer, impurities, crystallizer's geometry and volume etc. (Bogacz et al., 2016). Hence, as clearly indicated, crystallization is inherently a very complex stochastic phenomenon and developing an understanding of its mechanisms and fundamentals is essential.

Therefore, in this Chapter, the mechanisms along with the most fundamental framework for modelling crystallization are briefly presented with the scope of providing to the reader the necessary theoretical background for interpreting the content of the thesis. For a more comprehensive study of the phenomenon of crystallization the reader is referred to the numerous textbooks that have been published through the years with respect to crystallization and its subsequent mechanisms (Davey and Garside, 2000; Mullin, 2001; Mersmann, 2001; Jones, 2002; Myerson, 2002; Karpinski and Wey, 2002). Additional literature is also presented in **Chapters 3, 4 and 5**, whenever required, related to the specific topic discussed within each Chapter. The remainder of this Chapter is organized as follows: In **section 2.2**, the fundamentals of crystallization are presented, while the mechanisms are discussed in detail in **section 2.3**. In **section 2.4**, the population balance equation (PBE) framework is presented in

detail with specific emphasis on the approaches that can be utilized for its solution (**section 2.5**). The Chapter ends with some concluding remarks in the **conclusions** section.

2.2 Fundamentals of Crystallization

The fundamental concepts of solubility and supersaturation are essential towards developing and characterizing the behaviour of a crystallization system (Aamir, 2010). The solubility, which is a thermodynamic property, can be defined as the maximum amount of substance (i.e. solute) that can be dissolved in a given amount of solvent under certain temperature and pressure conditions when thermodynamic equilibrium does apply. Typically, the solubility of solute in a solvent does increase by raising the temperature within the bulk and consequently it is commonly considered as a function of temperature (Mersmann, 2001; Schwartz, 2002). A phase diagram of a crystallization system is depicted in **Figure 2.1**, where the solubility curve is illustrated by a solid blue line. A solution which is located on the solubility curve is called saturated. Under certain conditions, however, a solution can dissolve more solute than is determined by the saturation condition, in which case a supersaturated solution is obtained.

A necessary, but not sufficient condition for the formation of a new phase is the existence of supersaturation, a thermodynamically metastable state (Mullin, 2001). In more detail, supersaturation, which typically depends on the solute concentration and bulk temperature, is the decisive driving force of the crystallization (Mersmann, 2001). Therefore, optimal supersaturation control is a prerequisite for the economical production of crystals with desired quality attributes, such as size, shape and purity.

Supersaturation (S_n) can be expressed as a function of the difference between the chemical potential of the solute molecules ($\mu_{solution}$) and solid (μ_{solid}) state respectively, while at the same time the effect of the temperature is also considered as shown below (Davey and Garside, 2000; Mangin et al., 2009):

$$S_n = \exp\left(\frac{\mu_{solution} - \mu_{solid}}{RT}\right) \quad (2.1)$$

In industrial applications, however, supersaturation has been calculated by utilizing expressions based on the solute concentration (c) and the saturated/equilibrium concentration (c_{sat}), which is more relevant for engineering applications comparing to the ones based on chemical potential (Simone, 2015; Borsos, 2016). Consequently, supersaturation is usually defined as absolute

supersaturation (Δc), or as supersaturation ratio (S) or as relative supersaturation (σ). The following expressions can be used to define the degree of supersaturation:

$$\Delta c = c - c_{sat} \quad (2.2)$$

$$S = \frac{c}{c_{sat}} = \sigma + 1 \quad (2.3)$$

$$\sigma = \frac{\Delta c}{c_{sat}} = S - 1 \quad (2.4)$$

As it is apparent the supersaturation is a substantial variable during crystallization since it can determine the size of the produced precipitate and could also have a major effect on the phase which is precipitated (i.e. polymorphism) (Davey and Garside, 2000).

Apart from the solution temperature, the supersaturation can be also affected by the difference between the total energy generated by the hydration of the precipitating ions, the lattice energy and the surface energy of the particles of the precipitate. Crystals with a high surface tension and high molecular weight generally have a strong tendency to form supersaturated solutions (Mullin, 2001).

In general, supersaturation in a solution (suspension crystallization: solution mediated crystallization) can be created by the following ways (Rielly, 2013):

- By using chemical reaction, very high supersaturation can be created and hence crystals can be produced from a solution.
- By cooling the solution, a temperature gradient is created (a solubility curve which is sensitive to temperature changes is required in this case) that drives the solution from the stable zone to the metastable zone and maybe into the labile region, where spontaneous nucleation will occur.
- By evaporation of the solution. During evaporation, the solvent mass fraction is reduced and as a result the concentration of the solution is increased above the solubility curve.
- By changing the pH, alterations in the solubility may occur and hence supersaturation can be created.
- By adding a non-solvent (or anti-solvent) to produce a reduction in the solubility. This is quite useful when the temperature coefficient of the solubility is small.

The solubility curve (see **Figure 2.1**), which can be determined by thermodynamics, indicates the saturation equilibrium and it represents the boundary between the stable and metastable region. The supersolubility curve, on the other hand, is rather more uncertain and it depends on system kinetics and other operating variables, such as the employed supersaturation rate, the hydrodynamics within the bulk, the presence of impurities (which may affect the solvent activity and/or the subsequent process kinetics) and the thermal history of the solution.

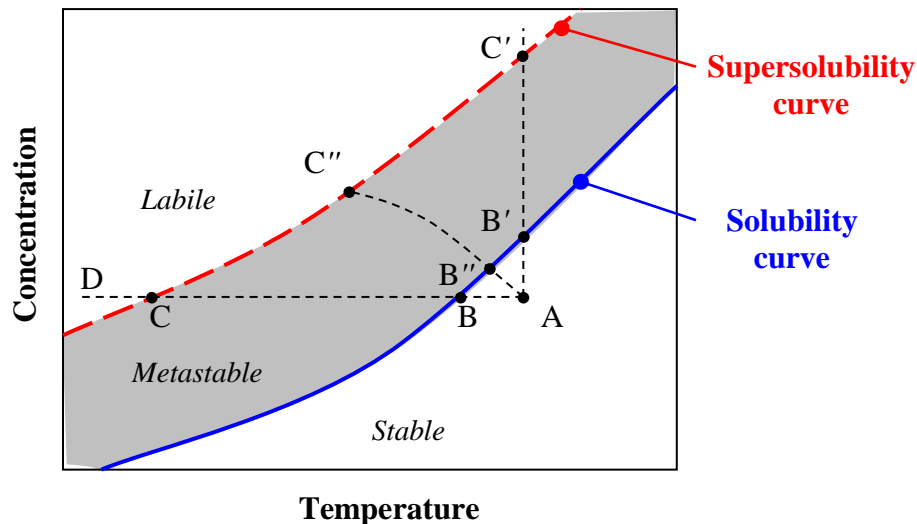


Figure 2.1. Solubility - Supersolubility diagram (Adapted from [Rielly \(2013\)](#)).

As it is evident, these curves divide the phase diagram into three distinctive areas: stable, metastable and labile region:

The Stable region is a region where the solution is undersaturated. Therefore, even if crystals are present within the bulk they will eventually dissolve and hence crystallization in this region cannot occur. The dissolution rate of the crystals can be related to the degree of undersaturation, which is typically expressed similarly to supersaturation (see **eq. 2.2 – 2.4**). Dissolution is a kinetic process which highly depends on mass transfer and fluid dynamics.

The Metastable region is an area where nucleation would not occur spontaneously, but if seeds are introduced, then crystal growth would occur. The metastable zone width (MSZW), defines a region which is bounded by the supersolubility and the solubility curves, it can be strongly affected by a variety of process parameters such as the rate of de-supersaturation and hydrodynamics. Typically, the MSZW can be significantly decreased with increasing agitation levels since the mass transfer during the formation of molecular clusters (aka embryos) is intensified ([Steendam et al., 2018](#); [Liu and Rasmuson, 2013](#)). Additionally, the MSZW can be

also decreased by employing slow de-supersaturation rates (Mullin, 2001). The solution history (e.g. the pre-heating period) is another operating variable that could impact the MSZW. More specifically, by applying high temperatures and prolonged holding times, during the pre-heating stage, a wider MSZW may be generated (Davey and Garside, 2000). The identification of the MSZW, along with the solubility curve is, of course, essential for the development and optimization of the crystallization processes (Barret and Glennon, 2002). For instance, knowledge of the MSZW is required to determine the seeding regime and the optimum operating supersaturation levels throughout the process (Chung et al., 1999; Aamir, 2010).

The Labile area, on the other hand, is a highly supersaturated region in which spontaneous nucleation would probably occur.

2.3 Mechanisms of Crystallization

Regardless of the way that supersaturation is achieved, the physicochemical process of crystallization, in general, proceeds in certain steps:

- Initially, **supersaturation** is required to be achieved (i.e. crystallization's driving force).
- Depending on the system's thermodynamic and kinetic properties and whether any dust or crystals are present, new particles can be formed. This phenomenon corresponds to the **nucleation** mechanism.
- After the formation of the first particles supersaturation is also utilized for the subsequent growth of the particles, corresponding to the **crystal growth** mechanisms. However, dissolution might occur instead if supersaturation obtains negative values.
- Further growth can also occur if **agglomeration** phenomenon is present.
- **Breakage** of the particles may also occur due to crystal-crystal, crystal-wall and/or crystal-stirrer collisions.

Although the aforementioned steps can occur simultaneously within the solution, there is a strict succession of the three first stages. It becomes evident, however, that it should not be assumed that these phenomena occur only sequentially. For instance, supersaturation is typically generated during the crystallization process. Also, material can continue to nucleate (primary and secondary nucleation) even after growth has started. It should be also highlighted that agglomeration and breakage phenomena are not always present during crystallization and in most cases occur after the crystals have reached a certain size.

2.3.1 Nucleation

Supersaturation is a necessary, but not sufficient condition to initiate crystallization within a metastable system (Mullin, 2001). The existence of nuclei or seeds in the solution, which could act as centres (or sites) for crystallization may be required as well. In general, nucleation is the primary particle formation process and can be either spontaneously or artificially induced. Spontaneous nucleation can occur due to random collisions and aggregation of solute molecules, while the additions of seeds or the presence of small inert particles can be utilized from the system as active centres for nucleation and growth.

Nucleation mechanisms can be classified into two different categories: primary and secondary nucleation (Mersmann, 2001; Jones, 2002; Myerson, 2002). A schematic summarizing all the potential nucleation mechanisms and their subgroups is presented in **Figure 2.2**. Primary nucleation, which is the formation of solid phase from clear unseeded solutions, can be further subdivided into homogeneous and heterogeneous nucleation. Homogeneous nucleation typically is considered to be the outcome of bimolecular interactions between molecules and/or ions of the solute phase resulting in the formation of molecular clusters (aka embryos) (Mullin, 2001). In the other case, small inert particles, such as dust particles or impurities, are present in the solution, nucleation can be facilitated, and the process is known as heterogeneous nucleation. Heterogeneous nucleation can also occur due to abnormalities on the surface of the crystallizers since they can be utilized to establish energy favourable active nucleation centres. Thus, heterogeneous nucleation requires lower supersaturation, and lower Gibbs free energy, as will be shown later, in comparison to the homogeneous case.

However, in semi-commercial and industrial crystallizers, nucleation occurs at very low supersaturation (Rawlings et al., 1993). This can be typically achieved when crystals of the same solute are present in the solution (e.g. addition of seed crystals, generation of attrition fragments etc.) and is known as secondary nucleation. Based on the way that secondary nucleation can be achieved further subgroups can be identified (see **Figure 2.2**). Regardless of their differences, both primary and secondary nucleation kinetics depend on the degree of supersaturation but typically to different orders, meaning that primary nucleation typically presents faster kinetics.

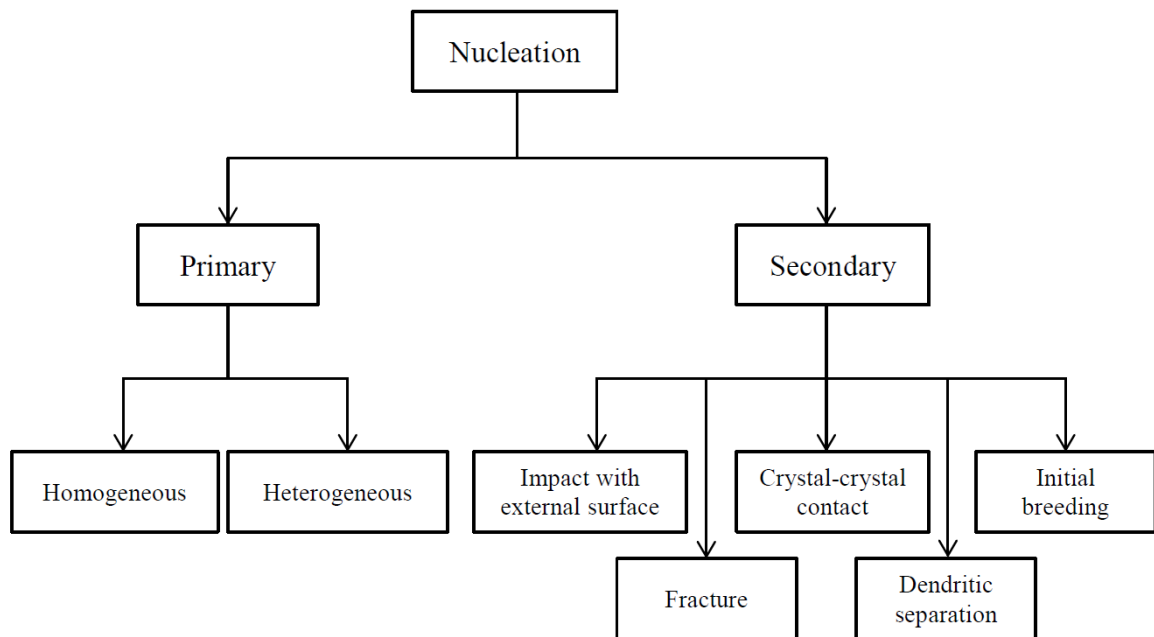


Figure 2.2. Nucleation mechanisms (Adapted from [Simone \(2015\)](#)).

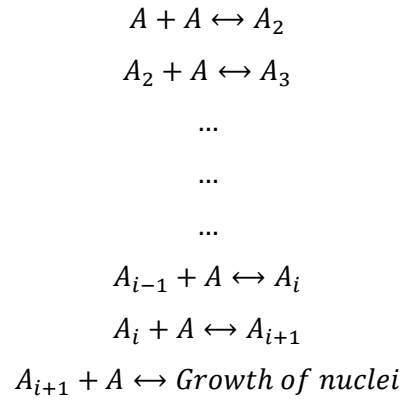
2.3.1.1 Primary Nucleation: Homogeneous

Primary nucleation, which typically occurs in clear solutions, is a highly nonlinear function of supersaturation and it is commonly modelled as a Dirac delta function. Moreover, when the supersaturation is low primary nucleation tends to be negligible, while it surges once the supersaturation threshold is reached, generating substantial amount of crystal nucleus ([Randolph and Larson, 1988](#)).

Until now, two opposing theories have been proposed to describe primary homogeneous nucleation:

- the classical nucleation theory (CNT), and
- the two-step nucleation theory.

The classical nucleation theory, assumes that clusters are formed in solution through bimolecular collisions, which can be illustrated as:



Further addition of structural units in the critical nucleus, r_c , results in an increase in the size of the macroscopic crystal. Clusters that do not reach the size of the critical nucleus are re-dissolved, since they are extremely unstable. The cluster structure of the critical nucleus is not known since it cannot be measured. Based on the hypothesis of the structure of the critical nucleus the two aforementioned theories have been proposed (i.e. CNT and two-step nucleation theory). The first one postulates that the critical nucleus is a tiny crystal with perfect structure, while the other supports that it is a diffuse particle, which contains molecules or solvated ions, that they have a similar state comparing to the bulk solution, without having, however, a clearly defined surface (Mullin, 2001).

CNT's thermodynamic basis, which was developed by Gibbs (1876;1878) and others (Volmer, 1939), defines the free energy change of the formation of this new phase, ΔG , as the sum of the free energy change of the formation of the nucleus surface, ΔG_s and the free energy change of the transformation phase, ΔG_v :

$$\Delta G = \Delta G_s + \Delta G_v = 4\pi r^2 \sigma_{int} + \frac{4}{3}\pi r^3 \Delta g_v \quad (2.5)$$

- ΔG_s is the surface excess free energy between the particle surface and the particle bulk and it is a positive quantity proportional to the interfacial tension, σ_{int} .
- ΔG_v is the volume excess free energy between a very big particle and the solute in solution and is a negative quantity in a supersaturated solution.
- Δg_v is the excess free energy per unit volume.
- ΔG is the overall excess free energy between a small particle of solute and the solute in solution.

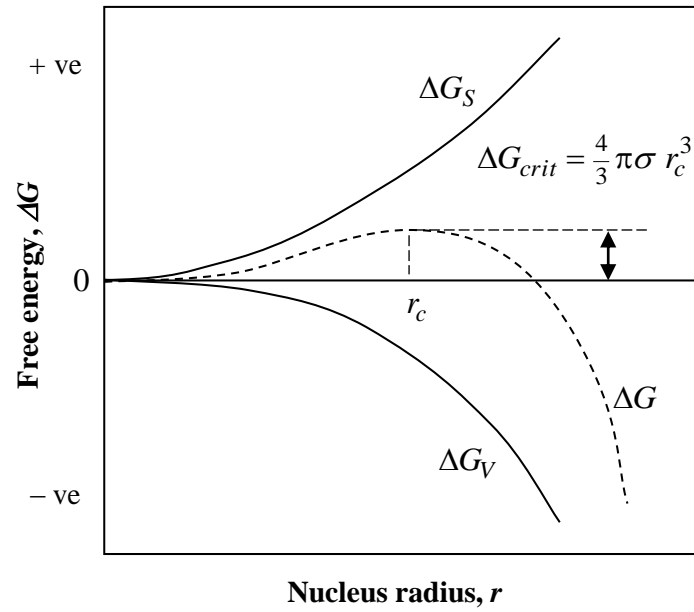


Figure 2.3. Free energy diagram for primary nucleation illustrating the existence of a critical radius, r_c (Adapted from Rielly (2013)).

Based on the CNT theory the subsequent free energy changes for a spherical nucleus can be qualitatively illustrated as depicted in **Figure 2.3**. As demonstrated, ΔG reaches a maximum critical threshold, before it starts declining. Therefore, it can be deduced that by forming clusters which have a larger size than the critical one, a transition to a more stable state occurs – free energy is reduced – which results in the generation of macroscopic nuclei. On the other hand, clusters with size smaller than the r_c are dissolved. Consequently r_c represents the smallest size of a stable nucleus and it can be estimated by minimizing the free energy function with respect to the radius ($\frac{\partial(\Delta G)}{\partial r} = 0$), resulting in the following expression:

$$r_c = -\frac{2\sigma_{int}}{\Delta g_v} \quad (2.6)$$

The rate of nucleus formation can be given by an Arrhenius type of expression and can be defined as the number of nuclei formed per unit volume per unit time:

$$B_p = A_p \exp\left(-\frac{16\pi\sigma_{int}^3 v^2}{3k_b^3 T^3 (\ln S)^2}\right) \quad (2.7)$$

where k_b is Boltzmann's constant and A_p is the preexponential factor and has a constant theoretical value for a certain temperature. Thus, it can be clearly perceived that there are three main variables affecting the rate of homogeneous nucleation: the absolute temperature, T , the

degree of supersaturation, S , and the surface energy (aka interfacial tension), σ_{int} . Therefore, by increasing the degree of supersaturation and temperature, the nucleation rate is also increased, while the opposite effect can be achieved by increasing the σ_{int} .

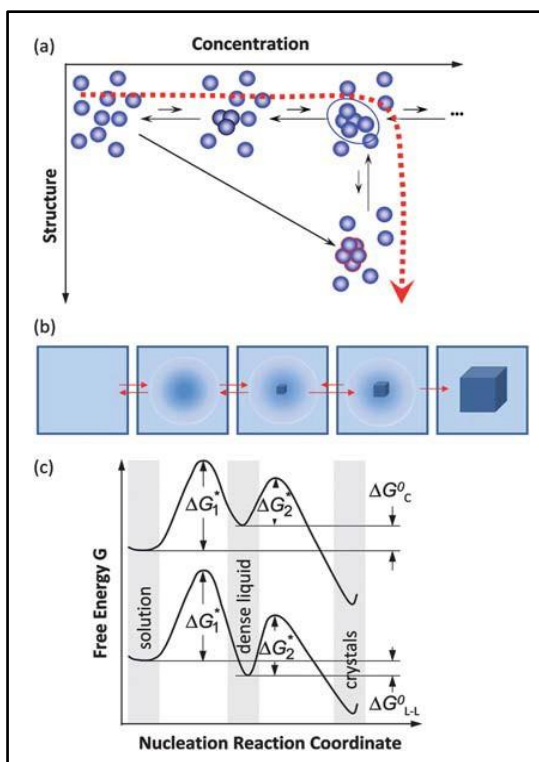


Figure 2.4. Schematic illustrating the two-step nucleation mechanism: Dense liquid cluster forms followed by the formation of nucleus inside the cluster. (a) Macroscopic viewpoint in the plane, (b) Macroscopic viewpoint of events along dashed line in (a) and (c) The free energy ΔG along two possible pathways for nucleation of crystals from solution (Adapted from Vekilov (2010)).

Nevertheless, it has been demonstrated that the CNT approach fails to predict accurately the nucleation rate of several proteins, organic and inorganic molecules (Vekilov, 2010). Therefore, the two-step nucleation theory was proposed with the scope of providing a more accurate way of determining the primary nucleation mechanism. According to this theory, transition from nucleus to crystals occurs through a sequential process where fluctuations are accounted for both concentration and structure. In other words, the generation of crystal nucleus is preceded by the formation of a dense liquid phase, as illustrated in **Figure 2.4** (Davey, 2013). The existence of metastable mesoscopic clusters of dense liquid was validated by monitoring the nucleation process in several protein solutions by utilizing dynamic light scattering (DLS): three haemoglobin variants, lysozyme and lumazine synthase were investigated and confirmed this hypothesis (Vekilov, 2010).

Therefore, the consideration of this additional metastable phase during primary nucleation is the main difference between the two approaches, since in the CNT it is assumed that the solute molecules form directly an ordered cluster without considering the dense liquid (Omar and Rohani, 2017). On the other hand, both theories postulate that the solute molecules are connected via weak forces (polar, hydrogen bonding etc.) to form clusters within the solution, which depending on the thermodynamics might generate nucleus (Simone, 2015). The reader is referred to literature for a more comprehensive review of the two nucleation theories (Vekilov, 2010; Karthika et al., 2016).

2.3.1.2 Primary Nucleation: Heterogeneous

Typically, the type of primary nucleation occurring during crystallization is heterogeneous nucleation (Mullin, 2001). Heterogeneous nucleation occurs due to the existence of small inert particles, such as dust particles or impurities, or rough surfaces which could act as active centres for nucleation (i.e. crystallizer walls and internal surfaces) since they could decrease the required interfacial surface energy.

Moreover, a foreign substance present in a supersaturated solution is generally known to reduce the required energy and consequently nucleation in a heterogeneous system generally occurs at a lower degree of supersaturation than a homogeneous system — the free energy barrier is lower in the case of a heterogeneous system (Mersmann, 2001; Jones, 2002; Myerson, 2002).

Therefore, heterogeneous and homogeneous primary nucleation free energies can be related with the following expression (Mullin, 2001):

$$\Delta G_{heterogeneous} = \varphi_{coeff} \Delta G_{homogeneous} \quad (2.8)$$

where φ_{coeff} is a coefficient less than one ($0 < \varphi_{coeff} < 1$) and it depends on the contact angle formed between the crystalline deposit, the heterogeneous solid surface and the liquid phase as illustrated in **Figure 2.5**.

Volmer (1939) demonstrated that the reduction in, ΔG , can be related to the contact angle (θ) of the solid phase. Based on this deduction, the following expression has been proposed for the estimation of the contact angle:

$$\cos \theta = \frac{(\sigma_{sl} - \sigma_{cs})}{\sigma_{cl}} \quad (2.9)$$

, where σ_{sl} , σ_{cl} and σ_{cs} are the interfacial tensions between solid surface – liquid phase, crystal deposit – liquid phase and the crystal deposit – solid surface, respectively (see **Figure 2.5**).

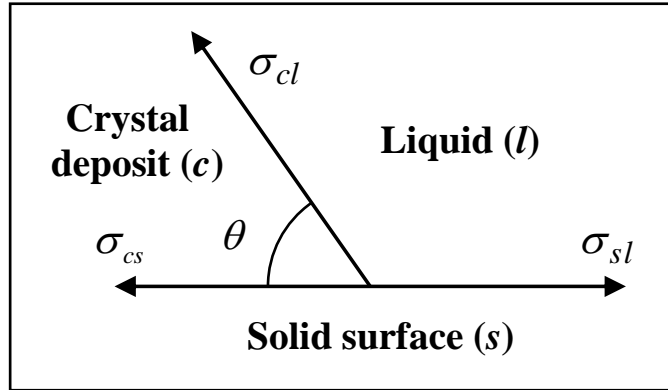


Figure 2.5. Arrays of interfacial tension between the three phases: liquid (*l*) Solid (*s*) and Crystal deposit (*c*) (Adapted from [Rielly \(2013\)](#)).

The coefficient, φ_{coeff} , on the other hand, can be estimated by utilizing the following equation:

$$\varphi_{coeff} = \frac{(2 + \cos \theta)(1 - \cos \theta)^2}{4} \quad (2.10)$$

Based on the equation above, when $\theta = 180^\circ$, $\cos \theta = -1$, $\varphi_{coeff} = 1$:

$$\Delta G_{heterogeneous} = \Delta G_{homogeneous} \quad (2.11)$$

meaning that complete crystalline incompatibility is presented. In other words, the free energies of heterogeneous and homogeneous nucleation obtain equal values. In principal this condition indicates that there are no dust particles and/or abnormalities within the crystallizer, meaning that heterogenous nucleation does not occur.

On the other hand, when $0 < \theta < 180^\circ$ and $\varphi_{coeff} < 1$:

$$\Delta G_{heterogeneous} < \Delta G_{homogeneous} \quad (2.12)$$

In this case, there is a partial crystalline compatibility resulting in heterogenous nucleation to be the dominant mechanism of primary nucleation over homogeneous nucleation. Finally, when $\theta = 0^\circ$ and $\varphi_{coeff} = 0$:

$$\Delta G_{heterogeneous} = 0 \quad (2.13)$$

The above criterion indicates that there is complete compatibility between the crystalline lattices of the newly formulated phase and the foreign particles. This can occur when the newly formed phase grows on the same surface. Thus, energy considerations show that spontaneous nucleation would occur for a system with zero contact angles. Nevertheless, no such systems exist in practice.

It should be highlighted, during the analysis it was considered that the substrate surface is flat, which is something that does not occur in practice. The substrate surface includes defects (particles that remain in cavities, or foreign particles in the walls of the reaction vessel) where the critical nuclei are formed and stabilized more easily. Therefore, based on the above, heterogeneous nucleation will always present a lower free energy barrier which consequently results on being the dominant mechanism of primary nucleation for each case.

For the estimation of the heterogeneous nucleation rate, an Arrhenius expression has been proposed by [Sohnel and Garside \(1992\)](#):

$$B_{p,h} = k_{b,h} \exp\left(-\frac{16\pi\sigma^3 v^2 f(\lambda)}{3k^3 T^3 (\ln S)^2}\right) \quad (2.14)$$

where factor $f(\lambda)$ corrects nucleation on foreign surfaces.

Although significant progress has been achieved in describing the phenomenon of primary nucleation, its pathway is still unclear, largely due to the difficulty of monitoring the process and its stochastic nature. Moreover, although during crystallization certain key operating variables can be set to certain values (e.g. applied temperature, supersaturation, etc.), there are other ones, such as the existence of dust particles, abnormalities on the crystallizer's internal surfaces, hydrodynamics, presence of impurities etc. that cannot be fully controlled, resulting in substantial variations on the systems nucleation mechanisms and kinetics. Therefore, as a result, a large number of, studies have been reported in literature with the scope of identifying appropriate ways of estimating the nucleation kinetics ([Kadam et al., 2011](#); [Kadam et al., 2012](#); [Sear, 2014](#); [Maggioni and Mazzotti, 2015](#)). In industrial applications, however, empirical expressions are utilized, which are functions of supersaturation, since they have been considered more relevant for engineering applications. In such a way, a deterministic average can be computed to provide an accurate estimate, which of course lies within certain confidence bounds.

It should be also mentioned that due to the complexity of the phenomenon substantial research has been conducted to identify potential factors that could be used to control the cluster formation. Moreover, it has been proven that nucleation can also be caused by agitation, mechanical vibration, friction and excessive pressures in solutions and melts. For example, [Liu and Rasmuson \(2013\)](#) investigated the potential influence of agitation and fluid shear on primary nucleation during suspension crystallization. They found that by increasing the input of mechanical energy the induction time can be decreased, meaning that primary nucleation is promoted. To describe the effect of shear rate on nucleation they proposed three different potential mechanisms: agitation enhanced mass transfer, agitation enhanced cluster aggregation and shear induced molecular alignment. Another approach that could impact the cluster formation is the acoustic cavitation. [Virone et al. \(2006\)](#), demonstrated that by applying ultrasound, a substantial reduction of induction times could be achieved. Moreover, ultrasound can cause cavitation (i.e. bubbles) within the bulk, which consequently result in inducing heterogeneous primary nucleation. In a similar way, [Miyasaka et al. \(2006\)](#) utilized ultrasonic irradiation to promote and inhibit nucleation. Utilization of laser light and application of electric and magnetic fields for inducing nucleation have also been reported in literature but until now none of these methods have been tested in large scale crystallization ([Mullin, 2001](#); [Sun et al., 2008](#); [Alexander and Camp, 2009](#); [Ward and Alexander, 2012](#)).

2.3.1.2 Secondary Nucleation

Secondary nucleation, which can be typically achieved when crystals of the same solute are present in the solution (e.g. addition of seed crystals, generation of attrition fragments etc.), is the dominant mechanism that is usually encountered in semi-commercial and industrial crystallizers. The pre-existence of crystals in the supersaturated solution, also known as parent crystals, decreases the required energy for inducing nucleation, leading to the formation of nucleus in lower degree of supersaturation comparing to primary nucleation ([Mersmann, 2001](#); [Jones, 2002](#); [Myerson, 2002](#)).

Although, secondary nucleation is often found in commercial crystallizers, it is a phenomenon that it not currently well understood in terms of mechanisms and kinetics mainly due to the difficulty of monitoring the process and its stochastic nature (i.e. like primary nucleation). Nevertheless, secondary nucleation can be easier manipulated by controlling the seeding process and the agitation. In general, by increasing the agitation higher secondary rates can be achieved, while seeding is a more complicated process and depends on the seed loading, size

and shape of the seeds ([Chung et al., 1999](#); [Kubota et al., 2001a](#); [Sarkar et al., 2006](#); [Aamir, 2010](#)).

Several mechanisms have been proposed for explaining the secondary nucleation, which can be summarized in the following categories (see also **Figure 2.2**):

- Initial or dust breeding
- Dendritic separation (needle breeding)
- Crystal-crystal contact (contact nucleation)
- Fracture (attrition)
- Fluid shear (e.g. solute layer removal)

In most of the cases secondary nucleation occurs due to parent crystals, whereas in the other cases it is initiated from the solute in the liquid phase. In initial breeding, secondary nuclei originate from the seed crystals. It occurs when a crystal surface contains tiny crystallites which can be detached and introduced into the supersaturated solution. Thus, the detached crystallites can become sites for nucleation in the supersaturated solutions. These crystallites are larger than the critical nucleus size and, as a result, the rate of nucleation is independent of the supersaturation of the solution. Dendritic separation (needle breeding), on the other hand, occurs when dendritic crystals are formed on the surface of a crystal at high supersaturation. These crystals can be detached from the surface and can be used as sites for nucleation in the solution. At even higher supersaturation, irregular polycrystalline aggregates may be formed. Attrition of these poly-crystals can serve as nucleation centres. This process is called polycrystalline breeding. However, this mechanism is not likely to be encountered in industrial crystallization ([Myerson, 2002](#)).

New nucleation sites can be also formed at high relative speeds of the fluid (i.e. fluid shear nucleation), since loosely bonded units from the growing crystals may be sheared off by fluid dynamical stresses and these may become nucleation sites when swept into regions of high supersaturation. Also, turbulence on the surface of the growing crystal, crystal - crystallizer wall or crystal - crystal or crystal - impeller collisions in an agitated vessel can provide nucleation sites for secondary nucleation. This category of secondary nucleation is called contact nucleation and it is quite significant from an industrial point of view ([Tai et al., 1975](#); [Wong et al., 2013](#)). Another category, which was not mentioned before, is the impurity

concentration gradient nucleation. In this theory it is stated that dissolved impurities in the solution can be embodied into the crystal surface and hence a concentration gradient can be created, which provides the possibility of nucleation.

Typically, simple power law models are utilized for the estimation of the secondary nucleation kinetics:

$$B_{sec} = k_{b,sec} \Delta c^b \quad (2.15)$$

which can be modified accordingly to take into consideration the effect of agitation:

$$B_{sec} = k_{b,sec} N_p^k \Delta c^b \quad (2.16)$$

where N^k is related to the mixing power input of a stirrer or a pump impeller. A comprehensive literature review with respect to the secondary nucleation mechanisms and models has been presented by [Agrawal and Paterson \(2015\)](#).

2.3.2 Crystal Growth and Dissolution

Although some of the steps of crystal growth can be monitored, it hasn't been possible so far to identify a general mechanistic model that can fully describe the phenomenon. Its inherent complexity is largely related to its stochastic nature since most of the factors affecting its kinetics cannot be fully controlled (e.g. hydrodynamics, impurities, density and viscosity of solvent, etc.).

Additionally, most of the steps involved occur before growth units incorporated into the crystal lattice. Hence, in several cases two or more mechanisms are present within the system affecting the crystal growth dynamics. Therefore, it becomes evident that, if the mechanisms act in parallel then the fastest one determines the development speed, while in the case that the mechanisms are consecutive, the crystal growth is determined by the slowest one. In addition, the complexity of the phenomenon is increased even more since a variety of growth units exist (atoms, molecules, ions, hydrated solute molecules, polymers, clusters, etc.) depending on the crystallizing system and the solvent.

The growth units are transferred from the bulk solution and incorporated into the crystal lattice based on the following steps ([Aamir, 2010](#)):

- Mass transport of the solute molecules from the solution to the crystal surface by diffusion, convection or by the combination of both mechanisms.
- Incorporation of the material into the crystal lattice through surface adsorption, also described as a surface reaction step.
- Adsorption of the growth unit on the crystal surface.
- Release part of its solvation shell followed by diffusion of growth unit into the adsorption layer until it is either incorporated into the lattice or leaves the adsorption layer and returns into the solution.
- If the growth unit reaches into the layer where it can be added to the lattice, it loses the remainder of its solvation shell before its incorporation in the lattice.

There are a lot of theories that have developed for the crystal growth through the years. One group of theories considers that growth results due to an adsorbed layer of solute atoms generated on the crystal surface (Borsos, 2016). Another group is based around diffusion-reaction theories. One of the early theories linked to the latter group, was proposed by Noyes and Whitney (1897), who described crystal growth as a diffusional process. Moreover, it was considered that the solid substances are bounded by a thin film of saturated solution. In this way diffusion does occur into all proportions of the solvent. Similar hypothesis was drawn with respect to dissolution which was treated as the exact opposite process comparing to crystal growth: diffusion in the opposite direction, when the supersaturation obtains negative values. Based on this theory, the gradient in concentration generated due to the difference between the liquid adjacent to the crystal (usually taken as the saturation concentration, c_{sat}) and the concentration in the liquid bulk, c , acts as the driving force in order crystal growth to occur and can be calculated by utilizing the following expression:

$$\frac{dm}{dt} = k_m A_{eff} (c - c_{sat}) \quad (2.17)$$

where m is the mass of deposited solid, A_{eff} is the effective mass transfer area and k_m is the overall mass transfer coefficient. However, the diffusion layer thickness can vary depending on agitation rate and hydrodynamics in general. Moreover, in systems that are not agitated the diffusion layer thickness can be increased to $150 \mu m$, while it can be substantially reduced when agitation already exists in the system (Mullin, 2001). Hence, considering the crystal

growth as a diffusional process seems that cannot provide an adequate description of the phenomenon.

These observations resulted in the modification of the mechanism of diffusion from [Berthoud \(1912\)](#) and [Valeton \(1924\)](#), who considered that crystal can grow is a two-step process of mass transfer (diffusion) followed by a surface reaction (1st order reaction). During the reaction step, the solute molecules can rearrange themselves in the crystal lattice. These two-steps can be described by the following equations:

$$\frac{dm}{dt} = k_d A_{eff} (c - c_i) \quad \text{Diffusion step} \quad (2.18)$$

$$\frac{dm}{dt} = k_r A_{eff} (c_i - c_{sat}) \quad \text{Reaction step} \quad (2.19)$$

where k_d is the diffusion coefficient, k_r is the surface reaction rate constant and c_i is the solute concentration at the interface between the crystal and the solution. A schematic representation of the two-step theory is illustrated in **Figure 2.6**.

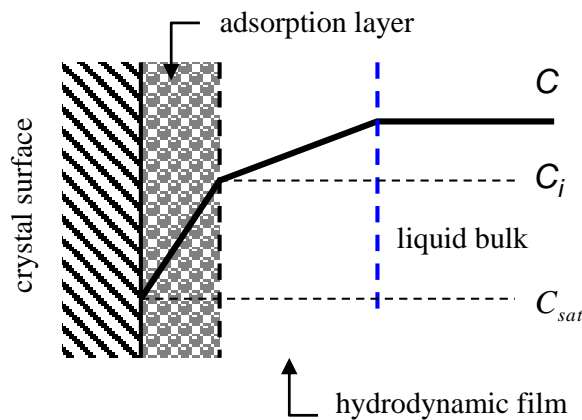


Figure 2.6. Two-step crystal growth theory: Growing crystal-solution interface (Adapted from [Rielly \(2013\)](#)).

Nevertheless, the latter equations cannot be utilized in practical applications since the concentration in the interface cannot be measured. Therefore, a general equation was proposed, that contains a term which indicates the total driving force:

$$\frac{dm}{dt} = k_G A_{eff} (c - c_{sat})^g \quad (2.20)$$

where K_G is an overall crystal growth coefficient and g is the exponent of growth rate.

Dissolution, which can be considered as the reverse process of crystal growth, it occurs when the solution becomes undersaturated. Based on that it can be modelled as two-step process as well:

- Surface reaction in order the crystal units to be detached from the lattice.
- Mass transfer via a diffusive layer in order the crystal units to be transferred into the bulk solution.

Of course, depending on the system thermodynamics (i.e. solubility), the rate limiting step can be either the surface reaction or the mass transfer (Omar and Rohani, 2017). Typically, the kinetics of dissolution are faster comparing to growth and can be affected by several factors such as crystal size and shape, crystal form, solvent, impurities etc. A summary of the available dissolution kinetics can be found in Aamir (2010).

2.3.3 Breakage and Agglomeration

Apart from nucleation, crystal growth and dissolution, other phenomena may be present during crystallization such as, breakage and agglomeration. These phenomena do not always take place during crystallization and in most of the cases they occur after the crystals have reached a certain size. The systems utilized in this work were dominated mainly by nucleation and growth phenomena. Therefore, the agglomeration and breakage phenomena have been neglected during the solution of the population balance model. Consequently, these phenomena will be briefly discussed.

Agglomeration is a particle size enlargement process which could have substantial impact on the final product's characteristics. Moreover, during agglomeration new crystals are created when smaller ones are clustered together. It should be mentioned that in literature the terms agglomeration and aggregation have been used interchangeably creating confusion with respect to the description of the phenomenon. Therefore, Nichols et al. (2002) suggested a distinction between these two terms. It was proposed that aggregation should refer to pre-nucleation events when supramolecular structures are formed, while the term agglomeration should be used when macroscopic events do occur. An additional classification has been reported that proposes that agglomeration should be divided further into hard and soft agglomerates with respect to the force required for agglomerates to fracture (Omar and Rohani, 2017).

Agglomeration can be described as a process occurring in two steps:

- Collision between two particles to form an agglomerative bond.
- Adherence of the crystals and the formation of the agglomeration bond.

Of course, sufficient time is required to form the agglomeration bond. Typically, the bond strengthens over time and consequently potential collisions could break the bond ([Omar and Rohani, 2017](#)).

Agglomeration phenomena are usually size and system dependent and can be affected by several factors such as the system hydrodynamics, crystallizer type and geometry, crystal characteristics (e.g. size, shape, surface structure etc.), utilized supersaturation, nature of the agglomeration bond, amount and size of crystals present etc. ([Mersmann, 2001](#); [Myerson, 2002](#); [Brunsteiner et al., 2005](#); [Yu et al., 2005](#)).

Typically, in industrial crystallization agglomeration is considered undesirable due to its highly intrinsic stochasticity. This potentially could result in increased product variability while at the same time substantial difficulties arise in large scale applications with respect to the prediction of its output. Nevertheless, by controlling the supersaturation within the MSZW, the agglomeration phenomenon can be also manipulated resulting in larger and more uniform crystals ([Fujiwara et al., 2002a](#)). More information regarding the agglomeration phenomenon and its mechanisms can be found in literature ([David et al., 1995](#); [Yu et al., 2005](#); [Pena et al., 2017b](#)).

Breakage, on the other hand, is a phenomenon where new particles of varying sizes are generated from the disintegration of an existing crystal, which is known as a parent crystal. In other words, a co-existing crystal can irreversibly lose a fraction of its material, which can then be used to create smaller size crystals with varying sizes. Crystal breakage occurs due to several mechanisms, including: crystal – crystal, crystal – wall and crystal – impeller collisions. As the rest of the phenomena presented, breakage is also a stochastic phenomenon which is dependent on the systems hydrodynamics, crystallizer type and geometry, amount, size and shape of crystals etc ([Bravi et al., 2003](#); [Sato et al., 2008](#); [Briesen et al, 2009](#)).

Another critical variable affecting breakage phenomena is process time. A study performed by [Mazzarotta et al. \(1996\)](#) in sugar crystals illustrated that at the beginning of the process a high number of fragments was produced which was gradually reduced until it became negligible.

Since a certain system was utilized this cannot be generalized, however it illustrates that process time could have a substantial effect. Additional information regarding the breakage phenomenon and its mechanisms can be found in literature ([Mersmann, 2001](#); [Myerson, 2002](#); [Bravi et al., 2003](#); [Yekeler, 2007](#); [Sato et al., 2008](#); [Briesen et al, 2009](#)).

Finally, it should be mentioned that although breakage and agglomeration present intrinsic stochasticity, they are typically modelled in a deterministic manner providing however an accurate estimation with respect to the CQAs' average dynamics ([Ramkrishna, 2000](#)). The models utilized are known as population balance models (PBMs) and they could provide the mathematical formulation involving all the aforementioned crystallization phenomena. A nice summary of the available kinetic models employed for both agglomeration and breakage has been presented by [Omar and Rohani \(2017\)](#).

2.4 Population Balance Modelling (PBM)

In general, models derived from first principles (mechanistic models) should be preferred comparing to data-driven, surrogate or hybrid models (gray box) since they typically offer advanced predictive capabilities and validity for a broader range of operating conditions ([Aamir et al., 2010](#); [Bonvin et al., 2016](#)). Since first principles models are based on laws of conservation, they can provide physical understanding of the process. Especially, in complex phenomena, such as crystallization, mechanistic models could provide an insight even in physical aspects of the system which cannot be directly measured.

The most fundamental mechanistic approach for modelling particulate processes, such as crystallization, is the population balance equation (PBE) framework, which was initially derived based on the work of [Randolph \(1964\)](#) and [Hulburt and Katz \(1964\)](#), and was further improved by [Randolph and Larson \(1988\)](#) and [Ramkrishna \(2000\)](#). It is highly remarkable that although the derivation of the PBE framework was reported around the same time, it was based on different principles. Moreover, [Randolph \(1964\)](#) employed the continuum mechanical principles to derive the equations, while [Hulburt and Katz \(1964\)](#) utilized the Boltzmann – like equations.

The PBE framework coupled with kinetic expressions, mass and energy balances yields a set of nonlinear integro-partial differential equations which could fully describe a crystallization process. Moreover, the set provides a rigorous approach to model the dynamic evolution of the

dispersed phase properties, such as the crystal size distribution and other state variables, across the temporal and spatial domains, with the latter one to consider both internal and external coordinates. External coordinates typically demonstrate the location of the crystals in physical space based on the ordinary cartesian system (x, y, z) , while the internal coordinates refer to the characteristic properties of the crystals (e.g. crystal length, crystal width, composition, chemical activity, etc.) (Ramkrishna, 2000; Omar and Rohani, 2017). The combination of the internal and external coordinates comprise the particle phase space. To fully characterize the particulate phase, considering i independent internal coordinates, $(i + 3)$ spatial dimensions and $(i + 3)$ dimensional distribution is required (Randolph and Larson, 1988).

Fundamental for the formulation of the PBE framework is the consideration of the existence of a number density of particles at every point in the particle phase space. The total number of particles in any region of the state space, Ω_x , can be computed by integrating the number density function, $n(t, \mathbf{X})$, over a certain region (Ramkrishna, 2000), such as:

$$N_{av}(\mathbf{X}, t) = \int_{\Omega_x} n(t, \mathbf{X}) dV_x \quad (2.21)$$

Similar expressions do also exist for the calculation of the volume and mass density.

The formulation of the PBE can be achieved by either utilizing an Eulerian or a Lagrangian approach. Typically, the Eulerian method is employed, which tracks the whole number of crystals as a continuous phase (Randolph and Larson, 1988; Omar and Rohani, 2017).

The general PBE equation can be expressed as:

$$\frac{\partial n(t, \mathbf{X})}{\partial t} + \nabla_x [(G_i n)] + n \frac{d(\log(V))}{dt} = B_{birth} - D_{death} - \sum_k \frac{Q_k n_k}{V} \quad (2.22)$$

, where $n(t, \mathbf{X})$ represents the number density function, as a continuous form, while G_i denotes the crystal growth (aka internal velocity, v_i). On the other hand, $\mathbf{X} = [x_1, x_2, \dots, x_N]$ is the vector containing the various characteristic lengths, t is the time, B_{birth} is the birth rate, D_{death} denotes the crystal death, V is the volume of the crystallizer and Q_k represents the volumetric flowrate streams. Since the PBE is a partial differential equation (PDE) boundary (B.C.) and initial (I.C.) conditions are required. For instance, in the case of an 1D PBM these conditions can be expressed as follows:

$$\text{B.C.} \quad G(\mathbf{x}_1, t=0, t) n(\mathbf{x}_1, t=0, t) = (B_p + B_s) \quad (2.23)$$

$$\text{I.C.} \quad n(\mathbf{x}_1, 0) = 0 \quad (2.24)$$

It should be mentioned that the discrete particles of the system are treated as a continuous distribution ($n(t, \mathbf{X})$). The validity of this hypothesis is justified due to the large number of sampling points of the crystal properties (Randolph and Larson, 1988).

As illustrated in eq. 2.22, the PBE framework can be formulated to account multiple crystal properties. One typical example is the consideration of multiple internal characteristic coordinates for growth. In such way apart from size, the shape evolution of the crystals can be also predicted (Sato et al., 2008; Briesen et al., 2009; Borsos, 2016). However other properties aside from size coordinates can be also deliberated. For instance, Gerstlauer et al. (2001) developed a population balance model (PBM) with two independent internal crystal characteristics: crystal length and the internal strain energy. In this way, the researchers managed to model the evolution of the internal lattice strain during crystal growth.

2.5 Numerical techniques for the solution of Population Balance

Equations (PBEs)

Solving the generic PBE framework is typically a computational intensive problem, which requires complex numerical solution techniques (Ramkrishna 2000; Aamir, 2010; Omar and Rohani, 2017). The difficulty of solving the PBEs arises from the integro-differential part of the PDE along with the nonlinear hyperbolic nature of the equations. Towards this end, several approaches have been proposed through the years for their efficient solution and they are presented below.

Under certain assumptions, the PBE framework can be solved by utilizing analytical solutions (Randolph and Larson, 1988). Nevertheless, substantial limitations do arise. For example, only continuous MSMR processes can be considered, while only nucleation and size-independent growth are taken into account. Terms for breakage and agglomeration can be included as well if additional simplifications are considered (Patil and Andrews, 1998; McCoy and Madras, 2003). Nevertheless, these simplification limit substantially the capabilities and applicability of the PBM.

A numerical technique which has extensively utilized for the solution of the PBMs is the method of moments, which was initially developed by [Hulburt and Katz \(1964\)](#) and [Randolph and Larson \(1988\)](#). The critical advantage of the method of moments is that it converts the PBE into a set of moment equations of the number density. In this way the PDE is transformed into a set of small number of ODEs, which can be consequently solved by the utilization of commonly used ODE solvers (e.g. 4th order Runge – Kutta). As will be discussed later, discretization techniques do transform the PDE into a set of ODEs as well but the number of generated equations is significantly higher, resulting in a more numerical challenging problem. By converting the number density into a set of moments, global mean values of the distribution can be computed, such as: total number, total length, total surface area, total volume, mean average size of the crystals, and the coefficient of variation of the distribution. The computational efficiency and simplicity of the method makes it very attractive for the solution of complex optimization and control problems. Nevertheless, only mean values of the number density function can be computed. Although techniques have been proposed for the reconstruction of the CSD through the moments ([Angelov et al., 2007](#); [Cogoni and Frawley 2015](#)), limitations do arise based on the accuracy of the reconstruction. Also, they do lack the capability of generating bimodal distributions and reconstructing the density function for multi-dimensional models (e.g. CSSD for a two-dimensional PBM).

The standard method of moments (SMOM) is the foundation of the method of moments. It has been broadly used for the solution of one – dimensional and multi – dimensional population balance models for simulation, optimization and control purposes ([Braatz and Nagy, 2003](#); [Nagy et al., 2008](#); [Majumder and Nagy, 2013](#); [Borsos, 2016](#)). Nevertheless, by utilizing the SMOM method, size-dependent growth, and agglomeration expressions cannot be considered, while breakage mechanisms can be only accounted under certain assumptions ([Borsos and Lakatos, 2014](#)).

The quadrature method of moments (QMOM) is an extension of the SMOM, providing solutions for crystallization problems involving nucleation, size-dependent/independent growth, breakage and agglomeration ([McGraw, 1997](#)). In QMOM the integrals are computed by a quadrature approximation as shown below:

$$\mu_k = \int_0^{\infty} x^k n(x, t) dx \approx \sum_{i=1}^N w_i x_i^k \quad (2.25)$$

Therefore, QMOM can be considered as a non-linear model reduction approach, where the number density function is approximated as a combination of linear basis functions (Aamir, 2010). Due to its characteristics QMOM has been utilized extensively for modelling PBM processes and it is the method typically employed when PBM – CFD coupling is required (Nagy et al., 2009; Rane et al., 2014; Gimbut et al., 2016). Several other methods have been proposed as improvements to the initial QMOM method, such as the direct quadrature method of moments (DQMOM), modified quadrature method of moments (M – QMOM), fixed pivot quadrature method of moments (FPQMOM) etc. For more information, the reader is referred to the work of Su et al. (2009), where a detailed review and discussion of the different QMOM approaches is presented.

Discretization techniques comprise a large category of different methods that can be utilized for the solution of the PBE framework. There are, undoubtedly, the preferred approach for solving a general PBM since the full distribution can be calculated, regardless of the internal coordinate dimensions. Discretization methods, as implied by their name, separate the internal coordinates of interest into finite number of grid points (i.e. bins) reducing the PBE to a set of ODEs. Depending on the PBM's number of internal coordinates and their subsequent size of the distribution, a large number of grid points might be required. This most potentially would increase the computational time significantly since each grid point is described by an ODE. Therefore, by increasing the grid points the number of ODEs that needs to be simultaneously solved is increased as well. Towards this direction, selecting an appropriate type of grid can reduce the computational type considerably. In the case of crystallization where nucleation is typically generated as a pulse at the beginning of the process, utilization of a geometrical instead of a linear grid seems to be the most efficient strategy (Qamar and Warnecke, 2007).

The method of characteristics (MOCH), which belong to the discretization methods, is an effective approach for solving PBMs. The method employs characteristic curves (for a first order PDE, lines are used) as basis function to reduce the partial differential equation to a set of ODEs (Fevotte and Fevotte, 2009). The method has illustrated remarkable accuracy during the prediction of CSD, comparing to other discretization techniques (Mesbah et al., 2009). Nevertheless, challenges may arise during its implementation since the spatial grid mesh, over which the crystal size distribution is discretized, is not fixed.

Finite – difference method (FDM), is one of the most applied discretization numerical techniques for solving PDEs, due its simplicity. However, in the case of the PBEs, the method

fails to provide sufficiently accurate results. Moreover, due to numerical diffusion, sharp discontinuities do arise during the solution (Mahoney and Ramkrishna, 2002). This problem can be eliminated if higher – order FDM schemes are utilized and/or the resolution of the mesh is increased. However, as a result the computational time is increased as well, making FDM not a preferred option for model based control and optimization. Finite volume (FV) schemes, on the other hand, have illustrated advanced capabilities at the conservation of the scalar quantities and hence they provide an improved alternative to finite difference. FV can be utilized for the solution of all crystallization phenomena (i.e. nucleation, crystal growth, breakage and agglomeration) and has been extensively investigated since it is the most promising technique that can be employed for the solution of hyperbolic PDE problems (LeVeque, 2002). Especially the high order – FV schemes have illustrated higher accuracy for the solution of crystallization processes comparing to the rest of the discretization techniques, aside MOCH (Qamar and Warnecke, 2007; Mesbah et al., 2009). They have been also implemented extensively for multi-dimensional PBMs (Gunawan, 2004; Majumder et al., 2010). Nevertheless, due the computational cost, the method cannot be employed for advanced control and complex optimization problems. Towards this direction Szilágyi and Nagy (2016) utilized parallel processing in combination to a graphical processing unit (GPU) to accelerate the numerical solution of the method. Based on that, they managed to reduce the computational cost by 50 – 250 times, enabling in this way the utilization of the FV method for real – time model based – control applications. The high order FV method has been utilized in this thesis for the solution of a complex multi-dimensional PBM. Therefore, the reader is referer to **Chapter 5** for more information regarding the FV algorithm.

Finite element method (FEM) is also another discretization technique which can be utilized for the solution of PBMs. Typically, the internal coordinate domain is discretized into a finite number of elements and the solution is approximated by employing piecewise low – order polynomials. Moreover, Rigopoulos and Jones (2003) employed a FEM scheme with linear collocation elements to solve a PBM considering nucleation, growth, breakage and agglomeration. By utilizing linear collocation, the authors managed to reduce the number of interpolations comparing to a higher order scheme with the scope of reducing the computational cost. On the other hand, Nichmanis and Hounslow (1988) applied collocation and Galerkin FEM algorithms to solve a steady – state PBM. In both cases, the results showed reasonable prediction capabilities. However, Mesbah and co – authors (2009) illustrated that high resolution FV methods present increased accuracy with lower computational cost comparing to

equivalent FEM schemes. Therefore, FEM doesn't appear as an attractive option for the solutions of PBEs.

In the Lattice Boltzmann method (LBM), on the other hand, instead of solving the hydrodynamic equations by discretization, pseudo-particle kinetics are employed to recover the PBEs at the appropriate scale. The LBM was recently applied for one – dimensional and multi – dimensional PBMs, considering smooth and non – smooth distributions by [Majumder et al. \(2010;2012a; 2012b\)](#). For both the cases the LBM demonstrated advanced capabilities with respect to accuracy and convergence time. Nevertheless, the method presents substantial implementation difficulties.

Finally, dynamic monte Carlo (DMC) methods are the most generic approach for the solution of the PBE framework. Apart that all the crystallization phenomena can be considered, DMC methods are easy to implement, with respect to both mono-dimensional and multi-dimensional models, and they present significant advantages in terms of numerical accuracy. The latter occurs since the stochastic nature of DMC can describe very accurately the physical nature of the crystallization processes. Therefore, several researchers have utilized stochastic DMC for the simulation of PBMs ([Ramkrishna, 1981](#); [Smith et al., 1998](#); [Yu et al., 2015](#)). Nevertheless, the method is too computationally expensive for complex optimization and/or advanced process control applications.

2.6 Conclusions

In this Chapter, an overview of the fundamentals of crystallization were discussed. The review mainly highlights the inherently stochastic nature of crystallization phenomena and the impact of this on process understanding and development. In other words, the intrinsic complexity of the process in combination with the limited capabilities of monitoring the dynamic evolution of the phenomena has resulted in utilizing mainly empirical/ semi-empirical kinetic mechanisms, which they discard the physicality of the problem. At the same time mechanistic approaches either fail to describe the phenomena or they are applicable for only certain systems.

Additionally, modelling of crystallization processes by utilizing the population balance equations framework was also presented. The formulation and the main principles describing the PBEs were discussed with specific emphasis, however, on its numerical solution. Towards this direction, the available numerical solution methods were demonstrated. As it was

concluded, the SMOM, QMOM and the high resolution – FV schemes do present advanced overall capabilities for process modelling optimization and control purposes.

Overall, the literature review reveals that although crystallization has been extensively applied, the phenomena describing crystallization haven't been fully understood. Therefore, the development of a generalised approach of investigating crystallization both theoretically and experimentally, could enhance the process understanding and operation of the industrial crystallizers.

NOMENCLATURE

A_i	-	Molecular unit i^{th} , [-]
A_p	-	Preexponential factor, [-]
A_{eff}	-	Effective mass transfer area, [m^2]
$a_{i,i}$	-	Area of the crystal per unit, [m^2]
B_{birth}	-	Birth rate, [#/ s]
B_p	-	Primary nucleation, [#/ s]
B_s	-	Secondary nucleation, [#/ s]
b	-	Exponent of nucleation kinetics, [-]
c	-	Concentration of crystals in the solution, [g/g solvent]
c_{sat}	-	Saturation concentration of the crystals in solution, [g/g solvent]
D_{death}	-	Death rate, [#/ s]
E_p	-	Kinetic energy of primary nucleation, [kJ/mol]
Fl_i	-	Pointwise flux of the i^{th} characteristic size, [#/ m^2]
Δc	-	Absolute supersaturation, [g/g solvent]
ΔG	-	Overall excess free energy, [kJ/mol]
ΔG_s	-	Surface excess free energy, [kJ/mol]
ΔG_v	-	Volume excess free energy, [kJ/mol]
ΔG_v	-	Excess free energy per unit volume, [$kJ/mol/m^3$]

g_i	-	Exponent of growth kinetic equation of the i^{th} characteristic facet, [-]
G_i	-	Crystal growth rate of the i^{th} characteristic facet, [m/s]
h	-	Discretization size interval, [-]
$J(p)$	-	Minimum sum of squared errors, [-]
k_b	-	Nucleation kinetic constant, [#m/s]
k_B	-	Boltzmann factor, [$m^2 kg s^{-2} K^{-1}$]
k_d	-	Diffusion coefficient, [-]
k_{gi}	-	Growth kinetic constant, [m/s]
k_G	-	Overall crystal growth constant, [m/s]
k_m	-	Overall mass transfer coefficient, [mol/s]
k_r	-	Reaction rate coefficient, [-]
$n_{i,j}$	-	Size and shape distribution, [#m ²]
$\bar{n}_{i,j}$	-	Cell average of $n_{i,j}(x_1, x_2, t)$ over the (i, j) cell, [#m ²]
N_{av}	-	Total number of particles per unit volume of physical space, [[#m ³]
NG_i	-	Number of discretization points of the i^{th} characteristic size, [#]
N_p	-	Power number input, [-]
Q	-	Volumetric flow rate, [m ³ s ⁻¹]
r	-	particle size, [m]
R	-	Ideal gas constant, [Pa m ³ mol ⁻¹ K ⁻¹]
S	-	Supersaturation ratio, [-]
T	-	Temperature, [K]
t	-	Time, [s]
V	-	Volume of the crystallizer, [m ³]

GREEK LETTERS

$\beta_{i,k}$	-	Constant of the effectiveness factor, [m/K]
---------------	---	---

γ_i	-	Edge free energy on the i^{th} crystal face per unit length, $[J/m]$
$\mu_{m,r}$	-	m, r^{th} order mixed moment of size variables
μ_{solid}	-	Chemical potential of the solid state, [-]
$\mu_{solution}$	-	Chemical potential of the solute molecules, [-]
$\sigma_{m,r}$	-	m, r order joint moment, [-]
σ	-	Relative supersaturation, [-]
σ_{int}	-	Interfacial tension, $[J/m^2]$
φ	-	Flux limiter function, [-]
φ_{coeff}	-	Contact angle coefficient, [-]
Ω^κ	-	Particulate Space, [-]

3 SYSTEMATIC MODEL – BASED DESIGN AND OPTIMIZATION OF BATCH AND CONTINUOUS COOLING CRYSTALLIZATION PROCESSES

The purpose of this chapter is to develop a systematic computer-aided methodology for the design of batch and continuous crystallization processes through the implementation of optimization frameworks to assess the achievable crystal quality attributes (CQAs) by manipulating the critical process parameters (CPPs). Paracetamol in water and potassium dihydrogen phosphate (KDP) in water are considered as the case studies. The systems are modelled utilizing single and multi-dimensional population balance models (PBMs) for paracetamol and KDP respectively. For the batch crystallization systems, single and multi-objective optimization are carried out to determine the optimal operating trajectories by considering mean crystal size and the crystal size distribution standard deviation, for both the 1D and 2D cases, and the mean aspect ratio of the crystals, for the 2D case, as the objective functions. For the continuous crystallization systems, the attainable region approach is employed to identify the performance of multi-stage MSMR for various operating conditions and configurations. As such, the attainable regions are estimated in diagrams of mean crystal size against total residence time. Multi-objective optimization is also applied to determine a Pareto optimal attainable region with respect to multiple CQAs, such as mean length size and aspect ratio versus total residence time. The capability of utilizing various optimization frameworks is exploited to determine the feasible range of the design space (DS) and whether a desired product specification can be attained for the studied systems in certain configurations.

This methodology proved to be an essential tool that can be applied as a reliable model-based design practise for the identification of robust attainable regions (ATRs). By identifying the feasible range of a crystallization system, the manufacturing capabilities of the process can be explored, in terms of mode of operation, CPPs recipes, and equipment configurations, that would lead to the selection (i.e. decision making) of optimum operation strategies for the manufacturing of products with desired CQAs under given operating and business constraints.

Highlights:

- Batch and Continuous 1D and 2D crystallization systems are modelled utilizing PBM.
- Design space determined via employing optimization frameworks for both systems.
- High dimensional attainable regions (ATRs) obtained for 1D and 2D PBMs.
- Single - objective and multi - objective optimization employed for 1D and 2D PBMs.

3.1 Introduction

In industrial crystallization, three different modes of operation are mainly utilized: batch, semi-batch and continuous (Mersmann, 1988; Nývlt, 1994; Kramer & Jansens, 2003). Batch crystallization has been the most common method of operation for decades and it remains prevalent today (Chen et al., 2011; Vetter et al., 2014), since it offers considerable advantages, such as easy control of CSD, simplicity of process equipment and good traceability of off-spec product (Park et al., 2016). The latter is quite critical for industries such as pharmaceuticals. Potential problems with certain batches can be easily identified to withdraw from the market, safeguarding, in this way, the quality and safety of the product (Smith, 2005). Also, batch operation provides flexibility in equipment utilization since it can be employed to manufacture a variety of products by using the same equipment and it provides flexibility with respect to the production (i.e. reacting to demand by decreasing/increasing the number of batches). It can be also used during the development stages for screening purposes to identify an optimized recipe in order high yield to be achieved (i.e. minimum material loss). However, batch-to-batch variability, low plant availability/asset utilization and poor-scheduling (i.e. equipment cleaning and maintenance) and high operating costs, since batch processing is more labour intensive, and it requires more storage and handling steps, leads to low production capabilities (Mullin, 2001; Smith, 2005; Lawton et al., 2009; Chen et al., 2011). Semi-batch operation, also known as fed-batch, has been also employed in pharmaceutical crystallization when higher supersaturation needs to be maintained in the crystallizer (Mesbah et al., 2011). Continuous

manufacturing offers significant advantages such as, consistent and reproducible product qualities (i.e. steady-state operation), lower capital and operating costs, improved process efficiency, reduced equipment footprint, improved control performance and lower inventory levels (Lawton et al., 2009; Benyahia et al., 2013; Mascia et al., 2013; Powell, 2017; Wang et al., 2017). Based on these advantages continuous processing is the preferred and widely-applied mode of operation in many large-scale industries, such as petrochemicals and polymers, since it can ensure product consistency and cost-effective manufacturing (Smith, 2005).

Despite the benefits of continuous processing, the pharmaceutical industry has been reluctant to adopt this concept mainly due to the strict regulatory guidelines imposed by the pharmaceutical approval agencies, FDA in USA and EMA in Europe, and due to the low required production volumes (Vetter et al., 2014). Moreover, if substantial changes are made during the manufacturing of a pharmaceutical product, regulatory uncertainty for the product's approval will be created that consequently will lead to additional costs and delays during the product development stage (Gonnissen et al., 2008; Sen et al., 2013; Su et al., 2015). Also, in most of the cases, the product volume demand cannot justify abandoning the existing batch production capabilities for the development of a continuous operated process dedicated to a specific active pharmaceutical ingredient (API) (Vetter et al., 2014).

Therefore, it becomes apparent that each mode of operation has pros and cons. The decision-making, of whether continuous manufacturing or batch operation should be adopted, is based on the following criteria:

1. Techno economics.
2. Targeted product.
3. Production scale.
4. Uncertainties (e.g. market demand).
5. In-house experience and willingness to invest in non-standard technologies.
6. Technology readiness.
7. Regulatory requirements.

To this end, process systems engineering (PSE) tools, such as model-based design and optimization, can be utilized for process understanding and consequently decision making. Moreover, decision making can be done more efficiently by employing model-based approaches for the determination of the ATRs. The ATRs comprises the multi-dimensional

feasible region defined from the input variables and operating conditions in which an acceptable product quality can be guaranteed (Rathore and Mhatre, 2008; Wang and Lakerveld, 2017). Thus, by identifying the ATRs, the achievable limits of each process for every CQA can be estimated and hence the process dynamics can be fully realized and eventually controlled (i.e. by applying process control approaches – Fujiwara et al, 2003; Nagy 2017; Cao et al., 2017).

Model-based design and optimization methodologies have been extensively applied for batch and continuous crystallization processes (Rawlings et al., 1993; Kramer et al., 2000; Kramer and Jansens, 2003; Costa et al., 2005; Larsen et al, 2006; Lindenberg et al., 2009; Paroli, 2012; Yang et al., 2014;). For instance, Lang et al. (1999), utilized dynamic optimization to maximize the mean crystal size under a fixed final time. On the other hand, Mesbah et al (2010) applied a real-time dynamic optimization with the scope to maximize the batch productivity without compromising the CQAs, while Nagy et al (2008) utilized moment based PBMs and successive quadratic programming to design and compare optimal control strategies, such as classical temperature control and concentration control for batch processes. Design and optimization studies have also been utilized in seeded crystallization processes since the seed characteristics have a great impact on the attained final CSD along with the applied temperature trajectory. To that end, Chung et al. (1999) presented a dynamic programming formulation that optimizes the CQAs with the supersaturation profile and the seed characteristics to be the control variables, while Aamir et al. (2010) presented a novel approach that employs dynamic optimization to determine the optimal seed recipe, which is generated by the combination of seeds from various sieved seed fractions with the scope of achieving a desired final CSD. Although identification of the optimum process operation trajectories considering a single objective function, such as maximizing the mean crystal size or minimizing the coefficient of variation, has been applied for numerous cases, application of multi-objective optimization in crystallization processes is rather limited (Bhat and Huang, 2009; Hemalatha and Rani, 2016). Sarkar et al. (2006) were the first who presented the application of multi-objective optimization to improve multiple CQAs of a seeded batch crystallization process by utilizing the non-dominated sorting genetic algorithm (NSGA). Similar analysis was recently performed by Hemalatha and Rani (2017), which considered both seeded and unseeded batch crystallization systems and different objective functions, such as mean size, coefficient of variation and nucleated mass. Also, Acevedo et al. (2015) applied a weighted, multi-objective gradient based algorithm (successive quadratic programming (SQP)) to evaluate and construct the Pareto front. For this system, a complex multi-dimensional PBM was employed with the scope of improving the mean size and

the mean aspect ratio of the population of crystals, which correspond to size and shape objectives respectively.

Continuous crystallization for pharmaceutical applications is currently an area of high interest and therefore, more and more, design and optimization studies have also been carried out by various researchers (Majumder et al, 2013a; Sen et al., 2013; Ridder et al, 2014; Vetter et al., 2014; Su et al, 2015; Power et al., 2015; Park et al., 2016). For example, Yang and Nagy (2015a) modelled and optimized a continuous cascade MSMPR system by taking into consideration both the start-up and steady-state behaviours for a combined cooling and anti-solvent crystallization system. For the same system, advanced process control schemes - decentralized proportional-integral-derivative (PID) control and nonlinear model predictive control (NMPC) - were also employed and compared by the same investigators (Yang & Nagy, 2015b) with the scope of developing a robust modelling framework for process design, optimization and control. Similarly, Su et al. (2015) presented a rigorous framework for mathematical modelling, optimization and control of single/multi-stage continuous Mixed Suspension Mixed Product Removal (MSMPR) crystallizers, while advanced control, C-control strategy, was utilized to ensure that the continuous MSMPR operation remains within the predetermined design space. Also, continuous API purification processes have been modelled and optimized employing integrated flowsheet modelling. Moreover, Sen et al. (2013) optimized the start-up cooling process of a continuous MSMPR crystallizer followed by filtration, drying and mixing of the API with an excipient. Also, Benyahia et al. (2013) developed a plant-wide mathematical model, based on continuous pharmaceutical pilot plant developed at Novartis-MIT centre (Mascia et al., 2013), that was used for design, optimization and process control purposes (Lakerveld et al., 2013; Mesbah et al., 2017). The effect of numerous process parameters was investigated with the scope of improving pilot plant performance, while at the same time alternative start-up strategies were used to reduce the time to steady-state and consequently minimize the product loss (Benyahia et al, 2013). Vetter et al. (2014), on the other hand, presented first a detailed process design methodology that allows the determination of attainable particle sizes for crystallization processes under a set of constraints utilizing moment-based PBMs. Moreover, attainable regions (ATRs) were estimated for multi-stage MSMPRs, plug flow and semi-batch crystallizers for three different case studies, where the supersaturation was generated by cooling, anti-solvent, and a combination of cooling/anti-solvent crystallization. It should be mentioned, that for these cases studies steady-state modelling was applied. Based on the latter work, Graham et al. (2015), estimated the ATR for a cascade

MSMPR configuration for the cooling crystallization of acetaminophen (paracetamol) in aqueous isopropanol solution by employing analytical expressions for the solution of the PBM and simple kinetic expressions for describing the phenomena. Finally, the ATR theory was also employed for the determination of the design space of a hybrid technology for separation, which combines continuous crystallization and membranes (Wang and Lakerveld, 2017). It was proved that membranes can enlarge the ATR, providing process flexibility since they can allow solvent removal that consequently can generate additional supersaturation if needed.

Although significant research has been already conducted for the design and optimization purposes for 1D crystallization purposes, a process design methodology for multi-dimensional PBMs is an open subject in the literature. Therefore, in this chapter, a computer-aided methodology is developed for the design of batch and continuous mode operated processes through the implementation of various optimization frameworks (i.e. single and multi-objective) to assess the achievable crystal quality attributes (CQAs) by manipulating the critical process parameters (CPPs) for both single and multi-dimensional PBMs. Moreover, the objective of this chapter is to investigate how model-based approaches can be employed for the identification of the design spaces for different modes of operation by considering two different chemical systems characterized by 1D and 2D PBMs. After the mathematical models are formulated, single and multi-objective optimizations are applied to systematically estimate those ATRs for both batch and cascade MSMPR configurations. In this way, the design space for each process can be compared and decisions can be made regarding the operating conditions and mode of operation for each system. Systematic studies for the construction of the ATRs for multi-dimensional pharmaceutical processes have not been published to the best of our knowledge. Also, it is the first time that multi-objective optimization is presented as a robust way of determining the design space for both 1D and 2D PBM crystallization processes.

The remainder of this Chapter is organized as follows: In **section 3.2**, a summary of the mathematical formulation of the population balance equation (PBE) will be presented. In **section 3.3**, the single and multi-objective optimization procedure utilized for both case studies is presented and detailed description of the performance objectives is given, while the methodology of employing ATR theory for the determination of the design space is also presented in detail. In **section 3.4**, the optimization and ATR results obtained for each case study are presented and discussed, while the Chapter ends with some concluding remarks in the **conclusions** section.

3.2 Process Models

To date, there are three main setups that have been utilized for continuous crystallization development: the mixed - suspension mixed - product removal (MSMPR) crystallizer ([Larson and Randolph, 1988](#)), the plug flow crystallizer (PFC) ([Alvarez and Myerson, 2010](#); [Simon and Myerson, 2011](#); [Koswara and Nagy, 2015](#)) and the continuous oscillatory baffled crystallizer (COBC) ([Lawton et al., 2009](#); [Briggs et al., 2015](#); [Brown et al., 2015](#); [Pena et al, 2017a](#)). Among these alternatives, the MSMPR offers the most efficient route to continuous crystallization development for pharmaceutical applications, since it is based on the stirred tank reactor (STR) design. PFCs, on the other hand, present a considerable implementation obstacle which is related with the need to retain the crystals suspended by operating at high velocities to achieve a turbulent flow behaviour within the pipe ([Vetter et al., 2014](#)). As a result, low process productivity can be achieved which makes it impractical for pharmaceutical applications. Another significant drawback that PFCs present is that fouling seems to occur in higher frequency comparing to other platforms, such as MSMPR ([Majumder and Nagy, 2015](#)). On the other hand, new continuous crystallization platforms, such as COBC, are not fully understood and have not been broadly implemented, which could lead to regulatory impediments ([Su et al., 2015](#)). It should also be mentioned that MSMPR crystallizers provide increased process flexibility, comparing to the rest of crystallization platforms, since the operating volumes and the residence time could be easily manipulated to meet system targeted operating conditions. Most significantly, a variety of crystallization systems (e.g. having fast and slow kinetics) can be handled more easily in comparison to other configurations. One drawback however is that the MSMPR crystallizer generates a CSD that is broader compared to the ones attained from tubular crystallizers, such as PFC or COBC ([Ferguson, 2012](#)). So, it becomes apparent that the process design of multi-stage MSMPR is of significant interest for the ongoing shift from batch to continuous operation and hence in this study that configuration will be explored and will be compared with the corresponding non-isothermal batch crystallization setup.

To model crystallization processes, and consequently determine the CQAs of the system, such as size and shape, population balance equation (PBE) models coupled with mass and energy balance equations are employed, as mentioned in more detail in **Chapter 2** ([Randolph and Larson, 1988](#); [Ramkrishna, 2000](#)). Assuming that the batch and continuous crystallizers to be modelled are well-mixed at both macro-scale and micro-scale level (i.e. no classification occurs), are unseeded, and no agglomeration or breakage phenomena are present, the population

balance models with the corresponding initial (I.C.) and boundary conditions (B.C.) can be given respectively by:

$$\begin{array}{l} \text{PBEs} \\ \text{Batch} \end{array} \quad \frac{\partial n(t, \mathbf{X})}{\partial t} + \nabla_{\mathbf{X}}[G n(t, \mathbf{X})] = B \delta(\mathbf{X} - \mathbf{X}_0) \quad (3.2)$$

$$\text{I.C.} \quad n(\mathbf{X}, t = 0) = 0 \quad (3.2)$$

$$\text{B.C.1} \quad \begin{array}{l} \lim_{\substack{X_1 \rightarrow L_n \\ X_2 \rightarrow L_n \\ \vdots \\ X_N \rightarrow L_n}} [\mathbf{G}_1 + \mathbf{G}_2 + \dots + \mathbf{G}_3] = 0, \quad X \in \partial\Omega \end{array} \quad (3.3)$$

$$\begin{array}{l} \text{PBEs} \\ \text{MSMPR} \end{array} \quad \frac{\partial n(t, \mathbf{X})}{\partial t} + \nabla_{\mathbf{X}}[G n(t, \mathbf{X})] = B \delta(\mathbf{X} - \mathbf{X}_0) - \frac{1}{\tau} n(t, \mathbf{X}) \quad (3.4)$$

$$\text{I.C.} \quad n(\mathbf{X}, t = 0) = n_0(\mathbf{X}) \quad (3.5)$$

$$\text{B.C.1} \quad \begin{array}{l} \lim_{\substack{X_1 \rightarrow L_n \\ X_2 \rightarrow L_n \\ \vdots \\ X_N \rightarrow L_n}} [\mathbf{G}_1 n(\mathbf{X}, t) + [\mathbf{G}_2 n(\mathbf{X}, t) + \dots + [\mathbf{G}_N n(\mathbf{X}, t)] = 0, \quad X \in \partial\Omega \end{array} \quad (3.6)$$

$$\text{B.C.2} \quad \begin{array}{l} \lim_{\substack{X_1 \rightarrow \infty \\ X_2 \rightarrow \infty \\ \vdots \\ X_N \rightarrow \infty}} n(\mathbf{X}, t) = 0 \end{array} \quad (3.7)$$

where $n(\mathbf{X}, t)$ is the number density function, $\mathbf{X} = [x_1, x_2, \dots, x_N]$ is the vector containing the various characteristic lengths, B is the nucleation rate, $\mathbf{G} = [\mathbf{G}_1, \mathbf{G}_2, \dots, \mathbf{G}_N]$ is the vector of the crystal growth rate of the characteristic crystal facets, t is the time and $\partial\Omega$ is the boundary of the size space. Also, $\delta(\mathbf{X} - \mathbf{X}_0)$ is the delta distribution that characterizes the formation of the nuclei and is zero for all the values of \mathbf{X} , except when $\mathbf{X} = \mathbf{X}_0$. It should be noted that the expressions describing the kinetics are typically nonlinear functions of supersaturation, temperature but also CSD (e.g. kinetics incorporating the secondary nucleation effect).

In the present study, two systems are considered, namely paracetamol in aqueous solution and potassium dihydrogen phosphate (KDP) in water, for design and optimization. The dynamic and steady state models for the case studies are discussed below. It should be mentioned that all the developed models were solved and optimized by using the numerical computing environment, MATLAB®.

3.2.1 Unseeded Batch & Continuous Cooling Crystallization of Paracetamol

Initially, the unseeded cooling crystallization of paracetamol (also known as acetaminophen) in water, as studied by [Nagy et al. \(2008\)](#), is modelled and optimized. For this system, a 1D PBM model is considered, meaning that the generated crystals are assumed to have a fixed shape (i.e. one characteristic length: $X = [x_1]$). This simplification is quite common in crystallization modelling. Similar principles are also employed in PAT in order to provide useful information regarding the CQAs of the population. For instance, laser diffraction, which is the most common approach for measuring CSD, assumes the measured crystals are spherical in shape and reports the diameter of the volume-equivalent sphere. As expected, when laser diffraction is applied to crystals of a non-ideal shape, such as needles or plate-like crystals, the measured CSDs present a broader size distribution than they should actually have ([Polawoski et al., 2014](#)). Typically, to take this measurement error into account, constant and/or relative correction factors are applied to the quantile that can improve the accuracy of measurements.

The general PBE ([eq. 3.1 & 3.4](#)) is usually reduced to a set of ordinary differential equations (ODEs) by utilizing the standard method of moments (SMOM) since in this way the set becomes more efficient with respect to the required computational time, and consequently they can be used for simulation and optimization purposes (see [Chapter 2](#) for a detailed review on the numerical solution of PBEs).

The i^{th} moment for one characteristic dimension (x_1) is

$$\mu_i = \int_0^{\infty} x_1^i n(x_1, t) dX_1 \quad (3.8)$$

Hence, by applying the moment transformation rule ([eq. 3.8](#)) to the PBE ([eq. 3.1](#)), considering the initial ([eq. 3.2](#)) and boundary conditions ([eq. 3.3](#)), a finite set of ODEs can be acquired:

$$\frac{d\mu_0}{dt} = B \quad (3.9)$$

$$\frac{d\mu_i}{dt} = i G \mu_{i-1} + B r_0^i \quad (3.10)$$

$$\frac{dc}{dt} = -3 \rho_c k_v G \mu_2 - \rho_c k_v B r_0^3 \quad (3.11)$$

where c is the solution concentration expressed in mass of crystal per unit mass of solvent ($kg/kg_{solvent}$), r_0 is the initial nuclei size, ρ_c is the density of the crystals and k_v is the volumetric shape factor. It should be mentioned that in most of the modelling studies, describing crystallization processes, the initial nucleus size is set to zero ($r_0 \approx 0 \mu m$) for practical purposes since it leads to negligible modelling errors (Rawlings et al., 1993).

This set of ODEs (eq. 3.9 – 3.10) coupled with the component mass balance (eq. 3.11), for the solute, describes a comprehensive moment-based model for crystallization processes for modelling a 1D batch cooling crystallization process.

By following the same approach, the set of ODEs describing an N – stage MSMPR crystallizer coupled with the mass balance, can be given by (Yang and Nagy, 2015a):

$$\frac{d\mu_0^{(j)}}{dt} = \frac{V_j}{V_{j-1} \tau_{j-1}} \mu_0^{(j-1)} - \frac{1}{\tau_j} \mu_0^{(j)} + B_i \quad (3.12)$$

$$\frac{d\mu_i^{(j)}}{dt} = \frac{V_j}{V_{j-1} \tau_{j-1}} \mu_i^{(j-1)} - \frac{1}{\tau_j} \mu_i^{(j)} + i G_j \mu_{i-1}^{(j-1)} \quad (3.13)$$

$$\frac{dc_j}{dt} = \frac{V_j}{V_{j-1} \tau_{j-1}} c_{j-1} - \frac{1}{\tau_j} c_j - 3 \rho_c k_v G_j \mu_2^{(j)} \quad (3.14)$$

$$j = 1, 2, \dots, N$$

, where τ_j is the residence time at stage j and it can be given by dividing the volume of the crystallizer j (V_j) with the volumetric flow rate at the same stage ($F_{out}^{(j)}$):

$$\tau_i = \frac{V_j}{F_{out}^{(j)}} \quad (3.15)$$

It should be highlighted that in most modelling studies the solution volume of each crystallizer is considered to remain constant. The constant volume assumption, which can be easily implemented in practice by using a level controller in the vessel, is a quite reasonable assumption that should be made since during the manufacturing of a pharmaceutical product all variables should remain under steady-state operation. Moreover, potential disturbances in the system should be counteracted promptly since instabilities will potentially lead to inconsistent (i.e. out of specifications) product.

In most of the cases, the four lowest order moments (i.e., zeroth to third), calculated from the set of ODEs, could be related to the physical description of the CSD (Nagy et al., 2008; Kariwala et al., 2012), since some of them are proportional to the total number, total length, total surface area and total volume of the particles. In more detail, the interpretation of the most critical moments is as follows: μ_0 is the total number of crystals ($\#/kg \text{ Solvent}$), μ_1 is the total length of crystals ($\mu m/kg \text{ Solvent}$), μ_2 is the total surface area of crystals ($\mu m^2/kg \text{ Solvent}$) and μ_3 is the total volume of crystals ($\mu m^3/kg \text{ Solvent}$). These moments are not the only ones that have physical meaning, since their combination can also be used to determine other key properties of the crystal population, such as mean crystal sizes (eq. 3.16 – 3.18) and the standard deviation of the CSD (eq. 3.20), which can be related to the span of the distribution, as described below.

The number mean size (L_{10}) provides information about the mean crystal size of the population (more sensitive for small crystal sizes):

$$L_{10} = \frac{\mu_1}{\mu_0} \quad (3.16)$$

while the Sauter mean diameter (L_{32}) can describe the mean crystal size of the population based on the ratio between the volume of the dispersed phase to its surface area.

$$L_{32} = \frac{\mu_3}{\mu_2} \quad (3.17)$$

Similarly, the weight mean crystal size (L_{43}) can also be used to estimate the mean size of the population (more sensitive towards larger crystals).

$$L_{43} = \frac{\mu_4}{\mu_3} \quad (3.18)$$

The moments can also provide indirect information regarding the width of CSD, since they could be utilized for the estimation of the coefficient of variation and the standard deviation of the distribution respectively:

$$cv = \sqrt{\left(\frac{\mu_2 \mu_0}{\mu_1^2} - 1\right)} \quad (3.19)$$

$$S_d = \sqrt{\left(\frac{\mu_2}{\mu_0} - \frac{\mu_1^2}{\mu_0^2}\right)} \quad (3.20)$$

These expressions (eq. 3.16 – 3.20) are of high significance since they directly describe essential quality attributes of the population of crystals.

Typically, the expressions for primary nucleation and crystal growth kinetics are assumed to satisfy the following empirical power-law expressions (see full list of expressions that have been applied to crystallization processes in **Chapter 2**):

$$B = k_b \Delta c^b \quad (3.21)$$

$$G = k_g \Delta c^g \quad (3.22)$$

where k_b , k_g , b and g are kinetic parameters, where Δc denotes the absolute supersaturation (i.e. difference between the solute concentration (c) and the solubility (c_{sat}) for a specific temperature value – See **Chapter 2** for more information). It should be mentioned that supersaturation is the driving force for both nucleation and growth rates. Therefore, by tightly controlling the supersaturation, the nucleation can be suppressed while at the same time the growth can be enhanced potentially leading to the generation of crystals with desirable CQAs: Larger crystals with reduced CSD. The absolute supersaturation can be calculated by:

$$\Delta c = c - c_{sat} \quad (3.23)$$

The model parameters, physical properties and variables that are used for modelling the studied system are summarized in **Table 3.1**.

Table 3.1. Model parameters with 95% confidence intervals (C.I.), variables and physical properties utilized for the system Paracetamol in Water (Nagy et al., 2008)

Model Inputs	Values ± 95 % C.I.	Units
Nucleation rate constant, k_b	$12.97 \times 10^{-5} \pm 0.0013 \times 10^{-5}$	#/sec/ μm^3
Nucleation order constant, b	6.2 ± 0.9	-
Growth rate constant, k_g	277 ± 82	$\mu\text{m}/\text{sec}$
Growth order constant, g	1.5 ± 0.5	-
Density, ρ_c	1296	kg/m^3
Volumetric shape factor, k_v	0.24	-
Initial nucleus size, r_0	0	μm
Maximum temperature, T_{max}	318	K
Minimum temperature, T_{min}	293	K
Batch time, t_b	300	min
Solubility, c_{sat}	$(1.5846 \times 10^{-5}) T^2 - (9.0567 \times 10^{-3}) T + 1.3066$, with T in Kelvin	$\text{kg}/\text{kgSolvent}$

3.2.2 Unseeded Batch & Continuous Cooling Crystallization of KDP

In the second case study, the unseeded cooling crystallization of potassium dihydrogen phosphate (KDP) in water is modelled and optimized. The nucleation and growth kinetic parameters of KDP have been derived from the kinetic data given in Gunawan et al. (2004) and Majumder et al. (2013b). For this system, a two - dimensional (2D) PBM model is considered, meaning that the generated crystals are treated as having two characteristic lengths ($\mathbf{X} = [\mathbf{x}_1, \mathbf{x}_2]$). Furthermore, since two characteristic lengths are utilized which correspond to the length (\mathbf{x}_1) and the width (\mathbf{x}_2) of each crystal of the total population, respectively (see Fig. 3.1), bi- dimensional PBMs can be used to capture the dynamics of needle- or plate- like habit crystalline materials. Consequently, this mathematical representation can be utilized to model the **size and shape** of the crystals for batch and continuous non-isothermal crystallizers.

As before, the model, described by the general PBEs (eq. 3.1 and 3.4), can be reduced from a partial differential equation (PDE) to a set of ordinary differential equations (ODEs) by using the **joint** standard method of moments (SMOM). For the 2D case, utilizing the SMOM as a

reduction method is not only related with improving the computational efficiency of the process, but also with practical aspects. In more detail, only average properties are needed for the determination of the mean sizes and mean aspect ratio (AR), which are the only size and shape related CQAs that can be monitored reliably based on up-to-date process analytical tools (PAT) capabilities, that are limited to on-line microscopy (e.g. Lasentec Particle Vision and Measurement V819 (PVM)). These measurements can be directly related to the moments (see **eq. 3.31 – 3.33**) and hence, utilizing the SMOM approach, since only nucleation and crystal growth is taking place during the cooling crystallization of KDP in water, can be considered the most relevant approach for investigating the dynamics of the process. Of course, more advanced numerical solution approaches, such as high-resolution finite volume (HR – FV), can also be utilized, if needed, for the full reconstruction of the CSSD (see **Chapters 2 and 5** for more details).

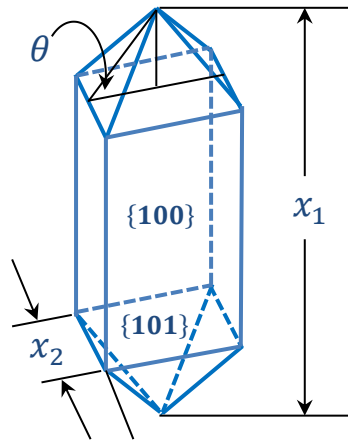


Figure 3.1. Graphical representation of the morphology of the KDP crystal.

The joint moments for two characteristic dimensions $\mathbf{X} = [x_1, x_2]$, can be calculated by:

$$\mu_{k,m}(t) = \int_0^{\infty} \int_0^{\infty} x_1^k x_2^m n(x_1, x_2, t) dx_1 dx_2, \quad k, m = 0, 1, 2 \dots \quad (3.24)$$

Hence, by applying the moment transformation rule (**eq. 3.24**) to the PBEs (**eq. 3.1**), considering the initial (**eq. 3.2**) and boundary condition (**eq. 3.3**), a finite set of ODEs can be acquired, which represents the PBEs coupled with the mass balance for a single batch stage operated at a constant volume:

$$\frac{d\mu_{0,0}}{dt} = B \quad (3.25)$$

$$\frac{d\mu_{k,m}}{dt} = k G_1 \mu_{k-1,m} + m G_2 \mu_{k,m-1} \quad , k, m = 0,1,2, \dots \quad (3.26)$$

$$\frac{dc}{dt} = -\rho_c (G_1 \mu_{02} + 2G_2 \mu_{11} - 2G_2 \mu_{02} \tan \theta) \quad (3.27)$$

where G_1 and G_2 are the size - independent growth rates along the length and width of the crystals and B is the nucleation rate (as before in the 1D case). This set of ODEs (eq. 3.25, 3.26) coupled with the component mass balance (eq. 3.27), for the solute, describes a comprehensive moment - based model for crystallization processes suitable for a 2D batch cooling crystallization process.

Similarly, the set of ODEs describing an N – stage MSMMPR crystallizer coupled with the mass balance, can be given by:

$$\frac{d\mu_{0,0}^{(j)}}{dt} = \frac{V_j}{V_{j-1} \tau_{j-1}} \mu_{0,0}^{(j-1)} - \frac{1}{\tau_j} \mu_{0,0}^{(j)} + B_i \quad (3.28)$$

$$\begin{aligned} \frac{d\mu_{m,r}^{(j)}}{dt} = & \frac{V_j}{V_{j-1} \tau_{j-1}} \mu_{m,r}^{(j-1)} - \frac{1}{\tau_j} \mu_{m,r}^{(j)} + m G_1 \mu_{m-1,r}^{(j)} \\ & + r G_2 \mu_{m,r-1}^{(j)} \end{aligned} \quad (3.29)$$

$$\frac{dc^{(j)}}{dt} = \frac{\varepsilon_{j-1}}{\tau_j \varepsilon_j} (c_{j-1} - c_j) - \left(\frac{\rho_c - c}{\varepsilon_j} \right) R_V \quad (3.30)$$

$$\frac{dc_{sv}^{(j)}}{dt} = \frac{\varepsilon_{j-1}}{\tau_j \varepsilon_j} (c_{sv,j-1} - c_{sv,j}) - \left(\frac{c}{\varepsilon_j} \right) R_V \quad (3.31)$$

$$j = 1, 2, \dots, N$$

where c_{sv} denotes the concentration of the solvent and therefore the mass balance of the solvent is given by eq. 3.31. Also, ε_j is the volumetric ratio of solution (i.e. partial volume of solution in the suspension) and R_V denotes the rate of change of the total volume of the crystals in a unit volume of suspension and these properties can be calculated respectively from the following expressions:

$$\varepsilon_j(t) = 1 - V_c(t) = 1 - \mu_{1,2}(t) \quad (3.32)$$

$$\begin{aligned}
R_V(t) &= \left(\int_0^\infty \int_0^\infty G_1(x_1, t) x_2^2 n(x_1, x_2, t) dx_1 dx_2 \right. \\
&\quad \left. + \int_0^\infty \int_0^\infty G_2(x_2, t) x_1 x_2 n(x_1, x_2, t) dx_1 dx_2 \right) \\
&= (G_1 \mu_{0,2} + 2 G_2 \mu_{1,1})
\end{aligned} \tag{3.33}$$

More information regarding the mathematical formulation presented above coupled with mass and heat balance for a 2D MSMPR can also be found in the literature (Lakatos, 2007; Szilágyi et al., 2015). It is critical to be emphasized that the generated set of ODEs for the continuous 2D case present strong stiffness and therefore a transformation into normalized dimensionless state variables was performed in this work, as described comprehensively by Lakatos (2007). It should be also noted that for the same reason mentioned before, the solution volume of each crystallizer is considered to remain constant (see subsection 3.1.1 for more information).

2D PBM moment- based models require a higher number of joint moments for the estimation of the CSSD comparing to 1D PBMs. The interpretation of the most critical joint moments is as follows: $\mu_{0,0}$ is the total number of crystals and $\mu_{1,2}$ represents the crystal volume in a unit volume of suspension. Although these are the only joint moments that have a physical meaning, other ones can also be used to determine other key properties of the crystal population. Furthermore, moments can be utilized to determine the mean crystal sizes (eq. 3.34, 3.35) of the total population of each characteristic length, while the mean aspect ratio of the crystals (eq. 3.36) can be estimated by the division of the mean sizes as illustrated below:

$$\text{Mean length: } \bar{x}_1 = \frac{\mu_{0,1}}{\mu_{0,0}} \tag{3.34}$$

$$\text{Mean width: } \bar{x}_2 = \frac{\mu_{1,0}}{\mu_{0,0}} \tag{3.35}$$

$$AR = \frac{\bar{x}_1}{\bar{x}_2} \tag{3.36}$$

Table 3.2. Crystallization model parameters, variables and physical properties utilized for modelling the system potassium dihydrogen-phosphate (KDP) in Water (Togkalidou et al., 2001; Gunawan et al., 2004; Majumder et al., 2013b; Szilágyi et al., 2015; Borsos et al., 2016)

Model Inputs	Values	Units
Nucleation rate constant, k_b	7.49×10^{-8}	$\#/\mu\text{m} / \text{s}$
Nucleation order constant, b	2.04	-
Growth rate constant, k_{g1}	100.75	$\mu\text{m}/\text{s}$
Growth order constant, g_1	1.74	-
Growth rate constant, k_{g2}	12.1	$\mu\text{m}/\text{s}$
Growth order constant, g_2	1.48	-
Volumetric shape factor, k_v	0.040	-
Initial nucleus size, r_0	0	μm
Maximum temperature, T_{max}	313	K
Minimum temperature, T_{min}	293	K
Batch time, t_b	180	min
Solubility, c_{sat}	$(9.3027 \times 10^{-5}) T^2$ $- (9.7629 \times 10^{-5}) T$ $+ 0.2087$, with T in Kelvin	kg/kgSolvent

The volume of a single crystal takes the form:

$$u_c = x_1 x_2^2 \quad (3.37)$$

, while the macroscopic total volume of crystals can be estimated by

$$V_c(t) = \mu_{1,2}(t) \quad (3.38)$$

The empirical power - law expressions utilized for the calculation of the nucleation and crystal growth kinetics are the following ones:

$$B = k_b \sigma^b \quad (3.39)$$

$$G_1 = k_{g1} (\sigma)^{g_1} \quad (3.40)$$

$$G_2 = k_{g2} (\sigma)^{g_2} \quad (3.41)$$

$$\sigma = \frac{c - c_{sat}}{c_{sat}} \quad (3.42)$$

, where $k_b, b, k_{g1}, g_1, k_{g2}$ and g_2 are the kinetic parameters, while σ denotes the relative supersaturation.

The model parameters, physical properties and variables that are used for modelling the studied system are summarized in **Table 3.2**.

3.3 Optimization Problem Formulation

Mathematical optimization, which is inextricably linked to chemical process design, has been mainly utilized in crystallization for many years with the scope of identifying optimum process operation conditions that will improve single key performance indicators (KPIs) associated with a process or a combination of processes (e.g. flowsheet modelling). Consequently, applying optimization techniques by considering different KPIs can lead to the identification of the boundaries, which define a certain feasible region (FR), comprising the values of the final product attributes, which can be attained for a certain process. It should be mentioned that other model-based approaches have also been proposed through the years for the construction of the attainable region, which are simulation-based ([Giordano et al., 2011](#)). Although the latter methodology can be accurately calculated by incorporating certain constraints, it presents limitations when more complexity is added to the process (e.g. superstructures commonly used in flowsheet modelling). In more detail, utilizing large number of simulations to map the FR cannot be used as a robust methodology since implementing constraints for multiple processes can become quite challenging. Also, solution of high number of simulations is required in order the FR to be estimated accurately making this approach computational demanding. Hence, employing optimization approaches seems to be more relevant.

The idea of utilizing optimization techniques to identify all possible attained states was first presented by [Horn \(1964\)](#) for the process design of chemical reactors, which formed the basis of what is called today ATR theory. ATR theory is essentially a graphical method that can be utilized to explore the entire feasible operation space, and consequently can be used for the identification of a reactor superstructure (see **Figure 3.2**) that will yield products with the desired or optimal attributes. Moreover, ATR theory is a systematic methodology that accounts all possible outputs (related to product's attributes) that can be generated not only by varying

the CPPs (i.e. inputs) but also exploring all possible combinations of different reactor types, mixing conditions, potential recycle loops and/or side streams and etc. (Ming et al., 2016).

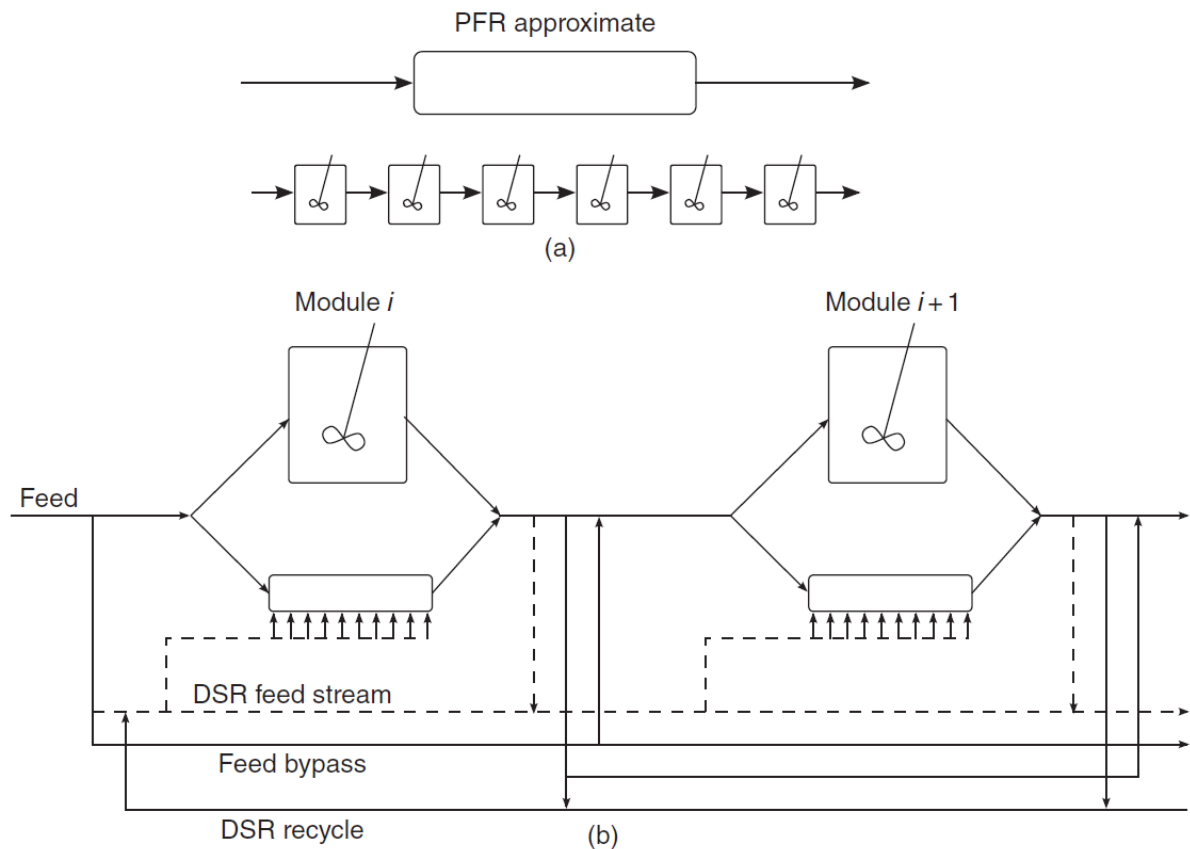


Figure 3.2. (a) A continuous stirred tank reactor (CSTR) configuration that approximates a plug flow reactor (PFR) (b) Example of a reactor superstructure (Adapted from Ming et al. (2016)).

Although this theory has been extensively applied in the areas of chemical reaction engineering, mixing and separation (Glasser et al., 1987; Hildebrandt and Glasser, 1990; Nisoli et al., 1997; Feinberg and Hildebrandt, 1997; Ming et al., 2013; Ming et al., 2016), it was only recently applied for crystallization processes utilizing 1D PBMs for perfectly mixed MSMPRs, semi-batch crystallizers and PFCs (Vetter et al., 2014; Power et al., 2015; Wang and Lakerveld, 2017). A schematic that could illustrate potential combinations of only two crystallizers is depicted in **Figure 3.3**. Hence, it becomes apparent that even with just considering a small number of crystallizers, a variety of operational alternatives exist which should be explored. Of course, some of these alternatives could be easily excluded based on the design constraints or prior in-house experience. For instance, for the reasons mentioned above, the utilization of PFCs and COBCs can be excluded since they cannot be considered as a practical option for continuous cooling crystallization. As it is clearly illustrated in **Figure 3.3**, introducing process recycle could also be a possibility to increase the residence time. However, it has been

demonstrated both experimentally and numerically by [Benyahia et al. \(2012\)](#) that introducing recycle streams can create systematic saturation with the impurities, which is why typically a purge is required on all recycle streams. Consequently, the implementation of recycling will require enhanced purification, while it decreases the capacity of the configuration with respect of rejecting non-routine process disturbances. Based on that, recycling is not going to be considered in the current work.

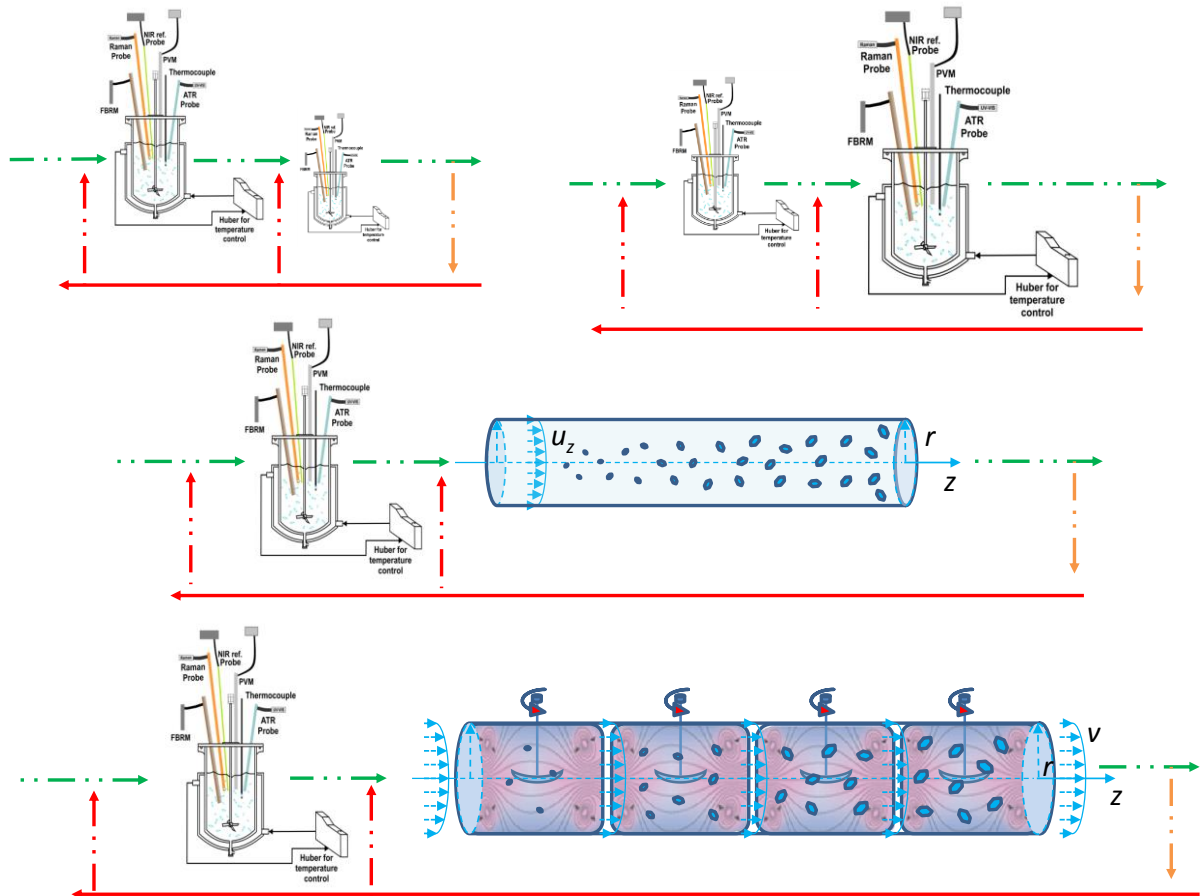


Figure 3.3. Graphical representation of possible combinations of different types of crystallizers, including potential recycle loops, feed and outflow streams.

The solution approach for the construction of ATRs can be summarized in three basic steps:

1. Consider different combinations of the available equipment
2. Find best configuration
3. Optimize based on the identified best configuration

Although, 2 and 3 are presented as separate steps, they should be considered simultaneously. In more detail, the comparison needs to be representative and therefore it should be based on the optimum performance of the potential configurations.

The superstructures can be illustrated mathematically by a system of differential algebraic equations (DAEs). To optimize the generated model, the key performance parameters are checked against one or multiple objective functions (i.e. higher dimensional ATRs) to determine optimal performance. The optimization problem formulation can be described **as maximizing and minimizing the objective functions** (e.g. Objective functions: mean crystal size, standard deviation of the distribution, process time, etc.) which are **subject to a set of constraints**, such as yield, initial and final temperature conditions.

As has already been mentioned, in the design of crystallization processes, the crystal size and shape and their corresponding distribution, are the CQAs for many pharmaceutical applications. Therefore, the ATRs of crystal size and the standard deviation related to the size distribution is investigated for the 1D case study, while the attained mean sizes, shape (i.e. mean aspect ratio) and their corresponding deviation are considered for the 2D case. Of course, depending on the number of CQAs assessed, either single-objective or multi-objective optimization problems can be formulated. Hence, optimization studies are carried out in different ways.

Since cooling batch crystallization processes are considered, the aim is to determine the optimal cooling rate/profile, which will generate the appropriate level of supersaturation over the time to produce particles with the desirable CQAs defined by the objective functions and subjected to several constraints. The optimization problem can be formulated as shown below:

$$\max/\min_{T(1),T(2),\dots,T(P)} J_{obj}(t) \quad (\text{obj.3.1})$$

$$\text{subject to: } T_{min} \leq T_i \leq T_{max} \quad (\text{c.3.1})$$

$$0 \leq R_{min} \leq \frac{dT}{dt} \leq R_{max} \quad (\text{c.3.2})$$

$$t \leq t_{final} \quad (\text{c.3.3})$$

$$\text{yield1} = c(t_{final}) - 0.6 c_0 \leq 0 \quad (\text{c.3.4})$$

where T_{min} , T_{max} , R_{min} and R_{max} are the minimum and maximum temperature and temperature ramp rates respectively. Different objective functions were utilized, $J_{obj} = [L_{10}]$, $J_{obj} = [S_d]$ and $J_{obj} = [L_{10}, S_d]$ for the 1D PBM and $J_{obj} = [\bar{x}_1, AR]$, $J_{obj} = [\bar{x}_1, AR, S_{d1}]$ and $J_{obj} = [\bar{x}_1, AR, S_{d1}, S_{d2}]$ for the 2D PBM. The total batch time (t_{final}) is set at fixed value and used as a constraint (**c.3.1**). The inequality constraint described by the expression **c.3.2** guarantees that the temperature trajectory is monotonically decreasing which prevents dissolution, while the expression **c.3.1** sets the upper and lower temperature bounds. The implementation of the temperature ramp rates (**expression c.3.2**) is related to the cooling capabilities of the utilized heat exchangers and, in this case, was selected to keep the cooling rates boundaries within the range of 0 to -2 °C/min. The final constraint (**c.3.4**) allows the consideration of the desirable yield. The problem defined above is a dynamic optimization problem where the temperature $T(t)$ is the control variable. Hence, the input temperature trajectories were discretized as a piecewise linear function (piecewise continuous) with a finite number of decision variables over time (Sarkar et al., 2006; Acevedo et. al., 2015; Hemalatha and Rani, 2017). The batch time is discretized into P equal steps in the time interval $[0, t_{final}]$ – by the expression described in **equation 3.43**. Then, by solving the optimization problem, an optimal control vector can be determined at each iteration (**eq. 3.44**).

$$t = 0: \frac{t_{final} - t_0}{P} : t_{final} \quad (3.43)$$

$$T(t) = T(l) + \frac{(T(l+1) - T(l))(t - t(l))}{t_{final}/P} \quad (3.44)$$

$$l = 1, 2, \dots, P.$$

In contrast to optimize the MSMR configurations, the methodology is simpler since the optimization is a traditional nonlinear programming (NLP) problem where a steady-state model is used and the control variables are time independent. The maximal/minimal attainable mean crystal size of the N stage crystallizer ($\bar{x}_{mean,N}$), considering a certain number of MSMRs and fixed total residence time, can be estimated by solving the following single-objective nonlinear optimization problem:

$$\max/\min_{T_i, \tau_i} \bar{x}_{mean, N} \quad (\text{obj.3.2})$$

$$\text{subject to: } \sum_i^N \tau_i = \tau_{total} \quad (\text{c.3.5})$$

$$T_{min} \leq T_i \leq T_{max} \quad (\text{c.3.6})$$

$$\text{yield2} = \frac{c_0 - c_N}{c_0 - c_{sat}} \geq 0.95 \quad (\text{c.3.7})$$

where c_0 , c_N and c_{sat} are the feed (i.e. initial) stream concentration, the MSMPR steady-state concentration in stage N and the equilibrium concentration of the corresponding operating temperature also in stage N respectively. For the MSMPR case studies, the fractional yield is utilized, which represents the amount of material obtained in a specific stage during the crystallization process relative to the amount of the available supersaturation and it can be described by **expression c.3.7**. The yield requirement is set to be ≥ 0.95 , meaning that only configurations yielding more than this value can be considered as valid solutions of the optimization problem. Of course, in general, this can change depending on the system and the imposed design requirements. It has been proven by [Vetter et al. \(2014\)](#) that the more stringent the yield constraint is, the narrower the boundaries of the ATR should be. Also, the total residence time (τ_{total}) in the multi-stage MSMPR is introduced as a constraint (**expression c.3.5**) and it is a fixed value.

The decision variables of the presented optimization problem are the temperature and the residence time of each crystallizer, while the remaining process variables, such as the total residence time, number of crystallizers and the initial and final temperature are kept fixed. Of course instead of $\bar{x}_{mean, N}$ other objective functions can be employed, as described before (i.e.

$$J_{obj,1D} = [L_{10}, S_d] \text{ and } J_{obj,2D} = [\bar{x}_1, AR, S_{d1}, S_{d2}].$$

The solution of the objective function (**obj.3.2**) provides the boundaries of the ATR, meaning the maximal/ minimal points with respect to different process time, as shown in **Figure 3.4**. However, in order to construct the whole feasible region an additional single point is required. Moreover, an extra optimization problem needs to be performed for the identification of the minimum time needed in order all the requirement constraints posed in the latter optimization problem to be fulfilled. This corresponds to the point that both local minima/maxima are located

to the same exact point and consequently the system reaches its limit under certain constraints (see **Figure 3.4**).

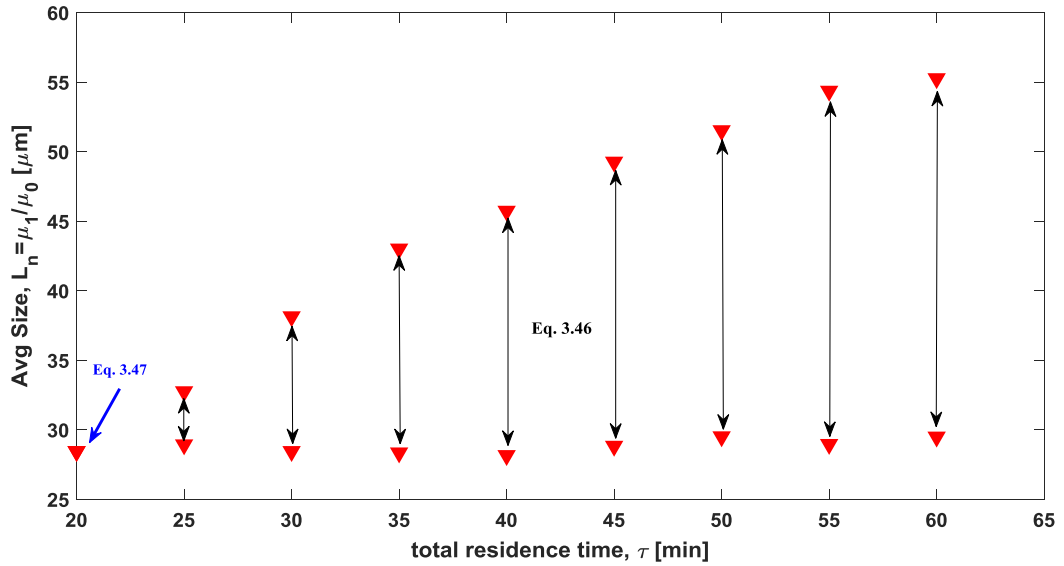


Figure 3.4. Construction of the attainable region of particle size for a cascade of 3 MSMPR crystallizers for the cooling crystallization of paracetamol in water. The optimization problems solved for the determination of the FR are indicated by the equations and the arrows respectively.

This single point can be directly estimated through the following optimization (**obj.3.3**):

$$\min_{T_i, \tau_i} \tau \quad (\text{obj.3.3})$$

$$\text{subject to: } \sum_i^N \tau_i = \tau_{total} \quad (\text{c.3.8})$$

$$T_{min} \leq T_i \leq T_{max} \quad (\text{c.3.9})$$

$$\text{yield2} = \frac{c_0 - c_N}{c_0 - c_{sat}} \geq 0.95 \quad (\text{c.3.10})$$

The formulated optimization problems (**obj. 3.1, 3.2 and 3.3**) belong to the category of constrained nonlinear programming problems (NLP). The optimization problems are expected exhibit many local optima and therefore, classical derivative-based optimization algorithms are not recommended since they could easily be stuck in local maxima/minima. Although global nondeterministic optimization algorithms cannot guarantee that the global optimum can be found, they can increase considerably the probability of doing so. Hence, in this work, global and hybrid approaches were utilized to calculate the operating profiles. Moreover, the global

approach was comprised by the application of genetic algorithm while the hybrid method consisted of the combination of genetic algorithm with sequential quadratic programming (SQP), which is a local gradient based algorithm (Beers, 2006). It should be mentioned that for the multi-objective optimization, a real-coded elitist nondominated sorting genetic algorithm (NSGA) was employed (Deb, 2001).

The genetic algorithm (GA) is a stochastic (heuristic) optimization method widely utilized for solving both constrained and unconstrained optimization problems. The algorithm fundamentally mimics the biological evolution (i.e. natural selection) to find the best individuals within given generations. By mutation, crossover and selection the individual solutions evolve from one generation to the other and converge towards an optimal solution based on biological principles of selection. The modification of the population consists in selecting the fittest individuals of the population and rejecting the rest of them, which are significantly outperformed by the former ones. The genetic algorithm presents major differences compared to the gradient based methods. Instead of generating one point at each iteration, as in the case of the gradient based methods, a population of points is created. From this population the best points (i.e. fittest points) – which are the ones that outperform the rest of the generations – are retained and used for crosslinking to generate new offspring that will improve the next generation. Additionally, individuals randomly generated are added to complete the next generation and prevent the algorithm from being stuck at a local optimum. In contrast, the classical methods chose the next point in the sequence by utilizing a deterministic computation. More information regarding the employed optimization algorithms could be found in the literature (Deb, 2001; Beers, 2006; Sivanandam and Deepa, 2008; Sharma and Rangaiah, 2013; Wang and Wu, 2013).

In this section, a general systematic methodology is presented for the determination of the FR for both batch and continuous crystallization systems. The presented methodology can account numerous combinations of different crystallizers but also it can be easily extended to account additional process variants such as, recycle operations, product classifiers, fines dissolutions loops, membranes etc. (Vetter et al. 2014; Wang and Lakerveld, 2017).

3.4 Results and Discussion

To validate the methodology described in **section 3.3** two well-studied cooling batch crystallization systems have been used as case studies: the cooling crystallization of paracetamol grown from an aqueous solution and the cooling crystallization of potassium dihydrogen phosphate (KDP) in water. For both case studies, batch and continuous mode of operation were considered. It should be highlighted that the same kinetic expressions and parameter values were employed for modelling and optimization of both modes of operation.

Even though, the same experimental configurations as presented in literature were considered, the kinetics of a chemical system can vary depending on the corresponding mode of operation, since different operating conditions will be generated. Although, some of the key operating variables could be set to certain values (e.g. initial and final temperature, initial supersaturation, etc.) there are other ones, such as the hydrodynamics, the supersaturation, the suspension density, the residence time and its corresponding distribution, and the heat transfer within the bulk (i.e. cooling rate and temperature trajectory) that will significantly vary. Therefore, in order to account of these variations, the parameters should be re-estimated when a different mode of operation is employed, otherwise there is the possibility that the kinetics may not represent the true rates, which consequently will lead in calculation errors. At the same time, it has been demonstrated ([Garside et al., 1982](#); [Palwe et al., 1985](#)) that the parameter identification studies should be conducted in a batch mode, since data with higher information content due to the dynamic nature of the batch operated crystallization can be obtained compared to utilizing a continuous steady-state MSMR crystallizer ([Rawlings et al., 1993](#)). Moreover, by employing batch crystallization, transient responses can be used to identify the kinetic parameters reliably since the whole range between the metastable zone width (MSZW) can be investigated. Other advantages relate to the large number of operating conditions that can be studied in a short time, while minimum development time and investment is required for the operation of a batch crystallizer ([Rawlings et al., 1993](#)). Thus, even when kinetics are needed for the description of a continuous process, batch experiments should be conducted in combination with continuous ones for the efficient determination and validation of the model parameters. Hence, it is common in modelling studies, during the initial development stages, for parameter kinetics from batch crystallization to be utilized for the process design and development of continuous processes ([Mersmann, 2001](#); [Lakatos, 2007](#); [Vetter et al. 2014](#); [Vetter et al. 2015](#); [Szilágyi et al., 2015](#)). In this study the same assumption was adopted for practical purposes since the

availability of kinetic data is rather limited for both modes of operation. Therefore, it was considered that the parameter estimates for both systems do not deviate significantly with respect to the mode of operation and they can be used reliably in the design of both batch and continuous cooling crystallization processes based on the same process geometry (i.e. stirred tank reactor (STR) design) agitation conditions and dimensions.

Another point of discussion is related to the construction of the ATR. The crystallization kinetic parameters and certain operating process variables are required for the determination of the ATR. The crystallization kinetic parameters that were obtained from the literature (see **Table 3.1** and **Table 3.2**) characterize primary nucleation and crystal growth phenomena, which are the main mechanisms observed during the crystallization of the investigated systems. Of course, the same methodology can be employed to cope with additional complexity and phenomena, but limitations arising from the numerical solution of the PBM should also be considered. The implementation of SMOM, for example, is limited to describe primary and secondary nucleation, size-independent growth phenomena and binary breakage (see **Chapter 2** for more details). Therefore, more advanced schemes, such as HR-FVM, need to be utilized if additional phenomena are present. Also, it should be noted that MSMR crystallizers can exhibit multiple steady states depending on the dominant nucleation mechanism and the employed kinetic expressions ([Sherwin et al, 1967](#); [Lakatos, 2007b](#)) and consequently stability analysis should be conducted if there is uncertainty regarding the uniqueness of the steady state. Moreover, the presence of secondary nucleation might generate multiple (e.g. one, two or even three) steady states ([Lakatos, 1996](#)). In contrast, the presence of primary nucleation can eradicate the steady state output multiplicity. Especially, in the case where primary nucleation is the dominant mechanism, it can be guaranteed that the crystallizer will demonstrate a unique steady state ([Lakatos, 1992](#)). Therefore, the considered case studies are considered to exhibit unique steady states and no further stability analysis should be conducted. The second aspect, is associated with the operating variables, such as the temperature initial and final values. Whereas the feeding conditions and/or properties are usually determined by the process preceding crystallization, and therefore cannot be manipulated, the outlet properties can be varied with respect of achieving the desired KPIs under certain economic and supply chain constraints. For instance, obtaining a specific yield is more critical than producing crystals of a certain size ([Power et al., 2015](#)). Besides improving the process efficiency and production level (i.e. maximize the recovered solute fraction), achieving high yield is also critical since it is related with the exit temperature and exit supersaturation. In more detail, obtaining a low yield means

that the solute concentration within the bulk would be high after the end of crystallization. Hence, this means that potential changes of temperature (i.e. hot slurry that cools down) and/or concentration (i.e. solvent removal) during filtration might create local supersaturation gradients. Consequently, uncontrolled crystallization can take place causing changes in CSSD. Additional to that, it can also increase significantly the probability of blockage to occur. As a result, this can have a major impact on the filtration and drying time (i.e. processability) and flowability of the product. Therefore, it becomes essential a high yield to be achieved during crystallization processes. Without doubt, changing these constraints would have an immediate effect on the FR with respect to the absolute attained states. In consideration of the foregoing, the operating variables, CPPs and constraints were chosen to be realistic for pharmaceutical applications.

3.4.1 Case Study 1: Unseeded Batch & Continuous Cooling Crystallization of Paracetamol

3.4.1.1 Batch Crystallization of Paracetamol

The modelling of the paracetamol crystallization is conducted by utilizing the kinetic, thermodynamic properties and operating conditions as presented in **Table 3.1**. The temperature limits were set to 318 K (45°C) and 293 K (20°C) corresponding to the maximum and minimum allowed temperature respectively, while the yield was constrained by the expression **C.3.4**, which forces the system to reach the temperature bounds in order the desirable yield to be achieved. Initially, three different cooling profiles were applied: natural, linear and cubic (aka controlled) for comparison purposes followed by the optimum profile, as shown in **Figure 3.5**.

For the estimation of the optimum profile, cooling trajectories were generated randomly through the utilization of the genetic algorithm in conjunction with SQP algorithm (i.e. hybrid algorithm) with the scope of maximizing the number mean size L_{10} . The cooling rate and the subsequent applied temperature trajectory are critical since they dictate, in conjunction with the system's kinetic parameters, the position in the metastable region and the temperature before the nucleation is generated. This is illustrated clearly in **Figure 3.5**, where the implementation of different temperature profiles leads to the generation of different trajectories on the phase diagram (see **Figure 3.5c**).

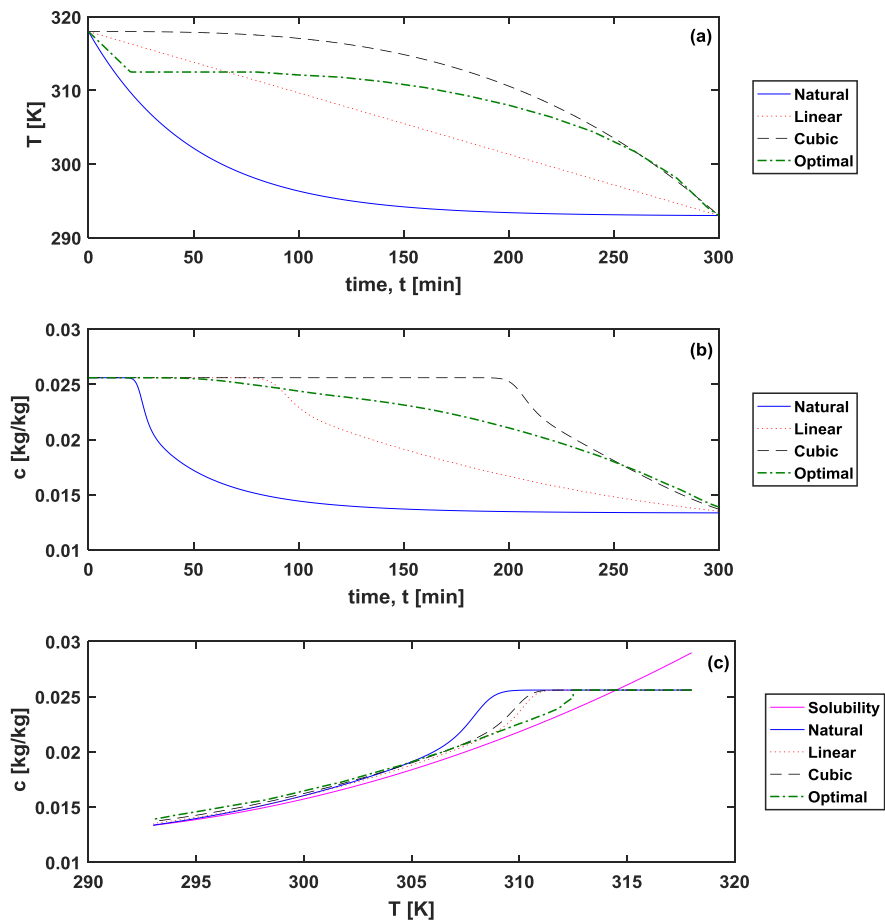


Figure 3.5. (a) Temperature, (b) solute concentration and (c) phase diagram trajectories obtained from the implementation of different cooling strategies: Natural, Linear, Cubic and Optimal cooling.

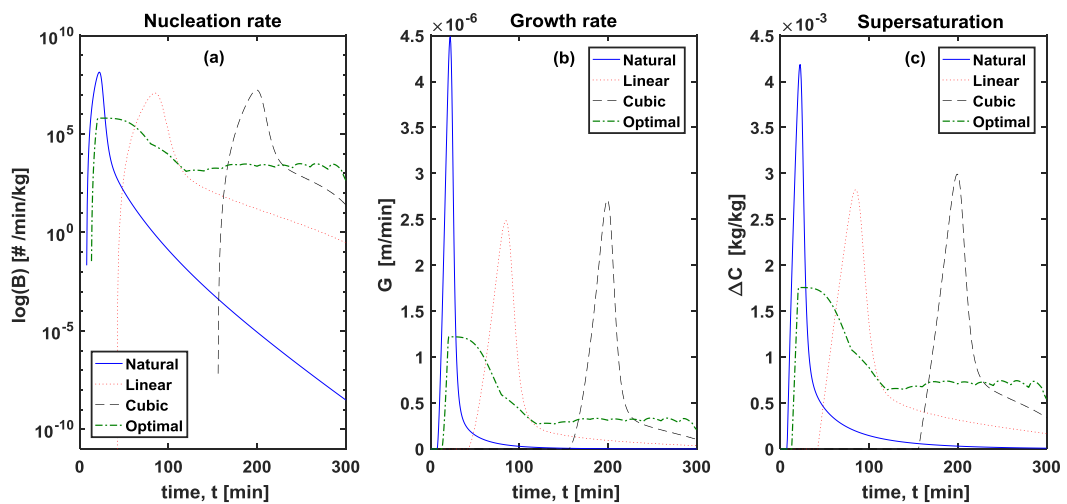


Figure 3.6. (a) Nucleation rate, (b) growth rate and (c) supersaturation trajectories obtained from the implementation of different cooling strategies: Natural, Linear, Cubic and Optimal cooling.

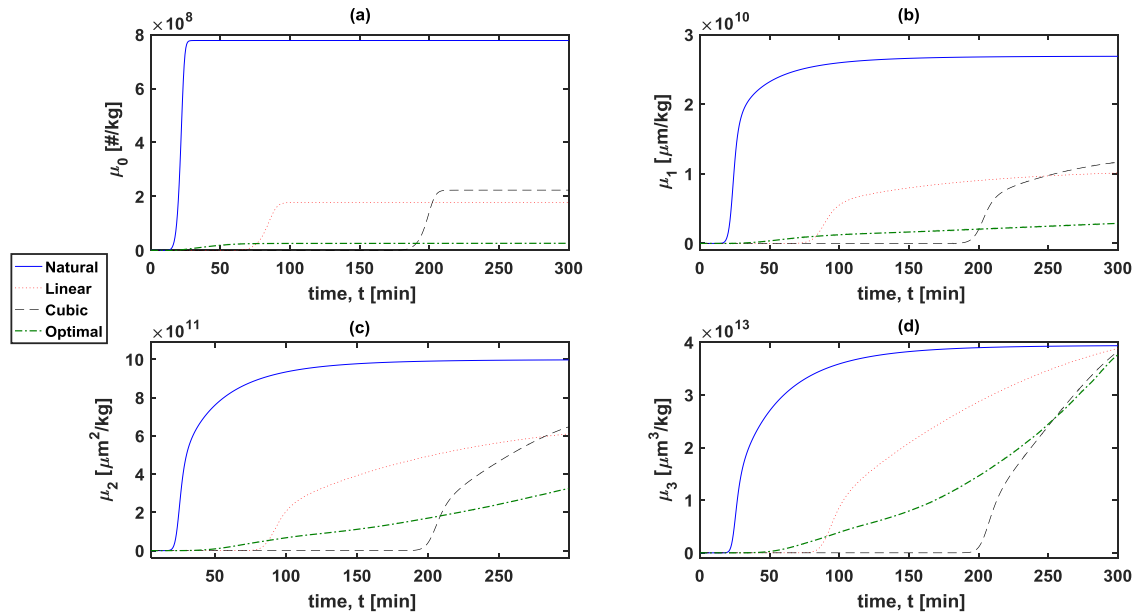


Figure 3.7. (a) μ_0 , (b) μ_1 , (c) μ_2 and (d) μ_3 trajectories obtained from the implementation of different cooling strategies: Natural, Linear, Cubic and Optimal cooling.

Applying a fixed temperature set-point during the cooling stage of a crystallization process will result in a natural profile following an exponential trajectory, as presented in **Figure 3.5**. The initial high cooling rate induced in a natural cooling profile, can create very high supersaturation, which consequently will result in excessive uncontrolled nucleation, as illustrated in **Figure 3.6**. This high cooling rate creates a large temperature gradient which consequently leads to high supersaturation. During the cooling process the system crosses the solubility curve and enters the metastable zone, after being initially in an undersaturated state (see **Figure 3.5c**). In the case of natural cooling, the increased cooling rate might lead the system to cross the MSZW and enter the labile region, where uncontrolled excessive primary nucleation occurs (see **Figure 3.6**). Therefore, at this stage, a high number of nucleus (embryos) are formed, which will consequently generate a large number of crystals, as illustrated by the high value of μ_0 (see **Figure 3.7**). Most significantly, the formed crystals present the lowest mean crystal size (see **Figure 3.8**) in comparison with the other utilized temperature trajectories, since the generated supersaturation (i.e. driving force of crystallization), is depleted for rapid growth of a large number of small crystals. In more detail, the high supersaturation which is created at the beginning, and reaches its peak at $t = 20$ mins, is used to produce high nucleation rates until $t = 40$ mins, when it can be noticed that due to the depletion of the supersaturation the nucleation and growth rate are considerably reduced, reaching gradually (after 20 mins) a steady-state, which signifies the end of the crystallization process (**Figures 3.5 – 3.9**). Of course, it should be highlighted that by utilizing a natural profile the width of the

CSD seems to obtain the smallest value in comparison with the rest of the temperature trajectories, which can be seen by noticing the dynamic trajectory of the standard deviation of the distribution in **Figure 3.9**. This was highly expected since the natural cooling trajectory presents/ high nucleation and low growth rates under a short time-span, which results in the generation of a high number of crystals with very low supersaturation for their subsequent growth, and consequently with the limited capability to vary considerably with respect to their size. Another consequence of employing a natural profile might be excessive growth at the crystallizer wall generated by local high supersaturation at the cooling surface (Tung et al., 2008).

On the other hand, the optimum profile creates high supersaturation at the beginning to initiate crystallization, and then maintains the supersaturation at a nearly constant value within the metastable zone for the rest of the batch (**Figure 3.6c**). Due to the initial temperature drop, a small number of nucleus are generated, which corresponds to the lowest number of formed crystals comparing to the rest of the profiles, as presented in **Figure 3.7a**. The growth rate corresponding to the optimum trajectory remains constant after the initiation of nucleation, resulting to a nearly linear increase of the mean size. It can also be noticed that the rest of the moments follow similar trends (see **Figure 3.7**). The linear and cubic profile on the other hand, utilize cooling rates that are much slower at the initial stages of the natural cooling and their results are presented in in **Figures 3.5 – 3.9**.

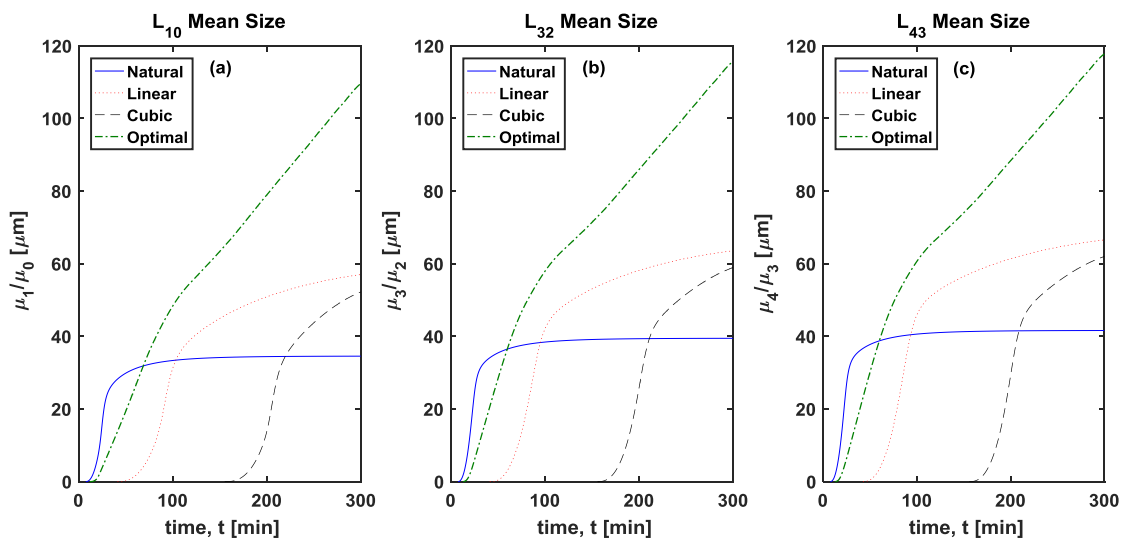


Figure 3.8. (a) Number, (b) Sauter and (c) weight mean size trajectories obtained from the implementation of different cooling strategies: Natural, Linear, Cubic and Optimal cooling.

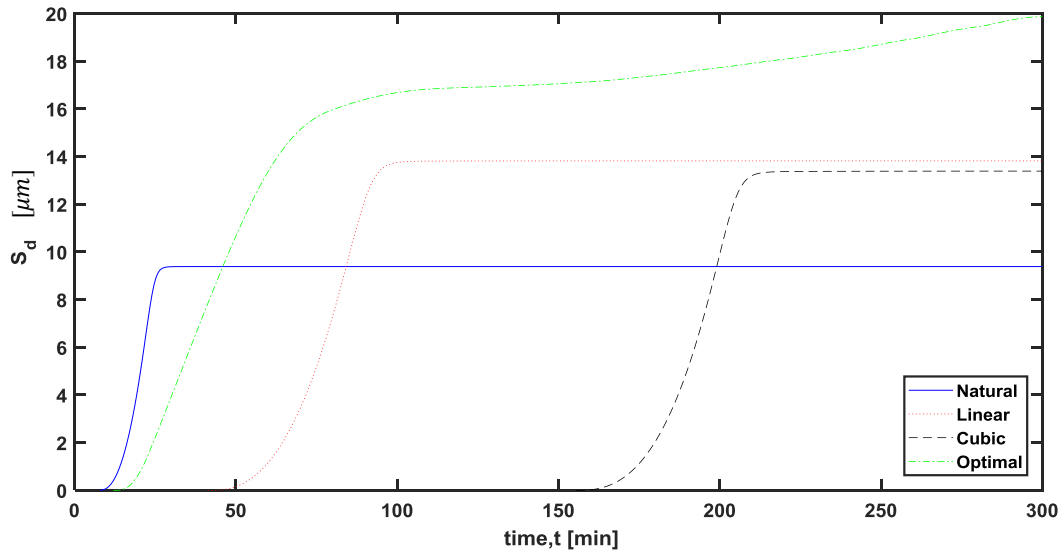


Figure 3.9. Standard deviation (S_d) trajectories obtained from the implementation of different cooling strategies: Natural, Linear, Cubic and Optimal cooling.

So, it becomes rather obvious that there is a trade-off between nucleation and growth rates and the optimum temperature trajectory for nucleation (i.e. high number of crystals) does not correspond to the optimum one for promoting crystal growth (i.e. larger crystals). Essentially, in order for crystal growth to be promoted, the supersaturation needs to be maintained low when the available crystal surface area for growth is low and it can be gradually increased with respect to the growing surface area. In other words, ideally the utilized temperature trajectories should match the corresponding cooling rate with respect to the increasing surface area of the crystals (i.e. μ_2). Based on that, by utilizing the optimum temperature trajectory a population of crystals with the largest mean size, which has been the objective function for this study, can be obtained, since the supersaturation is generated dynamically over the whole batch time, allowing crystals to grow. The utilization of the optimum temperature profile has also an immediate effect on the products' CSD since it is significantly broader comparing to the rest of the presented profiles, as illustrated in **Figure 3.9**.

Therefore, it becomes apparent that by running the process under different operating conditions, such as various cooling trajectories with respect to different process time, a region can be obtained that corresponds to the systems' ATR. Moreover, with the objective to $\max/\min_{T(1),T(2),\dots,T(P)} L_{10}$, dynamic optimization is performed by considering different end batch time, t_{batch} . The results of the generated ATR are illustrated in **Figure 3.10**. The optimum dynamic trajectories corresponding to the $\max/\min L_{10}$ are described by the blue lines, while the black dotted lines demonstrate the dynamic trajectories in the case that linear cooling is applied for

comparison purposes. By connecting the end points of the attained states of the dynamic profiles (red dotted line) the FR of the process can be obtained and consequently the boundaries of the FR are determined for the cooling crystallization of paracetamol in water system under the given process operating and supply chain constraints. It is also confirmed that the utilization of a linear cooling profile, provides a quite narrow feasible design space and it cannot be used for the determination of the “real” ATR.

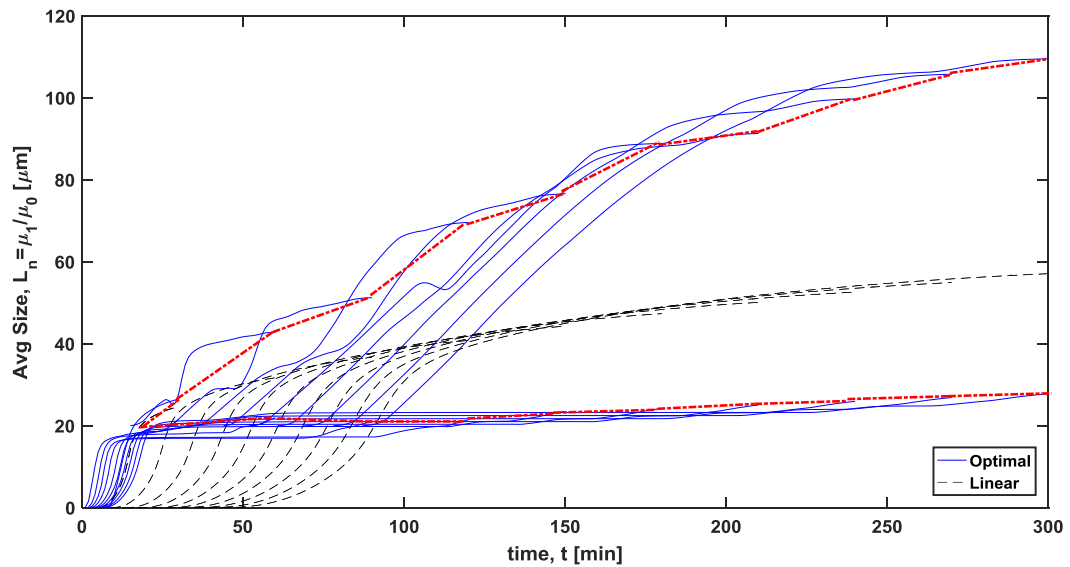


Figure 3.10. Attainable region of particle size with respect to time for the cooling batch crystallization of paracetamol in water. (–. *Indicating the attainable region (ATR)*; – *Optimal max / min trajectories*;))

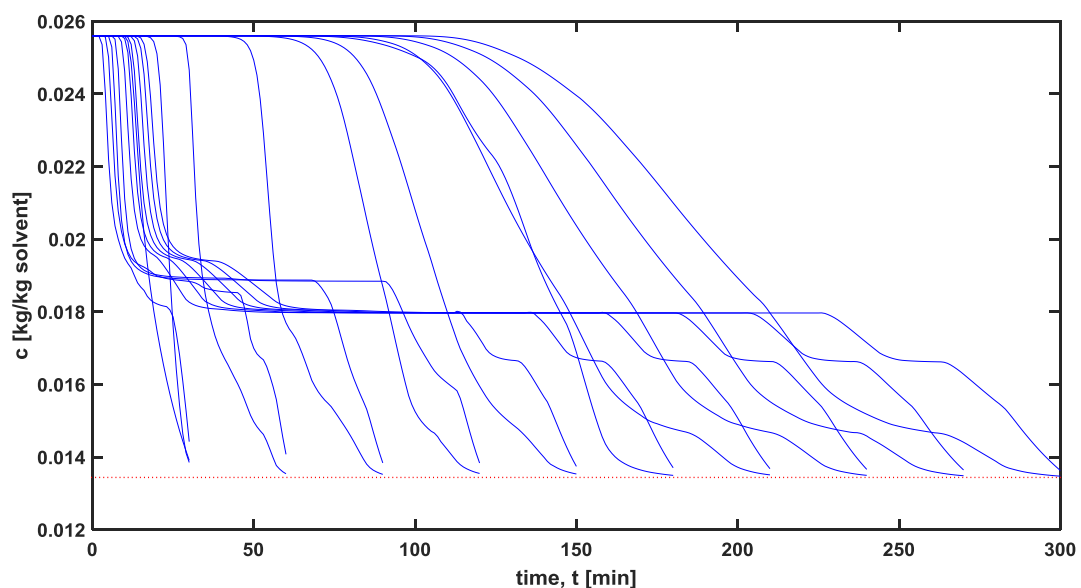


Figure 3.11. Solute concentration profiles obtained corresponding to the attainable states.

Besides the determination of the ATR for the number mean crystal size, L_{10} , simulating the dynamic trajectories of the rest of the CPPs is also essential for process understanding purposes. Furthermore, in **Figure 3.11**, the dynamic profiles of the solute concentration are presented corresponding to the optimum profiles for a certain time. Also, alongside the number mean size and the Sauter mean size (L_{32}), the dynamic profiles and the attained states of the standard deviation (S_d) are illustrated as well in **Figure 3.12**, while the trajectories of the remaining key moments, in terms of information content, are presented in **Figure 3.13**.

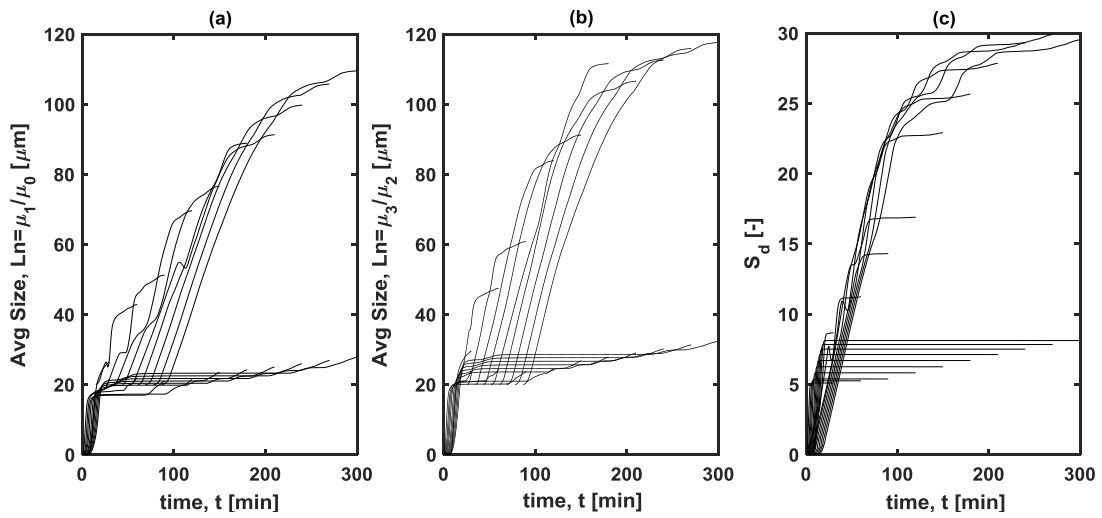


Figure 3.12. Attainable regions of (a) number mean size (L_{10}), (b) Sauter mean size (L_{32}) and (c) standard deviation (S_d) with respect to batch time.

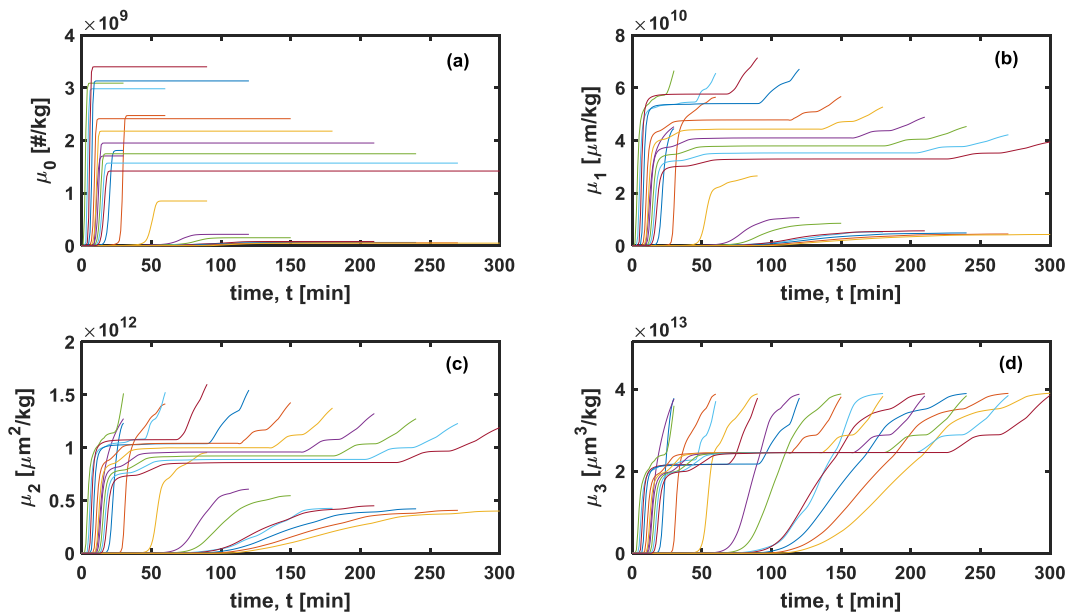


Figure 3.13. Attainable regions of (a) μ_0 , (b) μ_1 , (c) μ_2 and (d) μ_3 with respect to time.

One key point that should be discussed is related with the trade-off between mean size and CSD. It can be easily observed by **Figures 3.8, 3.9 and 3.12**, that the mean size and the standard deviation of the distribution are non-linear competing objectives: In this case, for instance, by maximizing the mean size the S_d may increase as well, which is of course undesirable since the final product quality performance indicators (e.g. bioavailability, tablet stability, dissolution, dosage form etc.), as well as the downstream processability (e.g. filtration, drying etc.) can be significantly affected. In most cases, the desired product crystals should have large L_{10} and low S_d as the efficiency of the filterability of the product slurry can be significantly increased. Consequently, in order for the analysis to be more comprehensive both objectives need to be considered.

Typically, real-life optimization problems encountered in industry, are posed as optimization problems dealing with multiple objectives, which are often conflicting in nature. This category of problems is known as multi-objective optimization problems (MOPs) where more than one objectives are involved during their simultaneous optimization. In most of the cases, these problems have been solved by combining the objective functions into one objective function composed by a weighted sum of all objectives, or by optimizing one objective while the others are set as constraints ([Sarkar et al., 2006](#)). Although by utilizing these methodologies the problem is simplified, a priori knowledge of the weights is required which is subject to individual perception making this an arbitrary process ([Benyahia et al., 2011a](#)). Distributing uniformly set of weights, for example, does not guarantee a distributed set of optimal solutions, while two different set of weight vectors does not necessarily lead to two different solutions ([Miettinen, 1999](#)). Moreover, the selection of the weights becomes a non-trivial problem especially when several objective functions of different natures (i.e. physical meaning, magnitudes and etc) is required.

It should be clear that conceptually single and multi-objective optimization problems differ in terms of solution and results. In multi-objective optimization there is no single optimal solution with respect to all the objective functions as traditionally can be found in a single-objective optimization. Instead, MOPs give rise to a set of non-dominated/non-inferior optimal solutions (Pareto-optimal solutions – **see Figure 3.14**) which constitute the best trade-offs among the objective functions considered. Since none of these optimal solutions in the Pareto-optimal set can be classified as better, all of them can be considered. Therefore, utilizing Pareto optimal solutions provide the engineers a set of design and operational options for process design and

decision making which will eventually increase the probability of identifying and consequently designing more efficient processes (Benyahia et al., 2011a).

Extensive research has been conducted on the algorithms utilized for the identification of the entire Pareto optimal solutions (Stewart et al., 2008; Sharma and Rangaiah, 2013). Among other approaches, utilizing evolutionary algorithms for the solutions of MOPs has been considered the most relevant and robust since the whole set can be constructed accurately in a single run opposing to the classical algorithms. Also, since they are stochastic by nature no prior information needs to be known about the problem being solved (i.e. initial guess), the evolutionary algorithms are robust and parallelization can be implemented (Sarkar et al., 2006). As mentioned before, in this work, the real-coded elitist nondominated sorting genetic algorithm (NSGA) is utilized for the solution of the MOP. In this case, for the NSGA, the following input parameters were set to fixed values for both case studies: The population size was selected to be equal to 200, the number of generations was set to 400, and the mutation probability was predetermined as an adaptive feasible function. The latter function randomly generates directions that are adaptive with respect to the last successful or unsuccessful generation, while at the same time the bounds and linear constraints can be satisfied. For the sake of clarity, it should be mentioned that crossover parameters determine the way that two individuals (i.e. parents) are combined to form a crossover child for the subsequent generation, while the mutation parameters specify the way that GA varies the population randomly, to create mutation children, which consequently ensure the genetic diversity and enable the GA to search efficiently at a broader parameter space.

The application of the NSGA for the determination of the FR, by maximizing the number mean size (L_{10}) and minimizing the standard deviation of the distribution (S_d) as the two fitness functions, is illustrated in **Figure 3.14**. During the implementation of the algorithm, different cooling trajectories are generated randomly, simulations are carried out and eventually the objective functions are evaluated. By doing this for different t_{batch} , the Pareto fronts presented in **Figure 3.14** can be generated indicating the system's attainable states. As expected, competing interaction is shown since by maximizing the L_{10} , the S_d is maximized as well, which is something undesirable since S_d needs to be minimized. The generated Pareto fronts are in agreement with the results presented before during the single objective optimization analysis. Moreover, longer batch times offer the capability of larger particles to be produced with high S_d of the distribution since improved control of supersaturation can be achieved through the

implementation of an optimum temperature trajectory. Also, for the same reason the higher the t_{batch} , the wider is the span of the optimal region for both the objectives, which is something that can be drawn from single objective optimization analysis as well. Additionally, the upper part of the Paretos corresponds to high values for L_{10} and S_d , while an opposite trend can be detected at the lower part of the Paretos.

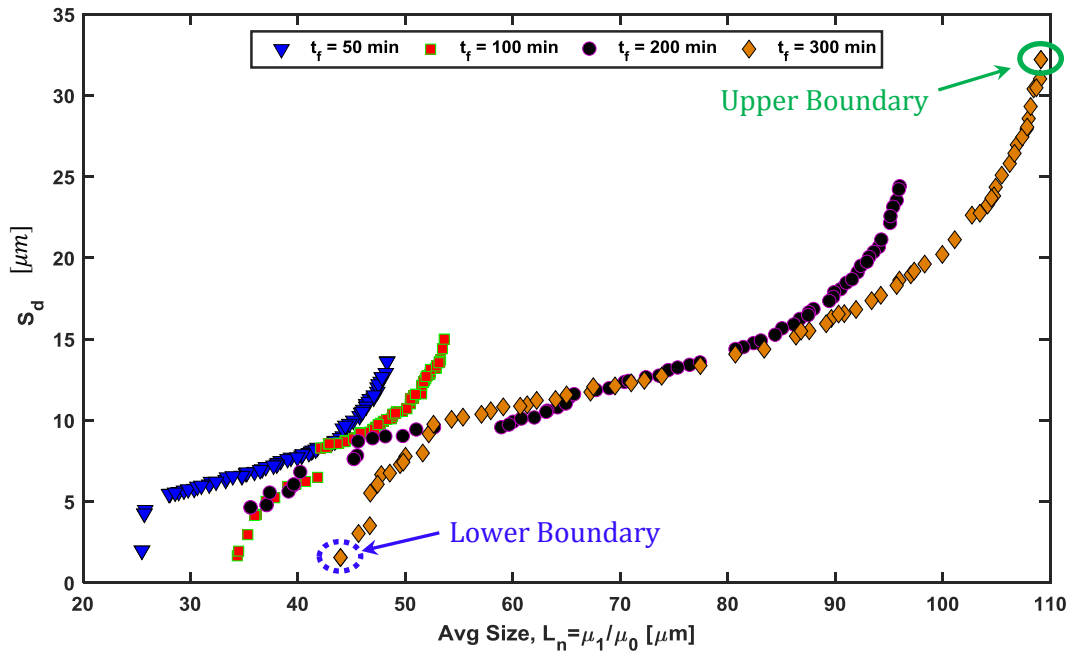


Figure 3.14. Pareto optimal-front obtained for the multi-objective optimization problem of maximizing the number mean size and minimizing the standard deviation of the distribution.

The Pareto's points, as mentioned, correspond to optimal cooling trajectories. For illustration purposes, the two boundaries for $t_{batch} = 300 \text{ mins}$ were selected and the optimum cooling trajectories were employed for the analysis of the boundaries of the operating region for a variety of process conditions, as shown in **Figures 3.15-3.17**. In more detail the dynamic cooling trajectories and solute concentration profiles are presented in **Figure 3.15**, while the corresponding supersaturation, nucleation and growth rates are illustrated in **Figure 3.16**. It should be mentioned that although a different algorithm (i.e. genetic algorithm) is utilized comparing to SOO (i.e. hybrid algorithm: genetic algorithm combined with the SQP algorithm), the same optimum cooling profile was generated with respect to the upper boundary. However, that's not the case regarding the lower boundary since a different temperature trajectory is utilized. The S_d of the distribution is depicted in **Figure 3.17**.

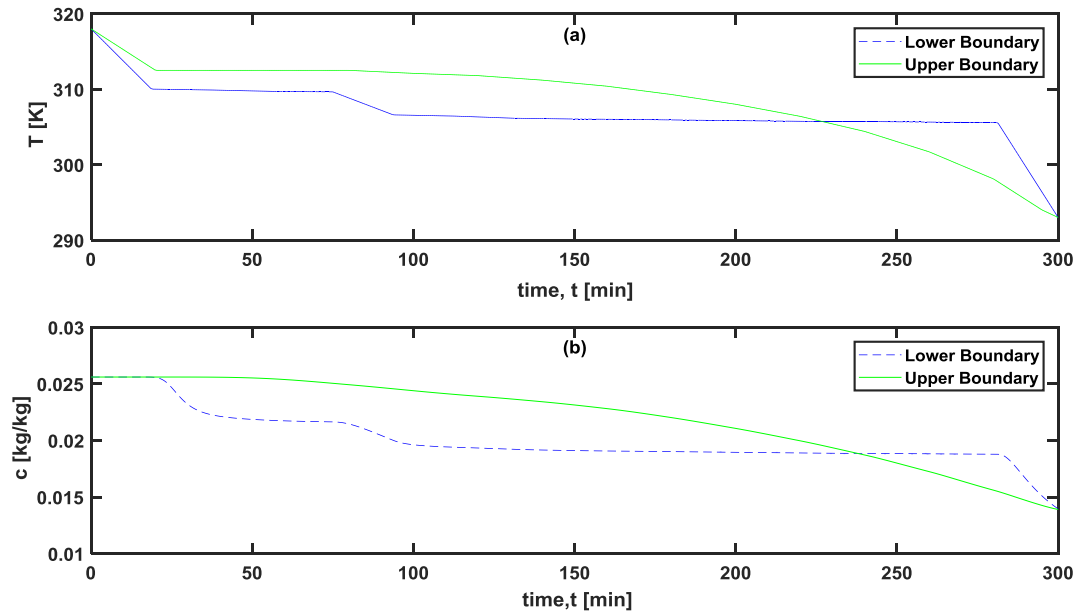


Figure 3.15. (a) Temperature and (b) solute concentration trajectories obtained from the implementation of two different cooling strategies corresponding to the boundaries of the Pareto front for $t_{batch} = 300$ mins.

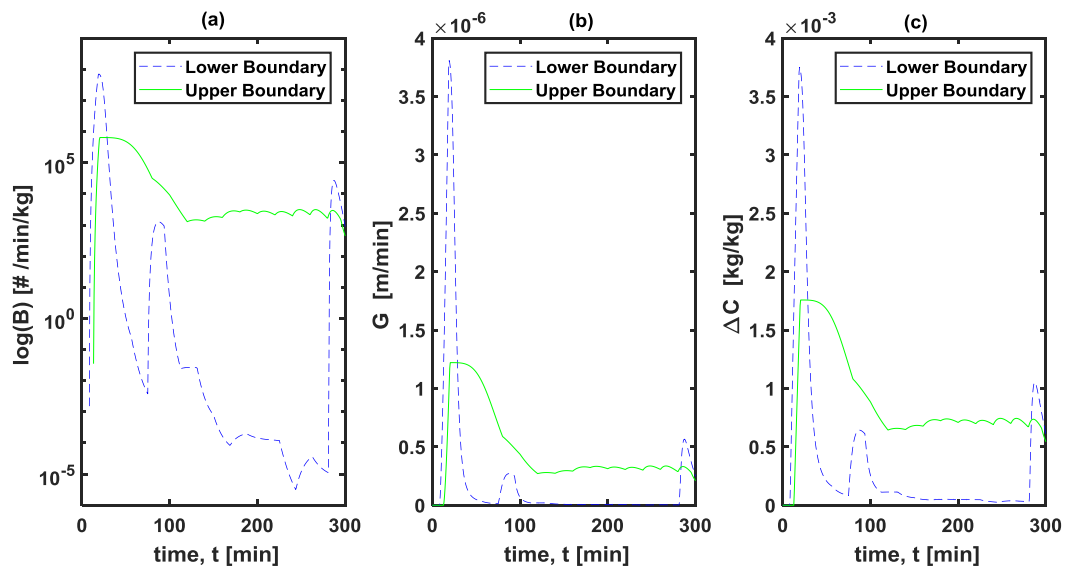


Figure 3.16. (a) Nucleation rate, (b) growth rate and (c) supersaturation trajectories obtained from the implementation of two different cooling strategies corresponding to the boundaries of the Pareto front for $t_{batch} = 300$ mins.

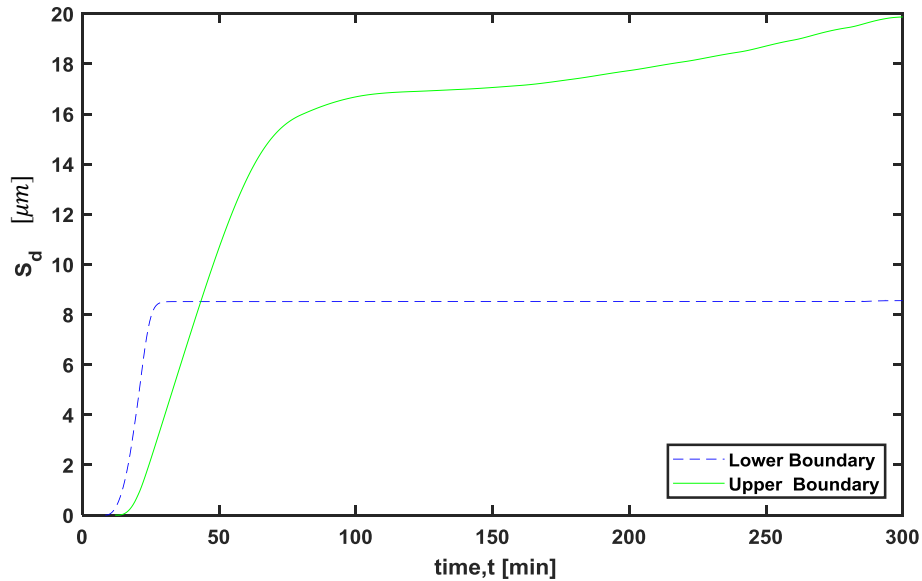


Figure 3.17. Standard deviation (S_d) trajectories obtained from the implementation of two different cooling strategies corresponding to the boundaries of the Pareto front for $t_{batch} = 300$ mins.

3.4.1.2 Continuous Crystallization of Paracetamol

In this subsection, the conceptual design of cascades of MSMPRs for the cooling crystallization of paracetamol in aqueous solution is investigated. Moreover, the scope is to determine the ATR with respect to single and multiple CQAs and how this could be altered by varying the number of stages of the MSMPR configuration and the independent operating variables, such as the residence time, operating temperature and supersaturation. The temperature limits were set to 318 K (45°C) and 293 K (20°C) corresponding to the maximum and minimum allowed temperature respectively, while the yield was constrained by the expression **C.2.4**. The analysis is conducted by utilizing the kinetics, thermodynamic properties and operating conditions as presented in **Table 3.1**.

As mentioned earlier, different operating modes (e.g. batch STR vs continuous MSMPR) could eventually affect the systems' kinetics. This may be extended to the case of different multistep operating models, such as multi-stage MSMPR crystallizers. Moreover, the kinetics of each crystallizer may differ from each other due to differences in the operating volume, residence time, hydrodynamics (e.g. specific power input, mixing conditions), supersaturation and suspension density. However, in these modelling studies, these variations are considered negligible and the same kinetics are applied to each stage.

Of course, the operating strategies of a continuous process differ significantly compared to a batch one, since the first one is operated under steady-state conditions whereas the latter is

characterized by dynamic trajectories. Thus, the presented set of ODEs (eq. 3.12 – 3.14), which comprises a comprehensive moment-based model for a continuous cooling crystallization process, can be simplified by converting the set of ODEs to a system of non-linear equations. Although it won't be presented, the set of dynamic equations were also solved to ensure the validity of the results and to observe the nature of the oscillations, which eventually reach a plateau (stability was assessed for long process times as well).

For the optimization problems, the vector of the decision variables comprises the residence time and the temperature setpoint of each crystallizer considered in the analysis. The optimization problem is solved for different total residence time by maximizing and minimizing the objective function (L_{10}), which generates the attainable points depicted in **Figure 3.18**. These points can be connected by smooth lines constructing in this way the particle size ATRs. The points corresponding to $\tau = 25 - 60$ mins are estimated by utilizing eq. 3.46, while the single point corresponding to $\tau = 20$ mins can be calculated by eq. 3.47 (for more information see **Section 3.3 – Figure 3.4**). Hence, the maximum and minimum front lines converge to a single point corresponding to a small total residence time.

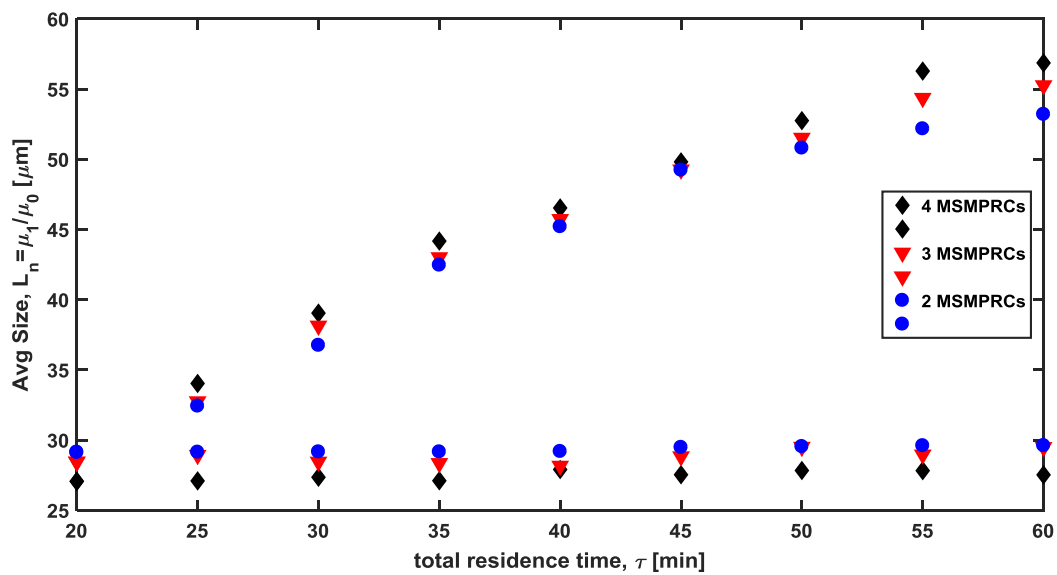


Figure 3.18. Attainable regions of particle size with respect to total residence time for a cascade of: 2, 3 and 4 MSMPR crystallizers.

The ATRs for different numbers of stages were investigated. As depicted, in **Figure 3.18**, the ATRs of particle size with respect to the total residence time are illustrated for two, three and four stages. As expected, by increasing the number of stages from two to four, broader ATRs can be obtained. This outcome can be justified based on the additional flexibility that is

provided to the system's temperature dynamics which results in improved supersaturation control. Depending on the investigated system (i.e. different kinetics) and the total residence time, the benefits of this additional flexibility varies (Vetter et al., 2014; Wang and Lakerveld, 2017). For instance, in this case, the additional flexibility doesn't demonstrate considerable benefits, especially for short residence times. For higher total residence times ($\tau_{tot} > 50$ mins), however, the benefits become rather obvious. Of course, the gain by adding more stages varies and it presents a nonlinear behaviour. So, by increasing the number of stages the ATRs will be become wider.

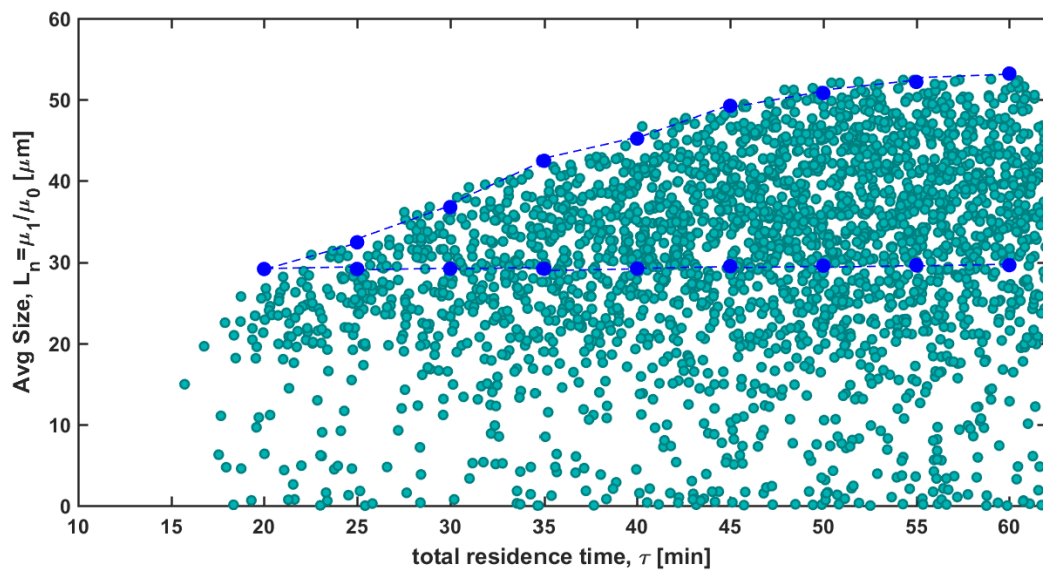


Figure 3.19. Determination of the attainable region of particle size for a cascade of 2 crystallizers through optimization (—•) and Monte Carlo simulations (•).

The shape of the generated ATRs resembles to the ATRs reported in literature for different systems (Vetter et al., 2014; Wang and Lakerveld, 2017). In this case, as can be seen in **Figure 3.18**, the upper limits of the ATRs (maximum line) increase with the increase of the total residence time, while the lower limits of the region (minimum line) remain almost the same with respect to time. Most specifically, the lower limits seem to maintain the value determined by **eq. 3.47**. The increase of the ATR of mean crystal size with respect to residence time can be attributed of course to the increased flexibility of controlling the temperature dynamics additionally to the prolonged retention time for crystals to experience more growth.

The most common continuous experimental configuration for industrial crystallization considering both the performance and operating complexity is the two-stage MSMPR (Yang et al., 2015). Therefore, based on that and the fact that no significant gain is observed in **Figure**

3.18 when more than two stages are utilized, the rest of the analysis will be carried out considering a two-stage MSMPR. Hence, in **Figure 3.19**, the ATR of particle size for a cascade of two crystallizers is illustrated through optimization (—•) and Monte Carlo simulations (•).

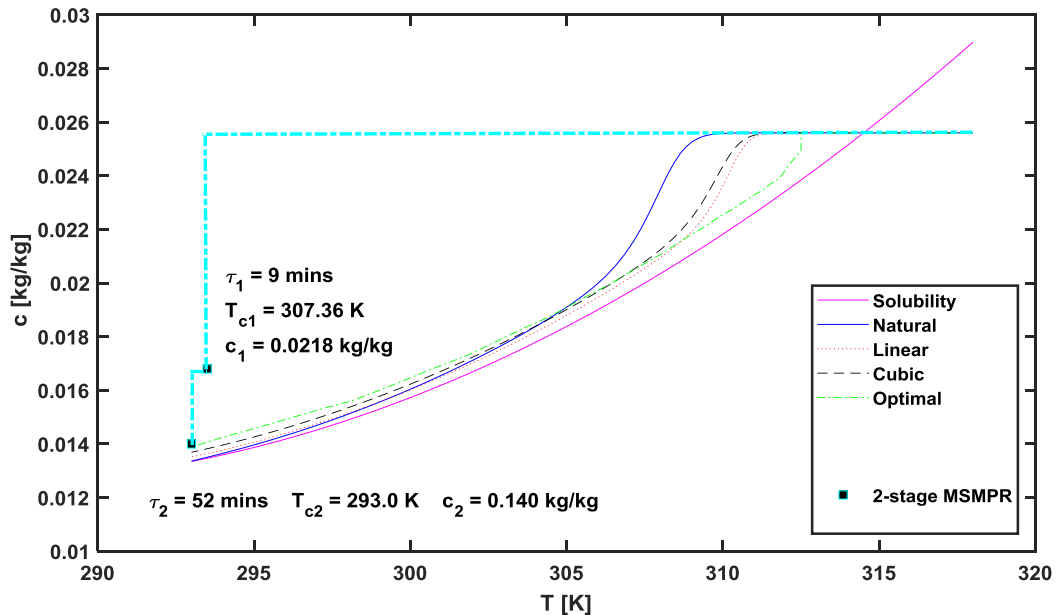


Figure 3.20. Operating policy for *minimum* point marked in figure 3.16 (—•) for total residence time $\tau = 60$ mins considering a two-stage MSMPR in comparison to the batch operating profiles.

For the simulation – based study, a stochastic Monte Carlo approach was utilized. The Monte Carlo method performs multiple model evaluations with probabilistically selected model inputs (i.e. control variables). The outputs of these evaluations are then used to determine the formed ATR. The ranges and distributions of the input variables under consideration are carefully selected since they can considerably affect the generated results. Monte Carlo simulations was essentially employed for validation purposes. In more detail, the results clearly indicate that the optimization successfully determined accurately the upper boundary of the ATR. Regarding the lower boundary, a major difference can be noticed, which is related to the selection of the yield constraint. Moreover, all possible solutions are accepted when the simulation-based approach is considered, while in the case of the optimization a significantly narrower region of valid solutions can be generated due to the yield constraint (expression **C.3.8**). It should be also evident that most of the simulation points are concentrated within the area defined as the ATR by optimization. Therefore, it is illustrated that there is a higher probability the results to be located within the FR defined by the optimization-based method.

As highlighted, all the points defining the ATR correspond to certain combination of control variables. For example, the optimum operating policies describing the minimum and maximum points for total residence time $\tau = 60 \text{ mins}$ are presented in **Figures 3.20** and **3.21** respectively. The minimum point can be achieved by operating the crystallizers at the lowest temperature values creating very high nucleation rates. By applying this policy, the highest possible supersaturation will be generated at the beginning of the process resulting in very high nucleation rates. In this way, a large amount of nucleus can be produced which can contribute to the rapid depletion of the solute. Hence, the crystals wouldn't experience considerable crystal growth. This would result in a large population of crystals with low mean crystal size, as happening during batch crystallization by following a natural cooling trajectory. The distribution of the residence time between the crystallizers are also determined through the optimization and is based on the kinetics and their subsequent interaction depending on the system. In contrast, the optimum operating policy for obtaining the maximum L_{10} dictates that the supersaturation trajectory needs to be gradually increased with respect to the population's available crystal surface (**Figure 3.21**). In more detail, an initial quick drop in temperature in the first crystallizer can generate a smaller number of nucleus than before. In order to achieve this objective a higher temperature setpoint is utilized. Also, the residence time is considerable higher than before, since by increasing this variable the formed nucleus can grow larger and be used as seeds to the second crystallizer. Then the second crystallizer can be operated in such a way that the depleted supersaturation will be mainly employed to promote crystal growth and consequently to produce crystals with the maximum L_{10} .

Multi-objective optimization is also performed for the determination of the ATR for the two stage MSMR cascade. As in **subsection 3.4.1.1**, the NSGA is utilized for the solution of the MOP, while the same input parameters are used regarding the algorithm's properties (population size: 200, number of generations: 400, and mutation probability: adaptive feasible function). The optimization routine generated the Pareto fronts with respect to different residence times as depicted in **Figure 3.22**. The capability of achieving the target objectives can be identified from the Pareto fronts. It is evident, that the S_d is increased monotonically with increasing L_{10} , while by increasing the residence time larger particles can be obtained with lower or similar S_d . It can be also noticed that the rate of change (**Figure 3.22**) varies depending the position on the Pareto front. The upper part of the Pareto for $\tau = 30 \text{ mins}$, for instance, presents a relatively slow increase of S_d by increasing L_{10} , while Pareto's lower part presents an opposing trend. It is expected, as can be seen for $\tau = 30 \text{ mins}$ and $\tau = 40 \text{ mins}$, that by

increasing the time, the Pareto fronts will become larger and larger in terms of target objectives range. However, this trend is not confirmed for $\tau = 50$ mins since the cooling rate setpoints are restricted based on certain cooling rate constraints. Moreover, very fast cooling rate trajectories, as such that would generate very low values of S_d , are discarded from the output.

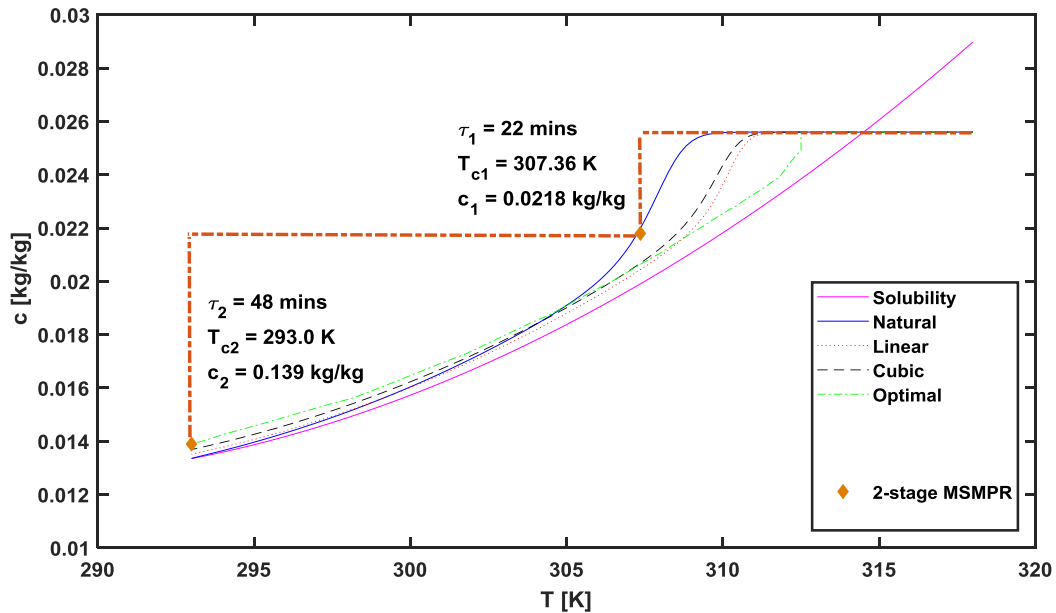


Figure 3.21. Operating policy for *maximum* point marked in figure 3.16 (— — •) for total residence time $\tau = 60$ mins considering a two-stage MSMPR in comparison to the batch operating profiles.

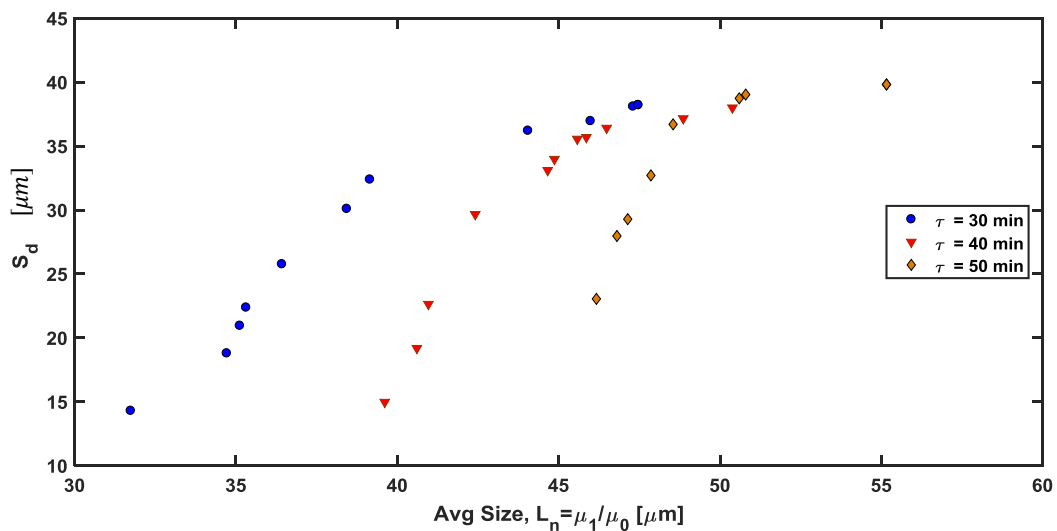


Figure 3.22. Pareto optimal-front obtained for the multi-objective optimization problem of maximizing the number mean size and minimizing the standard deviation of the distribution with respect to different residence times.

3.4.2 Case Study 2: Unseeded Batch & Continuous Cooling Crystallization of KDP

3.4.2.1 Batch Crystallization of potassium dihydrogen phosphate (KDP)

It becomes evident that by conducting a systematic design methodology on the 1D case study, the impact of potential operating strategies and configurations can be evaluated, supporting, in this way, the decision – making during the process design. However, the 1D PBMs do consider one characteristic length meaning that they could be utilized accurately only to characterize crystals with certain shape. This limiting factor can be eliminated by employing multi-dimensional PBMs, which can be used to fully characterize the crystal shape by considering two or three characteristic lengths depending its complexity. Therefore, the model-based design methodology, utilized before, is now extended to a two-dimensional batch cooling crystallization process.

The modelling of the KDP crystallization is conducted by utilizing the kinetic, thermodynamic properties and operating conditions as presented in **Table 3.2**. The temperature limits were set to 313 K and 293 K corresponding to the maximum and minimum allowed temperature respectively, while the yield was constrained by the expression **C.3.4**. Since, multiple objectives need to be accounted, only the MOP framework was considered for the identification of the ATR, with the scope of:

- (1) maximizing the mean length size ($\max(\frac{\mu_{0,1}}{\mu_{0,0}})$),
- (2) minimizing the aspect ratio in order a target shape to be achieved ($AR \rightarrow 1$) and
- (3) minimizing the standard deviation in x_1 direction ($S_{d,1}$).

For the estimation of the optimal Pareto front the NSGA was utilized again. Due to the higher complexity of the multi-dimensional PBMs the analysis becomes more computational expensive and a trade-off needs to be accounted between computational burden and accuracy. Although most of the input parameters were kept to the same setpoints, as before, the number of generations was reduced without however compromising the accuracy of the algorithm (population size: 200, number of generations: 200, and mutation probability: adaptive feasible function).

By implementing the NSGA, the fitness functions were evaluated for different cooling trajectories resulting in an optimal Pareto front, as shown in **Figure 3.23**. From the analysis, a 3D Pareto front was obtained which illustrates the trade-off interactions between the three different objectives with respect to different t_{batch} . For visualization purposes the XY, XZ and YZ planes of the 3D Pareto front are also presented in **Figures 3.24 – 3.26**. It has been proven experimentally that the KDP is a growth dominated system and therefore its CQAs, such as L_n , AR and S_d , can be considerably varied by the application of different temperature trajectories (Acevedo et. al., 2014; Acevedo et. al., 2015). This is also confirmed by the generated Pareto front that can span a broad range of solutions for all investigated objectives. For instance, for $t_{batch} = 180 \text{ min}$, it is illustrated in **Figures 3.24 – 3.26** that $L_n \approx 201.7 - 413.6 \mu\text{m}$, $AR \approx 1.8 - 3.3$ and $S_{d,1} \approx 15.5 - 110$. As expected, in order the target shape ($AR \rightarrow 1$) to be obtained the mean size of the final crystals needs to be compromised (**Figures 3.24**). Trade-off between AR and L_n arises since each crystal facet experiences different growth rates. As a result, different size is obtained along different characteristic lengths. In this case, larger sizes are obtained along x_1 direction, where faster kinetics do apply, comparing to x_2 , leading to the formation of crystals with needle-like habit. However, this attribute can be modified by manipulating the temperature trajectory. Furthermore, by controlling the cooling rate and subsequently the supersaturation, the growth rates can be directed to generate crystals with $L_{n,1} \approx L_{n,2} \leftrightarrow AR \rightarrow 1$. Spherical shape was selected as the target one since it presents improved flowability and processability characteristics (Mersmann, 2001). For this case study, a virtually linear correlation does occur between these two objectives as presented in **Figure 3.24**.

On the contrary, the interaction between $L_{n,1}$ and $S_{d,1}$ can be described by an exponential function, as depicted in **Figure 3.25**. As in the **Case Study 1**, the $S_{d,1}$ of the distribution can be improved only at the expense of reducing the $L_{n,1}$ of the final product. Each of the three Pareto fronts can be divided in three distinct regions: (1) The lower part of the Pareto, where low sensitivity of the $S_{d,1}$ is demonstrated by increasing the $L_{n,1}$, (2) the middle part, where a linear trade-off is presented between the two attributes and can be considered as a transition stage between the upper and lower part and (3) the upper part, where a surge of $S_{d,1}$ occurs by increasing the mean size. Same comments can be deduced for the trade-off interaction between AR and $S_{d,1}$ demonstrated in **Figure 3.26**.

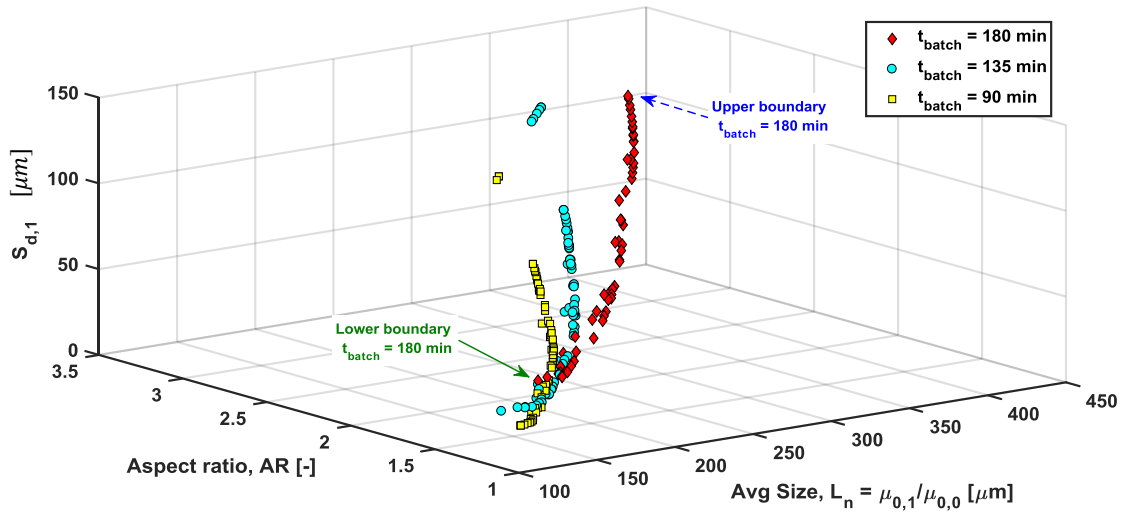


Figure 3.23. 3D Pareto optimal-front obtained for the multi-objective optimization problem of maximizing the number mean size ($\bar{x}_1 = \frac{\mu_{0,1}}{\mu_{0,0}}$), minimizing the mean aspect ratio (AR) and minimizing the standard deviation of the distribution in x_1 direction ($S_{d,1}$) with respect to different batch time (t_{batch}).

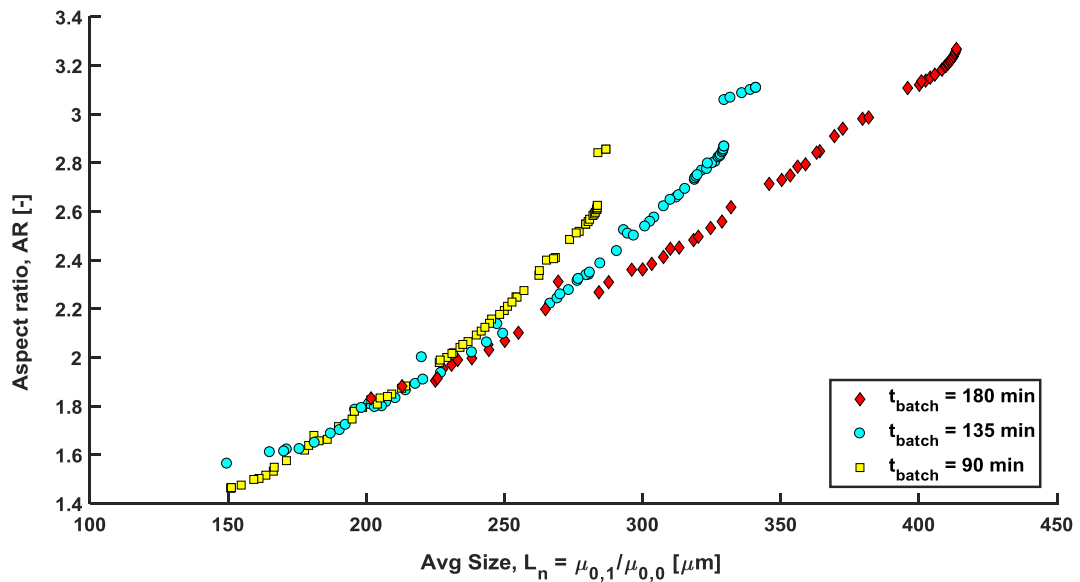


Figure 3.24. XY cartesian plane of the 3D Pareto optimal-front obtained for the multi-objective optimization problem of maximizing the number mean size ($\bar{x}_1 = \frac{\mu_{0,1}}{\mu_{0,0}}$), minimizing the mean aspect ratio (AR) and minimizing the standard deviation of the distribution in x_1 direction ($S_{d,1}$) with respect to different batch time (t_{batch}).

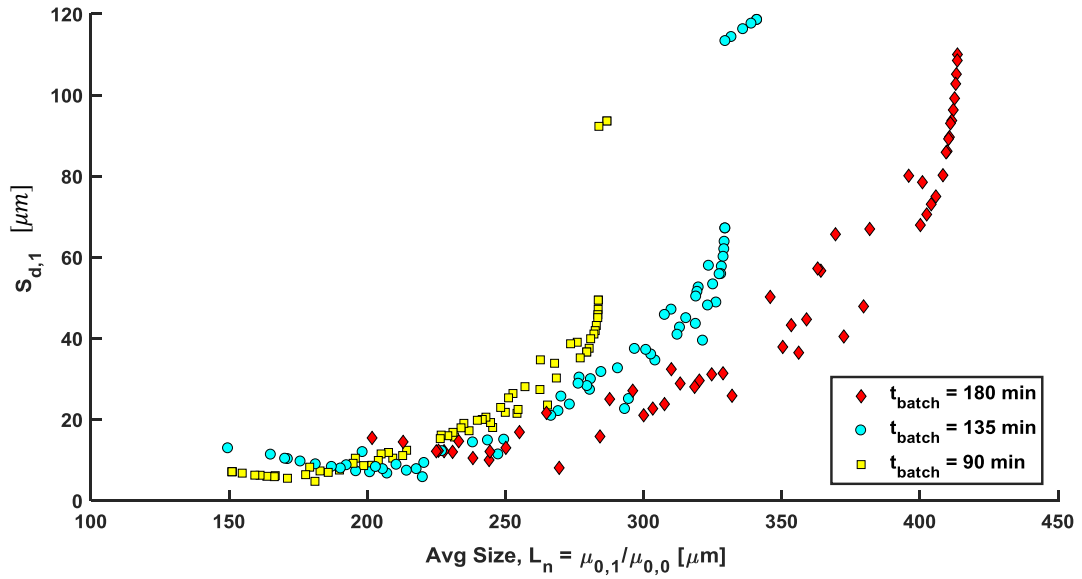


Figure 3.25. XZ cartesian plane of the 3D Pareto optimal-front obtained for the multi-objective optimization problem of maximizing the number mean size ($\bar{x}_1 = \frac{\mu_{0,1}}{\mu_{0,0}}$), minimizing the mean aspect ratio (AR) and minimizing the standard deviation of the distribution in x_1 direction ($S_{d,1}$) with respect to different batch time (t_{batch}).

The effect of the batch time on the optimal trajectories and the CQAs of the final product was also evaluated for three different residence times ($t_{batch} = 90, 135$ and 180 min). Regardless the t_{batch} , the generated optimum Pareto fronts exhibit analogous shape profile. However, the magnitude of the attained states and, also, the span of the FR is largely increased with respect to time. Moreover, by increasing the batch time, larger $L_{n,1}$ could be achieved, while corresponding to lower $S_{d,1}$ and AR , which can be justified due to increased flexibility with respect to the supersaturation control. The benefits of this additional flexibility vary with respect to time in a nonlinear way. For instance, the rate of augmentation of the FR differs with respect to time as can be clearly seen by comparing the gain between the following time periods: $t_{batch} = 90 - 135$ and $t_{batch} = 135 - 180$.

Two cooling trajectories were selected corresponding to the upper (— —) and lower boundary (—) of the Pareto frontier for $t_{batch} = 180$ min (**Figure 3.27**). In this case study, a coarser discretization of the time domain was utilized for the piecewise continuous dynamic optimization due to the high computational burden of the system (see **eq. 3.43** and **3.44**). The temperature profile representing the lower boundary of the Pareto front resembles a cubic profile. Initially a step change occurs during the cooling stage in order the first nucleus to be

formed that will be used as seeds. Due to that, the supersaturation is slightly reduced, and it is kept approximately steady at about $\sigma \cong 0.01$ (**Figures 3.28 and 3.29**). Then a progressively increased cooling rate is applied which however doesn't affect the supersaturation significantly. Moreover, as demonstrated in **Figure 3.29**, the system remains close to the solubility line sustaining a low level of supersaturation. By operating at low supersaturation, a more controlled utilization of the driving force could be achieved with the scope of minimizing the difference between the growth rates of the two characteristic sizes resulting in a population of crystals with lower *AR* and narrower *CSD* but with the expense of producing smaller mean size crystals in both directions. These observations can be determined by **Figures 3.30**, where the dynamic evolution of the *AR*, and the mean sizes are illustrated. Of course, during the process, a fraction of the supersaturation is depleted for the formation of nucleus (primary nucleation).

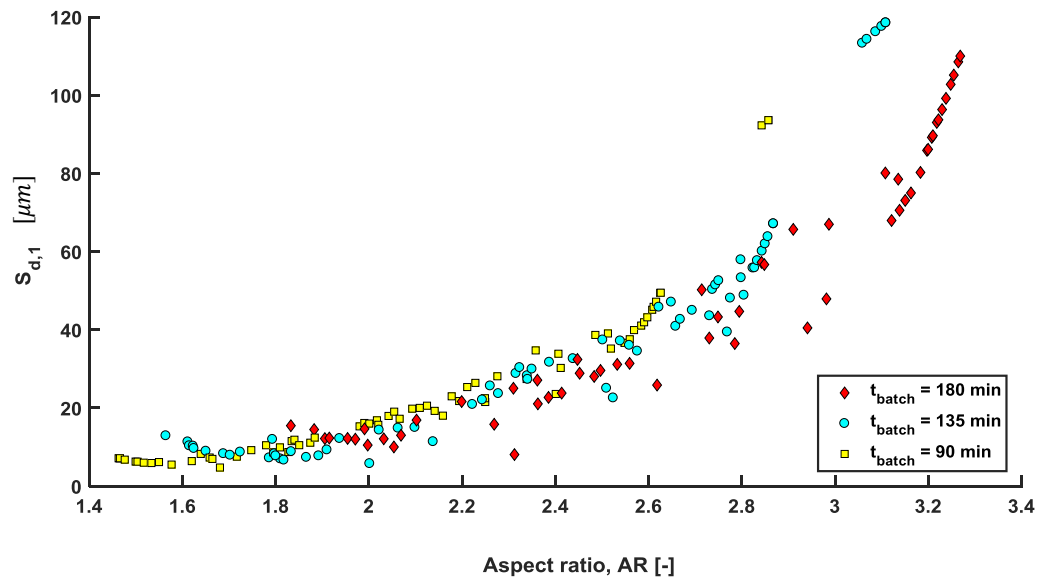


Figure 3.26. YZ cartesian plane of the 3D Pareto optimal-front obtained for the multi-objective optimization problem of maximizing the number mean size ($\bar{x}_1 = \frac{\mu_{0,1}}{\mu_{0,0}}$), minimizing the mean aspect ratio (AR) and minimizing the standard deviation of the distribution in x_1 direction ($S_{d,1}$) with respect to different batch time (t_{batch}).

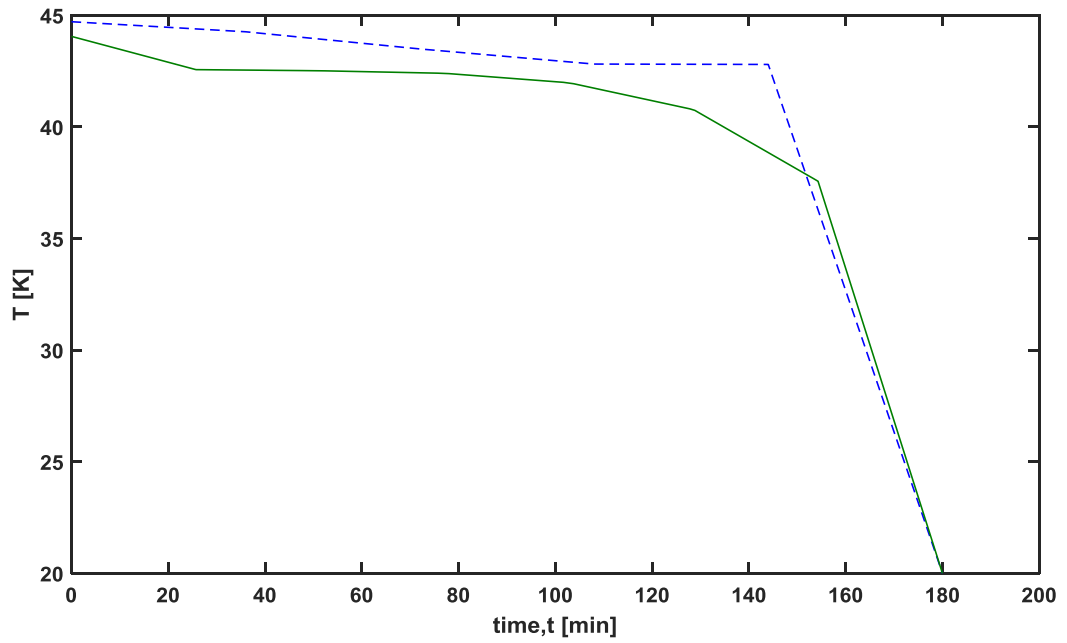


Figure 3.27. Implementation of two different cooling strategies corresponding to the boundaries of the Pareto front for $t_{batch} = 180$ mins: Upper (---) and Lower boundary (—)

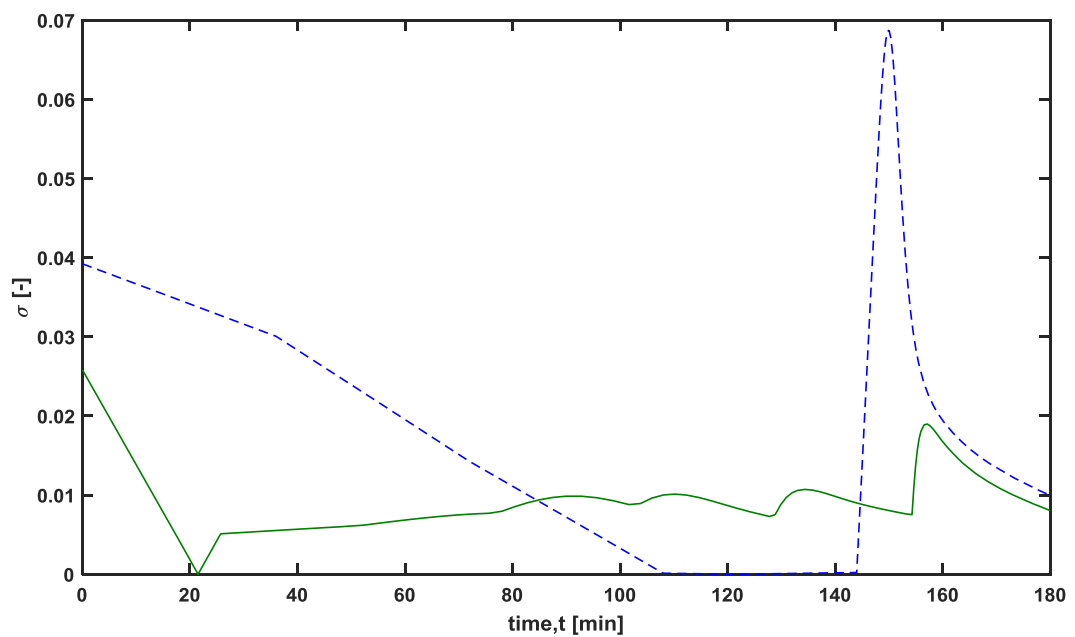


Figure 3.28. Relative supersaturation (σ) trajectories obtained from the implementation of two different cooling strategies corresponding to the boundaries of the Pareto front for $t_{batch} = 180$ mins: Upper (---) and Lower boundary (—).

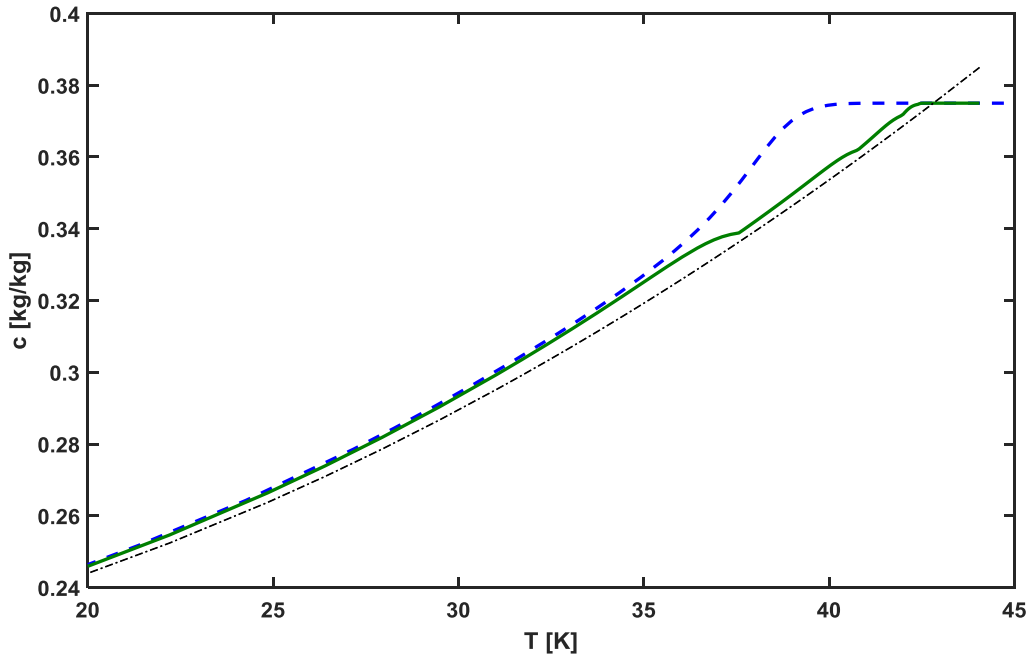


Figure 3.29. Phase diagram trajectories obtained from the implementation of two different cooling strategies corresponding to the boundaries of the Pareto front for $t_{batch} = 180 \text{ mins}$: Upper (—) and Lower boundary (—).

On the other hand, the cooling strategy corresponding to the upper boundary determines the optimum solution that satisfies the maximization of the $L_{n,1}$. Initially a very slow cooling rate is applied in order new nucleus to be formed (**Figure 3.28**), which can be used as seeds during the growth stage. This way of operation is typically met during the optimization of unseeded cooling crystallization processes (Nagy et al, 2008; Acevedo et. al, 2015). Since KDP is a growth dominated system, the imposed excess supersaturation is utilized mainly to promote mainly crystal growth instead of nucleation, opposing to the system presented in **Case Study 1**. The rapid cooling rate stage should be associated with the imposed yield constraint. Moreover, the system is forced to attain a temperature and concentration value within the certain batch time, which will satisfy the yield constrain. Of course, this should be also related with the system kinetics since both cooling strategies reach a supersaturation peak at about the same time. Either way, the introduced cooling trajectory yields higher mean size crystals by compromising other CQAs, such as CSD and aspect ratio.

This analysis elaborated the effect of the supersaturation dynamics on the evolution of the CQAs during the unseeded cooling batch crystallization of a growth dominated system. Its validity can be easily assessed by comparing with the experimental results presented in literature (Yang et al., 2006; Acevedo et. al, 2014; Acevedo et. al, 2015).

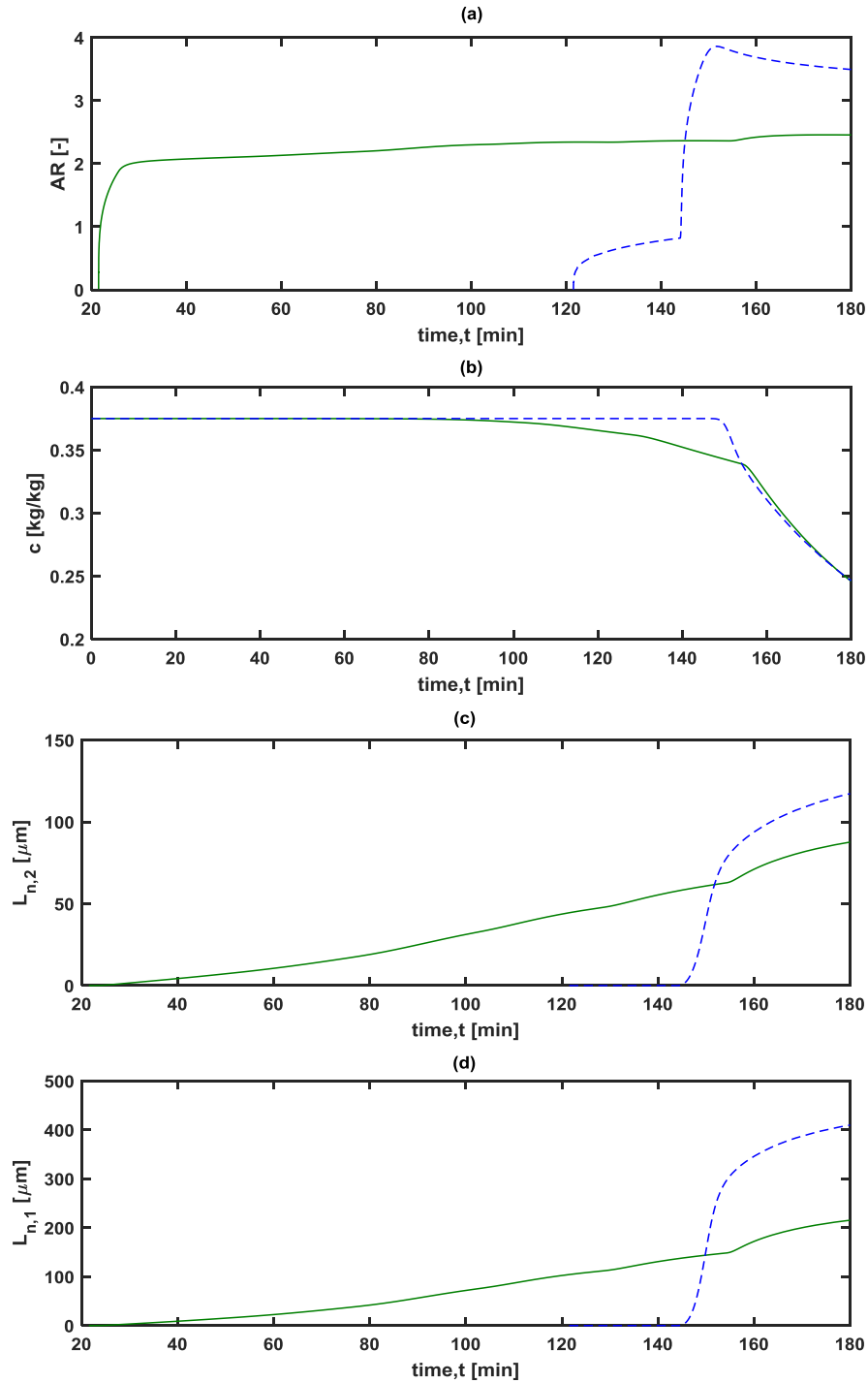


Figure 3.30. (a) Aspect ratio (AR), (b) Solute concentration, (c) mean crystal width size ($L_{n,2}$) and (d) Mean crystal length size ($L_{n,1}$) trajectories obtained from the implementation of two different cooling strategies corresponding to the boundaries of the Pareto front for $t_{batch} = 180$ mins: Upper (---) and Lower boundary (—).

3.4.2.2 *Continuous Crystallization of potassium dihydrogen phosphate (KDP)*

In this subsection, the conceptual design of cascades of MSMPRs for the cooling crystallization of potassium dihydrogen phosphate in aqueous solution is investigated. Moreover, the scope is to determine the ATR with respect to multiple CQAs and how this could be altered by varying the independent operating variables, such as the residence time, operating temperature and supersaturation. The temperature limits were set to 313 K and 293 K corresponding to the maximum and minimum allowed temperature respectively. The analysis is conducted by utilizing the kinetics, thermodynamic properties and operating conditions as presented in **Table 3.2**. The analysis was performed by considering a two-stage MSMPR setup since is the most common continuous experimental configuration in the pharmaceutical industry regarding both the performance and operating complexity (Yang et al., 2015).

As mentioned before, in **Subsection 3.4.1.2**, differences do exist between modelling batch and continuous processes since the first is one is a dynamic process while the latter one is operated under steady-state conditions. Thus, the presented set of ODEs (**eq. 3.28 – 3.31**), which comprises a comprehensive moment-based model for modelling a 2D continuous cooling crystallization process, is converted to a system of non-linear equations.

Stochastic Monte Carlo simulations were used to evaluate the ATRs. Random combinations of model inputs (i.e. control variables) are generated within certain allocated limits. These sets of values correspond to the assigned ranges and distributions of the input variables under consideration. Then multiple random model evaluations are performed with their outputs to eventually determine the FR. To ensure that the optimum FR was identified, a high number of model evaluations were performed ($\cong 1 \times 10^3$) without increasing significantly the computational burden of the process. Of course, the results were validated using different number of evaluations to ensure consistency and robustness of the results.

The generated outputs, form an area of points which clearly demonstrate the ATRs, as depicted in **Figures 3.31 – 3.34**. Initially, the 3D representation of the FR with respect to mean length size, AR and total residence time is illustrated, indicating the volume of the FR. Furthermore, for visualization purposes the 2D diagrams of mean crystal length size, AR and $S_{d,1}$ with respect to the total residence time, are presented in **Figures 3.32, 3.33** and **3.34** respectively. The shape of the generated ATRs resembles the ATRs reported in literature for different 1D systems (Vetter et al., 2014; Wang and Lakerveld, 2017). As expected, the utilization of the continuous

two stage MSMPR configuration leads to a considerable reduction of the ATR comparing to the batch operating mode due to the reduced operational flexibility. The spans with respect to the three considered CQAs can be summarized as following:

- mean length size ($L_{n,1} \approx 68 - 95 \mu m$),
- aspect ratio ($AR \approx 2.85 - 4.0$) and
- standard deviation of the distribution in x_1 direction ($S_{d,1} \approx 65 - 95$).

Also, it should be mentioned that similar trends are obtained regarding the trade-off interaction among the three simulated CQAs comparing to the batch crystallization presented in **subsection 3.4.2.1**. Moreover, larger mean crystal length size can be achieved by compromising the AR and the $S_{d,1}$, while lower AR and $S_{d,1}$ values could be obtained by minimizing the $L_{n,1}$.

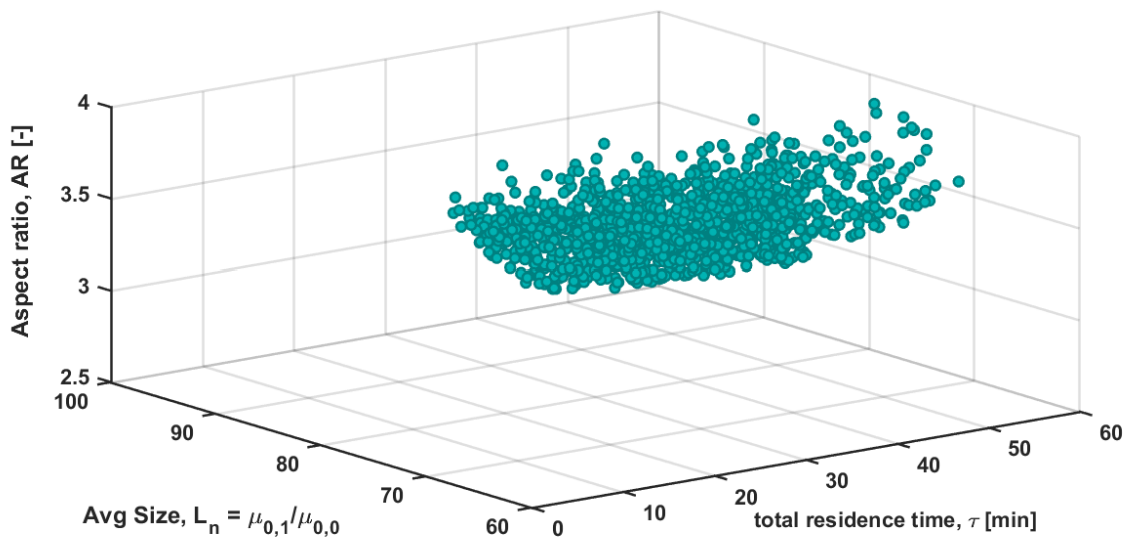


Figure 3.31. Determination of the 3D attainable region via stochastic simulation analysis of the: mean particle size ($L_n = \mu_{0,1}/\mu_{0,0}$) and mean aspect ratio (AR).

Most of the simulation points present the tendency to accumulate within certain solutions areas. This effect is utterly based on the assigned probability distribution functions. Moreover, the model inputs values are determined by a uniform distributed distribution function. The latter would result in generating a large amount of random numbers around its mean value. Regardless though, the high number of model evaluations can statistically guarantee the validity of the results since all possible model input combinations are assessed.

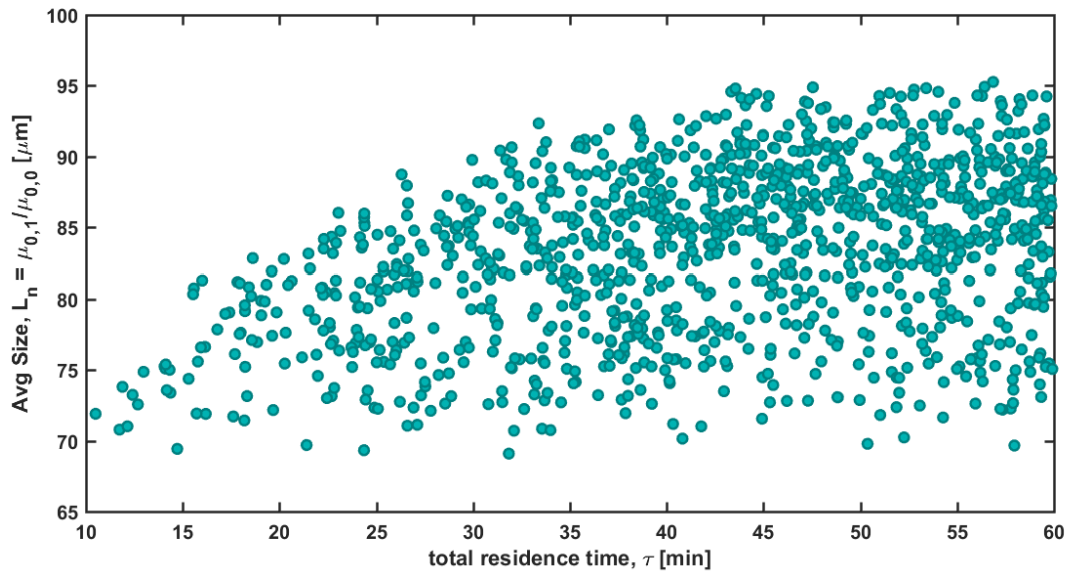


Figure 3.32. Determination of the attainable region of the mean crystal length size ($L_n = \mu_{0,1} / \mu_{0,0}$) via stochastic simulation analysis.

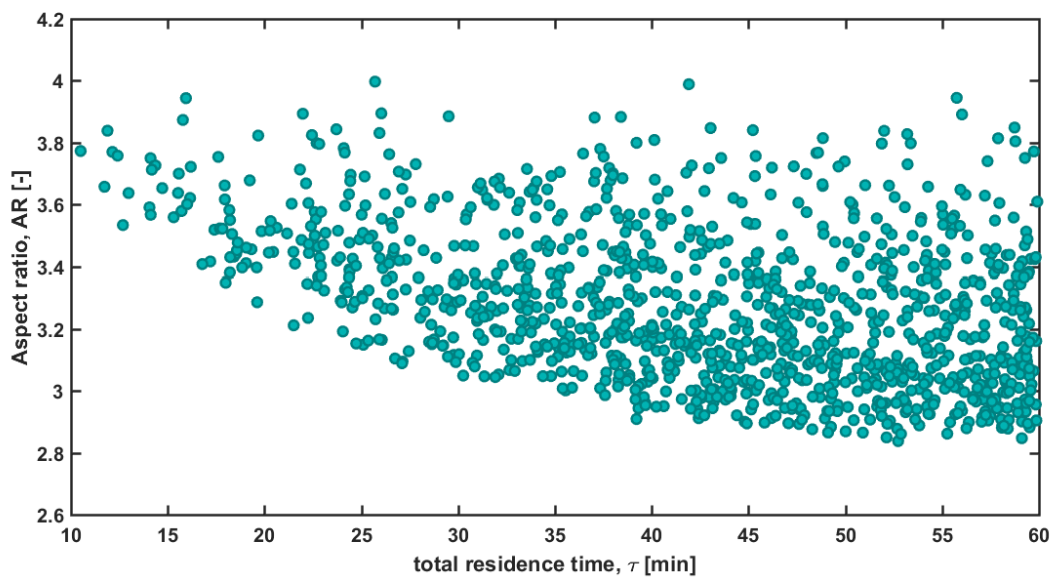


Figure 3.33. Determination of the attainable region of the aspect ratio (AR) via stochastic simulation analysis.

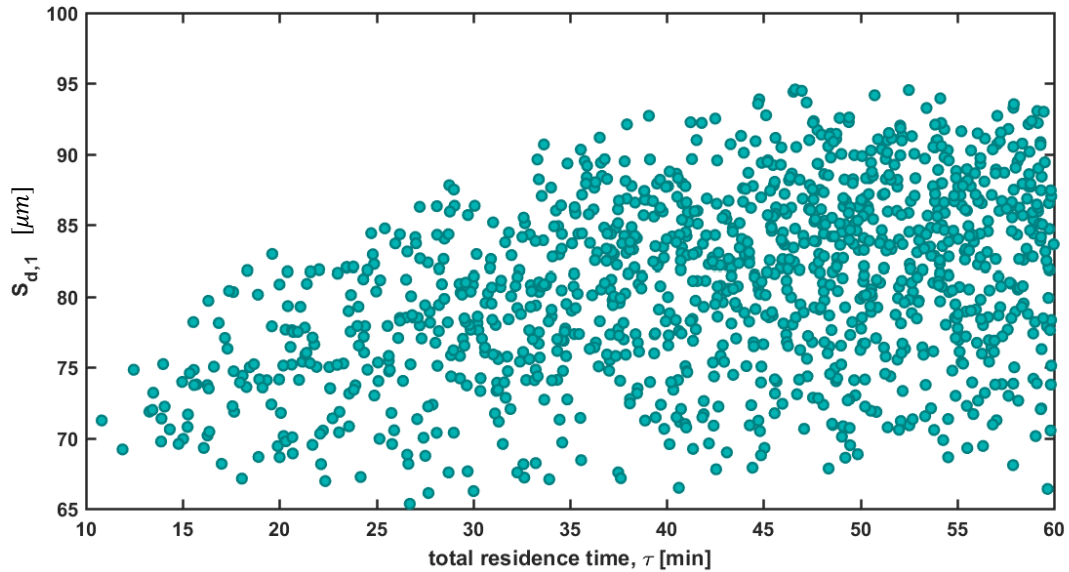


Figure 3.34. Determination of the attainable region for the standard deviation of the distribution in x_1 direction ($S_{d,1}$) via stochastic simulation analysis.

3.5 Conclusions

Process systems engineering (PSE) tools, such as model-based design and optimization, has been proven essential over the years to support process understanding and consequently decision making during the development and design stages. Within this perspective, a generic and systematic model-based design methodology for a wide range of crystallization processes is proposed for the identification of the ATR by incorporating single- and multi-objective optimization algorithms. The methodology's applicability was appraised through two case studies involving the crystallization of paracetamol and potassium dihydrogen phosphate (KDP). These two crystallization processes were selected since they could be modelled by the utilization of 1D and 2D PBMs, respectively, and hence the effect of the model's complexity on the methodology could be assessed. Initially, the analysis demonstrated the effect of the supersaturation dynamics on the evolution of the CQAs during the unseeded cooling batch crystallization of a nucleation dominated system, such as paracetamol in water. The system was optimized with respect to multiple objectives and the solutions corresponding to the Pareto's front boundaries were simulated in order the different trade-offs among the objectives to be evaluated. The same investigation by considering three objectives (L_n, AR, S_d) was also conducted for the unseeded batch cooling crystallization of a growth dominated 2D crystallization system, such as KDP in water. Further analysis was performed for both systems

by considering continuous mode of operation instead of batch. Not surprisingly, the FR obtained by operating in a continuous mode for both systems illustrated considerable smaller span since the capability of supersaturation control is significantly reduced. In addition, it was shown that the addition of more crystallizers to an MSMR cascade, enlarges the FR. The outputs of the continuous operated case studies were also validated by stochastic simulation-based analysis. For all case studies, the optimization results demonstrated the correlation between the crystallization kinetics and the achievable attributes. As expected, the growth dominated system presented considerable higher variability capabilities with respect to size, shape and other CQAs comparing to the nucleation dominated system. Regardless the complexity of the PBM model, 1D and 2D, mode of operation or the dominated mechanism during crystallization, the implementation of the methodology managed to identify the optimum attainable region for all case studies efficiently and with high accuracy. Therefore, the proposed systematic optimization-based method can be extremely valuable for model-based design of crystallization processes and it can be easily extended to include more crystallization phenomena (e.g. size-dependent growth, secondary nucleation, breakage and agglomeration), process alternatives or additional constraints, which is something commonly encountered in real applications. The method's accuracy, however, is not only related to the utilization of a systematic optimization but also to the developed models' predictive capability which can be very challenging due to the complexity of the underlying phenomena, inherent to Population balance models (PBMs) and the large number of parameters that need to be identified from experimental data. Therefore, prior to the design/optimization methodology another analysis, which is illustrated in **Chapter 4**, should be conducted to ensure that the model parameters (i.e. kinetics) have been accurately and reliably estimated.

NOMENCLATURE

AR	-	Mean aspect ratio of the population of crystals, [-]
B	-	Primary nucleation kinetic rate, [# / s / kg]
b	-	Nucleation order constant, [-]
c	-	Concentration of crystals in solution, [kg/kg _{solvent}]
c_{sat}	-	Saturation concentration of crystals in solution, [kg/kg _{solvent}]
cv	-	Coefficient of Variation, [-]
F_{out}	-	Volumetric flow rate, [m ³ /s]
g_i	-	Exponent of the growth kinetic equation of the i^{th} characteristic facet, [-]
G_i	-	Crystal growth rate of the i^{th} characteristic facet, [m/s]
J_{obj}	-	Objective function
k_b	-	Nucleation kinetic constant, [# / m / s]
k_{gi}	-	Growth kinetic constant, [m/s]
k_u	-	Volumetric shape factor, [-]
$L_{n,i}$	-	Number based mean size of the i^{th} characteristic size, [m]
L_{10}	-	Number based mean size, [m]
L_{32}	-	Sauter mean diameter, [m]
L_{43}	-	Weight mean crystal size, [m]
$n(t, x)$	-	Size distribution, [# / m]
$n(t, x_1, x_2)$	-	Size and shape distribution, [# / m ²]
r_0	-	Initial nucleus size, [m]
R	-	Ideal gas constant, [Pa m ³ mol ⁻¹ K ⁻¹]
R_V	-	Rate of change of the total volume of crystals, [m ³ /m ³]
S_d	-	Standard deviation of the distribution, [μm]
T	-	Temperature, [K]
t	-	Time, [min]
u_c	-	Volume of a single crystal, [m ³]
v_d	-	Variance of distribution, [-]
V_c	-	Macroscopic total volume of crystals, [m ³ /m ³] or [m ³ /kg _{solvent}]

V	-	Crystallizer's volume, [m^3]
\bar{x}_i	-	Number based mean size of the i^{th} characteristic facet, [m]
X	-	Vector containing the various characteristic lengths, [m]
X_0	-	Vector containing the initial conditions for the various characteristic lengths, [m]

GREEK LETTERS

δ	-	Dirac delta function, [-]
Δc	-	Absolute supersaturation, [-]
ε_i	-	Volumetric ratio of solution, [m^3/m^3]
$\mu_{m,r}$	-	m, r^{th} order mixed moment of size variables
μ_m	-	m^{th} order moment of size variables
ρ_c	-	Density of the crystals, [kg/m^3]
σ	-	Relative supersaturation, [-]
τ	-	Residence time, [min]
Ω^k	-	Sample Space, [-]

SUBSCRIPTS

0	-	Initial value
1	-	Length coordinate, [m]
2	-	Width coordinate, [m]
i	-	Characteristic crystal facet indices, [-]
p	-	Primary nucleation, [m]
sat	-	Saturation (solubility curve), [$kg/kg_{solvent}$]
sv	-	Solvent, [$kg/kg_{solvent}$]

SUPERSCRIPTS

j	-	Number of MSMPR stages indices, [-]
-----	---	---------------------------------------

4 MODEL REALIABILITY AND ESTIMABILITY ANALYSIS OF A MULTI – IMPURITY POPULATION BALANCE MODEL FOR CRYSTALLIZATION PROCESSES

The development of reliable mathematical models for crystallization processes may be very challenging due the complexity of the underlying phenomena, inherent to Population Balance Models (PBM), and the large number of parameters that need to be identified from experimental data. Due to the poor information content of the experiments, the structure of the model itself and correlation between model parameters, the mathematical model may contain more parameters than can be accurately and reliably identified from the available experimental data. A novel framework for parameter estimability for guaranteed optimal model reliability is proposed then validated by a complex crystallization process. The latter is described by a differential algebraic system which involves a multi-dimensional population balance model that accounts for the combined effects of different crystal growth modifiers/impurities on the crystal size and shape distribution of needle-like crystals. Two estimability methods were combined: the first is based on a sequential orthogonalization of the local sensitivity matrix and the second is Sobol, a variance-based global sensitivity technic. The framework provides a systematic way to assess the quality of two nominal sets of parameters: one obtained from prior knowledge and the second obtained by simultaneous identification using global optimization. A cut-off value was identified from an incremental least square optimization procedure for both estimability methods, providing the required optimal subset of model parameters. In addition, a model-based design of experiments (MBoE) methodology approach is also reported to determine the

optimal experimental conditions yielding the most informative process data, which can be used for the accurate identification of the nucleation, crystal growth and pinning mechanism parameters. The implemented methodology showed that, although noisy aspect ratio data were used, the eight most influential and least correlated parameters could be reliably identified out of twenty-three, leading to a crystallization model with enhanced prediction capability.

Highlights:

- Robust selection of the most influential and least correlated parameters.
- Estimability analysis based on sequential orthogonalization and Sobol.
- Local and Variance-based global sensitivity analysis.
- Optimum parameter subset for guaranteed model reliability.
- Multidimensional PBM model with Multi-Impurity Adsorption Model.
- Optimal model-based design of experiments (MBD_{oE})

4.1 Introduction

The benefits of the mathematical models are widely accepted, however, setting a unified rigorous framework for building reliable and predictable models is still an open subject, particularly for pharmaceutical processes. In order to obtain accurate model predictions, identification of the unknown model parameters is often required. In many cases, first-principles models are comprised by a large number of parameters which often cannot be estimated reliably from the available experimental data. In addition, the quality and the information content of the available experimental data can be affected by many factors such as noisy measurements, limited number of data points, poor design of experiments (DoE) and limited range of operating conditions (Perregaard et al., 1993; Chu et al., 2011). Additionally, strong influence of a parameter on one or more of the measured responses, high correlation between the parameters' effects and/or the effects of a parameter on model predictions can also lead to unreliable and inaccurate identification of the unknown parameter values, which in turn degrades the prediction capability of the mathematical model (Kravaris et al., 2013; Benyahia et al., 2013; Eghtesadi et al., 2014). Of course, mismatch could also arise from the model structure itself, since several assumptions are typically made in order to simplify the numerical representations of the system and reduce its complexity with the risk of neglecting some of the key underlying phenomena and consequently reducing the prediction capabilities of the model.

Several approaches have been developed to cope with some of these problems, such as modifying the model structure, incorporating additional measured outputs (e.g. using different process analytical technology (PAT) tools) and improving the information content of the experimental data by utilizing DoE approaches. However, before deciding whether the mathematical equations should be modified or supplementary experiments should be designed and performed, one key step is to investigate whether the available experimental data contain enough information to identify uniquely and reliably the overall model parameters, or alternatively, the subset of the model parameters that could be identified reliably whose optimal estimates can lead to the most predictable mathematical model. This could be achieved by evaluating the structural identifiability and estimability (i.e. practical identifiability) of the model parameters (McLean et al. 2011; Sin et al., 2010). The structural identifiability approach evaluates whether the parameters are locally or globally identifiable based utterly on the model structure, while estimability appraises whether the parameters can be identified uniquely by using the available experimental data or data from a proposed set of experiments (McLean et al. 2011; Walter and Pronzato, 1997). The estimability or practical identifiability methodology depends on the domain of variability of model parameters and experimental conditions whereas the structural identifiability is totally independent from both. The objective of the estimability analysis is to identify how many of the model parameters can be estimated accurately from the available data, while the ones with low estimability potential can be set to certain nominal values without degrading the prediction capability of the model (Benyahia et al., 2013; Chu et al., 2011). Consequently, estimability potential can be defined as a measure of the effects of parameters on the experimental outputs and/or correlation among the model parameters. In this work, only the estimability of the model parameters is evaluated without considering the structural identifiability of the model.

Different approaches have been developed and proposed to help identify the most appropriate subset of parameters for estimation based on the estimability approach. Degenring et al. (2004) proposed an approach for parameter selection based on principal component analysis (PCA), which is a statistical procedure that converts a set of observations of possibly correlated variables into a set of values of linearly uncorrelated variables. A parameter selection was obtained by using three different PCA methods (Jolliffe et al., 1972), which provided different parameter ranking outcomes. The PCA-based approach was applied in more recent investigations (Schittkowski et al., 2007; Quaiser et al., 2009) and was proven to be less robust compared to the orthogonalization and the eigenvalue method discussed below. The eigenvalue

method, introduced by [Vajda et al. \(1989\)](#) and was improved independently by other researchers ([Schittkowski et al., 2007](#); [Quaiser et al., 2009](#)), determines the most estimable subset of parameters based on the eigenvector and eigenvalues of the fisher information matrix (FIM). Although, the method has been shown better accuracy compared to other methods, sometimes it becomes challenging to match eigenvalues with specific parameters ([McLean et al. 2011](#)). The singular value decomposition ([Velez-Reyes et al., 1995](#)) and the correlation and collinearity methods ([Jacquez et al., 1985](#); [Brun et al., 2001](#); [Quaiser et al., 2009](#); [Sin et al., 2010](#)) were also proposed for the estimability analysis. The main drawback of the correlation and collinearity techniques is that they consider only directions of the sensitivity vectors without taking into account the magnitude of the sensitivities ([McLean et al. 2011](#)). This led [Brun et al. \(2002\)](#) to propose a robust combinational approach that combined a method based on a scalar measure of the fisher information matrix (FIM) and the collinearity method. A more robust approach for performing the estimability analysis is based on the orthogonalization of the sensitivity matrix. The method, that was initially introduced by [Yao et al. \(2003\)](#) and improved by [Lund et al. \(2008\)](#) and [Thomson et al. \(2009\)](#), ranks the parameters according to both their individual effect on the measured responses and the correlation between the parameters. Due to the efficiency of this forward-selection method, it has been employed widely in complex chemical and biochemical systems ([Benyahia et al., 2013](#); [Kou et al., 2005](#); [Surisetty et al., 2010](#); [Thomson et al., 2009](#); [Jayasankar et al., 2009](#)). Despite the popularity of the estimability analysis in numerous scientific areas, such as polymer science, environmental engineering and biology, this class of methods is still novel in the area of crystallization and its inherent benefits are not well understood, as only very limited number of studies have been reported in the literature.

[Chen et al. \(2004\)](#) presented a model-discrimination for model-based design by using the D-optimal criterion for the parameter set selection. However, only four parameters were considered making the benefits of the method unclear. Some of the benefits of the parameters selection methods were discussed by [Czapla et al. \(2009\)](#) who used an approach proposed by [Brun et al. \(2002\)](#) to select the most sensitive model parameters of a preferential batch crystallization of enantiomers. However, both studies utilized an arbitrary cut-off value for the parameter selection. A more comprehensive study was presented by [Samad et al. \(2012; 2013\)](#) where two global sensitivity analysis techniques, Morris screening and the standardized coefficients, are utilized to identify the most significant parameters. Although, these techniques can be useful for the classification of the parameters in terms of sensitivity measure, the

correlation of the parameters is not considered during the ranking procedure but it is estimated later on.

Considering all the challenges inherent to parameter selection and identification discussed above and with the scope of improving the current methodology for parameter identification for crystallization processes, a new framework (**Figure 4.1 – see next section**) is proposed for a systematic and optimal selection of the parameter subset with the highest estimability potential for guaranteed model reliability.

As a case study, a batch cooling crystallization process is considered under the presence of multiple impurities, more specifically crystal growth modifiers (CGMs), which can affect, besides product purity, the growth and potentially the nucleation kinetics and hence the size and shape distribution of the final crystals. A novel morphological multi-dimensional population balance model (MIAM model) that incorporates mechanisms for multisite competitive adsorption of the impurities on the crystal faces, coupled with mass balance equations is used ([Borsos et al., 2016](#)).

To the best of our knowledge, it is the first time that the modified Gram Schmidt Orthogonalization algorithm and Sobol analysis are combined and applied in the area of crystallization and equally the first time that the estimability analysis in general is being applied to assess the model reliability of a PBM that takes into consideration the presence of impurities. The complexity of the case study provides an opportunity to show the capabilities of the methodology with the scope of building more reliable and high-fidelity models for the pharmaceutical industry for process design, optimization and advanced control that would enhance the implementation of model-based Quality-by-Design (QbD).

4.2 Method

The proposed methodology (**Figure 4.1**) combines a sequential orthogonalization method, which takes into account the overall magnitude of the local sensitivities and the correlation between the parameters, with a variance-based global sensitivity ranking method. In both cases, a rigorous approach is used to identify the cut-off values based on the minimization of the maximum likelihood criterion. To assess the consistency and quality of the methodology, the correlation coefficients are calculated and the parameter estimates are assessed against their confidence domains. The proposed methodology enables a more robust classification of the

model parameters based on the estimability potential and provides a key tool to analyse the information content of the experimental data and consequently the quality of the measurements and the employed sensors (PAT). As such, the method helps identify the parameters that could be estimated accurately from the available data and whether additional data are required to identify a specific model parameter (e.g. new experiments or additional data from another sensor) would enhance the estimation process. To this end, the proposed framework is also coupled with a design of experiments (DoE) approach in case that the reliability of the model is not satisfactory.

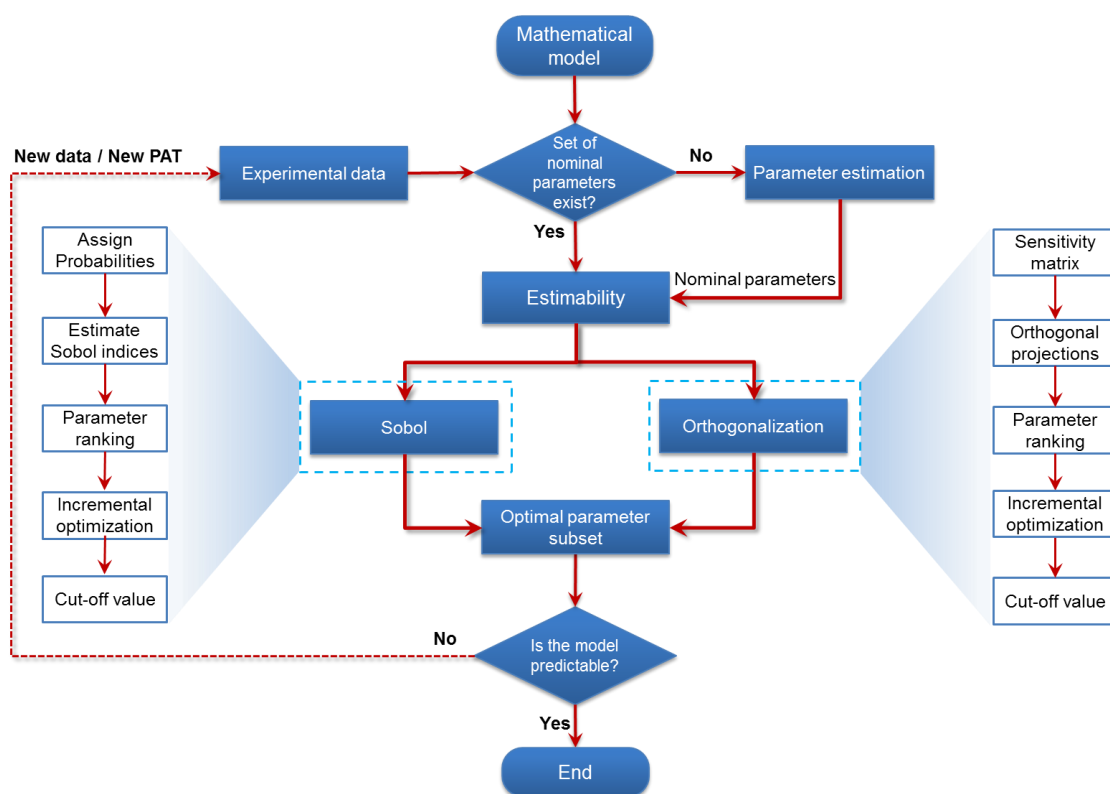


Figure 4.1. Schematic of the parameter identification and estimability analysis framework.

Although the estimability approach aims at identifying more reliably the model parameters from the existing data, it initially requires a nominal vector of model parameters, commonly obtained from prior knowledge of the process. In the case of lack of prior knowledge or uncertain model parameters (extremely poor estimates or broad confidence intervals), the estimability framework described in the paper provides a methodology to help identify the set of the nominal parameters. Although a variety of different approaches (e.g. Kalman Filters, polynomial fitting, Bayesian estimation etc.) has been applied for the determination of the unknown model parameters of complex, highly nonlinear chemical processes, utilizing

nonlinear optimization algorithms has been considered the most accurate and precise methodology due to their accuracy and efficiency (Rawlings et al., 1993; Janaideh et al., 2008; Kou et al., 2005; Fujiwara et al., 2002b). Typically, the least-squares error optimization approach is applied, unless the data measurements have different scales and/or different degree of reliability. In the latter case, weighted least squares approaches are usually utilized (Cao et al., 2012). A good review of the available optimization techniques (global and local ones) for crystallization processes can be found in Besenhard et al. (2015), where it was reported, that hybrid optimization techniques, provided the most accurate results, regardless the number and the quality (e.g. noise) of the experimental data, while the global optimization algorithms techniques proved to be ineffective when they employed alone. Hence, it is proposed that hybrid optimization techniques should be utilized for the identification of the unknown parameters. In this work, a hybrid global optimization technique that combines a genetic algorithm and local deterministic method (sequential quadratic programming) was used to identify the unknown parameters.

To maximize the benefits of the methodology, the estimability approach was implemented in both cases: the case where the initial nominal vector of parameters exists from prior process knowledge and the case where all parameters of the nominal vector should be identified globally and simultaneously by minimizing the weighted least square error. Both estimability approaches, the sequential orthogonalization and Sobol (variance-based method), rank the model parameters by order of importance. The ultimate objective of the estimability approach is then to find the optimal subset of model parameters that guarantee maximum model reliability. As a consequence, an estimability threshold or cut-off value is required to identify the subset of parameters that should be subject to re-estimation, to maximize model accuracy, and the subset of parameters that should be kept at nominal values, without degrading the prediction capability of the model. An optimal subset of parameters can be obtained by running a sequential parameter estimation procedure by identifying the top i^{th} parameters (where $i = 1, 2, \dots$) each time and calculating the corresponding objective function value. The cut-off value can be obtained when the improvement in the objective function due to an additional parameter becomes insignificant. If the model prediction capability with the optimal parameter subset is unsatisfactory, the method suggests running additional experiments, redesign the experiments (e.g. optimal experimental designs) or/and select additional or alternative PAT tools with the scope of increasing the information content of the data. Ideally this can be done by incorporating a model-based design of experiments (MBDoE) methodology. To this end, a dynamic

optimization formulation is proposed to determine the optimal experimental conditions yielding the most informative process data, which can be used for the accurate identification of the model-parameters.

4.3 Process Model

Multidimensional PBM model with Multi-Impurity Adsorption Model (MIAM)

The MIAM model was recently developed by [Borsos et al. \(2016\)](#) as a novel mathematical model for crystallization processes considering multi-impurity adsorption mechanisms with the purpose of process design, optimization and control. The model was built to predict the dynamic evolution of size and shape distribution during crystallization under the presence of impurities. The effect of the crystal growth modifiers was monitored in real time by using an in-situ video imaging probe: Lasentec Particle Vision and Measurement V819 (PVM). Images were automatically obtained with a frequency equal to six images per second and analysed by Lasentec's image and stat acquisition software, where blob analysis was utilized for the monitoring of the aspect ratio. In more detail, the cooling crystallization of pure potassium dihydrogen phosphate (KDP) in deionized water was investigated under the presence of aluminum sulfate (Crystal Growth Modifier: CGM1) and sodium hexametaphosphate (CGM2) and aspect ratio measurements were obtained as experimental outputs. As it has been presented by [Borsos et al. \(2016\)](#), divalent and trivalent metal ions preferably adsorb onto the {100} KDP crystal facet hindering the crystal growth in that facet, while anionic growth modifiers have a propensity for adsorbing onto the {101} KDP crystal facet inhibiting the crystal growth of the corresponding length. Hence, CGM1 is likely to adsorb onto {100} facet leading to more needle-like shaped crystals while CGM2 tends to adsorb onto the {101} facet causing an opposite effect by generating crystals with lower aspect ratio. Thus, in this case, these CGMs have competing effects. Since the aspect ratio (AR) is needed, a two-dimensional (also called morphological) PBM model is required.

Thus, for the modelling of the evolution of the crystal shape distribution, multidimensional population balance equations (PBEs) with two characteristic lengths $\mathbf{x}_l = \{x_1, x_2\}$ were considered (**Figure 3.1**) that can be written as:

$$\frac{\partial n(t, \mathbf{x})}{\partial t} + \frac{\partial n[G_1 n(t, \mathbf{x})]}{\partial x_1} + \frac{\partial n[G_2 n(t, \mathbf{x})]}{\partial x_2} = B_p \delta(x_1 - x_{1,0}) \delta(x_2 - x_{2,0}) \quad (4.1)$$

where $n(t, x)$ is the number density function, $\delta(x - x_0)$ is the delta distribution that characterizes the formation of the nuclei, B_p is the primary nucleation rate and G_i is the crystal growth rate of the i^{th} characteristic crystal facet. The initial and boundary conditions of the PBE are respectively:

$$n(\mathbf{x}_l, t = 0) = n_0(\mathbf{x}_l) \quad (4.2)$$

$$G_i n(\mathbf{x}_l, t) = 0, \mathbf{x}_l \in \partial\Omega \quad (4.3)$$

where $\partial\Omega$ is the boundary of the size space.

The model can be reduced from a partial differential equation (PDE) to a set of ordinary differential equations (ODEs) by using the standard method of moments (SMOM). Since only average properties are needed for the determination of the mean crystal AR, the SMOM method can provide an efficient and accurate method for the estimation of the key characteristics of the crystal population.

The joint moments of internal variables can be calculated as:

$$\mu_{k,m}(t) = \int_0^\infty \int_0^\infty x_1^k x_2^m n(x_1, x_2, t) dx_1 dx_2, \quad m, n = 0, 1, 2, \dots \quad (4.4)$$

Hence, by applying the moment transformation rule (eq. 4.4) to the PBE (eq. 4.1), considering the initial (eq. 4.2) and boundary conditions (eq. 4.3), a finite set of ODEs can be acquired:

$$\frac{\partial \mu_{0,0}}{\partial t} = B_p; \quad \frac{\partial \mu_{m,r}}{\partial t} = m G_1 \mu_{m-1,r} + r G_2 \mu_{m,r-1}, \quad m, r = 0, 1, 2, \dots \quad (4.5)$$

This set of ODEs coupled with the component mass balances, for the solute and impurities, describes a comprehensive moment-based model for crystallization processes under the presence of one or multiple impurities/ additives. The interpretation of the most critical joint moments is as follows: $\mu_{0,0}$ is the total number of crystals ($\#/m^3$) and $\mu_{2,1}$ represents the crystal volume in a unit volume of suspension (m^3/m^3). However, although these are the only

joint moments that have a physical meaning, other ones can be used to determine other key properties of the crystal population. Furthermore, moments can be utilized to determine the mean crystal sizes (eq. 3.34, 3.35) of the total population of each characteristic length, while the mean aspect ratio of the crystals (eq. 3.36) can be estimated by the division of the mean sizes as has been already presented in Chapter 3.

To integrate/solve the PBM model, the concentrations of the solute and the impurities are also required, which are calculated by coupling the corresponding mass balances. The overall model is summarized in Table 4.1 and it consists of a set of ODEs (moment equations coupled with mass balances) combined with algebraic equations that describe the kinetics and thermodynamics.

The complete set of differential-algebraic equations (DAEs) is solved simultaneously. The interaction between the state variables is high particularly between the moments, as shown in the causal loop diagram depicted in Figure 4.2, where each state variable is fed to the next one. For instance, after the μ_{00} moment is computed, the value passes to μ_{01} and μ_{10} , where consequently their values pass to μ_{20} , μ_{02} and μ_{11} . This continues until all the required moments to be estimated coupled with the mass balances for the solute concentration and the impurities. Also, it should be mentioned that the algebraic equation that describes the nucleation expression is fed into μ_{00} , while the 2D crystal growth kinetics and algebraic equations, which describe the impurities effect, are passed to the rest of the ODEs.

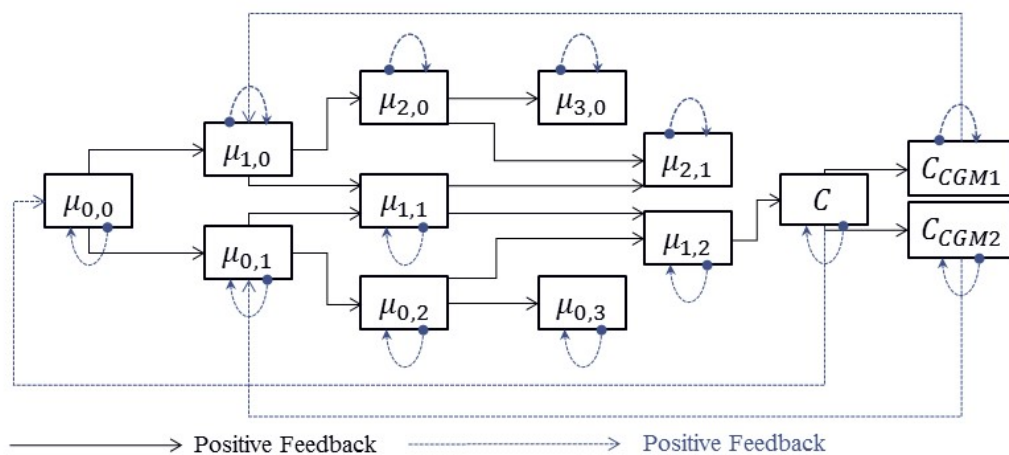


Figure 4.2. Causal loop diagram illustrating the interaction between the moments in the two-dimensional case.

It should be noted the model is based on a few assumptions among others:

- All the new formed crystals have a nominal size $L_{x_1,n} \approx L_{x_2,n} \geq 0$. Hence, it can be considered that the initial nuclei size is $L_n \approx 0$ (In most of the modelling studies, describing crystallization processes, the initial nucleus size is set to zero for practical purposes).
- The process operates under well-mixed conditions, so it could be assumed that the system is perfectly mixed. Hence a lumped parameter model is developed since the dependent variable does not change with spatial location (e.g. the density function, the concentration of the different chemical compounds and the moments are functions of time and not space).
- Only primary nucleation and crystal growth is considered since only these phenomena were detected experimentally. Thus, secondary nucleation, agglomeration and breakage can be neglected.
- Size-independent growth rates are assumed for the two characteristic faces since the SMOM is applied for the identification of the parameters
- Two different impurities and two different active sites are taken into account, which are located on two different crystal facets.
- There is no interaction between the active sites.
- Impurity effect on the solubility is considered negligible.
- Equilibrium adsorption model is considered.

The mathematical model requires 23 parameters and can be represented, for notational expediency, by the following general form of differential-algebraic equations (DAEs):

$$\dot{\mathbf{x}} = \mathbf{f}(\mathbf{x}(t), \mathbf{z}(t), \mathbf{p}, t), \quad \mathbf{x}(t = 0) = \mathbf{x}_0, \quad \mathbf{z}(t) = \mathbf{g}(\mathbf{x}(t), \mathbf{z}(t), \mathbf{p}, t) \quad (4.6)$$

where \mathbf{x} is the vector of the differential state variables, \mathbf{z} is the vector of the algebraic state variables, and \mathbf{p} is the vector of the parameters.

A multi-variate nonlinear dynamic regression model can be considered for the mathematical illustration of the interaction between the model prediction and measured output:

$$\mathbf{y}_{ij} = \hat{\mathbf{y}}_{ij}(\mathbf{p}, t_{ij}) + \varepsilon_{ij} \quad (4.7)$$

where \mathbf{y}_{ij} is the j^{th} measurement of the i^{th} experimental output, $\hat{\mathbf{y}}_{ij}$ is the corresponding model prediction, t_{ij} is the j^{th} sampling time of the i^{th} output and ε_{ij} is the measurement error assumed to be uncorrelated, Gaussian distributed, with zero mean.

Table 4.1. Complete set of differential-algebraic equations (DAEs) that represent the Multi-Impurity Adsorption Model (MIAM).

General form of the moment – based PBEs

$$\frac{\partial \mu_{0,0}}{\partial t} = B_p \qquad \frac{\partial \mu_{m,r}}{\partial t} = m G_1 \mu_{m-1,r} + r G_2 \mu_{m,r-1} \quad , \quad m, r = 0, 1, 2, \dots$$

Component Mass Balance – Solute Concentration

Component Mass Balance – Impurities Concentration

$$\frac{dC(t)}{dt} = -\rho_c \frac{d\mu_{1,2}}{dt} \qquad \frac{dC_{CGM,j}}{dt} = \frac{\chi_{c,j}}{1 - \sum_j \chi_{c,j}} \frac{M_{CGM,j}}{M_c} \frac{dC}{dt}$$

Primary nucleation rate

Crystal growth kinetic rate

$$B_p = k_{p,0} \exp\left(-\frac{E_p}{RT}\right) \exp\left(-k_e \ln^{-2}\left(\frac{C}{C_{sat}}\right)\right) \qquad G_i = k_{g,i} \left(\frac{C - C_{sat}}{C_{sat}}\right)^{g_i} \left\{1 - \left(a_{i,i} \frac{K_{i,CGM,i} C_{i,CGM,i}}{1 + K_{i,CGM,i} C_{i,CGM,i}}\right)\right\}$$

Mole fraction of the j^{th} CGMThermodynamic distribution coefficient of the j^{th} CGM

$$\chi_{c,j} = \sum_i K_{d,i,j} \frac{C_{CGM,j}}{M_{CGM,j}} \left(\frac{C}{M_c} + \sum_j \frac{C_{CGM,j}}{M_{CGM,j}}\right)^{-1} \qquad K_{d,i,j} = 1 - (1 - K_{e,j}) \sqrt{\frac{G_{min,i} k_{m,i,j}}{G_i k_{min,i,j}}}$$

Langmuir constant of the j^{th} CGM on the k^{th} site on i^{th} characteristic face

$$K_{i,j,k} = \frac{k_{ads,i,j,k}}{k_{des,i,j,k}} = \frac{k_{ads,0,i,j,k}}{k_{des,0,i,j,k}} \exp\left(\frac{\Delta G_{des,i,j,k} - \Delta G_{ads,i,j,k}}{RT}\right)$$

Absorption effectiveness factor of the k^{th} site on the i^{th} characteristic face

$$a_{i,k} = \frac{\gamma_i}{k_B T \left(\frac{C - C_{sat}}{C_{sat}}\right) L_{i,k}} = \frac{\beta_i}{T \left(\frac{C - C_{sat}}{C_{sat}}\right)}$$

Mass transfer coefficient when impurity distribution does and does NOT occur, respectively

$$k_{m,i,j} = G_i \left[1 - \exp\left(-\frac{G_i}{k_{m0,j}}\right)\right]^{-1} \qquad k_{min,i,j} = G_{min,i} \left[1 - \exp\left(-\frac{G_{min,i}}{k_{m0,j}}\right)\right]^{-1}$$

Unknown Parameters for Primary Nucleation & Crystal Growth in each characteristic face

$$p = [k_{ads,0,CGM1}, k_{des,0,CGM1}, \beta_1, G_{min,1}, k_{m,0,CGM1}, K_{e,CGM1}, \Delta G_{des,1}, \Delta G_{ads,1} \dots$$

$$k_{ads,0,CGM2}, k_{des,0,CGM2}, \beta_2, G_{min,2}, k_{m,0,CGM2}, K_{e,CGM2}, \Delta G_{des,2}, \Delta G_{ads,2} \dots g_1, k_{g1}, g_2, k_{g2}, k_{p,0}, E_p, k_e];$$

4.4 Estimability Analysis

In the current study, the estimability analysis consists of three main steps. In the first step, the relative effect of each model parameter on the measured outputs is determined through local sensitivity analysis of the dynamic system. Sensitivity analysis is a fundamental study that can determine how the variations of the outputs could be related to certain variations of the input variables. The second step is to apply the Orthogonalization algorithm with the scope of ranking the parameters in descending order, in terms of impact on the outputs and minimum correlation between the parameters. Finally, a parameter estimation procedure is performed incrementally and sequentially in order to identify the threshold (cut-off value) on the objective function, which in turn helps select of the optimum most estimable subset. These steps are thoroughly described below.

4.4.1 Ranking the Model Parameters – Orthogonalization Method

The development of an effective solution to the parameter selection problem requires the quantification of the influence of each parameter on the measured outputs. This approach indicates which parameters are the most important and most likely to affect the model predictions. The first step of the estimability analysis method is the evaluation of the sensitivity coefficients which can be calculated analytically or numerically. The numerical approach consists in applying a perturbation to the nominal values of the parameters according to the backward finite differences method as follows

$$s_{ij} = \frac{\partial \hat{y}_i}{\partial p_j} \approx \frac{\hat{y}_i(t, p_j) - \hat{y}_i(t, p_j - \Delta p_j)}{\Delta p_j}, \quad j = 1, 2, \dots, N_p \quad (4.8)$$

where N_p is the number of the parameters. It should be mentioned that the relative perturbation applied to the nominal values of the parameters was equal to -2% (i.e. $\Delta p_j/p_j$). As such the local sensitivity can be calculated for each sampling or measurement time

As the model parameters and outputs have different units and numerical values that could span several orders of magnitude, a normalization of the local sensitivities is often applied with respect to the parameters' nominal values and corresponding model output in order to make a more reliable comparison between the inherent effects of the parameters. The normalized sensitivity coefficients are given by the following equation:

$$s_{ij}|_{t=t_k} = \frac{\bar{p}_j}{\bar{y}_i|_{t=t_k}} \frac{\partial \hat{y}_i}{\partial p_j} \approx \frac{\bar{p}_j}{\bar{y}_i|_{t=t_k}} \frac{\hat{y}_i(t, p_j) - \hat{y}_i(t, p_j - \Delta p_j)}{\Delta p_j} \quad (4.9)$$

where \bar{p}_j is the nominal value of the j^{th} parameter, $\bar{y}_i|_{t=t_k}$ is the model prediction of the i^{th} output, evaluated at a sampling time t_k using the nominal vector of parameters $\bar{\mathbf{p}}_j$ and $j = 1, 2, \dots, N_p$.

After the sensitivity coefficients have been calculated, a sensitivity matrix \mathbf{Z} is constructed as follows:

$$\mathbf{Z} = \begin{bmatrix} s_{11}|_{t=t_1} & \dots & s_{1N_p}|_{t=t_1} \\ \vdots & \ddots & \vdots \\ s_{N_y 1}|_{t=t_1} & \dots & s_{N_y N_p}|_{t=t_1} \\ s_{11}|_{t=t_2} & \dots & s_{1N_p}|_{t=t_2} \\ \vdots & \ddots & \vdots \\ s_{N_y 1}|_{t=t_{N_m}} & \dots & s_{N_y N_p}|_{t=t_{N_m}} \end{bmatrix} \quad (4.10)$$

Thus, the sensitivity matrix has a dimension $N_y \times (N_p \times N_m)$, where N_y is the number of the measured outputs, N_m is the number of the measurements or sampling times, and N_p is the number of model parameters. Hence, each column represents the sensitivity coefficients with respect to one particular parameter, while each row captures the sensitivities of a specific output to the whole set of parameters at a particular sampling time.

One important property of the sensitivity matrix is that it can be related to the Fisher information matrix (FIM) by

$$FIM = \mathbf{Z}^T \mathbf{A} \mathbf{Z} \quad (4.11)$$

where \mathbf{A} is a square weighting matrix that represents the inverse of the measurement error covariance at the sampling points. The FIM matrix, which is also a square matrix (dimensions: $N_p \times N_p$), provides a key tool to assess parameters uncertainty and help determine the confidence intervals and correlation coefficients. In addition, the FIM rank gives an excellent indication on the number parameters that show high estimability potential. For instance, if two columns of the FIM are linearly dependent, the impact of one parameter can be affected significantly by the effect of the other one, and hence the identification of the corresponding parameters would lead to inaccurate estimations. Therefore, the FIM can provide

critical gen for estimability analysis as it contains information regarding measurement uncertainty and sensitivities of predicted response to model-parameters at all measurement times. Hence, in this work it is used to determine the covariance matrix and consequently the correlation coefficients as described below.

Table 4.2. Orthogonalization algorithm for estimability analysis (Benyahia et al. 2013).

Z_i : sensitivity vector corresponding to the parameter; p_i : λ : cut – off value;

r_i : orthogonal projection of Z_i ; P_j : set of estimable parameters;

X_j : the matrix of the selected parameters vectors at the j^{th} stage;

- 1. Select the parameter with the highest effect: find the index k such that:**

$$k = \mathop{\text{arg max}}_i (Z_i)^T Z_i, \quad i \in I_0 = \{1, \dots, n_p\}$$

$$\text{if } (Z_k)^T Z_k \geq \lambda \text{ set } P_1 = \{p_k\} \text{ and } X_1 = Z_k$$

otherwise stop

- 2. Orthogonalization: Compute the orthogonal projection of the matrix Z:**

$$R^j = (I - X_j(X_j^T X_j)^{-1} X_j^T) Z$$

- 3. Select the next parameter with the highest effect:**

$$l = \mathop{\text{arg max}}_i (r_i^j)^T r_i^j, \quad i \in I_j = (I_{j-1} - \{k, \dots\})$$

$$\text{if } (r_l^j)^T r_l^j \geq \lambda \text{ set } P_j = \{P_{j-1}, p_l\} \text{ and } X_{j+1} = \{X_j, Z_l\}$$

Return to step 2

Otherwise Stop

The Orthogonalization method provides an efficient forward-selection method that has been applied extensively for parameter ranking and selection. The technique is relatively simple to implement and most importantly it ranks the parameters more reliably, as both the magnitude of the effect of each model parameter on the outputs and the correlations between the effects of different parameters are considered simultaneously. This is paramount since both phenomena can reveal critical to process of parameters selection and discrimination, and consequently, to the prediction capabilities of the mathematical model. If a perturbation of a model parameter has minor effect on the outputs, then the parameter cannot be identified accurately from the data. This can be mathematically determined by calculating the norm of the sensitivity vectors (the norm of the columns Z_i). Conversely, large magnitudes/norms indicate significant effects on the outputs. At the same time, if a disturbance of two or more model parameters have similar

trends/effects on the outputs, and then the parameters are highly correlated. As a result, the impact of one parameter can't be isolated from the impact of the other, and hence these parameters cannot be reliably and uniquely identified from the data. It should be noted that the orthogonalization method selects sequentially the least correlated and most influential parameters (Benyahia et al. 2013). The correlation can also be evaluated using the FIM (e.g. linear dependency of the sensitivity vectors). Moreover, when two parameters p_i and p_j are orthogonal (i.e. linear independent - Not correlated) the element of the i^{th} and j^{th} of the FIM is zero, while the FIM obtains a value close to one ($FIM \rightarrow 1$) when the two parameters are linearly dependent (i.e. correlated parameters). The orthogonalization algorithm utilizes this criterion at step 2 (Table 4.2) to rank and select the optimal parameter set.

In this work, a modified Gram-Schmidt orthogonalization algorithm (Yao et al. 2003) is used to help rank sequentially the model parameters according to the magnitude of the sensitivities and the least correlation effect. The sequential orthogonalization algorithm is presented in Table 4.2. The first parameter is selected then all vectors of the scaled sensitivity matrix are sequentially projected onto an orthogonal basis (the sensitivity vectors with the highest magnitude).

Although, the ranking of the parameters regarding their estimability potential can be achieved with the orthogonalization method, selecting the optimal subset of parameters that can be reliably identified remains open, since in most of the cases arbitrary cut-off values are applied. In this work, an optimization-based approach is utilized for the optimum parameter selection based on the maximum likelihood approach:

$$J(p) = \min_p \left\{ \sum_{i=1}^{N_y} N_e \cdot \ln \left(\sum_{j=1}^{N_e} \left[(y_{ij}(p, t) - \hat{y}_{ij}(p, t))^2 \right] \right) \right\} \quad (4.12)$$

$$\text{s. t. } \dot{\mathbf{x}} = \mathbf{f}(\mathbf{x}(t), \mathbf{z}(t), \mathbf{p}, t), \quad \mathbf{x}(t=0) = \mathbf{x}_0, \quad \mathbf{g}(\mathbf{x}(t), \mathbf{z}(t), \mathbf{p}, t) = \hat{\mathbf{y}}_{ij}(t)$$

where $y_{ij}(p, t)$ is the experimental measurement; N_y is the number of outputs and N_e is the number of the experiments.

The maximum likelihood criterion was also used in the parameter estimation problem to identify the initial set of model parameters (i.e. nominal set).

4.4.2 Global Sensitivity Analysis

Sensitivity analysis has been extensively applied as a technique for model simplification, model calibration and process understanding through computer-aided design (Varma et al., 2005; Saltelli et al., 2004). LSA has widely been accepted by the research community due to the low computational cost. However, LSA techniques can only determine the sensitivity of each input separately, without taking into account the overall contributions of the input variables to the output predictions. In GSA methods, a simultaneous perturbation of all parameters (inputs) is performed within specific bounds, as opposed to LSA techniques where the parameters inputs are varied once at a time. Hence, the GSA approaches are capable of measuring not only the relative impact of each input variable, but also the interactions between them. The Variance-based global sensitivity techniques are used here, which they depend on the calculation of the following ratio:

$$\frac{Var_p[E(y_{ij}(\mathbf{p}, t)|\mathbf{p})]}{Var(y_{ij}(\mathbf{p}, t))} \quad (4.13)$$

where $E(y_{ij}(\mathbf{p}, t)|\mathbf{p})$ denotes the expectation of the output y on a fixed value, and the variance is calculated over all possible values of the inputs. In our case the inputs are the vector of the unknown parameters \mathbf{p} .

Many GSA techniques have been developed, with the most well established being the method of Sobol (Sobol, 2001). The Sobol method decomposes the output function $y(p_1, \dots, p_k)$ into terms of increasing degrees of interactions between the model inputs as follows:

$$\begin{aligned} \hat{y}(p_1, \dots, p_{N_p}) = & \hat{y}_0 + \sum_{i=1}^{N_p} \hat{y}_i(p_i) + \sum_{i=1}^{N_p-1} \sum_{j=i+1}^{N_p} \hat{y}_{ij}(p_i, p_j) + \dots \\ & + \hat{y}_{1,2,\dots,N_p}(p_1, p_2, \dots, p_{N_p}) \end{aligned} \quad (4.14)$$

In general, there are infinite ways to decompose the function $\hat{y}(p_1, \dots, p_{N_p})$. However, for independent factors, the decomposition based on orthogonal terms becomes unique (Sobol, 2001) and the functions can be calculated through multidimensional integrals as follows:

$$f_0 = E(y) = \int_{\Omega^k} f(\mathbf{p}) d\mathbf{p} \quad (4.15)$$

$$f_i = E(y|p_i) - E(y) = -f_0 + \int_0^1 \dots \int_0^1 f(p) dp_{\sim i} \quad (4.16)$$

$$f_{ij} = E(y|p_i, p_j) - E(y|p_i) - E(y) = \int_0^1 \dots \int_0^1 f(p) dp_{\sim ij} - f_0 - f_i \quad (4.17)$$

where $dp_{\sim i}$ and $dp_{\sim ij}$ denote the integration over all variables except p_i and p_i and p_j respectively, Ω^k is the sampling space. Sobol's method employs Monte Carlo approximations to calculate the integrals described in **equations 4.15 - 4.17** (Sobol, 2001; Saltelli et al., 2005).

Similarly, the **eq. 4.14** can be re-written as a variance (**eq. 4.18**) and sensitivity form (**eq. 4.19**) respectively:

$$V(y) = \sum_{i=1}^k V_i + \sum_{1 \leq i \leq j \leq k} V_{ij} + \dots + V_{1,2,\dots,k} \quad (4.18)$$

$$\sum_{i=1}^k s_i + \sum_{1 \leq i \leq j \leq k} s_{ij} + \dots + s_{1,2,\dots,k} = 1 \quad (4.19)$$

where V_i is the contribution of the parameter p_i to the total variance $V(y)$, while V_{ij} is the contribution inherent to the interactions between two parameters p_i and p_j .

Hence, these contributions (i.e. partial variances) can be used to calculate the first-order sensitivity index for the parameter p_i which evaluates the main effects of p_i on the output (i.e. partial variance of p_i to the total variance):

$$s_i = \frac{V_i}{V(y)} \quad (4.20)$$

In a similar way, the second-order s_{ij} and the total order sensitivity indices s_{Ti} can be determined from:

$$s_{ij} = \frac{V_{ij}}{V(y)} \quad (4.21)$$

$$s_{Ti} = 1 - \frac{V_{\sim j}}{V(y)} \quad (4.22)$$

The total sensitivity index s_{Ti} determines the total contribution of the parameter p_i considering both direct and indirect effects. Hence, the difference between s_{Ti} and s_i indicates the degree of interaction. More information regarding the method of Sobol and other variance method techniques can be found in [Saltelli et al. \(2008\)](#).

4.5 Optimal Experimental Design (OED)

The criteria of estimability analysis, however, cannot be always satisfied, indicating that the model-estimates may present high uncertainty or otherwise the model is inestimable (i.e. ill-conditioned). In this case, a model-based design of experiments (MBDoE) approach should be utilized sequentially, as indicated in **Figure 4.1**, in order the optimal experimental conditions yielding the most informative process data to be identified, resulting in accurate identification of the model-parameters. The optimal experimental design (OED) is in principal an optimization problem with the scope of minimizing the parameter uncertainty iteratively, which consequently leads to improved parameter precision ([Chen et al., 2004](#); [Schenkendorf et al., 2009](#)).

One way of assessing the parameter uncertainty is through confidence domains. So, in this study, for the estimation of the confidence intervals of the model-parameters, a method based on the fisher information matrix is used ([Walter and Pronzato, 1997](#); [Sin et al, 2010](#)). In more detail, the covariance matrix of the identified parameters, $COV(\mathbf{p})$, can be linearly approximated by:

$$COV(\mathbf{p})^{-1} \approx \frac{J(\mathbf{p})}{N_y - N_p} \left(\left(\frac{\partial \hat{y}}{\partial \mathbf{p}} \right)^T A \left(\frac{\partial \hat{y}}{\partial \mathbf{p}} \right) \right) = \frac{J(\mathbf{p})}{N_y - N_p} FIM \quad (4.23)$$

Then the confidence region (aka hyperellipsoid) of the parameters, \mathbf{p} , at a_t significance level is given as:

$$\mathbf{p}_{1-a_t} = \mathbf{p} \pm \sqrt{diag(COV(\mathbf{p}))} \cdot td(N_y - N_p, a_t/2) \quad (4.24)$$

, where $td(N_y - N_p, a_t/2)$ is the t-distribution value corresponding to the $a_t/2$ percentile with $N_y - N_p$ degrees of freedom and $diag(COV(\mathbf{p}))$ denotes the diagonal elements of the covariance matrix.

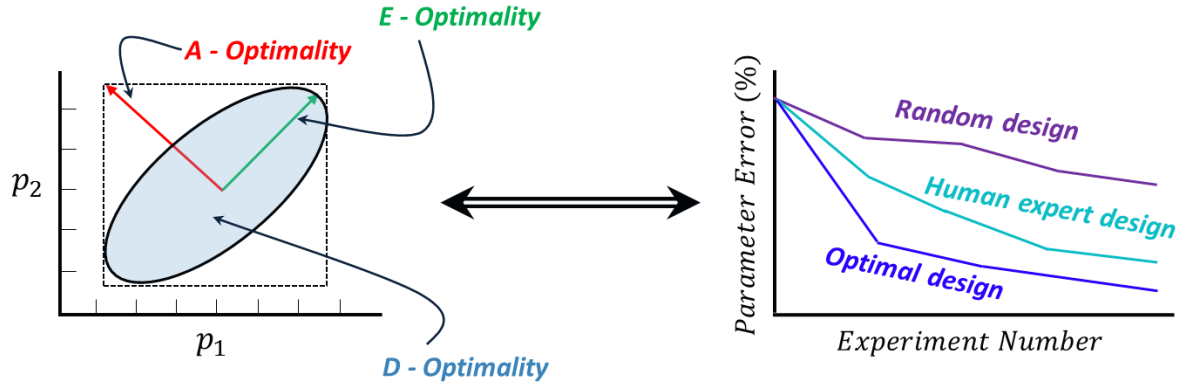


Figure 4.3. Graphical representation of how the optimal design criteria can be related to the parameter uncertainty and can be utilized to minimize the parameter error by identifying the optimum operating trajectory.

Therefore, a scalar function of the FIM is usually utilized as the objective function since it is directly related to the estimated confidence regions of the parameter estimates (see **Figure 4.3** - [Walter and Pronzato, 1997](#); [Sin et al, 2010](#)). Well known optimality criteria related to the FIM matrix are ([McLean and McAuley, 2012](#)):

$$A - \text{optimal design criterion: } \min(\text{tr}(FIM^{-1})) \quad (4.25)$$

$$D - \text{optimal design criterion: } \max(\det(FIM)) \quad (4.26)$$

$$E - \text{optimal design criterion: } \max(\lambda_{\min}(FIM)) \quad (4.27)$$

$$\text{Modified E - optimal design criterion: } \min\left(\frac{\lambda_{\max}(FIM)}{\lambda_{\min}(FIM)}\right) \quad (4.28)$$

, where $\lambda_{\min}(FIM)$ and $\lambda_{\max}(FIM)$ are the smallest and largest eigenvalues of the FIM respectively. The eigenvectors and eigenvalues of the FIM correspond to the direction and the length of the axes of the hyperellipsoid respectively. Hence, when the E – optimal design criterion maximizes the smallest eigenvalue of the FIM matrix is equivalent of minimizing the largest axis of the confidence ellipsoid. Similarly, when the condition number, which is the fraction of the largest and smallest eigenvalue, is minimized during the optimization of the modified E – optimal design criterion, the aspect ratio of the hyperellipsoid is minimized. Hence, the E – optimal design criterion utilizes only the size of the confidence ellipsoid, while the modified E – optimal design criterion is related only to the shape, which can be problematic since ideally both size and shape should be considered. Therefore, in this case study, the A – optimal and D – optimal design criteria, were utilized as the objective functions since they account both size and shape of the hyperellipsoid. More specifically, the A – optimal design criterion, minimizes the trace of the inverse FIM which is equivalent to minimizing the sum of squares of the length of the axes of the hyperellipsoid, while the D – optimal design criterion

maximizes the determinant of the FIM, which corresponds to minimizing the volume of the confidence ellipsoid.

Since, a cooling batch crystallization process is considered, the problem of designing dynamic experiments is posed as an optimal control problem that enables the estimation of the optimum temperature trajectory under different impurities' concentration, as shown below:

$$\max/\min_{T(1),T(2),\dots,T(P),C_{CGMi}} J_{obj,des}(t) \quad (\text{obj.4.1})$$

$$\text{subject to: } T_{min} \leq T_i \leq T_{max} \quad (\text{c.4.1})$$

$$R_{min} \leq \frac{dT}{dt} \leq R_{max} \quad (\text{c.4.2})$$

$$t \leq t_{final} \quad (\text{c.4.3})$$

$$0 \leq C_{CGMi} \leq 5ppm \quad (\text{c.4.4})$$

, where T_{min} , T_{max} , R_{min} and R_{max} are the minimum and maximum temperature and temperature ramp rates respectively. Two different objective functions were utilized, $J_{obj,des,A} = \min(\text{tr}(FIM^{-1}))$ and $J_{obj,des,D} = \max(\det(FIM))$ for the MIAM model. The total batch time (t_{final}) is introduced as a constraint (**c.4.3**) and it is a fixed value. The inequality constraint described by the expression **c.4.2** guarantees that the temperature trajectory is monotonically decreased since no dissolution is considered, while the expression **c.4.1** sets the upper and lower temperature bounds. The implementation of the temperature ramp rates (**expression c.4.2**) is related to the cooling capabilities of the utilized heat exchangers and, in this case, was selected to keep the cooling rates boundaries within the range of 0 to $-2 \text{ }^\circ\text{C}/\text{min}$. The final constraint (**c.4.4**) sets the upper and lower bounds with respect to the impurities' concentrations. The task defined by **obj.4.1** is a dynamic optimization problem with the temperature $T(t)$, which is a continuous function of time, to be the control variable. Hence, the input temperature trajectories were parametrized as a piecewise linear function with a finite number of decision variables over time (see **Chapter 3: section 3.3** for more information).

4.6 Results and Discussion

4.6.1 Parameter Estimability Analysis

Due to the large number of parameters commonly associated with the crystallization processes, a sequential parameter estimation approach has been extensively proposed. The method consists in splitting the model parameters to be identified into subsets with the aim of simplifying the optimization procedure, as limited number of parameters is considered each time. However, the approach doesn't rely on a rigorous or systematic selection procedure and no theoretical proof that the parameter subset can be optimally selected. As such, some authors claimed that the sequential approach outperforms the simultaneous one, which identifies all model parameters in one single step, while others observed non-inconsistencies between the prediction capabilities inherent to both methods. For instance, [Wohlgemuth & Schembecker, 2013](#), achieved better fitting by using the sequential approach for the concentration data, while the simultaneous method proved to be more accurate when the relevant model predictions were compared with CSD measurements. Hence, although the sequential approach can potentially simplify the parameter estimation process, it doesn't guarantee better estimates and consequently more predictable models.

Here, a rigorous selection procedure of the optimal subset of parameters, based on the estimability approach, is developed and implemented to the MIAM. The method combines two estimability methods: the first associates local sensitivities to a sequential orthogonalization procedure and the second uses a variance based global sensitivity selection. Only the optimal subset or parameters require identification (the rest of the parameters can be set to their nominal values) with a guaranteed minimum model mismatch (i.e. high prediction capability).

It should be emphasized that the parameters of the novel Multi-Impurity PBM model were previously identified by [Borsos et al. \(2016\)](#) using a sequential identification methodology and attempted to identify decoupled kinetic parameters while taking several parameters from literature. For instance, the parameters associated with the primary nucleation and the crystal growth of the two different facets were obtained from the literature, while the kinetic parameters inherent to the two crystal growth modifiers (i.e. impurities) were estimated from on-line image analysis data. However, the addition of additives/impurities might affect the kinetics of nucleation and growth ([Epstein, 1982; Kubota, 2001a](#)), and hence the nominal parameter vector might not be reliable enough.

Table 4.3. Nominal vector of the model parameters and their confidence intervals (C.I.)

Parameter	Nominal value from Borsos et al., 2016	Estimated nominal values Current work Value \pm C.I. %	Units	Corresponding Number
$k_{ads,0,CGM1}$	27.3	$6.131 \pm 90.64 \%$	-	1
$k_{des,0,CGM1}$	0.56562	$0.630 \pm 98.93 \%$	-	2
β_1	4.6	$10.626 \pm 87.50 \%$	m/K	3
$G_{min,1}$	4.5×10^{-4}	$2.812 \times 10^{-4} \pm 99.96 \%$	$\mu m/s$	4
$k_{m,0,CGM1}$	389.348	$19.135 \pm 0.0014 \%$	m/s	5
$K_{e,CGM1}$	0.999	$1.669 \pm 66.75 \%$	-	6
$\Delta G_{ads,1}$	$2.436 \times 10^{+3}$	$1.578 \times 10^{+3} \pm 2.24 \%$	kJ/mol	7
$\Delta G_{des,1}$	$2.2994 \times 10^{+4}$	$2.17 \times 10^{+4} \pm 2.37 \%$	kJ/mol	8
$k_{ads,0,CGM2}$	11.24	$4.046 \pm 86.78 \%$	-	9
$k_{des,0,CGM2}$	0.49127	$0.4566 \pm 98.36\%$	-	10
β_2	5.15	$5.1164 \pm 87.03\%$	m/K	11
$G_{min,2}$	246.952	$487.034 \pm 0.23\%$	$\mu m/s$	12
$k_{m,0,CGM2}$	61.1286	$79.096 \pm 0.99\%$	m/s	13
$K_{e,CGM2}$	0.994	$0.997 \pm 99.84 \%$	-	14
$\Delta G_{ads,2}$	$5.301 \times 10^{+3}$	$6.386 \times 10^{+3} \pm 1.09 \%$	kJ/mol	15
$\Delta G_{des,2}$	$2.4181 \times 10^{+4}$	$2.709 \times 10^{+4} \pm 0.88 \%$	kJ/mol	16
g_1	1.4776	$1.553 \pm 99.57 \%$	-	17
k_{g1}	12.2063	$21.028 \pm 74.11\%$	$\mu m/s$	18
g_2	1.692	$1.692 \pm 99.27 \%$	-	19
k_{g2}	1.7412	$98.109 \pm 24.15\%$	$\mu m/s$	20
$k_{p,0}$	100.751×10^{-18}	334.331×10^{-18} $\pm 0.35\%$	$\#/\mu m^{-3} s^{-1}$	21
E_p	$2.814 \times 10^{+3}$	$0.001 \pm 64.28\%$	kJ/mol	22
k_e	1.576×10^{-3}	$4.895 \pm 2.24\%$	-	23

Commonly, the estimability approach requires a set of nominal parameter values which represent a reasonable initial guess, usually obtained from literature or prior process knowledge. To guarantee a generic robust framework for parameter estimation and extend the discussions above, the estimability approach is developed for two case scenarios: the case where the model parameters obtained by Borsos et al. (2016), in conjunction with the literature, can be used as nominal values, and the case where no prior knowledge of the process parameter is available. In the latter case, a simultaneous identification approach, based on a hybrid global optimization approach, that combines a genetic algorithm and a local deterministic approach was used to identify the nominal values. The model-parameters that were estimated based on these techniques are presented in Table 4.3. In both cases the estimability approach will help identify

the best parameter estimates of the optimal subset that guarantees maximum prediction capability, given the available experimental data. It is worth mentioning that this forward estimability method can also be used for the optimum design of experiments for improved parameter estimation (Benyahia, 2009; Benyahia et al., 2011b).

One crucial step after the identification of the 23 unknown parameters is the evaluation of the uncertainty of the model estimates, since it could provide information regarding the robustness and the predictive capability of the model. One way of assessing these uncertainties is through confidence domains. In this study, a method based on the FIM is used to estimate the 95% confidence intervals of the model-parameters (Sin et al, 2010). The mean values of the identified model parameters for the simultaneous approach and the corresponding confidence intervals are presented in **Table 4.3**.

Although the confidence intervals associated with some of the nominal parameter estimates are reasonably narrow, most of the model parameters highlighted in red present broad confidence intervals. Statistically speaking, this indicates that the parameters are unidentifiable and consequently the parameter estimates are not reliable. Hence, a good fit should be combined with the estimation of confidence regions and the corresponding correlation matrix. In this way, the reliability of the estimated unknown parameters can be assessed (**Table 4.3**). In most of the cases, the cause of these broad confidence domains is associated with the existence of strong correlations amongst the parameters. The correlation effects will be thoroughly discussed in conjunction with the estimability analysis in the next sections.

4.6.2 Local Estimability Analysis: LSA and Orthogonalization Algorithm

Although the estimability aims in essence at improving the parameter estimates in order to enhance the model prediction capability, the initial parameter estimates, used as nominal values, can play a crucial role in the quality of the sensitivity analysis, both LSA and GSA, and consequently determines the outcome of the estimability analysis. Poor nominal model parameters would potentially lead to inaccurate parameter ranking that consequently would lead to a degradation of the predictive capability of the mathematical model (Benyahia, 2009). The investigation of the estimability analysis is carried out, as explained before, in three steps: a local sensitivity analysis is performed in order to evaluate the relative effect of the parameters on the process outputs, then the model parameters are ranked in descending order, in terms of sensitivity magnitude and correlation, by using the Orthogonalization algorithm (**Table 4.2**).

Finally, an incremental optimization approach that consists in a sequential identification of the top i^{th} parameters (where $i = 1, 2, \dots$) is utilized to determine the threshold or cut-off value and identify the optimal subset of model parameters.

In **Figure 4.4**, the variation of the dynamic sensitivity of some model parameters is presented. The first selected parameter (**Figure 4.4a**), g_1 , which is the exponent of the growth kinetic equation in the x_1 dimension (i.e. along the length of the crystal), shows very high sensitivities at all times. This means that g_1 has a strong effect on the model predictions (outputs) and consequently its estimability potential can be very high depending the concurrent correlation effects. The same stands for the second selected parameter (**Figure 4.4b**), $k_{e,CGM2}$, which describes the thermodynamic mass distribution coefficient for the CGM2 (i.e. sodium hexametaphosphate). These two parameters are likely to be ranked high in terms of estimability potential meaning that the information obtained from the measurements in the considered time window will be adequate for their accurate estimation. On the other hand, $k_{p,0}$ and $k_{m,0,CGM1}$ show very weak sensitivities at all times. For instance, the sensitivities associated with $k_{m,0,CGM1}$ are always below 6×10^{-7} which indicates that these model parameters are likely to be practically unidentifiable (inestimable).

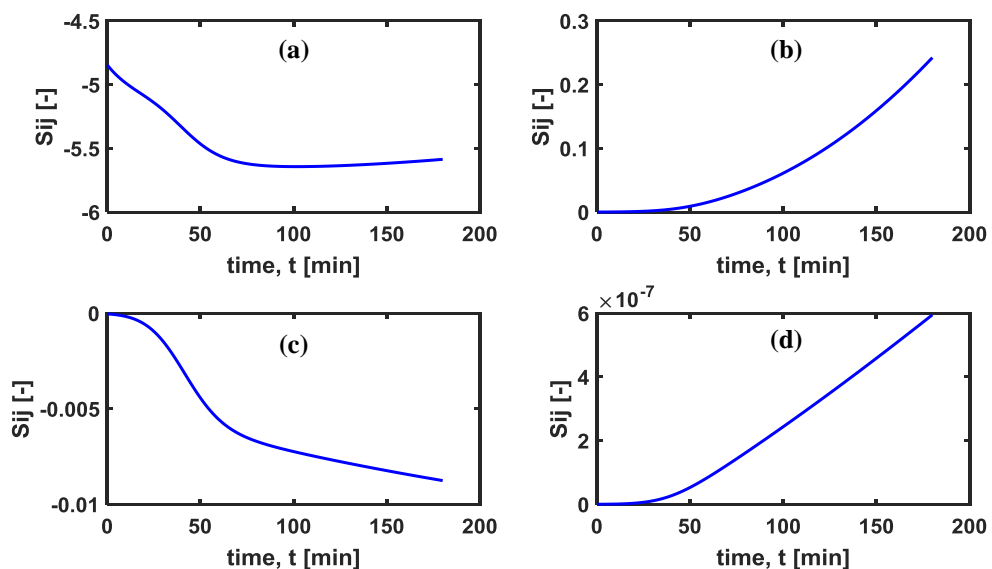


Figure 4.4. Comparison of the dynamic sensitivity of selected model parameters: (a) g_1 (b) $K_{e,CGM2}$ (c) $k_{p,0}$ (d) $k_{CGM1,m,0}$

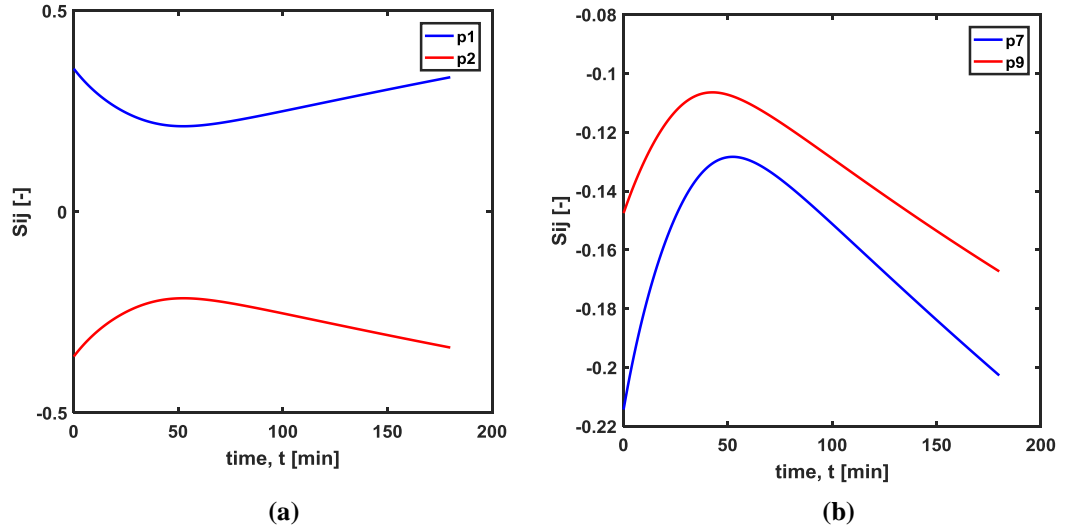


Figure 4.5. Comparison of the sensitivity profiles of selected model parameters: (a) $p_1 : k_{ads,0,CGM1}$ & $p_2 : k_{des,0,CGM1}$ and (b) $p_7 : \Delta G_{des,1}$ & $p_9 : k_{ads,0,CGM2}$

Besides the relative effect of the parameters on the outputs, the sensitivity analysis can give a very good indication of the existence of correlations between the parameters. Similar sensitivity trajectories indicate strong correlation as seen by comparing the sensitivity trajectories of $k_{ads,0,CGM1}$ and $k_{des,0,CGM1}$ (**Figure 4.5a**) and $\Delta G_{des,1}$ and $k_{ads,0,CGM2}$ (**Figure 4.5b**). These outcomes are also consistent with the correlogram (correlation matrix) depicted in **Figure 4.7**

Similar results could be drawn from **Figure 4.6**, where the whole parameter set is presented in a box plot. This diagram illustrates the variation of the estimated model parameters. The parameters can be classified in three different discrete subgroups according to their contribution to the output: high, moderate and low. As such, some of the parameters such as $\{k_{e,CGM2}, \Delta G_{ads,2}, \Delta G_{des,2}, g_1, k_{g1}, g_2, \Delta G_{des,1}\}$ can be classified as parameters with high impact. $\{k_{ads,0,CGM1}, k_{des,0,CGM1}, \beta_1, \Delta G_{ads,1}, k_{ads,0,CGM2}, k_{des,0,CGM2}, \beta_2, k_{g2}\}$ and $\{G_{min,1}, k_{m,0,CGM1}, K_{e,CGM1}, G_{min,2}, k_{m,0,CGM2}, k_{p,0}, E_p, k_e\}$, on the other hand, seem to present moderate and low sensitivity to the imposed perturbation respectively. Hence a considerable number of the parameters obtain low sensitivity values. This lack of sensitivity suggests that the model is over-parametrized (Saltelli et al., 2008). However, model discrimination is beyond the scope of this paper and all parameters are considered essential for other physical aspects of the model performance and may be set to their nominal values without degrading the prediction capabilities of the model. These observations indicate that the vector of the model parameters as a whole is practically unidentifiable (from the available data) and further analysis should be done in order to select an optimal subset of parameters. It should be highlighted that this

classification is based utterly on observation of the variation of the sensitivities and is presented as a preliminary qualitative analysis of the results. The formal implementation of the estimability approach and identification of the cut-off value will be discussed in the subsequent sections.

A robust approach for ranking the model parameters according to their estimability potential is based on the orthogonalization algorithm (**Table 4.2**), which takes into account both the sensitivity magnitude (i.e. Euclidean norm) and correlation during the sequential selection of the most estimable parameter. The results obtained based on modified Gram-Schmidt orthogonalization algorithm are presented in **Table 4.4**. The exponents of the growth kinetic equations in the $\{x_1, x_2\}$ dimensions (i.e. g_1 and g_2) indicate high estimability potential. This was expected since these parameters represent the exponential factors of the crystal growth rates used in the model algebraic equations (i.e. empirical power law expressions). The absorption energy of the impurities (i.e. $\Delta G_{ads,1}$ and $\Delta G_{ads,2}$) also appear to have a significant impact on the outputs since they are highly ranked on the list illustrating high estimability potential. It is also evident, that the kinetic parameters corresponding to the nucleation mechanism are ranked quite low $\{k_{p,o}, E_p, k_e\}$ because of their weak sensitivity coefficients at the sampling times. This reveals how critical is the incorporation of the estimability analysis in the development of the design of experiment and consequently in mathematical modelling. Moreover, it is known that the AR measurements can provide negligible information regarding the nucleation phenomena. This limitation maybe overcome by incorporating additional PAT to measure the concentration and number of counts (focussed beam reflectance (FBRM)) and considering these two variables as process outputs in the estimability framework.

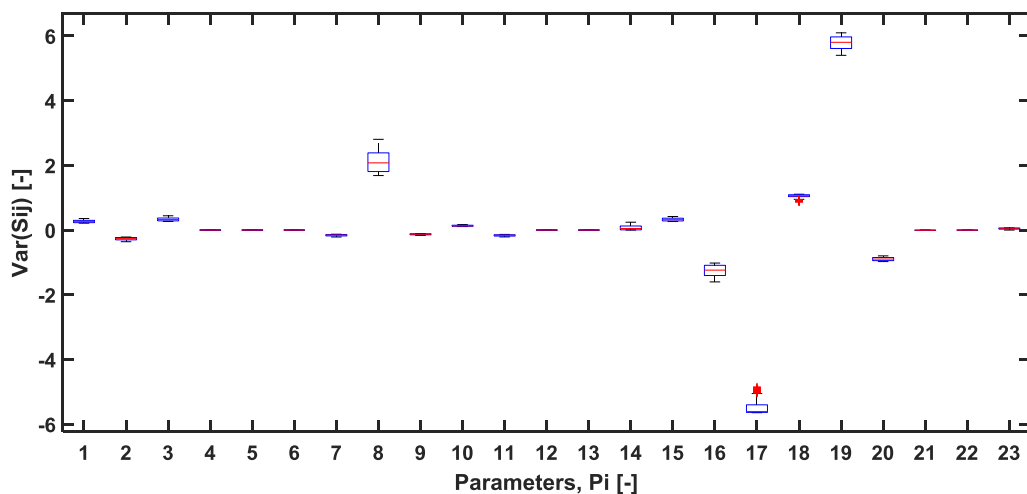


Figure 4.6. Box plot illustrating the variation of the sensitivity of the estimated model parameters.

The estimability analysis revealed that the data are not adequate to estimate accurately the nucleation kinetics. This is key, especially in systems utilizing different sensors. As such, the information content of each sensor may be assessed and consequently the number of parameters that can be estimated from each individual PAT or from their combination (e.g. sensors providing different outputs) may be determined. This may also be employed for the evaluation of the accuracy of the measuring method with the scope of collecting more accurate measurements. Hence, the estimability analysis can be utilized for the selection of the appropriate PAT and consequently the most efficient strategy to collect the experimental data to improve the accuracy of the model parameters, which in turns enhances the model reliability in key applications such as process design and control.

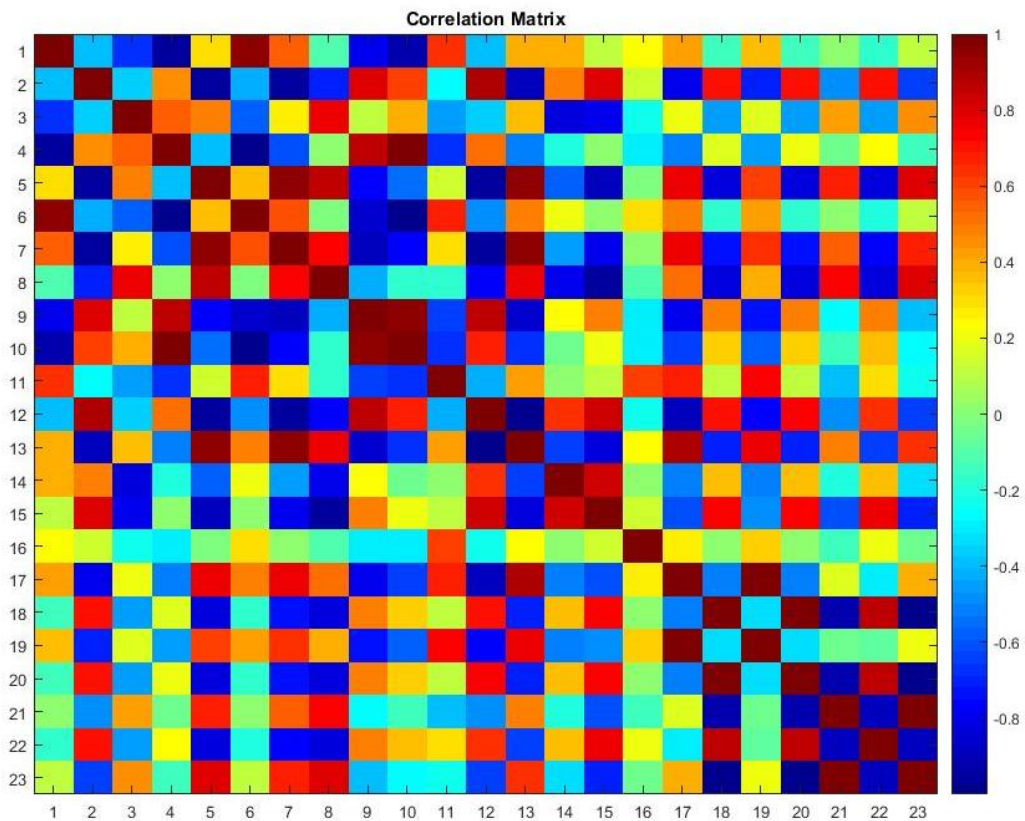



Figure 4.7. Correlation matrix for the estimated nominal parameter set.

The sequential orthogonalization approach helps select the parameters with the highest sensitivity and least correlation. To provide a more rigorous insight into the correlation effects, a correlation matrix, can be computed by using the Pearson method (Kendall et al., 1977). The 23×23 correlation matrix obtained from the covariance matrix (inverse of the FIM) is presented in **Figure 4.7**. As shown, strong positive or negative correlations exist between some parameters. For instance, the parameters p_{20} and p_{23} present very strong negative correlation.

Hence, any change that occurs in p_{20} can be compensated by an inverse change in p_{23} . Similar interaction patterns do occur between the kinetics describing the nucleation phenomenon (i.e. p_{21}, p_{22}, p_{23}), which present strong positive and negative correlation. In general, the presence of high correlations, especially if it corresponds to a high number of the estimated parameters, can make the identification process difficult and inaccurate (not unique).

In order to identify the optimal subset of parameters that maximize model reliability, a cut-off value should be selected to set a boundary between the parameters with high estimability potential, that can be identified reliably, and the remaining parameters that are poorly identifiable and should be set to their nominal value without degrading the prediction capability of the model. As such, the cut-off value is critical as it affects both the cost and quality of the estimability approach and the prediction capability of the model. Several methods were used in the literature to set a cut-off value as discussed earlier (**Section 4.4.1**).

Table 4.4. Ranking of parameters with the highest estimability potential

Method	Parameter ranking
Orthogonalization algorithm	$g_1, k_{e,CGM2}, \Delta G_{ads,1}, g_2, \Delta G_{ads,2}, \dots, k_{g1}, \beta_1, \Delta G_{des,2}, k_{ads,0,CGM1},$ $k_{des,0,CGM1}, k_{g2}, \Delta G_{des,1}, \beta_2, k_{des,0,CGM2}, k_{ads,0,CGM2}, k_e, K_{e,CGM1},$ $k_{p,0}, k_{m,0,CGM2}, G_{min,1}, E_p, G_{min,2}, k_{m,0,CGM1}$
	
	17, 14, 8, 19, 16, 18, 3, 15, 1, 2, 20, 7, 11, 10, 9, 23, 6, 21, 13, 4, 22, 12, 5
	High Estimability Potential Low Estimability Potential

To identify the cut-off value and consequently the optimal subset of parameters, an iterative approach is performed. It consists in identifying incrementally the subsets of model parameters, from the experimental data, according to their estimability potential (**Table 4.4**) starting with the top ranked parameter, then the top two parameters and so forth. This approach will help identify the optimal objective function threshold (i.e. cut-off value), beyond which all improvements are insignificant, and consequently the optimum identifiable subset of parameters. The results of the iterative incremental approach are depicted in **Figure 4.8**. Typically, when a mean square error approach is considered, the objective function, $J(p)$, decreases until a plateau is reached. The initial point of the plateau can be considered as the cut-off value as no significant improvement can be achieved from that point onwards, which consequently sets the limit of the optimal identifiable parameter set. **Figure 4.8a** indicates that the top 7 ranked parameters, in the case of the nominal values obtained from [Borsos et al.](#)

(2016), and the top 8 ranked parameters, in the case of the simultaneous optimization approach, are sufficient to capture the information contained in the experimental data.

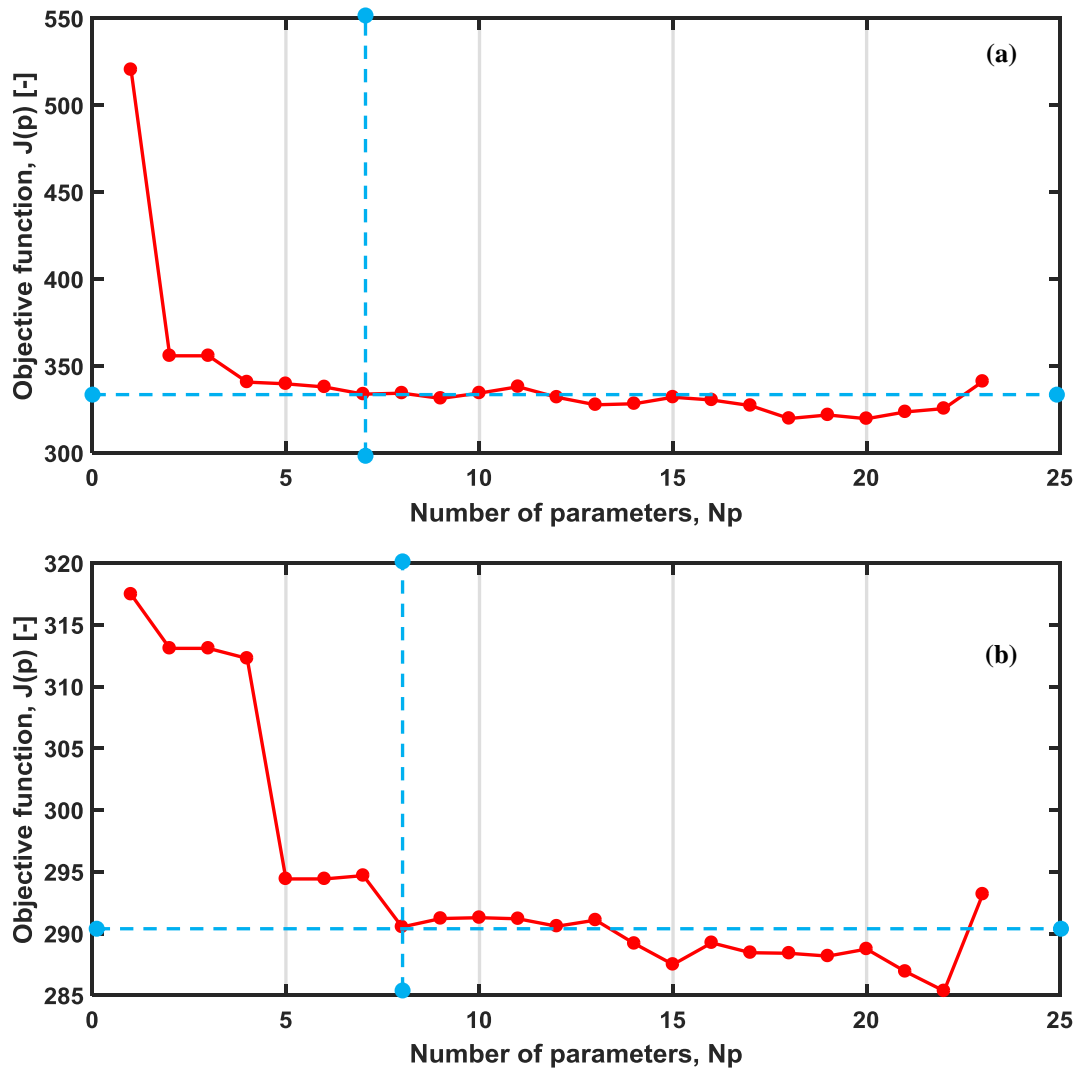


Figure 4.8. Maximum likelihood error vs the number of selected parameters for: (a) nominal set of parameters estimated by Borsos et al. (2016) – sequential approach and (b) nominal set of parameters estimated in this work – simultaneous approach.

Despite the fact that using more parameters may lead to a slight decrease in the objective function, as depicted in **Figure 4.8**, the estimability approach guarantees the best trade-off between model reliability and minimum set of parameters to be identified. **Figure 4.8** also confirms that different nominal parameter values, as clearly shown in **Figure 4.8a** and **b**, lead to different threshold values (340 in case a and 290 in case b). In this particular case, the estimability approach implemented with the nominal vector inherent to a simultaneous identification approach outperforms the quality of the one carried out with Borsos et al. nominal value obtained sequentially. It should be noted that the objective functions show non-

smoothness in both cases which is likely due to the high nonlinearity and stiffness of the set of ODEs and the increased correlation between the parameters as more parameters are being added. This non-smooth behaviour may also indicate that the local solver got stuck in local optima.

4.6.3 Global Sensitivity Analysis (GSA)

The global sensitivity analysis (GSA) is utilized here in order to assess the performance of the model itself and to cross-validate the local estimability analysis approach discussed earlier. The method provides another alternative to rank the model parameters and identify the optimal set of parameters that could be estimated from the experimental data. In this case the total order sensitivity index will be used to rank the parameters, followed by an incremental optimization-based selection approach whose performances will be compared against the previously described estimability approach, associated with the local sensitivities.

The Sobol analysis is performed as follows. Firstly, a nominal set of model parameters is defined followed by the definition of the probability distributions for each individual parameter. In this work a Gaussian distribution was assigned for every parameter by considering 2 % variance. Narrow limits are applied since the population balance models for crystallization processes present, in general, high stiffness, which might have a considerable effect on the computational burden. Random combination of parameter sets are generated from the assigned probability distribution functions. In this way, the output of the model is evaluated for different parameter sets along with the uncertainties. Consequently, the sensitivity indices are calculated in order to assess the effect of the parameters and rank them accordingly.

The global sensitivity analysis is performed here by taking into account two different scenarios. In the first scenario, the effects of the parameters are analysed considering only the model predicted outputs inherent to the set of the ODEs representing the studied system. Hence, the impact of the parameters on the joint moments and on the concentration of the solution and impurities is investigated based exclusively on simulations (i.e. without considering the sampling times). The second scenario considers the mean aspect ratio measurements. Hence, Sobol analysis is applied for the decomposition of the variance which is associated with the difference between experimental and simulation data (i.e. global estimability analysis). In more detail, the computation of the root mean square error can provide information with the scope of

parameter ranking and model selection (cut-off value determination). The 23 unknown model parameters estimated in this work and defined in **Table 4.3** are used as inputs for the sensitivity and estimability analysis.

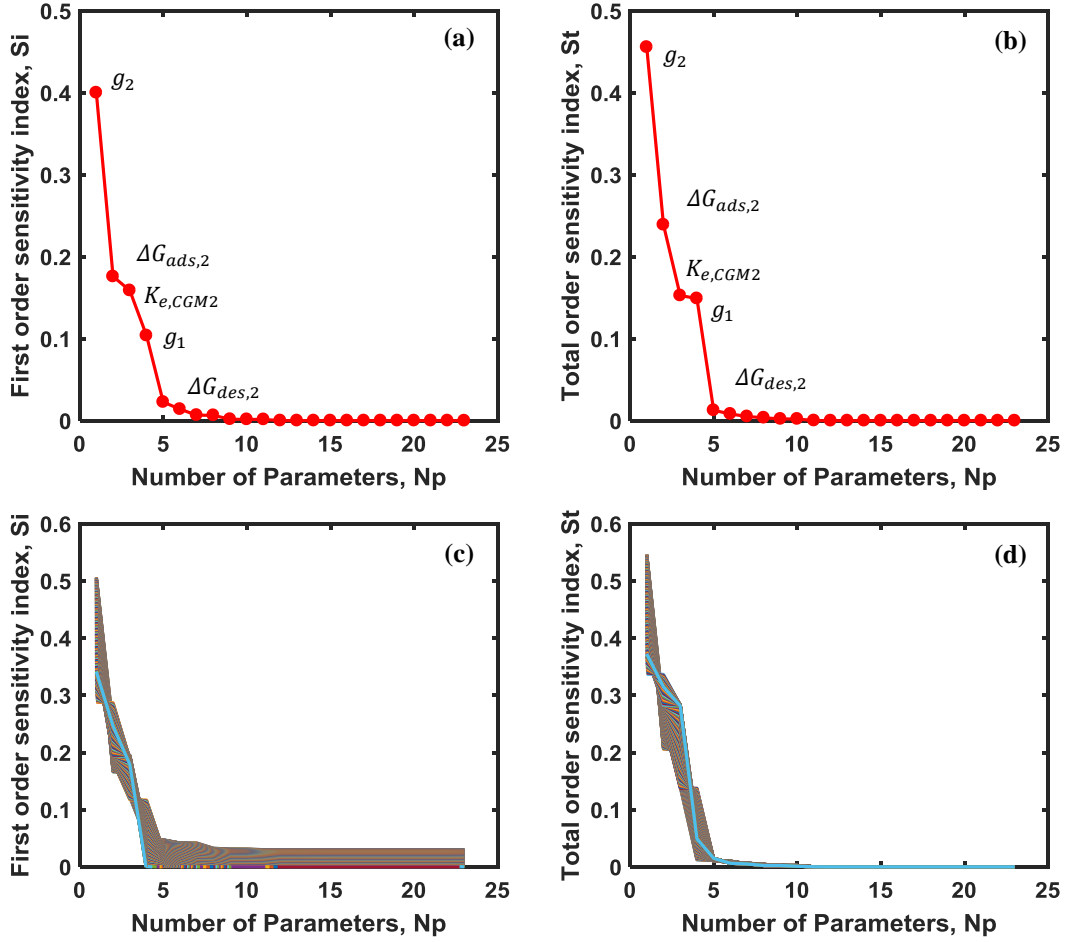


Figure 4.9. Sobol analysis for the 1st case scenario: (a) first order sensitivity indices of the 23 parameters in descending order (b) total order sensitivity indices in descending order (c) first order sensitivity indices for a sample of randomly generated sets of parameters (d) total order sensitivity indices for a sample of randomly generated sets of parameters.

It was demonstrated that a trade-off between computational accuracy and efficiency of the first and total order sensitivity indices can be achieved at a cost of $(N_p + 2)N$ model evaluations (Saltelli et al., 2005), where N is the number of samples that should be between 5×10^2 and 1×10^3 and N_p is the number of parameters (23 in our case). In this analysis, for both scenarios a conservative approach is selected by considering $N = 1 \times 10^3$ and the total number of evaluations as 25×10^3 . The results were validated using different numbers of samples (N) to ensure consistency and robustness of the results.

The results are summarized in **Figure 4.9** and **Figure 4.10**, where the first and total order Sobol sensitivity indices are presented in descending order for the two scenarios. **Figure 4.9a** and **4.9b** indicate that both first and total order Sobol sensitivity indices yield the same order of priority for the first scenario which illustrates that certain parameters have a considerable impact on the output variable (i.e. aspect ratio) both directly (relative impact of each input variable) and indirectly (interaction among the input parameters). On the other hand, **Figure 4.9c** and **4.9d** represent the first order and total order sensitivity indices respectively for each randomly generated parameter set, screening the effect of possible parameter combinations (i.e. inputs) on the model output (i.e. predicted mean aspect ratio in this case scenario). In a similar way to the discussion above, the effect of randomly generated subsets of parameters on the mean square error between the measured and predicted mean aspect ratio is analysed for the second scenario.

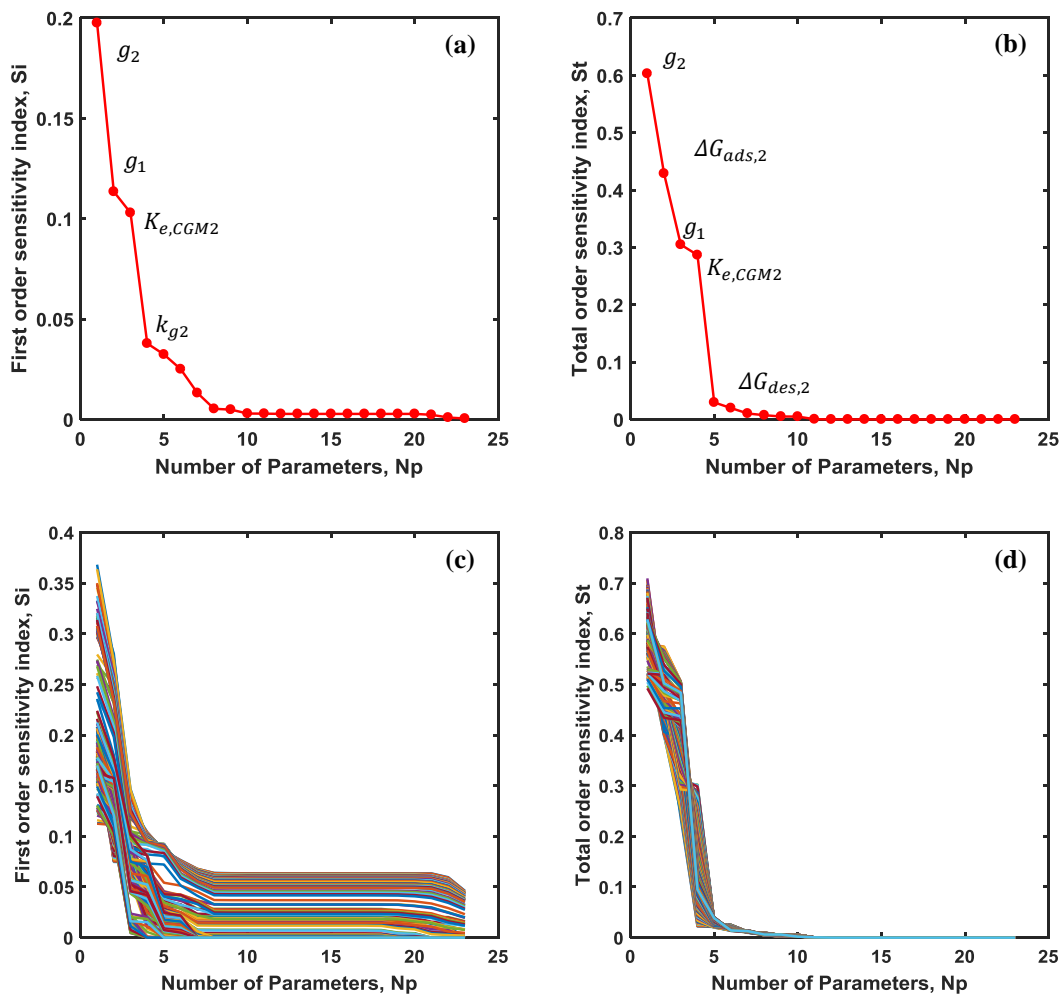


Figure 4.10. Sobol analysis for the 2nd case scenario: (a) first order sensitivity indices of the 23 parameters in descending order (b) total order indices in descending order (c) first order sensitivity

indices for a sample of randomly generated sets of parameters (d) total order sensitivity indices for a sample of randomly generated sets of parameters.

The greater the sensitivity indices are, the more critical the parameters are for the model. **Figure 4.9** and **Figure 4.10** show that the parameters g_1 and g_2 , which are the exponents of the growth kinetic equations in the x_1 and x_2 dimension respectively, possess the highest total sensitivity indexes. This was expected since a growth dominated physical system is under investigation. The analysis also demonstrates that $\Delta G_{ads,2}$, $\Delta G_{des,2}$ and $K_{e,CGM2}$, which represent the adsorption, desorption kinetics and the thermodynamic mass distribution coefficient for CGM2 respectively, can be reliably identified. This can be anticipated as well since it was experimentally proven (Borsos et al., 2016) that the CGM2 (i.e. sodium hexametaphosphate) has a more prominent effect compared to CGM1 (i.e. aluminum sulfate). When both growth modifiers are present in the system, the aspect ratio decreases which is caused by CGM2, even when lower amounts of CGM2 are used. The nucleation kinetics present low sensitivity values, which is consistent with the outcomes of the estimability analysis based on local sensitivities. By comparing the two scenarios, the majority of the parameters show significant lack of sensitivity. However, in both scenarios interesting patterns emerge. Sensitive parameters (high s_i values) affect the output through both direct and indirect effects (high s_t values). Thus, the parameters with moderate and low sensitivity values cannot affect the system even indirectly (i.e. through interactions) from a sensitivity point of view. Overall, the Sobol analysis demonstrates that a large number of parameters can be set to nominal values without degrading the model prediction capabilities.

The total order indices, presented in **Figure 4.9b** and **Figure 4.10b**, are used to identify the cut-off value for the selection of the optimal subset of model parameters. As it can be seen, the values of the total order indices are reduced until a plateau is reached. The initial point can be considered as the cut-off value since the additional parameters wouldn't improve the estimation process and hence the predictive capability of the model

The Sobol analysis indicate that a cut-off value can be identified directly from the total order indices and accordingly the top 7 and 8 parameters are sufficient to build a reliable model for the 1st and 2nd scenarios respectively. However, for the sake of consistency and in order to enable a reliable comparison between the two estimability methods, the cut-off value will be identified from the profile of the objective function associated with the parameter identification problem (minimization between the model predictions and the experimental data). The profile

of the objective functions for the two scenarios, obtained by an incremental iterative approach as described above for the case of LS-based estimability, are depicted in **Figure 4.11**. As noticed in the previous case, the objective functions decrease significantly with the introduction of the top few parameters. The diagram confirms that the selection of the top 8 parameters can be sufficient enough to maximize the prediction capabilities of the model. Despite these consistent outcomes, the selection process through an incremental iterative parameter estimation procedure is highly advised as it is more reliable compared to the selection based on the magnitudes of the total order sensitivity index. **Figure 4.11** also shows non-smooth behaviour similar to **Figure 4.8**.

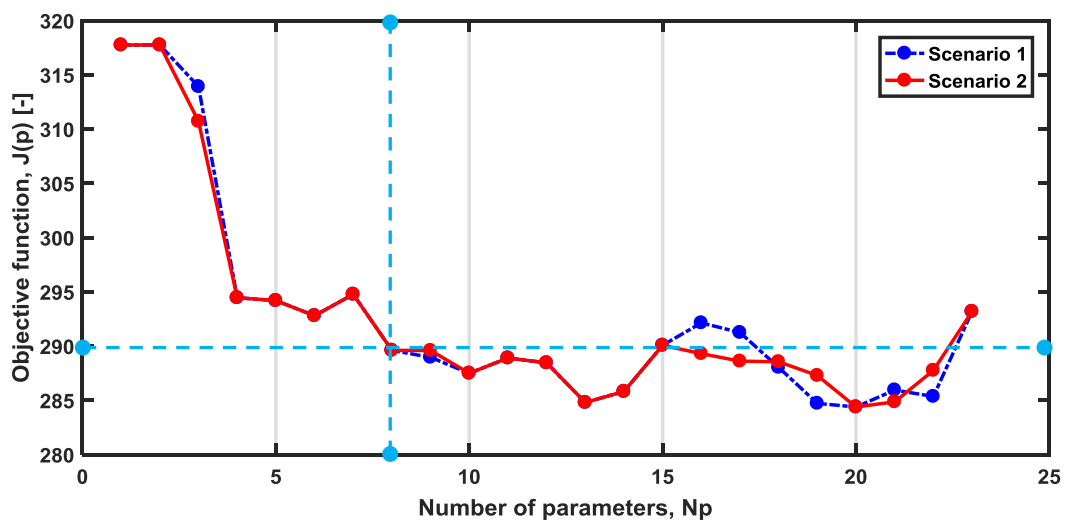


Figure 4.11. Maximum likelihood error vs the number of selected parameters for both Sobol scenarios.

To make a reliable and effective comparison between the two methods described in the paper (the estimability method based on LS and Sobol method with two scenarios), the parameter ranking and optimal parameter sets are summarized in **Table 4.5**. Although, each method yields a different classification, as expected, some consistency was achieved as the same four parameters, highlighted in red, which were identified by both methods as the ones with the most prominent effects. The inconsistencies can be explained by the fact that the methods use essentially different approaches, LSA and GSA, besides the quality of the nominal vector of parameters can play a key role in both cases. Although, both techniques can be used separately the outcomes of the analysis show that their combination can provide a more systematic and robust selection of the subset of parameters that provides guaranteed optimal prediction capabilities based on the available data. In addition, the methodology can provide a basis to assess the quality and quantity of the experimental data or alternatively inform or help design

the required experiments and/or measurements (DoE) that could improve the estimability potential of a specific parameter, which in turn helps improve the prediction capabilities of the mathematical model, particularly in the case of multi-dimensional population balance models.

Table 4.5. Summary of the parameter ranking based on Orthogonalization algorithm and the Sobol analysis

Orthogonalization (LSA)		Sobol Analysis (GSA)			
Nominal parameters from Borsos et al., 2016	Estimated nominal vector of parameters	Estimated nominal vector of parameters			
		1 st Scenario		2 nd Scenario	
		S_i	S_t	S_i	S_t
g_1 (p17)	g_1 (p17)	g_2 (p19)	g_2 (p19)	g_2 (p19)	g_2 (p19)
$k_{e,CGM2}$ (p14)	$k_{e,CGM2}$ (p14)	$\Delta G_{ads,2}$ (p16)	$\Delta G_{ads,2}$ (p16)	g_1 (p17)	$\Delta G_{ads,2}$ (p16)
g_2 (p19)	$\Delta G_{ads,1}$ (p8)	$k_{e,CGM2}$ (p14)	$k_{e,CGM2}$ (p14)	$k_{e,CGM2}$ (p14)	g_1 (p17)
$\Delta G_{ads,1}$ (p8)	g_2 (p19)	g_1 (p17)	g_1 (p17)	k_{g2} (p20)	$k_{e,CGM2}$ (p14)
$\Delta G_{ads,2}$ (p16)	$\Delta G_{ads,2}$ (p16)	$\Delta G_{des,2}$ (p15)	$\Delta G_{des,2}$ (p15)	$\Delta G_{ads,2}$ (p16)	$\Delta G_{des,2}$ (p15)
k_{g1} (p18)	k_{g1} (p18)	k_{g2} (p20)	k_{g2} (p20)	$\Delta G_{des,2}$ (p15)	k_{g2} (p20)
β_1 (p3)	β_1 (p3)	k_{g1} (p18)	β_2 (p11)	$k_{ads,0,CGM2}$ (p9)	β_2 (p11)
k_{g2} (p20)	$\Delta G_{des,2}$ (p15)	β_2 (p11)	k_{g1} (p18)	k_{g1} (p18)	k_{g1} (p18)
$\Delta G_{des,2}$ (p15)	$k_{ads,0,CGM1}$ (p1)	k_e (p23)	$k_{des,0,CGM2}$ (p10)	$k_{des,0,CGM2}$ (p10)	$k_{ads,0,CGM2}$ (p9)
β_2 (p11)	$k_{des,0,CGM1}$ (p2)	$k_{ads,0,CGM2}$ (p10)	$k_{ads,0,CGM2}$ (p9)	$k_{p,0}$ (p21)	$k_{des,0,CGM2}$ (p10)
$k_{ads,0,CGM1}$ (p1)	k_{g2} (p20)	$k_{ads,0,CGM2}$ (p9)	k_e (p23)	E_p (p22)	k_e (p23)
$k_{des,0,CGM1}$ (p2)	$\Delta G_{des,1}$ (p7)	E_p (p22)	$k_{m,0,CGM2}$ (p13)	$G_{min,2}$ (p12)	$k_{m,0,CGM2}$ (p13)
$\Delta G_{des,1}$ (p7)	β_2 (p11)	$G_{min,2}$ (p12)	$k_{p,0}$ (p21)	$k_{m,0,CGM1}$ (p5)	$k_{p,0}$ (p21)
$k_{des,0,CGM2}$ (p10)	$k_{des,0,CGM2}$ (p10)	$G_{min,1}$ (p4)	E_p (p22)	$K_{e,CGM1}$ (p6)	E_p (p22)
$k_{ads,0,CGM2}$ (p9)	$k_{ads,0,CGM2}$ (p9)	$\Delta G_{ads,1}$ (p8)	$G_{min,2}$ (p12)	$k_{des,0,CGM1}$ (p2)	$G_{min,2}$ (p12)
$k_{p,0}$ (p21)	k_e (p23)	β_1 (p3)	β_1 (p3)	$\Delta G_{des,1}$ (p7)	$k_{m,0,CGM1}$ (p5)
k_e (p23)	$K_{e,CGM1}$ (p6)	$\Delta G_{des,1}$ (p7)	$k_{ads,0,CGM1}$ (p1)	β_1 (p3)	$k_{ads,0,CGM1}$ (p1)
$K_{e,CGM1}$ (p6)	$k_{p,0}$ (p21)	$K_{e,CGM1}$ (p6)	$k_{des,0,CGM1}$ (p2)	$G_{min,1}$ (p4)	$\Delta G_{ads,1}$ (p8)
$k_{m,0,CGM2}$ (p13)	$k_{m,0,CGM2}$ (p13)	$k_{ads,0,CGM1}$ (p1)	$K_{e,CGM1}$ (p6)	$\Delta G_{ads,1}$ (p8)	β_1 (p3)
E_p (p22)	$G_{min,1}$ (p4)	$k_{des,0,CGM1}$ (p2)	$\Delta G_{ads,1}$ (p8)	$k_{ads,0,CGM1}$ (p1)	$G_{min,1}$ (p4)
$G_{min,2}$ (p12)	E_p (p22)	$k_{m,0,CGM1}$ (p5)	$G_{min,1}$ (p4)	$k_{m,0,CGM2}$ (p13)	$k_{des,0,CGM1}$ (p2)
$G_{min,1}$ (p4)	$G_{min,2}$ (p12)	$k_{p,0}$ (p21)	$\Delta G_{des,1}$ (p7)	β_2 (p11)	$K_{e,CGM1}$ (p6)
$k_{m,0,CGM1}$ (p5)	$k_{m,0,CGM1}$ (p5)	$k_{m,0,CGM2}$ (p13)	$k_{m,0,CGM1}$ (p5)	k_e (p23)	$\Delta G_{des,1}$ (p7)

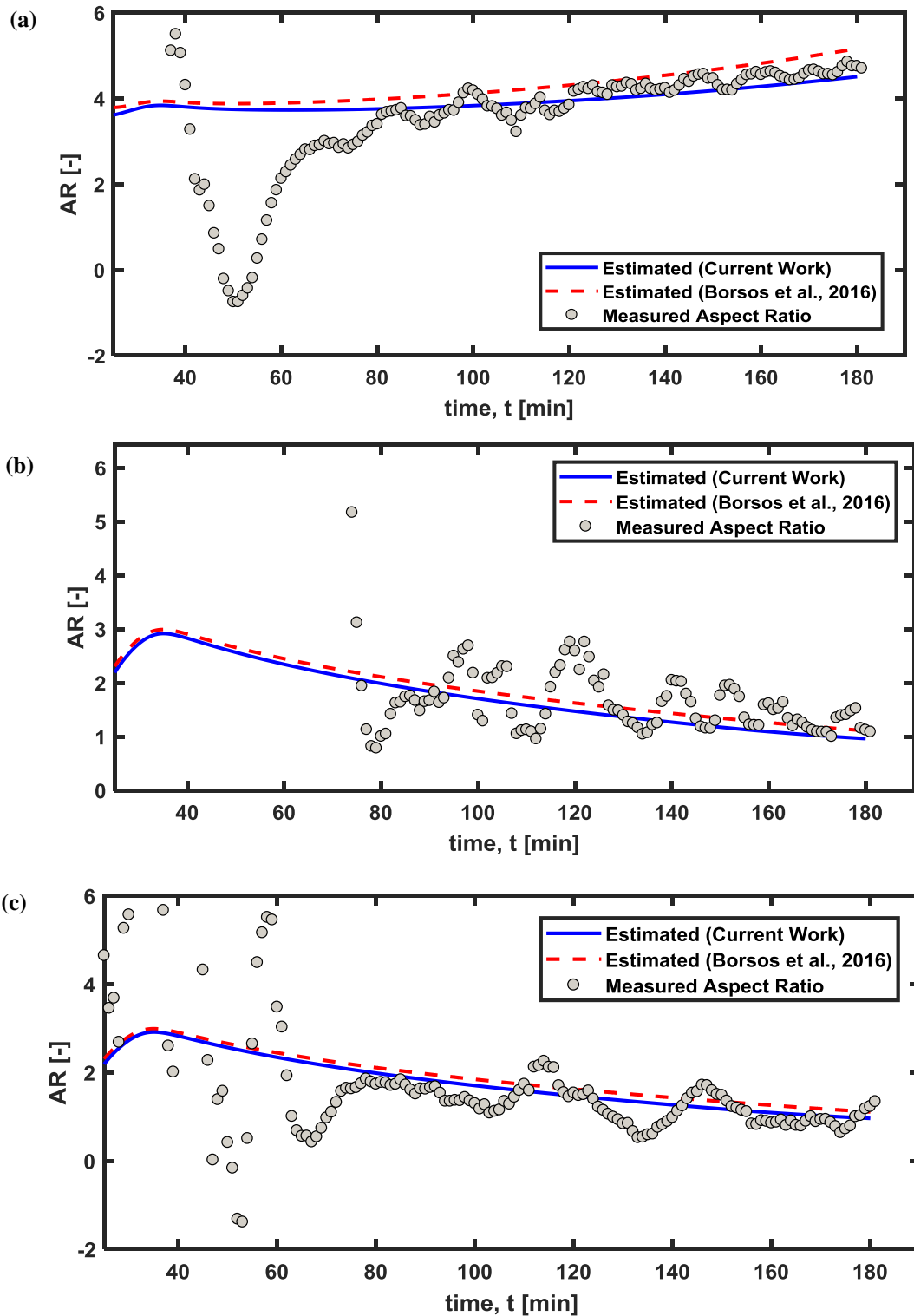


Figure 4.12. Comparison between the experimental and simulated mean aspect ratio dynamic evolution: (a) Experiment 1 (400 g H₂O ; 150 gr KDP; 12.5 ppm CGM1; 0.0 ppm CGM2), (b) experiment 2 (400 g H₂O ; 150 gr KDP; 12.5 ppm CGM1; 7.5 ppm CGM2) and (c) experiment 3 (400 g H₂O ; 150 gr KDP; 0.0 ppm CGM1; 5.0 ppm CGM2).

Although the Sobol analysis provides one of the most accurate methods for calculating the sensitivities of the parameters, the method doesn't consider the correlation between the parameters systematically during the ranking process as opposed the local estimability which addresses quite effectively the correlations issue, as the sequential orthogonalization approach is used precisely to exclude the parameters showing high correlations from being selected amongst the top ranked parameters.

Finally, to further demonstrate the benefits of the estimability analysis and appraise the prediction capability of the model built with the optimal subset of parameters, the model predictions are compared against the experimental data as well as the predictions of the model built without the estimability approach (Borsos et al., 2016), three different experiments that consider mean aspect ratio measurements are used as shown in **Figure 4.12**. It should be noted that obtaining accurate aspect ratio data is very challenging which explains the noisy data used here. For instance, the dynamic evolution of the mean AR shouldn't have exhibited a dynamic cyclic behaviour but instead should have increased monotonically, as correctly is captured by the model. Currently, real time image monitoring is the only online available technique that can be used for monitoring the size and shape evolution of the population of crystals and unfortunately it is inherently noisy.

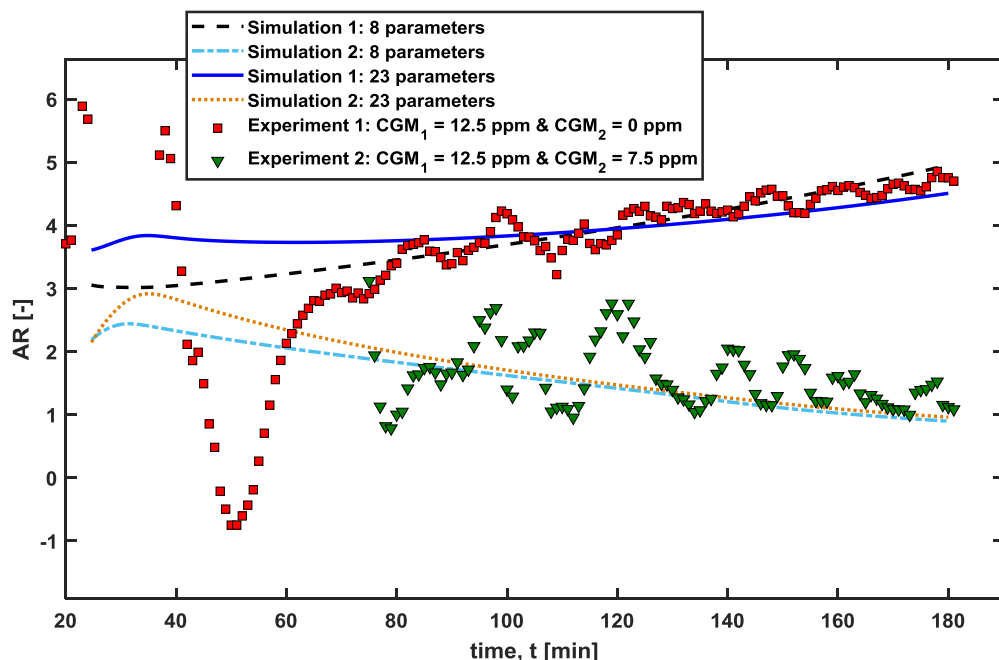


Figure 4.13. Comparison between the experimental and simulated mean aspect ratio dynamic evolution: Experiment 1 (400 g H₂O ; 150 gr KDP; 12.5 ppm CGM₁; 0.0 ppm CGM₂) and experiment 2 (400 g H₂O ; 150 gr KDP; 12.5 ppm CGM₁; 7.5 ppm CGM₂) by considering 8 and 23 parameters.

Although both models seem to provide a good fitting, **Figures 4.12a and 4.12b** show that the mathematical model with estimability approach demonstrates better prediction capability. This outcome is consistent with the incremental objective function analysis (**Figures 4.8**). The results show that the model build by identifying the 8 most estimable parameters outperforms the one build by identifying all parameters sequentially, as can be seen also in **Figure 4.13**. It becomes clear that the estimability approach makes the identification process more accurate and less laborious, as a reduced set of parameters is identified while the rest of the parameters are kept to their nominal values without compromising the prediction capability of the mathematical model.

4.6.4 Optimal Experimental Design (OED)

In the case that the estimability of the model doesn't illustrate satisfactory results, MBDoE can be used iteratively for designing new experiments that could yield the highest quality data for parameter estimation purposes, as illustrated in **Figure 4.1**. After the nucleation, growth and the pinning mechanism parameters were identified and further improved based on the parameter estimation and estimability analysis described in this study, they can now be used to perform MBDoE. Of course, the performance of the OED approach highly depends on the applied nominal values of the model parameters. Considerable deviation from the true parameter values will probably lead to a poor design strategy. In this case study, at least eight out of twenty-three parameter nominal values are expected to be close to the true values, while no guarantees can be given for the rest of them. This can be deduced from the estimability analysis performed in advance (see **subsection 4.6.2 and 4.6.3**).

The optimal experimental design, which is posed as a single objective optimization (SOO) problem, is solved using a hybrid optimization approach: Utilization of genetic algorithm (GA) in combination with sequential quadratic programming (SQP). A – optimal and D – optimal design criteria, were utilized as the objective functions while the temperature trajectory, $T(t)$, and the initial impurities concentrations, C_{CGM1} and C_{CGM2} were set as the control variables. By optimizing the FIM, and consequently the covariance – variance matrix, the magnitude and the correlation effects between the parameter inputs are also accounted. In more detail, correlation between the model-parameters results in reducing the determinant of the FIM which consequently leads to decreasing the confidence region volume along with the uncertainty. Also, the FIM quantifies the information content of the data: The higher its value (i.e. sensitivity magnitude) the more informative the data are.

As mentioned before (see **section 4.5**), the D – optimal design criterion maximizes the determinant of the FIM, which corresponds to minimizing the volume of the confidence ellipsoid and consequently minimizing the uncertainty. Similarly, the A – optimal design criterion, minimizes the trace of the inverse FIM which is equivalent to minimizing the sum of squares of the length of the axes of the hyperellipsoid, which eventually minimizes the average variance (i.e. uncertainty) of the model estimates.

Table 4.6. Parameter precision design using D-optimal and A-optimal criteria with respect to different initial impurities concentration

Virtual Experiment	C_{CGM1} (ppm)	C_{CGM2} (ppm)	D – Optimal	A – Optimal
1	0	0	1.396×10^{-66}	8.544×10^{-5}
2	5.0	0	2.016×10^{-60}	1.058×10^{-4}
3	0.0	5.0	2.741×10^{-46}	7.101×10^{-5}
4	5.0	5.0	2.680×10^{-28}	6.920×10^{-5}
5	2.5	2.5	1.117×10^{-41}	9.844×10^{-5}

In **Table 4.6** the objective function values for A – and D – optimal criteria are depicted for improving parametric precision. The maximum allowed concentration for each impurity was set arbitrarily to 5 ppm. In general, constraints should exist regarding the acceptable amount of impurities with respect to the investigated chemical system properties. For instance, the constraints can be more flexible if the additive is generally recognized as safe (GRAS) compound. As can be seen, for both design criteria the optimum value, can be reached when both impurities do present their highest values: $C_{CGM1} = C_{CGM2} = 5$ ppm. This was expected since it has been noticed that the best values of OED can be typically, but not invariably, found on the boundary of the experimental region (Rippin, 1988). This could be easily justified based on the stronger effects that a larger concentration of additives can have on the systems' dynamics, even when the impurities present competing impact. Moreover, the D – optimal

value is constantly increasing by increasing the concentration of the additives. On the contrary, A – optimal is decreased by increasing the C_{CGM2} , while the addition of $CGM1$ results to the opposite undesired effects (compare **virtual experiments 2, 3 and 5**). For both cases, temperature and composition optimization could improve the criteria by several orders of magnitude.

The model predictions using the precision design based on A – and D – optimal criteria are presented in **Figures 4.14 – 4.17**. It is evident that each criterion provides different optimal design inputs, which depends on the optimal design criterion and the impurities composition applied. However, all cases do present some distinctive similarity: An initial fast cooling rate is always introduced for every case. This trend is potentially generated since no crystallization occurs during the initial stage. Therefore, a high cooling rate would initiate nucleation and crystal growth quickly, which consequently would result in decreasing the time span where no information for the system could be obtained.

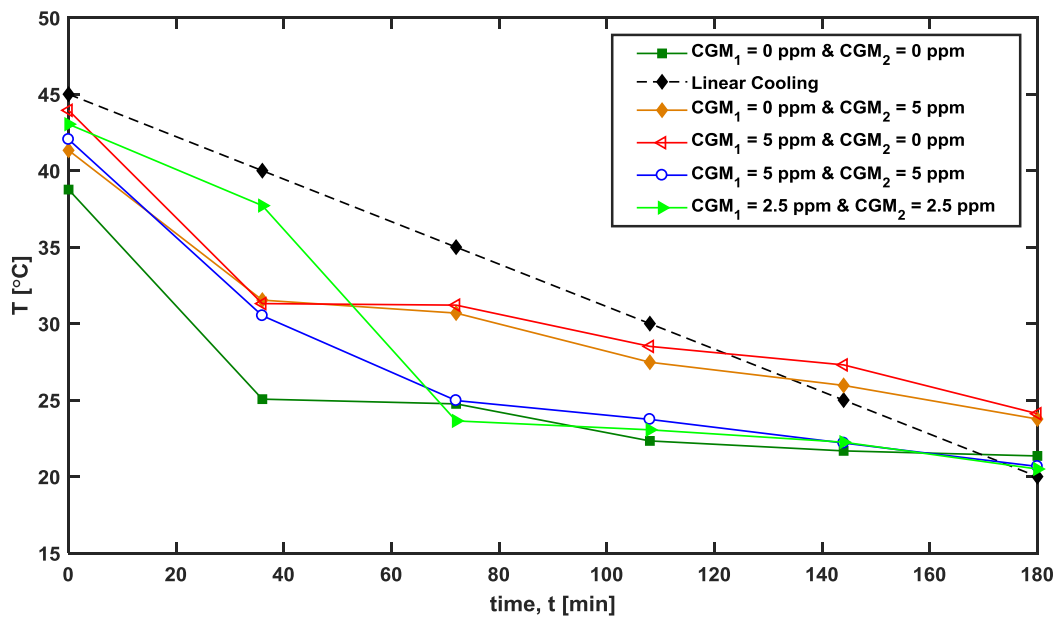


Figure 4.14. Optimal operating temperature trajectories for experimental design based on D-Optimal criterion.

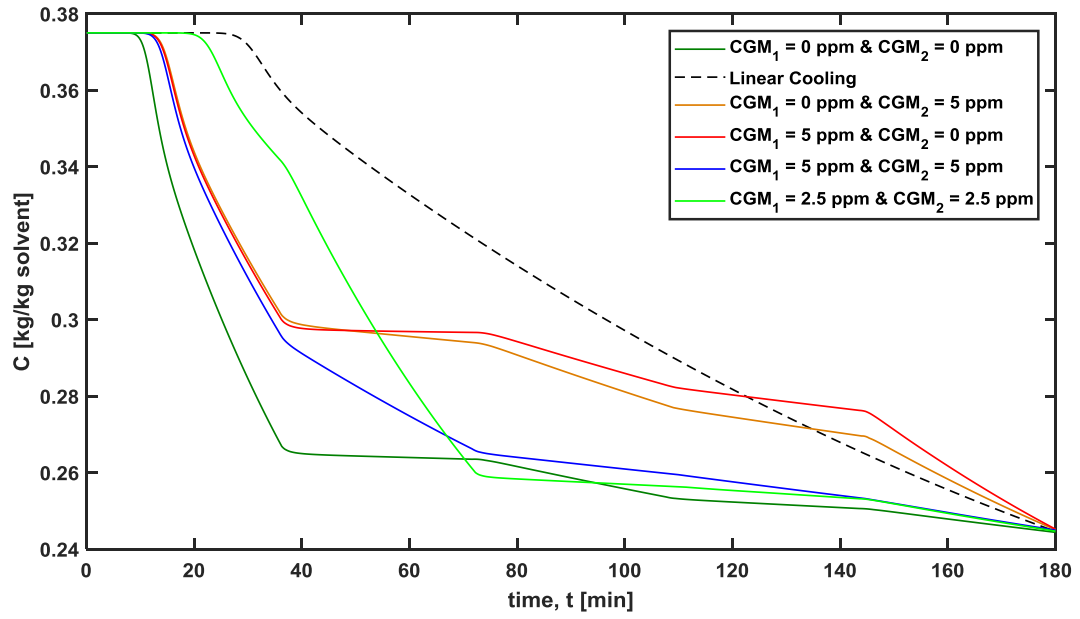


Figure 4.15. Optimal operating concentration trajectories for experimental design based on D-Optimal criterion.

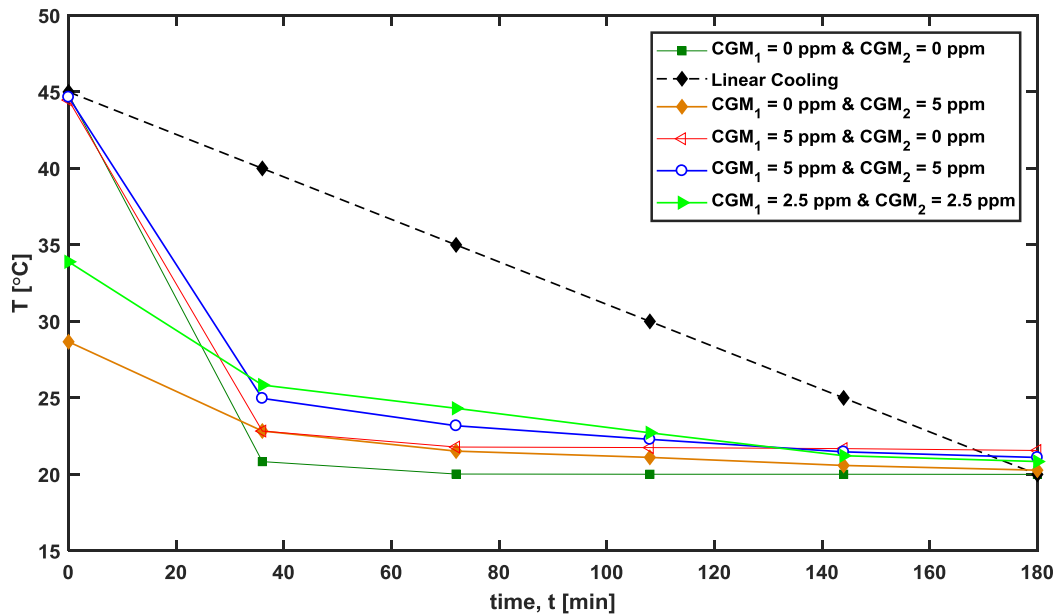


Figure 4.16. Optimal operating temperature trajectories for experimental design based on A-Optimal criterion.

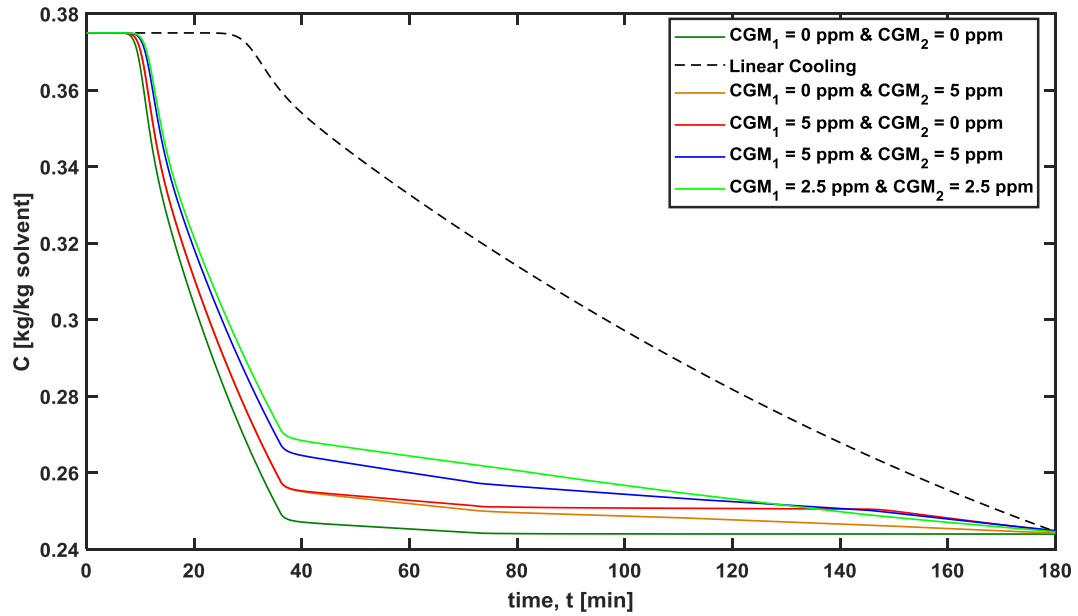


Figure 4.17. Optimal operating concentration trajectories for experimental design based on A-Optimal criterion.

After the initial temperature drop, each trajectory continues to cool down by utilizing different cooling rates until the end of the process time. This is a very interesting outcome since it is indicated that multiple new linear cooling experiments are taking place within one experiment with different conditions, such as different cooling rates and supersaturation. In more detail, the model separates the process into distinctive areas, where different conditions do apply to optimize the information content of the supplied data. This can be clearly seen by investigating the supersaturation, nucleation and crystal growth trajectories as depicted in **Figures 4.18 – 4.20**. For instance, in **Figure 4.18**, where the dynamic evolution of the relative supersaturation is illustrated, four distinctive zones can be identified: 1) $t_{span,1} \approx 0 - 18 \text{ mins}$, 2) $t_{span,2} \approx 18 - 38 \text{ mins}$, 3) $t_{span,3} \approx 38 - 77 \text{ mins}$ and 4) $t_{span,4} \approx 77 - 180 \text{ mins}$. In each of these areas different supersaturation set-point is applied which generates different effects opposing to the linear case where the supersaturation is constantly changing (i.e. exponentially declining). Based on D – optimal design criterion this can generate data with enhanced information content.

Finally, it should be mentioned that the DoE of non-linear models, such as the one presented here, cannot be generally valid and it must be iteratively improved/updated until an acceptable level of information content is reached. In this case, the analysis indicated that the virtual experiment 4, should be selected as the next OED. However, additional experimental data

would potentially change this design in future iteration, since the new parameter set would most probably define different DoE operating strategies.

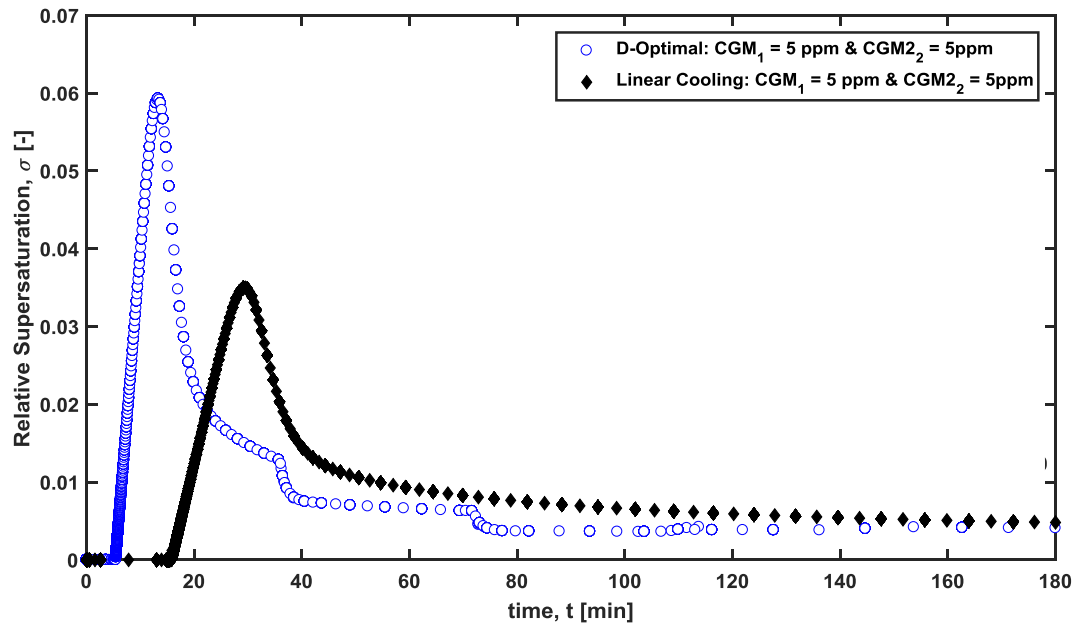


Figure 4.18. Relative supersaturation trajectories: Linear and D-Optimal cooling design with $C_{CGM1} = C_{CGM2} = 5$ ppm.

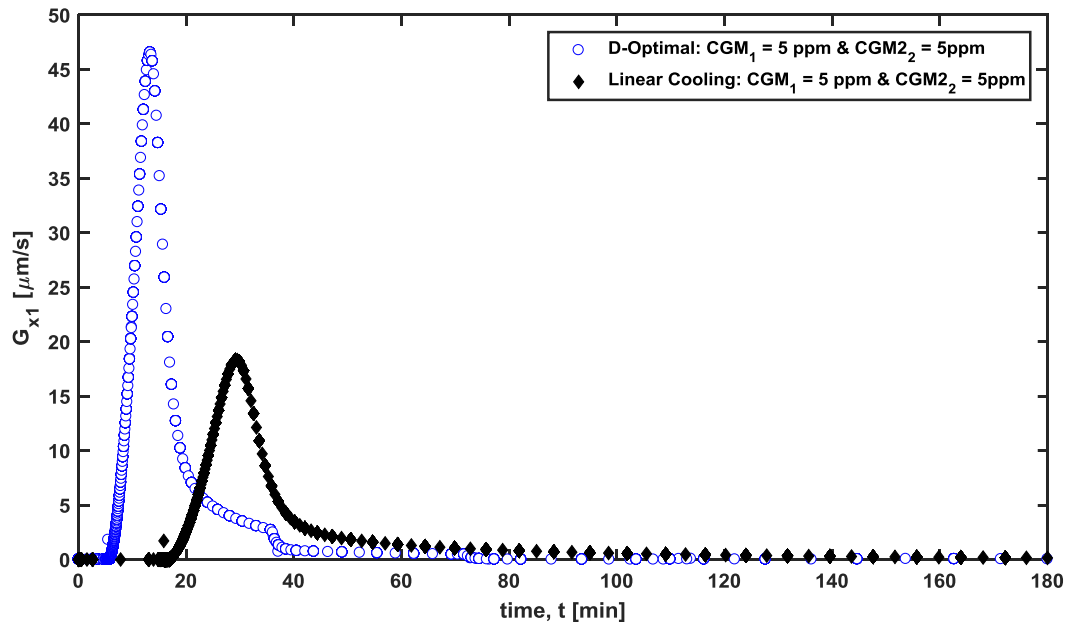


Figure 4.19. Crystal growth rates along the x_1 axis: Linear and D-Optimal cooling profiles with $C_{CGM1} = C_{CGM2} = 5$ ppm.

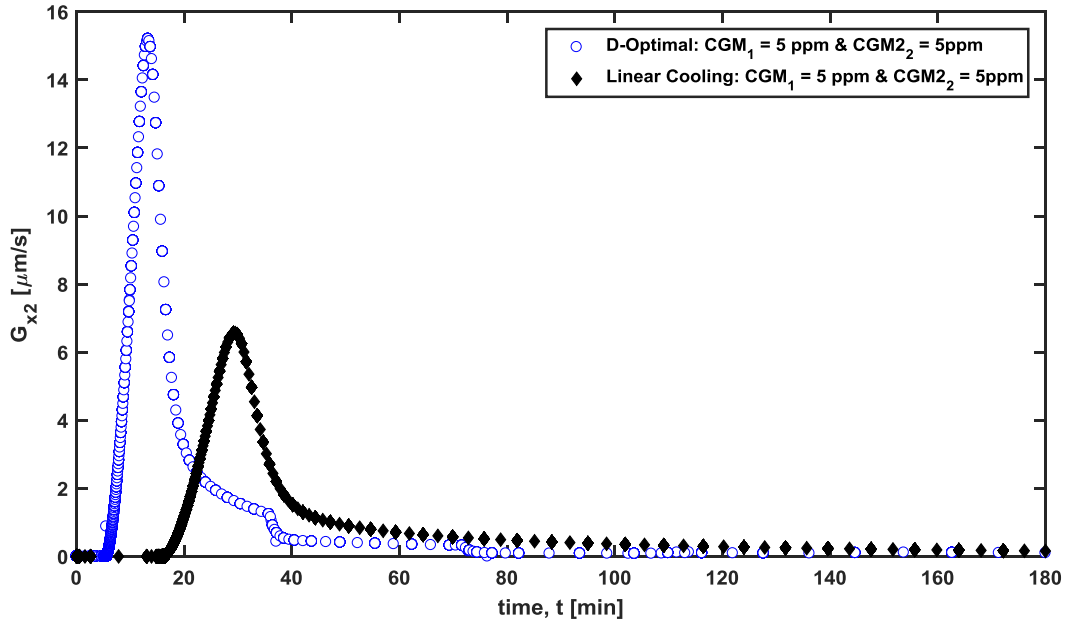


Figure 4.20. Crystal growth rates along the x_2 axis: Linear and D-Optimal cooling profiles with $C_{CGM1} = C_{CGM2} = 5 \text{ ppm}$.

4.7 Conclusions

Parameter estimability is essential to assess whether the model parameters can be reliably identified from existing data, which consequently provides a key step towards more predictable and robust mathematical models. Within this perspective, a novel estimability framework that combines a sequential orthogonalization of the local sensitivity matrix and Sobol, a variance-based global sensitivities technic, was proposed. The estimability analysis requires an initial or nominal vector of model parameters. When either of the two situations occurs: a nominal vector of parameters is not available or the initial parameter estimates are considered as highly uncertain, the framework suggests a simultaneously identification of the whole set of parameters using a hybrid global optimization approach. The estimability procedure can be then conducted using the nominal vector of parameters in conjunction with the available experimental data. The systematic combination of two different estimability methods guarantees a robust selection of the optimal subset of parameters: the set that can be identified more reliably with a guaranteed maximum model prediction capability. As such, both parameters significance and correlations should be considered to rank the model parameters. The framework suggests a systematic methodology, based on the parameter identification

objective function, to identify the cut-off value which indicates the boundary between the parameters that can be reliably identified (the optimal subset) and those who should be set to their nominal values. When the resulting model prediction capability is not satisfactory or/and very limited number of parameters can be identified reliably, the method suggests extracting additional experimental data that can be based on appropriate design of experiments.

As a validation step, the methodology was implemented to a complex multi-dimensional morphological population balance for batch crystallization processes, which combines the effects of different crystal growth modifiers/ impurities on the crystal size and shape distribution of the population of needle-like crystals. Initially, two situations were considered regarding the nominal vector of parameters: parameters obtained from literature and those identified using a simultaneous global optimization. The first evaluation of the quality of the nominal vector of parameters revealed that most of the nominal parameters are inherently uncertain, based on the confidence domains, which justifies the need for the estimability analysis. The 23 model parameters were ranked accordingly in terms of highest local sensitivity magnitude and least correlation, in the case of the sequential orthogonalization method, and total order sensitivity indices, in the case of Sobol. The correlation patterns confirmed the existence of strong correlation between some parameters, which helped explain the resulting parameter ranking. The least square incremental parameter identification procedure helped determine the cut-off value and consequently the optimal subset of parameters which turned out to be 8 parameters using both methods. Despite some slight parameter ranking differences, the two different estimability methods managed to capture consistently the most significant parameters. However, it is highly recommended to run both methods to maximize the benefits of the estimability approach and minimize the least square value at the cut off value, which guarantees maximum model prediction capability. The case study showed that although noisy aspect ratio data with low information content were used, a set of the most influential and the least correlated parameters could be identified, providing enhanced prediction capabilities of the dynamic model of the studied crystallization process. As a consequence, the framework can be extremely valuable in complex model systems when a large number of parameters needs be identified from low information content data, which is commonly encountered in real systems. The proposed framework can also embed an optimization of the experimental design to maximize the information content and reduce the cost inherent to redundant experimental information. In the case of systems utilizing different sensors, the information content of each sensor can be assessed and consequently the number of parameters that can be estimated from

each individual process analytical tool (PAT) or from their combination (e.g. sensors providing different outputs) can be determined, which helps select the most appropriate PAT depending on the targeted level of prediction capability and application (e.g. process control). Since the estimability analysis has been conducted and the reliability of the model has been assessed, the MIMA model can be utilized to perform model-based design analysis for the studied system. Moreover, through optimization and simulation studies the effect of the impurities/ CGMs on the transient behaviour of the CQAs can be further investigated, as will be presented in the following **Chapter**.

NOMENCLATURE

A	-	Inverse covariance matrix
AR	-	Mean aspect ratio of the population of crystals, [-]
$a_{i,i}$	-	Area of the crystal per unit, [m^2]
B_p	-	Primary nucleation, [#s/kg]
C	-	Concentration of KDP crystals in the solution, [g/g solvent]
$C_{CGM,j}$	-	Concentration of the j^{th} crystal growth modifier, [g/g solvent]
C_{sat}	-	Saturation concentration of KDP crystals in solution, [g/g solvent]
$COV(\mathbf{p})$	-	Covariance matrix of the estimated parameters
E_p	-	Kinetic energy of primary nucleation, [kJ/mol]
g	-	Aggregate vector of the variables, [-]
$\Delta G_{ads,0,i,j,k}$	-	Adsorption energy, [kJ/mol]
$\Delta G_{des,0,i,j,k}$	-	Desorption energy, [kJ/mol]
g_i	-	Exponent of growth kinetic equation of the i^{th} characteristic facet, [-]
G_i	-	Crystal growth rate of the i^{th} characteristic facet, [m/s]
$G_{min,i}$	-	Specific growth rate when distribution does not occur, [m/s]
$J(\mathbf{p})$	-	Minimum sum of squared errors, [-]
k_B	-	Boltzmann factor, [$m^2 \text{ kg s}^{-2} \text{ K}^{-1}$]
$K_{d,i,j}$	-	Distribution coefficient, [-]
$k_{ads,0,i,j,k}$	-	Adsorption rate constant of the j^{th} crystal growth modifier, [-]
$k_{des,0,i,j,k}$	-	Desorption rate constant of the j^{th} crystal growth modifier, [-]
k_e	-	Kinetic constant of Primary nucleation, [-]
$K_{e,j}$	-	Thermodynamic distribution coefficient, [-]
k_{gi}	-	Growth kinetic constant, [m/s]
$k_{m,i,j}$	-	Mass transfer coefficient with crystal growth, [m/s]

k_{m0}	-	Mass transfer coefficient without crystal growth, [m/s]
$k_{p,0}$	-	Coefficient of primary nucleation, [$m^{-3} s^{-1}$]
$L_{i,k}$	-	Average distance between k^{th} type of sites, [m]
$M_{CGM,j}$	-	Molecular weight of CGM, [g]
M_c	-	Molecular weight of KDP, [g]
n	-	Size and shape distribution, [$\#/m^2$]
$P_{imp,i}$	-	Impurity factor of the growth rate of i^{th} characteristic facet, [-]
N_p	-	Number of the model parameters, [#]
N_y	-	Number of measured outputs, [#]
N_m	-	Number of measurements of sampling times, [#]
N_e	-	Number of measurements, [#]
p	-	Vector of the input parameters (estimated parameters)
p_{1-ad}	-	Vector of confidence domain boundaries, [-]
R	-	Ideal gas constant, [$Pa m^3 mol^{-1} K^{-1}$]
R_{max}, R_{min}	-	minimum and maximum temperature ramp rates, [$^{\circ}C/min$]
r_i	-	Orthogonal projection of Z , [-]
s_i	-	First – order sensitivity index, [-]
s_t	-	Total – order sensitivity index, [-]
s_{ij}	-	Second – order sensitivity index, [-]
S_{ij}	-	Sensitivity coefficients, [-]
T	-	Temperature, [K]
t	-	Time, [s]
t_{ij}	-	j^{th} sampling time of the i^{th} output, [s]
V_i	-	Variance, [-]
x	-	Vector of the differential state variables, [-]
\hat{y}_{ij}	-	Vector of numerically calculated aspect ratio at k^{th} point in time, [-]
y_{ij}	-	Vector of measured aspect ratio at k^{th} point in time, [-]

z	-	Vector of the algebraic state variables, [-]
Z	-	Sensitivity Matrix, [-]

GREEK LETTERS

α_t	-	Significance level of the t-distribution, [-]
$\beta_{i,k}$	-	Constant of the effectiveness factor, [m/K]
γ_i	-	Edge free energy on the i^{th} crystal face per unit length, [J/m]
ε_{ij}	-	Stochastic measurement error, [-]
η_{ij}	-	Time spent by a particle in the presence of impurities, [s]
λ	-	Cut-off value, [-]
$\mu_{m,r}$	-	m, r^{th} order mixed moment of size variables
ρ_c	-	Density of the KDP crystals, 2.338 [kg/m^3]
$\sigma_{m,r}$	-	m, r order joint moment, [-]
σ	-	Relative supersaturation, [-]
σ_{ij}^2	-	Variance, [-]
$\tau_{i,j,k}$	-	Adsorption time constant, [s]
$\chi_{c,j}$	-	Mole fraction of the CGM in the crystal phase, [-]
Ω^κ	-	Sample Space, [-]

SUBSCRIPTS

0	-	Initial value
1	-	Length coordinate, [m]
2	-	Width coordinate, [m]
i	-	Characteristic crystal facet indices, [$-$]
p	-	Primary nucleation, [m]

<i>sat</i>	-	Saturation (solubility curve), [$kg/kg_{solvent}$]
<i>sv</i>	-	Solvent, [$kg/kg_{solvent}$]

5 OPTIMAL CONTROL STRATEGIES OF CSSD BASED ON THE COMBINATION OF SUPERSATURATION CONTROL AND ADDITION OF CGMS

Controlling the crystal size and shape and their subsequent distribution is a critical consideration in industrial crystallization. Towards this direction, the combination of supersaturation and additives control can be a promising approach. In this work, a systematic model-based design approach is utilized to identify the impact of this method on the crystal quality attributes (CQAs). A morphological population balance model (PBM) is utilized for the modelling of the cooling crystallization of pure potassium dihydrogen phosphate (KDP) in aqueous solution, as a case study, under the presence of two competitive crystal growth modifiers/ additives: aluminum sulfate and sodium hexametaphosphate. The effect of the optimal temperature control with and without the additives on the CQAs is presented via utilizing multi-objective optimization. The results indicate that the attainable size and shape attributes, in general, can be considerably enhanced due to advanced operation flexibility. Especially it is shown that the shape of the KDP crystals can be affected even by the presence of small quantity of additives and their morphology can be modified from needle-like to spherical, which is more favourable for processing. In addition, the multi-impurity PBM model is extended by the utilization of a high-resolution finite volume (HR-FV) scheme, instead of the standard method of moments (SMOM), in order the full reconstruction and dynamic modelling of the crystal size and shape distribution to be enabled. Both numerical schemes utilized for the resolution of the PBM, illustrated fast and accurate simulation of the transient

features of the crystal size and shape attributes. The implemented methodology, inextricably linked to the framework presented prior in **Chapter 4**, illustrated the capabilities of utilizing high-fidelity computational models for the investigation of crystallization processes in impure media for process and product design and optimization purposes.

Highlights:

- Modelling crystallization under the presence of multiple impurities.
- Standard method of moments (SMOM) and high-resolution finite volume method (HR-FVM) utilized for the solution of the multi-dimensional population balance model (PBM).
- Effect of multiple additives on crystal growth modelled using the pinning mechanism.
- An extended multicomponent Langmuir adsorption model considered.
- Multiple CQAs can be determined via multi-objective optimization considering both supersaturation and impurity effects with respect to crystal size and shape attributes.
- Deliberately addition of impurities in combination with optimal supersaturation control can considerably enhance the attained states.

5.1 Introduction

In crystallization, control over the crystals' quality attributes such as size and shape has a predominant impact on the function and physical properties of the final solid-form product. Especially for pharmaceutical compounds, the product effectiveness, such as bioavailability or tablet stability, as well as the efficiency of downstream operations, such as filtration, drying, milling and compaction, can be substantially affected ([Mullin, 2001](#); [Mersmann, 2001](#)). For most commercial purposes rod- (i.e. needles) and plate-like crystals, for instance, are usually undesirable since they could form impermeable layers during filtration resulting in poor process efficiency, whereas spherical or block shaped crystals can enhance the processability competence ([Davey and Garside, 2000](#); [Chianese and Kramer, 2012](#)).

In industrial crystallization habit modification is required and consequently several approaches have been implemented to control the size and the shape during the process. Optimal control of the supersaturation trajectory is the most common approach for shape modification, however, its operating window is rather narrow ([Acevedo and Nagy, 2014](#)). [Yang et al. \(2006\)](#) managed

to modify the crystal morphology of KDP crystals, grown in a batch non-isothermal crystallizer, by utilizing different temperature trajectories and seed recipes to investigate the effect of supersaturation on the relative growth rates of different facets. In a similar way, [Acevedo and Nagy \(2014\)](#) and [Acevedo et al. \(2015\)](#) studied both experimentally and computationally the effect of the temperature trajectories with respect to the attainable final shape of crystals for various systems. Shape control is also possible via mechanical processing. In-situ milling, wet-milling and even intense mixing have been successfully employed to modify the size and shape attributes of the product crystals by inducing crystal breakage and/or attrition ([Sato et al., 2008](#); [Acevedo et al., 2016](#); [Yang et al., 2016](#); [Yang et al., 2017](#)).

Size and shape modification can be also achieved by temperature cycling, which is an approach where the system is sequentially cycled through positive and negative supersaturation and is mainly utilized for dissolving the generated fines while the product crystals can grow larger ([Bakar et al., 2009](#); [Eisenschmidt et al., 2016](#); [Wu et al., 2016](#)). Prolonged temperature cycling however, can significantly affect the shape of the crystals since different faces of the same crystals experience different relative growth and dissolution rates ([Snyder et al., 2007](#); [Lovette et al, 2012](#); [Borsos et al., 2017](#)). Consequently, by utilizing consecutive temperature cycling crystal shapes can be attained that wouldn't be feasible to obtain solely by optimal supersaturation control ([Eisenschmidt et al., 2016](#)). However, as shown by [Lovette et al. \(2012\)](#) in order considerable shape change to be achieved twenty to eighty temperature cycles were required. [Jiang et al. \(2014\)](#), on the other hand, managed to reduce significantly the required number of cycles through deep temperature cycling. Moreover, considerable changes on the size, shape and number of the crystals are reported for each cycle (only 5 cycles were employed). However, the experiment was stopped before steady-state condition could be detected as it was indicated from the focused beam reflectance measurement (FBRM).

Habit modification can be also achieved by deliberately adding an impurity (e.g. additives) which could cause shape modification or by deactivating an impurity which is already present within the system ([Mullin, 2001](#)). The existence of even small amounts (i.e. ppm) of impurities can have a substantial effect on thermodynamic properties, such as solubility, but also on the kinetics of crystallization, such as nucleation, growth and dissolution rates ([Davey and Garside, 2000](#); [Mersmann, 2001](#)). To this end, extensive work has been done considering how impurities can affect the CQAs of the final product, especially with respect to the crystal morphology, which is highly related to the crystal growth mechanism ([Li et al., 1994](#); [Dowling et al., 2010](#); [Kestur et al., 2013](#); [Saleemi et al., 2013](#)). For example, [Xie et al. \(2010\)](#) utilized polymeric

additives and surfactants to modify the morphology of the salbutamol sulfate by antisolvent crystallization. In more detail, the researchers managed to modify the morphology of the obtained crystals in the presence of small quantities of polyvinylpyrrolidone (PVP 25) from needle-like to block-like crystals with a lower aspect ratio. On the other hand, [Klapwijk et al. \(2016\)](#) managed to change the shape of crystals from plate-like to block-like in a fully reproducible manner by adding triblock copolymer Pluronic P123, which is generally recognized as safe (GRAS) compound, in succinic acid - water system. Most importantly, this research was extended by combining the impurity addition with temperature cycling (static and convergent cycling), as presented by [Simone et al. \(2016\)](#). The latter work proved that the application of a hybrid methodology can substantially enhance the capability of controlling the shape by extending the attainable crystal morphology states.

Additives, which in most of the cases present some sort of chemical affinity with respect to the crystallizing substance, usually are consisted by two parts: One part that is structural similar with a certain crystal facet on which it is adsorbed and the second one which disrupts or promotes the bonding sequence inhibiting or promoting crystal growth respectively. Most probably the additives tend to adsorb on chemical structures, where hydrogen bonding acceptor or donor sites may be positioned ([Berkovitch-Yellin et al., 1982](#); [Trasi and Taylor, 2012](#)). Several mathematical models were developed for crystallization processes to quantitatively describe the rate of crystal growth under the presence of a single impurity ([Davey, 1976](#); [Sizemore and Doherty, 2009](#); [Nagy et al, 2013](#)). One of the proposed models is based on the Langmuir adsorption isotherms with a modified pinning mechanism ([Kubota and Mullin, 1995](#); [Kubota, 2001b](#); [Kubota et al., 2004](#)). The pinning mechanism was coupled with population balance equations (PBEs) and mass balance by [Févote and Févote, \(2010\)](#) to model the effect of additives on crystal growth and crystal size distribution (CSD). This model was extended from single dimensional to a multi-dimensional PBM by [Majumder and Nagy \(2013\)](#). The established modelling framework was utilized for the dynamic modelling and control of crystal size and shape attributes of KDP crystals, as well as the dynamic variation of crystal purity. Recently the latter modelling framework was further developed by [Borsos et al. \(2016\)](#) for modelling the crystal purity, size and shape evolution under the presence of multiple impurities, by considering an extended multicomponent Langmuir adsorption model ([Gu et al., 1991](#); [Lim et al., 1995](#); [Rabe et al., 2011](#)).

Therefore, it becomes evident that the deliberate addition of impurities (preferably GRAS compounds) in combination with supersaturation control could potentially enhance the ATR by

achieving crystal size and shape attributes that wouldn't be feasible to attain solely by optimal supersaturation control or by temperature cycling. The existence of the comprehensive and robust modelling frameworks, mentioned before, can enable the accurate and fast construction of ATRs while at the same time they can reduce the amount of the experimental work required. To the best of our knowledge it is the first time that a systematic model-based study is implemented to map the ATRs of a pharmaceutical process under the presence of multiple impurities.

In this study, the systematic model-based design and optimization methodology, presented in **Chapter 3**, is implemented for the investigation of the impact of multiple impurities, in conjunction with supersaturation control, on the ATR. Multi-objective optimization is systematically applied for the identification of the attainable regions with respect to size and shape attributes. The cooling crystallization of pure potassium dihydrogen phosphate (KDP) in deionized water, under the presence of aluminum sulfate (CGM1) and sodium hexametaphosphate (CGM2), is utilized as the model system (same system investigated in **Chapter 4**). The mathematical model is based on the novel morphological multi-dimensional population balance model (MIAM model) presented initially by [Borsos et al. \(2016\)](#), which accounts nucleation and crystal growth of different crystal facets. The modelling framework is also extended, for the first time, with the utilization of high-resolution finite volume (HR-FV) schemes in order the full reconstruction of the size and shape distribution (CSSD) to be enabled.

The remainder of this chapter is organized as follows: In **section 5.2** the mathematical model of the bivariate PBM and the mechanisms/kinetics are presented. In **section 5.3** the multi-objective optimization procedure utilized for identifying the ATR is presented and detailed description of the performance objectives is given, while in **section 5.4** the results obtained from the analysis are discussed. The **Chapter** ends with some concluding remarks in the conclusions section.

5.2 Process Model

The multi-impurity adsorption model (MIAM) consists a state-of-the-art mathematical framework for modelling crystallization processes under the presence of multiple impurities, which are adsorbed on different crystal facets to modify mainly the shape and size of the crystals and their subsequent distribution. This multi-dimensional PBM, denoted by **eq. 4.1**, can be used

to predict the dynamic evolution of size and shape attributes by simultaneously considering the supersaturation and impurities effects. The overall model is illustrated in **Table 4.1** and it consists of a set of ODEs (moment equations coupled with mass balances) combined with algebraic equations that describe the system's kinetics and thermodynamics. A detailed description of the mathematical MIMA model and its solution by utilizing the standard method of moments (SMOM) is presented in **Chapter 4**. It should be mentioned that due to inherent stiffness of the PBMs, stiff solvers are usually employed for the solution of complex PBMs. In this case, the ode23s solver is utilized for the SMOM method, which is based on a modified Rosenbrock formula of order two ([Shampine and Reichelt, 1997](#)).

Although the SMOM method provides significant information regarding average values of the crystal population and contributes to the characterization of the CQAs, this technique cannot be used for the full reconstruction of the crystal size and shape distribution (CSSD). The high-resolution finite volume method (HR-FVM), on the other hand, which was initially developed for the solution of hyperbolic PDEs ([LeVeque, 2002](#)), has been applied successfully for the computation of the CSD and CSSD of PBMs illustrating at the same time increased accuracy especially near to sharp variations ([Gunawan et al., 2004](#); [Qamar and Warnecke, 2007](#); [Mesbah et al., 2009](#); [Majumder et al., 2010](#)).

FV techniques, which belong to the discretization methods for the solution of partial differential equations (PDEs), are based on the integral form of the conservation law ([Majumder and Nagy 2013b](#)). So, when this technique is applied, the spatial variable domain is discretised in a finite number of NG grid cells (i.e. discretization points) for each direction (2-D domain in our case) and piecewise functions are used to approximate the derivatives (i.e. fluxes at the cell face) with respect to the spatial variable ([Mesbah et al., 2009](#)). In this way, the average value of the conserved variable can be calculated for each grid cell, providing accurate solutions even for discontinuous solutions.

The discretization of the PDE (**eq. 5.1**) can be achieved by utilizing either fully discrete or semi-discrete methods. By employing fully discrete methods the PDE is discretized in both space and time, resulting in a set of algebraic equations. However, when methods with high order of accuracy (i.e. greater than two) or methods considering two or more dimensions (multi-dimensional problems) need to be developed, it is usually beneficial to discretize the PDE only with respect to space, leaving the problem continuous in time ([LeVeque, 2002](#)). This approach is known as semi-discrete method and it reduces the PDE to a set of ODEs, which finally is

solved by further discretizing the set of ODEs with respect to time using a standard numerical ODE solver. By decoupling the spatial and temporal variables, high order interpolation, with respect to the spatial variables, can be initially applied to the flux at a cell boundary, and then solved by using high order ODE solvers resulting in high order temporal accuracy. Consequently, in this case a semi-discrete FV method is utilized since MIMA is a multi-dimensional PBM. The utilized method employs a finite volume discretization scheme of the two-dimensional probability density function for the MIMA considering a uniform 2D grid, as illustrated in **Figure 5.1**.

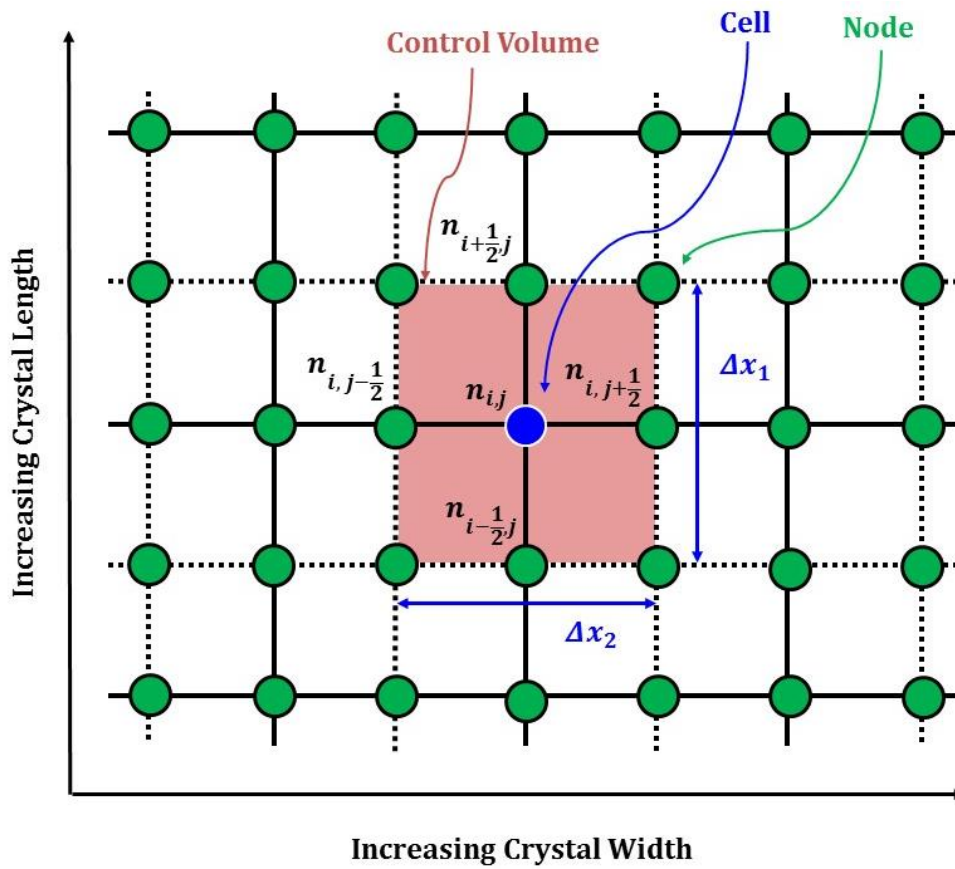


Figure 5.1. Representation of the finite volume discretization of a two-dimensional CSD considering a uniform 2D grid.

To solve a 2D PBM, we need first to introduce an approximation of the average population density, $n_{i,j}$, as shown below:

$$n_{i,j}(x_1, x_2, t) \approx \frac{1}{h^2} \int_{(i-1)h}^{ih} \int_{(j-1)h}^{jh} n(x_1, x_2, t) dx_1 dx_2 \quad (5.1)$$

where $n_{i,j}(x_1, x_2, t)$ is the number density function, h denotes the size interval, and i and j are integers such that $i, j \geq 1$. Hence, this expression can calculate the properties of crystals located in each discrete size domain.

Based on **eq. 5.1**, the PBE given by **eq. 4.1** is integrated over the (i, j) cell to obtain the following finite set of ODEs, after certain approximations have been made based on the semi-discrete method (see [LeVeque, 2002](#) for more information):

$$\begin{aligned}
\frac{d}{dt} \bar{n}_{i,j}(x_1, x_2, t) & \\
& \approx -\frac{1}{h^2} \int_{x_{1,i-\frac{1}{2}}}^{x_{1,i+\frac{1}{2}}} G_1 n(x_1, x_{2,j+\frac{1}{2}}, t) - G_1 n(x_1, x_{2,j-\frac{1}{2}}, t) dx_1 \\
& - \frac{1}{h^2} \int_{x_{2,j-\frac{1}{2}}}^{x_{2,j+\frac{1}{2}}} G_2 n(x_{1,i+\frac{1}{2}}, x_2, t) - G_2 n(x_{1,i-\frac{1}{2}}, x_2, t) dx_2 \approx \\
& \approx -\frac{1}{h} [G_1 Fl_1(n_{i,j}, i, j) - G_1 Fl_1(n_{i,j}, i-1, j) \\
& + G_2 Fl_2(n_{i,j}, i, j) - G_2 Fl_2(n_{i,j}, i, j-1)]
\end{aligned} \tag{5.2}$$

where $\bar{n}_{i,j}(x_1, x_2, t)$ is the cell average of $n_{i,j}(x_1, x_2, t)$ over the (i, j) cell, while the Fl_1 and Fl_2 terms are pointwise fluxes which approximate the appropriate integrals, as shown below:

$$Fl_1(n_{i,j}, i, j) \approx \frac{1}{h} \int_{x_{1,i-\frac{1}{2}}}^{x_{1,i+\frac{1}{2}}} n(x_1, x_{2,j+\frac{1}{2}}, t) dx_1 \tag{5.3}$$

$$Fl_2(n_{i,j}, i, j) \approx \frac{1}{h} \int_{x_{2,j-\frac{1}{2}}}^{x_{2,j+\frac{1}{2}}} n(x_{1,i+\frac{1}{2}}, x_2, t) dx_2 \tag{5.4}$$

The evaluation of these fluxes ($G_1 Fl_1(n_{i,j}, i, j)$ and $G_2 Fl_2(n_{i,j}, i, j)$) is done through the utilization of the available cell average values. Conceptually, the numerical accuracy and computational efficiency of the FV approach depends on how these cell-face fluxes are

calculated since different ways of estimating the numerical flux do exist. By applying backward differences, for example, a first-order accurate upwind scheme can be achieved, as has been shown in literature (LeVeque, 2002). However, a higher order accuracy, which is generally desirable, can be achieved by utilizing Taylor series expansion or piecewise polynomial interpolation (Qamar et al., 2006). In this case the employed flux approximations are calculated through the following expressions:

$$\begin{aligned}
 Fl_1\left(n_{i,j}, i + \frac{1}{2}, j\right) & \\
 &= Fl_1(n_{i,j}, i, j) + \frac{1}{2} \varphi(r_{x_1, i+\frac{1}{2}})(Fl_1(n_{i,j}, i+1, j) \\
 &\quad - Fl_1(n_{i,j}, i, j))
 \end{aligned} \tag{5.5}$$

$$\begin{aligned}
 Fl_2\left(n_{i,j}, i, j + \frac{1}{2}\right) & \\
 &= Fl_2(n_{i,j}, i, j) + \frac{1}{2} \varphi(r_{x_2, j+\frac{1}{2}})(Fl_2(n_{i,j}, i, j+1) \\
 &\quad - Fl_2(n_{i,j}, i, j))
 \end{aligned} \tag{5.6}$$

where $\varphi(r_{x_1, i+\frac{1}{2}})$ and $\varphi(r_{x_2, j+\frac{1}{2}})$ are the flux limiter functions for the x_1 and x_2 coordinates respectively. The flux limiters are highly depended on the smoothness of the solution and its estimation is done prior to the calculation of the flux limiter functions. The smoothness of the solution can be quantified by calculating the ratio of the two consecutive gradients, given by the following equations:

$$r_{x_1, i+\frac{1}{2}} = \frac{Fl_1(n_{i,j}, i, j) - Fl_1(n_{i,j}, i-1, j) + \varepsilon}{Fl_1(n_{i,j}, i+1, j) - Fl_1(n_{i,j}, i, j) + \varepsilon} \tag{5.7}$$

$$r_{x_2, j+\frac{1}{2}} = \frac{Fl_2(n_{i,j}, i, j) - Fl_2(n_{i,j}, i, j-1) + \varepsilon}{Fl_2(n_{i,j}, i, j+1) - Fl_2(n_{i,j}, i, j) + \varepsilon} \tag{5.8}$$

where $\varepsilon = 10^{-10}$ is a small number employed to avoid division by zero (Majumder and Nagy 2013b).

After the quantification of the smoothness, a robust upwind Van Leer flux limiter (Van Leer, 1985), is utilized, which provides a $\mathcal{O}(h^2)$ accuracy, where the solution is smooth and can be computed for x_1 and x_2 coordinates as shown below:

$$\varphi \left(r_{x_1, i+\frac{1}{2}} \right) = \frac{r_{x_1, i+\frac{1}{2}} + \left| r_{x_1, i+\frac{1}{2}} \right|}{1 + \left| r_{x_1, i+\frac{1}{2}} \right|} \quad (5.9)$$

$$\varphi \left(r_{x_2, j+\frac{1}{2}} \right) = \frac{r_{x_2, j+\frac{1}{2}} + \left| r_{x_2, j+\frac{1}{2}} \right|}{1 + \left| r_{x_2, j+\frac{1}{2}} \right|} \quad (5.10)$$

In general, flux limiter functions are usually employed along with the interpolation schemes to guarantee the monotonicity of the solution by suppressing spurious oscillations (wiggles) and/or negative solution values that would otherwise occur during the implementation of high-order spatial discretization schemes due to sharp changes or discontinuities of the solution domain (Majumder and Nagy, 2013b). Essentially, the flux limiters change the flux approximation from higher to lower order and vice versa depending on whether the solution is smooth (higher order) or non-smooth (lower order). Several flux limiters have been proposed in literature, such as Van Leer, Koren, superbee, minmod and MC limiters, which of course lead to a different FV scheme (LeVeque, 2002). In this case the Van Leer flux limiter function was employed since it has demonstrated high accuracy and efficiency for the solution of PBMs (Qamar et al., 2006; Mesbah et al., 2009; Majumder and Nagy 2013b). More information regarding the HR-FV method could be found in literature (LeVeque, 2002; Gunawan et al., 2004; Qamar et al., 2006; Qamar and Warnecke, 2007; Mesbah et al., 2009; Majumder et al., 2010).

It should be highlighted that the right-hand side of **eq. 5.2** represents only the source terms, which in this case correspond to the growth terms of the two different internal coordinates. Consequently, the methodology described above is utilized for modelling the crystal growth terms. The nucleation term on the other hand, is introduced at the inlet boundary (i.e. source term at the first corner cell) as the boundary condition (see **eq. 4.3**).

To sum up, in this work, the MIAM model was extended by applying a high-resolution finite volume technique (HR-FV) which arises from combining a semi-discrete FV method with the robust upwind Van Leer flux limiter, which provides a $\mathcal{O}(h^2)$ accuracy, where the solution is smooth. In more detail, the PBEs (**eq. 5.2**) that characterize the MIAM system were discretized

into a finite number of ODEs, NG_i , in each direction (i.e. $NG_{x_2} = 150$, $NG_{x_1} = 300$ grid cells) resulting in equivalent number of size bins increased by one. The resulting set of ODEs continuous in time was solved by utilizing an explicit fourth-order Runge-Kutta ODE solver.

5.3 Optimization Problem Formulation

The reader is referred in **Chapter 3 – Section 3.3** where a detailed description and discussion of the optimization formulation problem has been presented for the dynamic multi-objective optimization of the investigated system. In terms of coherence, the optimization problem is briefly presented below as well.

Since cooling batch crystallization processes are considered, the aim is to determine the optimal cooling rate/profile, which will generate the appropriate level of supersaturation over the time to produce particles with the desirable CQAs defined by the objective functions and subjected to several constraints. In this case an additional control variable is considered, which is the use of additives to control the CSSD. **The addition of the CGMs takes place at the beginning of the process and hence, they are implemented in the system as initial conditions of the corresponding mass balances.**

Therefore, the optimization problem can be formulated as shown below:

$$\max/\min_{T(1), T(2), \dots, T(P)} J_{obj}(t) \quad (\text{obj.5.1})$$

$$\text{subject to: } T_{min} \leq T_i \leq T_{max} \quad (\text{c.5.1})$$

$$R_{min} \leq \frac{dT}{dt} \leq R_{max} \quad (\text{c.5.2})$$

$$t \leq t_{final} \quad (\text{c.5.3})$$

$$\text{yield1} = c(t_{final}) - 0.6 c_0 \leq 0 \quad (\text{c.5.4})$$

, where T_{min} , T_{max} , R_{min} and R_{max} are the minimum and maximum temperature and temperature ramp rates respectively. The objective functions considered are the following ones:

$$J_{obj} = [\bar{x}_1, AR, S_{d1}] \text{ for the 2D PBM.}$$

5.4 Results and Discussion

After the parametric analysis has been conducted and the reliability of the model has been assessed, as presented in **Chapter 4**, model-based design and optimization analysis can be performed to investigate the impact of multiple impurities on the ATR. The analysis is divided into two parts. First simulations are performed by applying different operating conditions to investigate how the impurities affect the transient performance of the CQAs. Then the impact of the multiple impurities in conjunction with supersaturation control (i.e. hybrid approach) is explored via multi-objective optimization since multiple attributes are considered.

It should be highlighted that although both SMOM and HR-FV numerical schemes are utilized for the simulation of the dynamic evolution of the moments and the CSSD of the batch cooling crystallization process, only the SMOM is employed for optimization purposes due to its superior computational efficiency. In more detail, multi-objective optimization, which is systematically applied for the identification of the attainable regions (ATRs) with respect to size and shape attributes, can be very computationally expensive especially for complex optimization problems, such as the one investigated in this work. Of course, if the full reconstruction of the CSSD is required, the HR-FV can be used after the optimization process for the simulation of the optimum conditions.

Since the cooling crystallization of pure potassium dihydrogen phosphate (KDP) in deionized water, under the presence of aluminum sulfate (CGM1) and sodium hexametaphosphate (CGM2), is investigated in this work, the kinetics identified in **Chapter 4** and presented in **Table 4.3** are utilized. In general, the existence of even small amounts (i.e. ppm) of additives can have a considerable impact on the kinetics and thermodynamic properties of the system (Mullin, 2001). For the investigated system the presence of additives has demonstrated a substantial effect especially with respect to the crystal morphology (Borsos et al., 2016), which is highly related to the crystal growth mechanism. However, this doesn't guarantee that other properties are not affected and consequently, in the future, additional experiments should be conducted to explore the potential effect of these additives with respect to thermodynamic properties (e.g. solubility) and kinetics, which were not considered here or in previous studies reported in literature. For example, conducting seeded experiments would provide additional information of the effect of additives on the secondary nucleation kinetics.

5.4.1 Simulation – based analysis of MIAM model

The main operating variable in an unseeded cooling crystallization process is the applied cooling trajectory combined with the initial saturated concentration amount. The generated temperature gradient creates the driving force (i.e. supersaturation) that leads the system in a supersaturated state, where spontaneous nucleation occurs. Of course, depending on the metastable zone width (MSZW) and the thermodynamic behaviour of the system, the induction time in order for the nucleation to occur varies. After the nuclei are formed, the operating concentration profile is reduced, since molecules from the liquid phase start forming crystal nucleus, and it is positioned between the solubility and supersolubility curve (i.e. within the MSZW). Within this region, apart from nucleation crystal growth also occurs and supersaturation is utilized in order new nucleus to be formed and more structural units to be incorporated on the crystal lattice. The concentration keeps diminishing until steady state is reached. Therefore, it becomes apparent that the applied temperature trajectory should have a major impact of the way that the phenomena would evolve since it determines, in conjunction with the system's kinetics, the pathway of the process (see **Chapter 3** for more details).

Table 5.1. Process variables and physical properties.

T_0 [°C]	T_{end} [°C]	<i>time</i> [mins]	ρ_c [kg/m ³]	m_{H_2O} [kg]	m_{KDP} [kg]
45	20	180	2338	0.40	0.15

However, in this section, the scope of the investigation lays in identifying solely the effect of the CGMs on the CSSD and not in determining an optimum operating strategy. Therefore, a linear cooling profile is used for all the cases presented in this subsection, while the initial concentration of the CGMs is varied in each run, providing in this way the effect of the CGMs on the CSSD. The rest of the process conditions, whose values are specified in **Table 5.1**, were kept constant.

Based on previous experimental data (Borsos et al., 2016), it is expected that the utilized additives can enhance the attainable product habit since they can adsorb on different crystal facets hindering the relative growth rates in different directions. It should be mentioned that the faster the growth in a certain direction is, the smaller the crystal facet area becomes. For example, in this case, where needle-like crystals are generated (see **Figure 4.2**), the growth rate

along the x_1 direction is faster comparing to x_2 . Hence, reducing the crystals' aspect ratio (AR) can be achieved by adding an impurity, which is going to be adsorbed on the crystal facet $\{101\}$ vertical to x_1 direction, as shown in **Figure 4.2**. This reduction would be the outcome of decreasing the relative growth rates between the two directions. It should be mentioned that for this system, sodium hexametaphosphate (CGM2) is preferably adsorbed onto the $\{101\}$ KDP crystal facet, while aluminum sulfate (CGM1) has a propensity for adsorbing onto the $\{100\}$ crystal facet (see **Chapter 4 – Section 4.3** for more details).

The results of applying the same linear cooling profile, as shown in **Figure 5.2**, for all simulations with respect to different initial impurities concentrations are presented below.

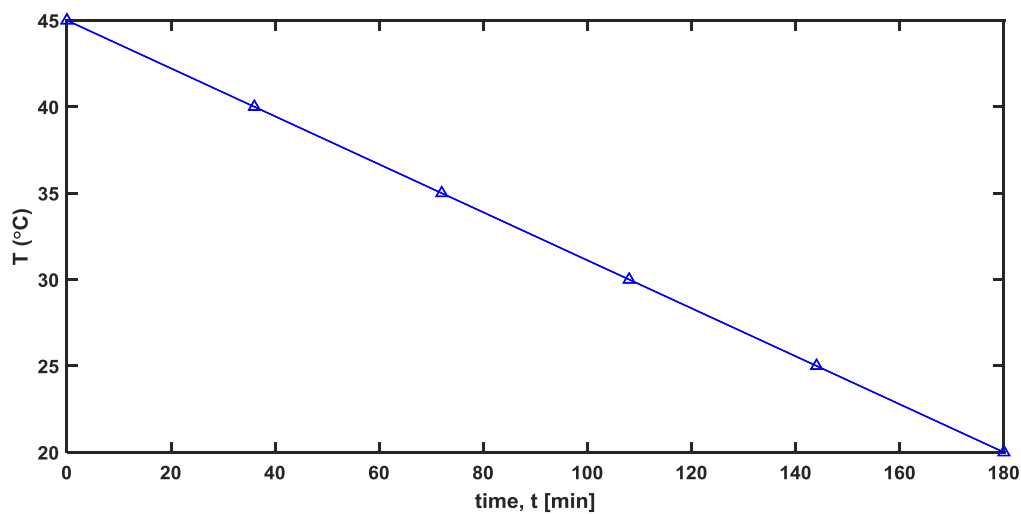


Figure 5.2. Linear cooling profile is utilized for all the simulations.

In **Figure 5.3a**, the dynamic evolution of the solute concentration trajectories is illustrated under the presence of different amount of *CGMs*. It is demonstrated that minor variations on the evolution of the solute concentration do occur under the presence of impurities within the bulk solution. These variations occur owing to the effect that impurities have on the system's kinetics, as depicted in **Figures 5.4** and **5.5**. Moreover, the presence of *CGMs* can cause substantial variations of the dynamics of the supersaturation, which become more evident when relatively high concentrations of additives are employed (**Figure 5.4a**). Consequently, the growth kinetics, G_{x_1} and G_{x_2} , are also affected significantly, as presented in **Figures 5.4b** and **5.4c**, since each *CGMi* can be adsorbed on a certain crystal facet hindering the relative growth rates in different directions. By inhibiting crystal growth (**Figure 5.4b** and **5.4c**), the excess supersaturation can be utilized for the formation of new nuclei (i.e. primary nucleation occurs) which develop into new crystals. Therefore, the nucleation dynamics, which can be directly

related to the total number of generated crystals can be accelerated by increasing the quantity of *CGMs* within the bulk. It should be mentioned that although the $\mu_{0,0}$ illustrate high sensitivity to the variation of the concentration of *CGMs*, the crystal volume in a unit volume of suspension ($\mu_{1,2}$) presents minor effects. Similarly, to what was stated before, these variations can be attributed based on the variations of the dynamics of the supersaturation and the corresponding kinetics. It can be also noticed that $\mu_{1,2}$ exhibits analogous effects compared to the solute concentration, which was highly expected since the component mass balance is calculated through the utilization of the crystal volume's gradient (see **Table 4.1**).

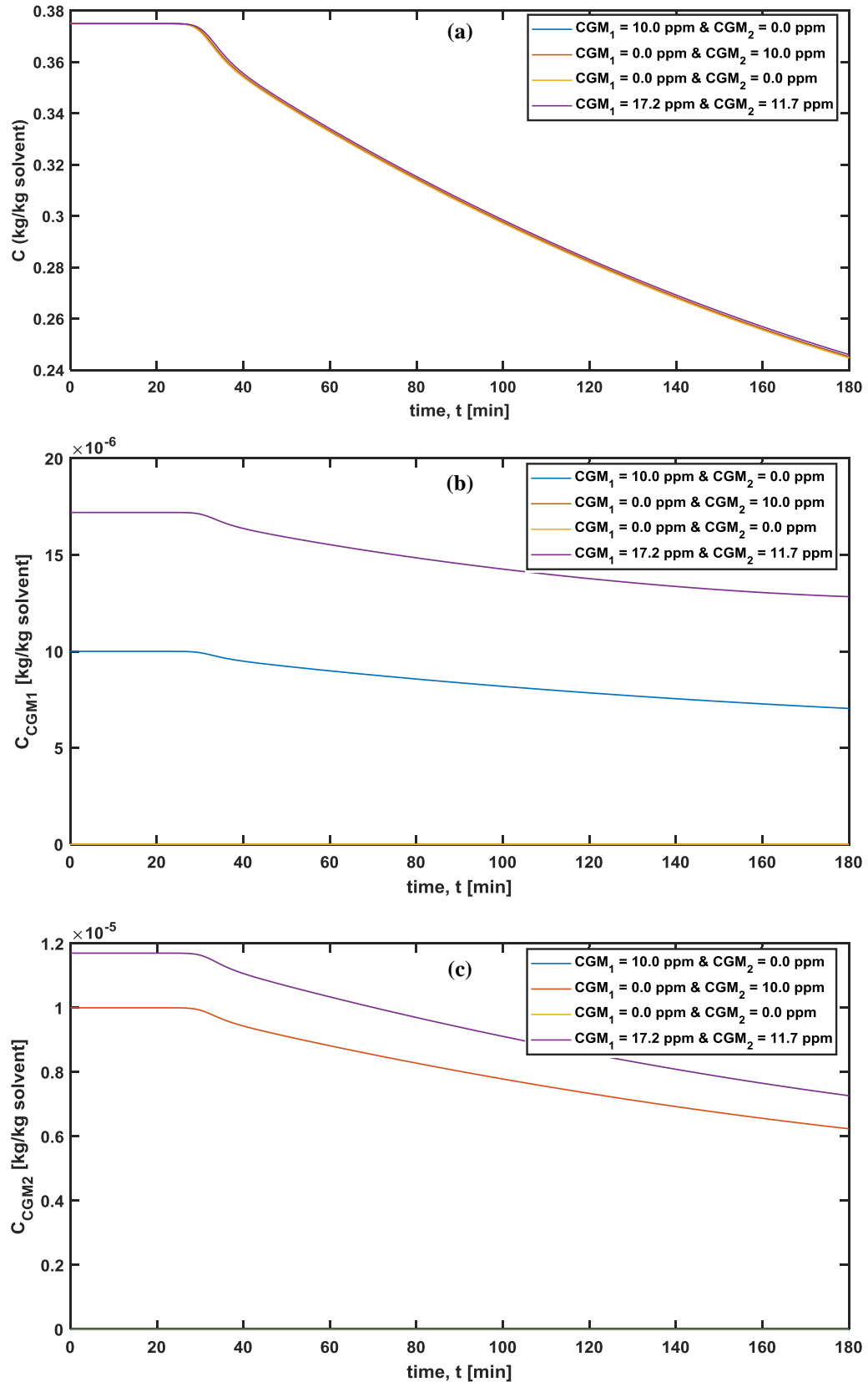


Figure 5.3. Dynamic evolution of the: (a) solute concentration trajectory in presence of different amounts of CGMs, (b) $C_{\text{CGM}1}$ impurity concentration and (c) $C_{\text{CGM}2}$ impurity concentration.

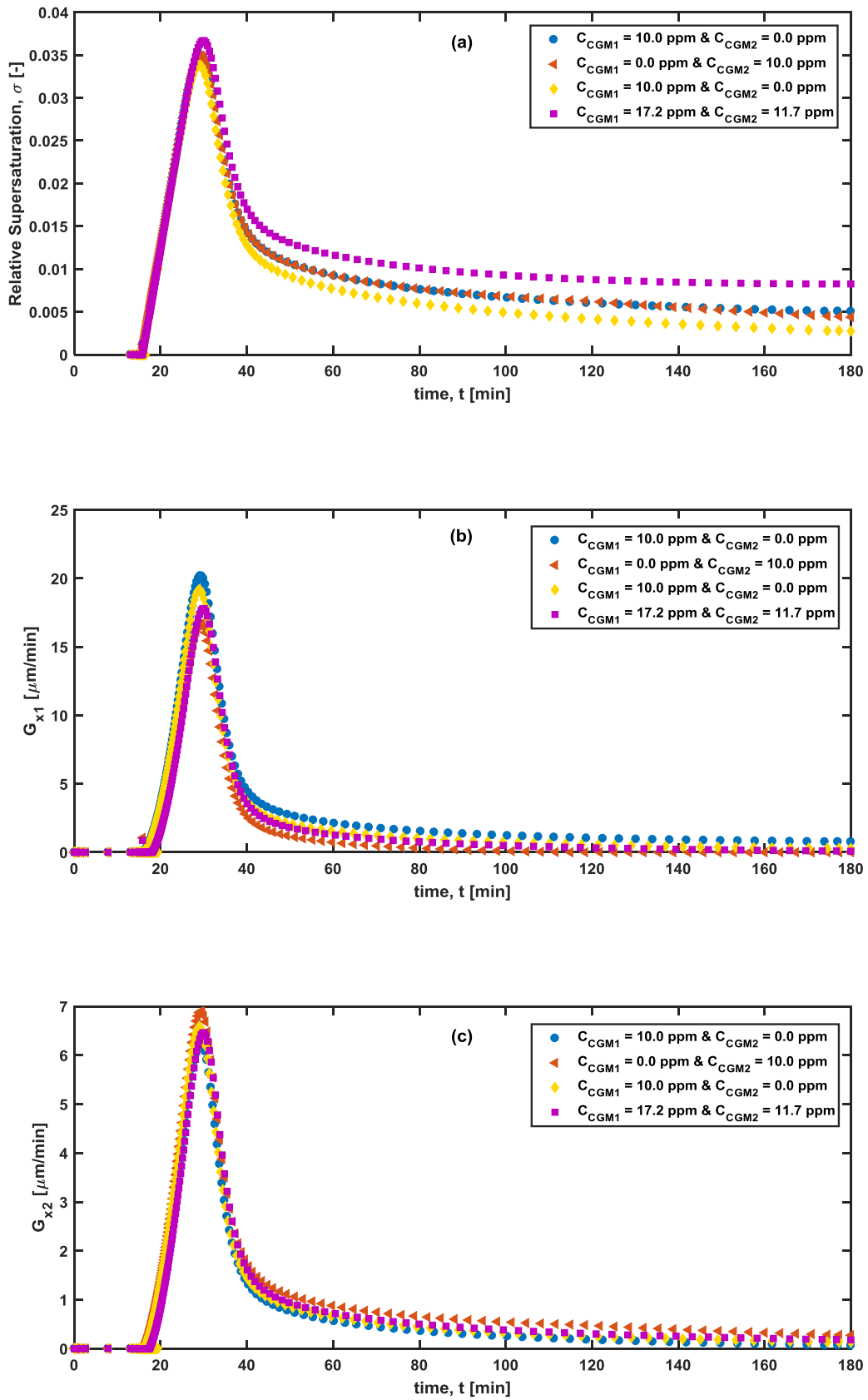


Figure 5.4. Effect of the CGMs concentration on (a) relative supersaturation (σ), (b) crystal growth along the characteristic length x_1 (G_{x_1}) and (c) crystal growth along the characteristic width x_2 (G_{x_2}).

The dynamic evolution of the $CGMs$ concentration, CGM_1 and CGM_2 , is also depicted in **Figure 5.3b** and **Figure 5.3c** respectively. Based on these figures, it becomes apparent that the adsorption of the impurities is initiated at about the same time with the induction of the crystallization process. Meaning that slightly after the first nuclei have been formed (i.e. nucleation occurs), the additives are incorporated onto the crystal lattice simultaneously with the growth structural units. Surprisingly, although the initial amount of $CGMs$ is limited to ppm levels, the corresponding $CGMs$ impurity level is rather low. For instance, with respect to the first simulation, where $CGM_1 = 10.0 \text{ ppm}$ and $CGM_2 = 0.0 \text{ ppm}$ (results corresponding to the blue line), the yield of the CGM_1 is less than 30%. Similar trend was obtained for the second simulation, where $CGM_1 = 0.0 \text{ ppm}$ and $CGM_2 = 10.0 \text{ ppm}$ (results corresponding to the red line). However, in the latter case a higher yield is demonstrated (i.e. 40%) for the same initial concentration, which could be potentially associated with the additive's (CGM_2) stronger effect on the system comparing to CGM_1 as will be shown later based on the dynamic responses of the mean sizes, mean aspect ratio (AR) and CSSD. Also, by evaluating the fourth simulation, where $CGM_1 = 17.2 \text{ ppm}$ and $CGM_2 = 11.7 \text{ ppm}$ (results corresponding to the purple line), it can be observed that by increasing the initial concentration of the $CGMs$, an upsurge of the impurity adsorption yield can be achieved.

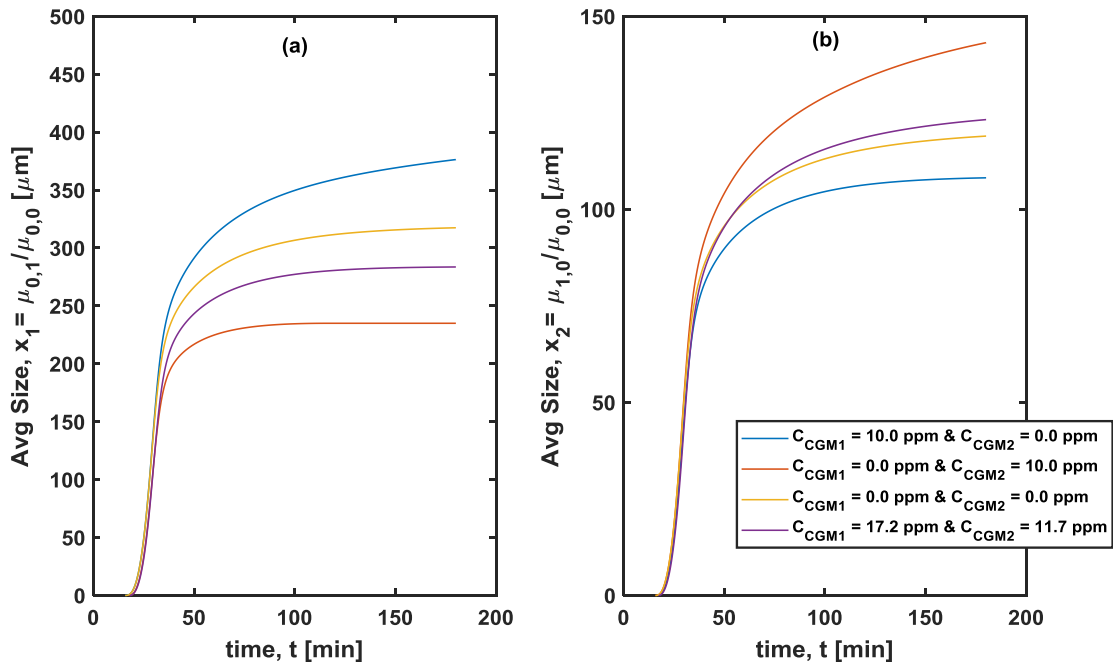


Figure 5.5. Effect of the $CGMs$ concentration on the (a) evolution of the mean crystal size of population along the characteristic length x_1 ($\mu_{0,1}/\mu_{0,0}$) and (b) evolution of the mean crystal size of population along the characteristic length x_2 ($\mu_{1,0}/\mu_{0,0}$).

The impact of the *CGMs* on the products size and shape attributes becomes rather obvious by investigating the dynamic evolution of the mean sizes for each direction and the AR, which are illustrated in **Figures 5.5** and **5.6** respectively. Moreover, the variation of the dynamic trajectories of the mean sizes (**Figures 5.5a** and **5.5b**) with respect to different initial *CGMs*' concentrations is presented illustrating the competitive effects of the two additives: The addition of CGM_1 increases the AR of the crystals ($\uparrow \bar{x}_1$ and $\downarrow \bar{x}_2$), while the addition of CGM_2 reduces the AR ($\downarrow \bar{x}_1$ and $\uparrow \bar{x}_2$), which is the desired effect (**Figure 5.6**). Through the simulated mean aspect ratio trajectories, it is also indicated that the CGM_2 has a more predominant role during the crystal growth comparing to CGM_1 , since a greater impact on the system's dynamics is observed when the same quantity of additives is utilized. The same outcome can be drawn by evaluating the results when both additives are present within the bulk (4th simulation: $CGM_1 = 17.2 \text{ ppm}$ and $CGM_2 = 11.7 \text{ ppm}$). As can be clearly seen, although a smaller amount of the CGM_2 is employed, compared to CGM_1 , CGM_2 presents a dominant effect resulting in the reduction of the AR.

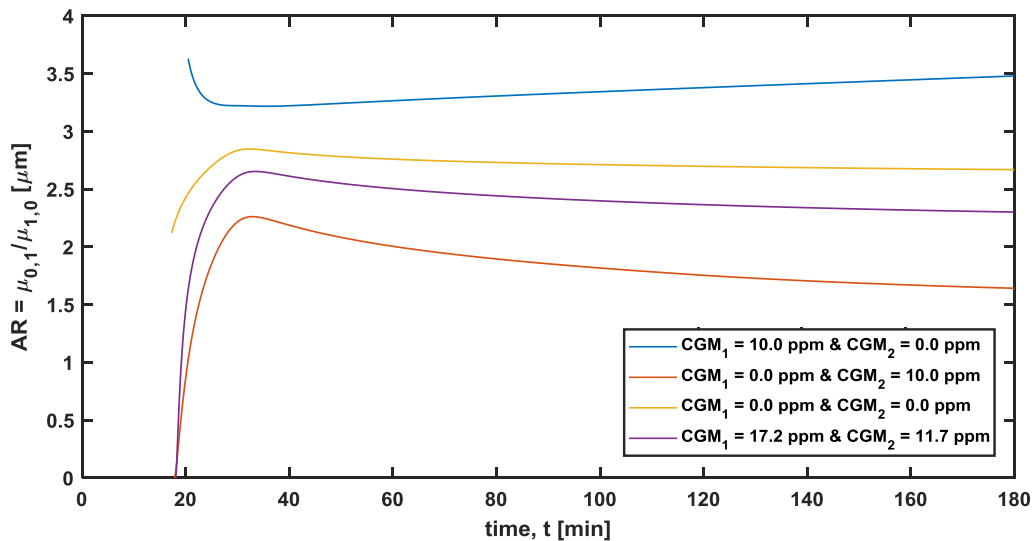


Figure 5.6. Effect of the *CGMs* concentration on the evolution of the mean aspect ratio.

The full reconstruction of the CSSD of the four simulated combinations of the *CGMs* is presented in **Fig. 5.7**, which is in complete agreement with the simulation results generated by using the SMOM solver. However, additional information can be obtained by investigating the evolution of the CSSD, which are related to its shape. As demonstrated, with or without the presence of additives a bimodal CSSD is generated which would most potentially compromise

the efficiency of the downstream processability (e.g. filtration, drying etc.) following the crystallization step.

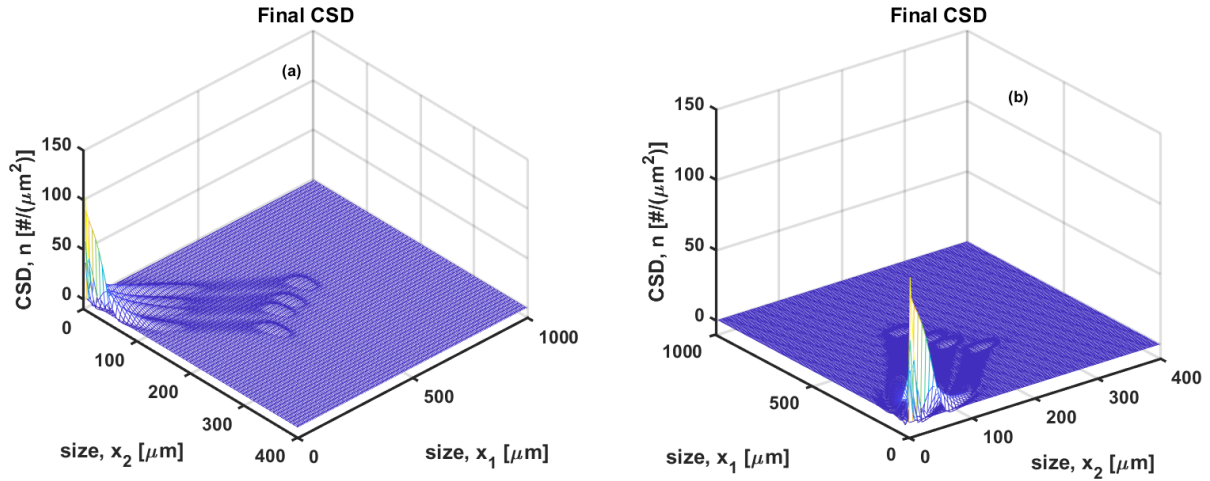


Figure 5.7. Effect of the *CGMs* concentration on the evolution crystal size and shape distribution (CSSD) for: (a) view 1 and (b) view 2.

5.4.2 Multi – objective Optimization Problem of MIAM

In this subsection, the conceptual design of the batch cooling crystallization of KDP in aqueous solution in impure medium is investigated. Moreover, the scope lays in identifying the attainable region with respect to multiple CQAs, corresponding to certain size and shape attributes, under the combined effect of additives **and** supersaturation control (hybrid approach). The temperature limits were set to 45°C and 20°C corresponding to the maximum and minimum allowed temperature respectively, while the yield was constrained by the expression **C.5.4**. The analysis is conducted by utilizing the thermodynamic properties and operating conditions as presented in **Table 5.1**.

To this end, a multi-objective optimization framework is considered, to evaluate the benefits of utilizing supersaturation control combined with *CGMs* addition, with the scope of:

- (1) maximizing the mean length size ($\max(\frac{\mu_{0,1}}{\mu_{0,0}})$),
- (2) minimizing the aspect ratio in order a target shape to be achieved ($AR \rightarrow 1$) and
- (3) minimizing the standard deviation in x_1 direction ($S_{d,1}$).

For the estimation of the optimal Pareto front the real-coded elitist nondominated sorting genetic algorithm (NSGA) was utilized (see **Chapter 3** for more information). Due to the higher complexity of the multi-dimensional MIAM PBM the analysis becomes more computational expensive and the trade-off between computational burden and accuracy needs to be considered. The population size was selected to be equal to 200, the number of generations was set to 200, and the mutation probability was predetermined as an adaptive feasible function. Different values with respect to the number of generations and population size, were applied in order the accuracy of the algorithm not to be compromised.

By implementing the NSGA, the fitness functions were evaluated for different cooling trajectories, which were generated randomly, and helped construct the Pareto front, as shown in **Figure 5.8**. From the analysis, a 3D Pareto front was obtained which illustrates the trade-off interactions between the three different objective functions under the presence of different concentrations of CGM_5 . For visualization purposes the XY, XZ and YZ planes of the 3D Pareto front are also presented in **Figure 5.9**.

It has been proven both experimentally and computationally (see **Chapter 3**) that the KDP in aqueous solution system is growth dominated and therefore its CQAs can be significantly controlled by implementing supersaturation control. This can be also confirmed based on the Pareto front generated here, that can span a broad range of solutions for all investigated objectives without the presence of any additives. For instance, it is illustrated that: $\bar{x}_1 \approx 150 - 465 \mu m$, $AR \approx 1.4 - 2.1$ and $S_{d,1} \approx 40 - 340$. In order the target shape ($AR \rightarrow 1$) to be achieved the \bar{x}_1 needs to be compromised (**Figure 5.8**). Thus, when fast cooling rates do apply growth occurs relatively faster along x_1 direction comparing to x_2 resulting in crystals with needle-like morphology. On the contrary, by manipulating the cooling trajectory and subsequently the supersaturation, the relative growth can be optimized to be: $(G_{x_1} \rightarrow G_{x_2}) \leftrightarrow (\bar{x}_1 \rightarrow \bar{x}_2) \leftrightarrow (AR \rightarrow 1)$. A comprehensive conceptual analysis for the KDP in aqueous solution without the presence of any additives has been conducted in **Chapter 3** and additional information could be found there.

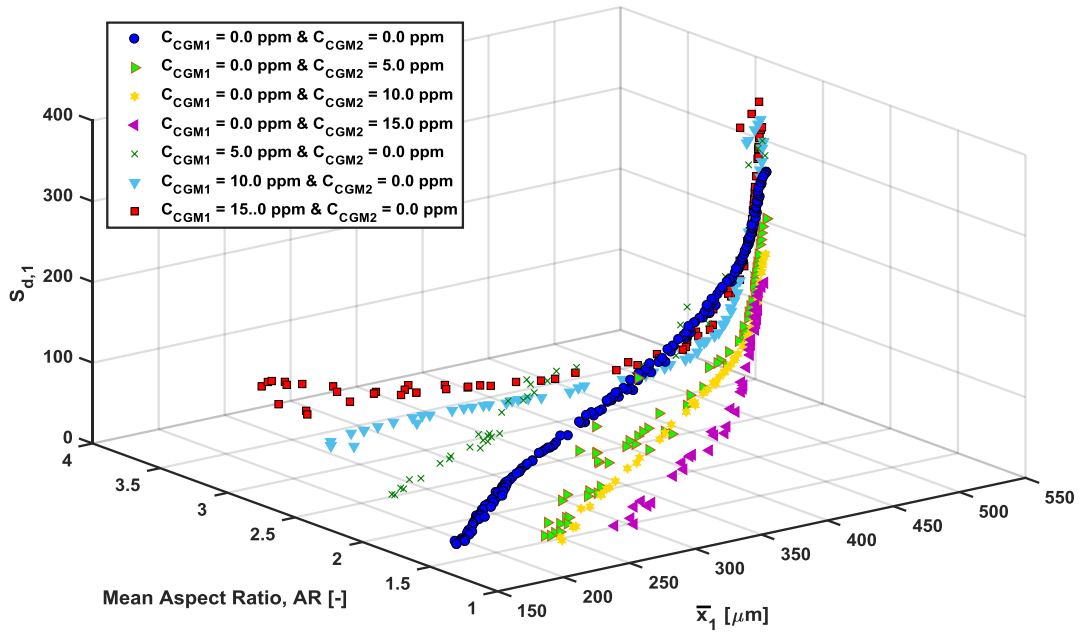


Figure 5.8. 3D Pareto optimal-front obtained for the multi-objective optimization problem of maximizing the number mean size ($\bar{x}_1 = \frac{\mu_{0,1}}{\mu_{0,0}}$), minimizing the mean aspect ratio (AR) and minimizing the standard deviation of the distribution in x_1 direction ($S_{d,1}$) with respect to different additives' (C_{CGMi}) concentration.

Although by implementing supersaturation control, the CQAs could be modified, the utilization of the combined effects of supersaturation control and additives inclusion, demonstrates enhanced capabilities resulting in increasing the Pareto ranges substantially (**Figures 5.8 and 5.9**). Moreover, the implementation of a hybrid approach provides advanced process flexibility and consequently crystal size and shape attributes, that wouldn't be feasible to be attained solely by one of these methods, can be achieved. The benefits from the inclusion of additives can be realized from the comparison of the blue scatter points, which correspond to the Pareto optimal-front obtained without the presence of any additives with the rest of the curves. For example, by utilizing a solution where 5 ppm of CGM_2 is included, a population of spherical crystals ($AR \approx 1$) with narrow distribution (i.e. low standard deviation) and mean size equal to about $200 \mu\text{m}$ can be obtained. These properties could be considered ideal for industrial applications. Of course, particles with a variety of CQAs can be generated by selecting the corresponding operating conditions. It should be reminded that every Pareto's point, correspond to a certain cooling trajectory. Of course, since systems with and without the presence of additives present different dynamics the optimum cooling operating policies vary. Nevertheless, the obtained Pareto optimal-front present some consistent trends as it is clearly illustrated in **Figure 5.9**. As

expected, the addition of CGM_1 will lead to the formation of crystals with high AR and consequently large mean values along the length characteristic size. Opposing to that, the inclusion of CGM_2 would generate low AR crystals that would have lower mean size and slightly lower CSD.

Undeniably, larger quantities of CGM_5 would generate a stronger effect on the system's dynamics, which was highly anticipated due to the nonlinear dynamic nature of the phenomena. Meaning that by increasing the CGM_1 by a factor of two wouldn't result in increasing the effect of CGM_5 on the system by the same factor. For instance, when comparing the system under the presence of $CGM_2 = 10.0 \text{ ppm}$ with the one with $CGM_2 = 15.0 \text{ ppm}$, it can be observed that the gain with respect to reducing some of the properties, such as the AR is not so substantial. On the contrary, the gain is significantly higher by comparing the systems under the presence of $CGM_2 = 5.0 \text{ and } 10.0 \text{ ppm}$. Similar observations are drawn with respect to the optimizations considering the addition of the CGM_1 instead.

The combination of supersaturation control and addition of $CGMs$ can increase the process flexibility and operability, which is demonstrated based on the extension of the feasible CQAs for the selected case study. In principal this can be extended and applied for numerous systems, especially for the ones, where crystal growth has a dominant effect opposing to nucleation. Finally, it should be highlighted that apart from the system's nature, the feasible attained states depend on the process and supply chain constraints, as well as the CQAs and their desired ranges. Therefore, this methodology could be used for quantitatively evaluating the influence of additives with or without combining it with supersaturation control.

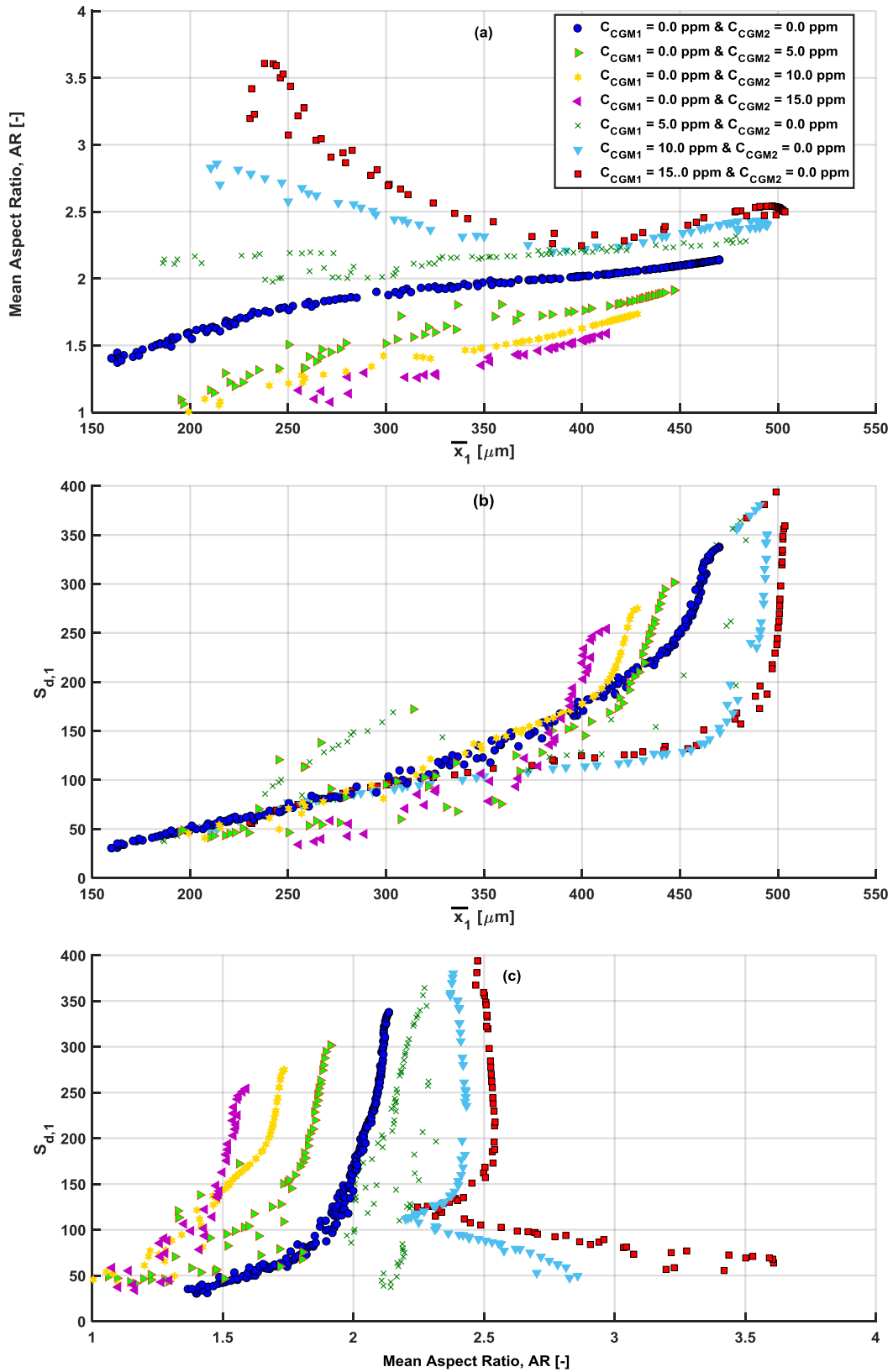


Figure 5.9. Pareto optimal-front obtained for the multi-objective optimization problem of maximizing the number mean size ($\bar{x}_1 = \frac{\mu_{0,1}}{\mu_{0,0}}$), minimizing the mean aspect ratio (AR) and minimizing the standard deviation of the distribution in x_1 direction ($S_{d,1}$) with respect to different additives' (C_{CGMi}) concentration.: (a) XY cartesian plane, (b) XZ cartesian plane and (c) YZ cartesian plane.

5.5 Conclusions

A systematic model-based design methodology for crystallization processes under the presence of multiple impurities (or additives) is proposed, in order to investigate the impurity effect on the size and shape attributes of the product crystals. The methodology's applicability was evaluated through the batch cooling crystallization of pure potassium dihydrogen phosphate (KDP) in aqueous solution under the presence of two crystal growth modifiers: aluminum sulfate and sodium hexametaphosphate. The crystallization process was modelled by using a morphological population balance model (PBM), which was solved by utilizing the standard method of moments (SMOM) and a high-resolution finite volume technique (HR-FV), which arises from combining a semi-discrete FV method with the robust upwind Van Leer flux limiter. Both numerical schemes utilized for the resolution of the PBM, illustrated fast and accurate simulation and optimization of the transient features of the crystal size and shape attributes.

Initially, a simulation-based analysis was conducted for the investigation of the influence of the two additives on the attainable crystal size and shape attributes. Therefore, the concentration of the additives was set as the control variable while the rest of the process conditions maintained the same values throughout the analysis. The results indicated that the two additives, which have a competing nature, can be utilized for controlling the crystal size and shape attributes since they present a direct impact on the system's kinetics. The impact of the combination of supersaturation control and *CGMs* addition on the control of the CSSD was investigated by using multi-objective optimization. The results indicated that by using this approach the CQAs can be substantially modified due to advanced operation flexibility. Specifically, it was shown that the attained size and shape attributes were considerably affected by even the presence of small quantities of additives and their morphology could change entirely from needle-like to spherical and vice versa. Significant effects were also demonstrated with respect to the crystals' mean sizes and their subsequent distribution. Therefore, the implemented methodology, illustrated the capabilities of utilizing additives combined with supersaturation control as a promising approach for process design and control purposes.

The proposed multi-objective optimization approach which can be currently utilized for the identification of the ATRs for cooling crystallization systems in impure medium can be easily extended to include additional crystallization phenomena, such as breakage and agglomeration for further studies.

NOMENCLATURE

AR	-	Mean aspect ratio of the population of crystals, [-]
$a_{i,i}$	-	Area of the crystal per unit, [m^2]
B_p	-	Primary nucleation, [#/ s]
C	-	Concentration of KDP crystals in the solution, [g/g solvent]
$C_{CGM,j}$	-	Concentration of the j^{th} crystal growth modifier, [g/g solvent]
C_{sat}	-	Saturation concentration of KDP crystals in solution, [g/g solvent]
E_p	-	Kinetic energy of primary nucleation, [kJ/mol]
Fl_i	-	Pointwise flux of the i^{th} characteristic size, [#/ m^2]
$\Delta G_{ads,0,i,j,k}$	-	Adsorption energy, [kJ/mol]
$\Delta G_{des,0,i,j,k}$	-	Desorption energy, [kJ/mol]
g_i	-	Exponent of growth kinetic equation of the i^{th} characteristic facet, [-]
G_i	-	Crystal growth rate of the i^{th} characteristic facet, [m/s]
$G_{min,i}$	-	Specific growth rate when distribution does not occur, [m/s]
h	-	Discretization size interval, [-]
$J(p)$	-	Minimum sum of squared errors, [-]
k_B	-	Boltzmann factor, [$m^2 kg s^{-2} K^{-1}$]
$K_{d,i,j}$	-	Distribution coefficient, [-]
$k_{ads,0,i,j,k}$	-	Adsorption rate constant of the j^{th} crystal growth modifier, [-]
$k_{des,0,i,j,k}$	-	Desorption rate constant of the j^{th} crystal growth modifier, [-]
k_e	-	Kinetic constant of Primary nucleation, [-]
$K_{e,j}$	-	Thermodynamic distribution coefficient, [-]
k_{gi}	-	Growth kinetic constant, [m/s]

$K_{i,j,k}$	-	Langmuir constant of j^{th} CGM on the i^{th} characteristic facet, [-]
$k_{m,i,j}$	-	Mass transfer coefficient with crystal growth, [m/s]
k_{m0}	-	Mass transfer coefficient without crystal growth, [m/s]
$k_{p,0}$	-	Coefficient of primary nucleation, [$m^{-3} s^{-1}$]
$L_{i,k}$	-	Average distance between k^{th} type of sites, [m]
$M_{CGM,j}$	-	Molecular weight of CGM, [g]
M_c	-	Molecular weight of KDP, [g]
$n_{i,j}$	-	Size and shape distribution, [$\#/m^2$]
$\bar{n}_{i,j}$	-	Cell average of $n_{i,j}(x_1, x_2, t)$ over the (i, j) cell, [$\#/m^2$]
$P_{imp,i}$	-	Impurity factor of the growth rate of i^{th} characteristic facet, [-]
NG_i	-	Number of discretization points of the i^{th} characteristic size, [#]
R	-	Ideal gas constant, [$Pa m^3 mol^{-1} K^{-1}$]
R_{max}, R_{min}	-	minimum and maximum temperature ramp rates, [$^{\circ}C/min$]
r_{x_i}	-	Ratio of the two consecutive gradients, [-]
$S_{d,i}$	-	Standard deviation of the distribution of the i^{th} characteristic size, [-]
T	-	Temperature, [K]
t	-	Time, [min]

GREEK LETTERS

$\alpha_{i,k}$	-	Effectiveness factor of the adsorption on i^{th} characteristic facet, [-]
$\beta_{i,k}$	-	Constant of the effectiveness factor, [m/K]
γ_i	-	Edge free energy on the i^{th} crystal face per unit length, [J/m]
ε_{ij}	-	Stochastic measurement error, [-]
ε	-	Small number to avoid division by zero, [-]
η_{ij}	-	Time spent by a particle in the presence of impurities, [s]
$\mu_{m,r}$	-	m, r^{th} order mixed moment of size variables

ρ_c	-	Density of the KDP crystals, 2.338 [kg/m^3]
$\sigma_{m,r}$	-	m, r order joint moment, [-]
σ	-	Relative supersaturation, [-]
$\tau_{i,j,k}$	-	Adsorption time constant, [s]
φ	-	Flux limiter function, [-]
$\chi_{c,j}$	-	Mole fraction of the CGM in the crystal phase, [-]
Ω^k	-	Sample Space, [-]

SUBSCRIPTS

0	-	Initial value
1	-	Length coordinate, [m]
2	-	Width coordinate, [m]
i	-	Characteristic crystal facet indices, [-]
p	-	Primary nucleation, [m]
sat	-	Saturation (solubility curve), [$kg/kg_{solvent}$]
sv	-	Solvent, [$kg/kg_{solvent}$]

6 CONCLUSIONS AND FUTURE WORK

6.1 Summary and Conclusions

Process systems engineering (PSE) tools, such as process design and optimization, have been proven essential over the years to support process understanding and consequently decision making during process development. Most significantly, utilization of PSE tools for complex systems, such as crystallization processes, which exhibit highly nonlinear and stochastic behaviour, and the application of PSE practises in conjunction with experimentation are the only viable and sustainable way to enhance the process' understanding and efficiency.

In this thesis, PSE tools were extensively used for design of batch and continuous crystallization processes subjected to certain constraints and various objective functions with the scope of identification of the optimum operating recipes and the feasible design spaces of the investigated systems. Towards this perspective, a generic and systematic design methodology was presented and applied for the identification of the attainable regions (ATRs) by considering single- and multi-objective optimization algorithms (see **Chapter 3**). The applicability of these methodologies was appraised through two case studies involving the crystallization of paracetamol and potassium dihydrogen phosphate (KDP). These two crystallization processes were selected since they could be modelled by the utilization of 1D and 2D PBMs, respectively, and hence the effect of the model complexity on the methodology could be assessed. The accuracy of the results was validated based on stochastic simulations and/or from literature data

whenever this was possible. In general, continuous operation demonstrated a significantly smaller ATR comparing to batch processing for both cases, which can be justified based on the reduced operation flexibility (i.e. supersaturation control was significantly reduced). Also, the addition of more crystallizers to an MSMR cascade, enlarged the feasible design range since the operation flexibility was increased as well.

However, the predictive capabilities of these models is not only related to the utilization of systematic optimization strategies and advanced numerical solvers, but also to the accurate estimation of the model-parameters, which are typically identified from experimental data. Therefore, prior to process design, estimability analysis should be conducted to ensure that the model parameters (e.g. in the kinetic rate laws) have been accurately and reliably estimated. In this perspective, a novel estimability framework that combines a sequential orthogonalization of the local sensitivity matrix and Sobol, a variance-based global sensitivities technic, was proposed, in **Chapter 4**. As presented, the systematic combination of two different estimability methods guaranteed a robust selection of the optimal subset of parameters resulting in enhanced model prediction capabilities. During the analyses, both parameter significance and correlations were considered to rank the model parameters, while the selection of the optimal subset was done via incremental optimization. As a validation step, the methodology was applied to a complex multi-dimensional morphological population balance for batch crystallization, which combines the effects of different crystal growth modifiers/ impurities on the crystal size and shape distribution of the population of needle-like crystals (MIAM model). The case study showed that although noisy aspect ratio data with low information content were used, a set of the most influential and the least correlated parameters could be identified, providing enhanced prediction capabilities of the dynamic model of the studied crystallization process. For further enhancement of the predictability of the model, an optimal experimental design was proposed in addition to the estimability analysis that maximize the information content of the experimental data and reduces the cost inherent to redundant experimental information. The applied model-based design of experiments (MBoE) was posed as a single objective optimization (SOO) problem considering A – optimal and D – optimal design criteria, as the cost functions. By utilizing MBoE the optimum operating policies that can yield the most informative experiments were identified.

After the reliability of the MIAM had been evaluated, the model was utilized to investigate the effect of the impurities/ CGMs on the transient behaviour of the CQAs (**Chapter 5**). The

morphological population balance model (PBM), was solved by utilizing the standard method of moments (SMOM) and a high-resolution finite volume technique (HR-FV), which arises from combining a semi-discrete FV method with the robust upwind Van Leer flux limiter. The SMOM method was employed during the optimization process, while the HR-FV was utilized for the full reconstruction of the CSSD. Both numerical schemes illustrated fast and accurate simulation of the transient features of the crystal size and shape attributes. The results indicated that the two additives, which have a competing nature, can be utilized to control the crystal size and shape attributes since they present a direct impact on the system's kinetics. The combined effect of supersaturation control and additives inclusion, was also evaluated as a promising hybrid approach for controlling the CSSD. It was clearly demonstrated that this hybrid approach offers enhanced operational flexibility resulting in broader ATRs. More specifically, it was predicted that the presence of small quantities of additives could change entirely the morphology of the needle-like crystals to spherical and vice versa. Significant effects were also demonstrated with respect to the crystal mean sizes and their subsequent distribution. The implemented methodology clearly demonstrates that additives inclusion combined with supersaturation control can be a promising approach for process design and control purposes.

6.2 Future Work

In this last section of the thesis, recommendations for future work are provided.

The systematic design approach for the identification of the attainable regions (ATRs) could be extended by incorporating recycle streams, fine dissolution loops, product classifiers and additional unit operations, such as wet-milling, filtration and drying. In this way, the feasible design space of the key performance indicators (KPIs) could be evaluated with the scope of optimizing the process design during crystallization development. Ideally, this could be extended even further to incorporate the whole range of the employed unit operations – plant-wide design – considering end-to-end manufacturing of active pharmaceutical ingredients. It would be also interesting to investigate the way that the inherent uncertainty of kinetic parameters propagates through the process and how it could impact the distribution of the CQAs. The effect of uncertainty during the identification of the ATRs was demonstrated by [Vetter et al. \(2015\)](#) for 1D PBM models by employing a stochastic Monte Carlo approach. Extending this methodology to 2D PBMs would be rather beneficial for the identification of

the effect of kinetics' uncertainty on size and shape attributes distributions. Therefore, it would be interesting to apply the same principal to a multi-dimensional PBM analysis in order to assess the impact of the parameter uncertainty on CSSD attributes.

Also, the parameter identification and estimability analysis framework could be easily extended to incorporate model-discrimination capabilities. In this work, we considered certain expressions to describe primary nucleation and crystal growth, but there are other model choices available. By evaluating different combinations of kinetic expressions of the available mechanisms, the optimum one could be identified via optimization (structural identifiability/model discrimination): i.e. by minimizing the maximum likelihood (**eq. 4.15**) for each possible combination and then comparing between them. It would be also beneficial for more advanced cost functions to be utilized for model-based design of experiments (MBD_{oE}). The Sigma point method, which has demonstrated superior predictability comparing to the conventional criteria related to the Fisher information matrix (FIM), could be considered ([Schenkendorf et al., 2009](#)). The parameter identification and estimability analysis framework could be also enhanced by improving the Sobol analysis method. In the current work, only the first and total order indices were employed to compute the direct and indirect effects respectively. By increasing the dimensionality of the sensitivity coefficients, the correlations between parameters sets can be estimated as well. In this way, the computation of the correlations can be cross-validated for increased accuracy. Most significantly, the proposed framework can potentially be utilized to evaluate the information content of the data measured by process analytical tools (PAT). In the case of systems utilizing different sensors, the information content of each sensor can be assessed and consequently the number of parameters that can be estimated from each individual PAT or from their combination (e.g. sensors providing different outputs) can be determined, which helps select the most appropriate PAT depending on the targeted level of prediction capability and application (e.g. process control). This, however needs to be validated by experimental results. The proposed validation experiments should utilize ultra-performance liquid chromatography as an on-line PAT tool for the measurement of the impurities' concentrations in combination with Raman spectroscopy and image analysis for the measurement of solute concentration and crystals' mean aspect ratio.

The effect of additives on the size and shape attributes was also investigated in this work. However, apart from growth, additives/impurities could have a major impact on several other properties, such as solubility, MSZW and crystallization kinetics in general. Therefore, this

work could be extended to estimate these potential effects. In addition to that, the proposed high-resolution finite-volume scheme can be extended for the solution of the multi-dimensional MIAM model by incorporating also breakage and agglomeration mechanisms. In this way a more general MIAM model can be proposed for a broader range of applications. Nevertheless, the implementation of these phenomena to a morphological PBM is not trivial (Salvatori and Mazzotti, 2017). It would be also interesting for morphological PBMs to be coupled with computational fluid dynamic (CFD) models to consider the non-ideal mixing effect on CSSD. This would not only enhance the predictability of the models but could also be employed for CSSD control. For example, by controlling the stirring frequency of the agitator, the breakage could be increased affecting the CSSD. Finally, the MIAM model could be applied to real-time closed loop control strategies. The moment-based MIAM could be used for on-line optimization and control of the CSSD, considering a nonlinear model predictive control framework.

7 REFERENCES

- Aamir, E., 2010. Population balance model-based optimal control of batch crystallisation processes for systematic crystal size distribution design. Doctoral thesis, Loughborough University, Loughborough, UK.
- Aamir, E., Nagy, Z.K., Rielly, C.D., Kleinert, T., Judat, B., 2009. Combined Quadrature Method of Moments and Method of Characteristics Approach for Efficient Solution of Population Balance Models for Dynamic Modeling and Crystal Size Distribution Control of Crystallization Processes. *Industrial & Engineering Chemistry Research*, 48, 8575–8584. doi:10.1021/ie900430t.
- Acevedo, D., Kamaraju, V.K., Glennon, B., Nagy, Z.K., 2017. Modeling and Characterization of an in Situ Wet Mill Operation. *Organic Process Research and Development* 21, 1069–1079. doi:10.1021/acs.oprd.7b00192.
- Acevedo, D., Nagy, Z.K., 2014. Systematic classification of unseeded batch crystallization systems for achievable shape and size analysis. *Journal of Crystal Growth* 394, 97–105. doi:10.1016/j.jcrysgr.2014.02.024.
- Acevedo, D., Tandy, Y., Nagy, Z.K., 2015. Multiobjective optimization of an unseeded batch cooling crystallizer for shape and size manipulation. *Industrial and Engineering Chemistry Research* 54, 2156–2166. doi:10.1021/acs.iecr.5b00173.
- Agrawal, S.G., Paterson, A.H.J., 2015. Secondary Nucleation: Mechanisms and Models. *Chemical Engineering Communications*. doi:10.1080/00986445.2014.969369.

- Aksu, B., De Beer, T., Folestad, S., Ketolainen, J., Lindén, H., Lopes, J.A., De Matas, M., Oostra, W., Rantanen, J., Weimer, M., 2012. Strategic funding priorities in the pharmaceutical sciences allied to Quality by Design (QbD) and Process Analytical Technology (PAT). *European Journal of Pharmaceutical Sciences*. doi:10.1016/j.ejps.2012.06.009.
- Alexander, A.J., Camp, P.J., 2009. Single pulse, single crystal laser-induced nucleation of potassium chloride. *Crystal Growth & Design* 9, 958. doi:10.1021/cg8007415.
- Alvarez, A.J., Myerson, A.S., 2010. Continuous plug flow crystallization of pharmaceutical compounds. *Crystal Growth and Design* 10, 2219–2228. doi:10.1021/cg901496s.
- Alvarez, A.J., Singh, A., Myerson, A.S., 2011. Crystallization of cyclosporine in a multistage continuous MSMPR crystallizer. *Crystal Growth and Design* 11, 4392–4400. doi:10.1021/cg200546g.
- Angelov, J.V., Öncül, A.A., Thévenin, D., 2007. Techniques for the reconstruction of a distribution from a finite number of its moments. *Chemical Engineering Science* 62, 2890–2904. doi:10.1016/j.ces.2007.02.041.
- Bakar, M.R.A., Nagy, Z.K., Saleemi, A.N., Rielly, C.D., 2009. The impact of direct nucleation control on crystal size distribution in pharmaceutical crystallization processes. *Crystal Growth and Design* 9, 1378–1384. doi:10.1021/cg800595v.
- Barrett, P., Glennon, B., 2002. Characterizing the metastable zone width and solubility curve using lasentec FBRM and PVM. *Chemical Engineering Research and Design* 80, 799–805. doi:10.1205/026387602320776876.
- Basu, P., Joglekar, G., Rai, S., Suresh, P., Vernon, J., 2008. Analysis of manufacturing costs in pharmaceutical companies. *Journal of Pharmaceutical Innovation* 3, 30–40. doi:10.1007/s12247-008-9024-4.
- Beers, K.J., 2006. Numerical methods for chemical engineering: Applications in MATLAB®, *Numerical Methods for Chemical Engineering: Applications in MATLAB*. Cambridge University Press, Massachusetts Institute of Technology, United States. doi:10.1017/CBO9780511812194.

-
- Benjamin, B.J., Madras, G., 2003. Analytical solution for a population balance equation with aggregation and fragmentation. *Chemical Engineering Science* 58, 3049–3051. doi:10.1016/S0009-2509(03)00159-3.
- Benyahia, B., 2009. Modélisation, expérimentation et optimisation multicritère d'un procédé de copolymérisation en émulsion en présence d'un agent de transfert de chaîne. Institut National Polytechnique de Lorraine, France.
- Benyahia, B., Lakerveld, R., Barton, P.I., 2012. A plant-wide dynamic model of a continuous pharmaceutical process. *Industrial and Engineering Chemistry Research* 51, 15393–15412. doi:10.1021/ie3006319.
- Benyahia, B., Latifi, M.A., Fonteix, C., Pla, F., 2011a. Multicriteria dynamic optimization of an emulsion copolymerization reactor. *Computers and Chemical Engineering* 35, 2886–2895. doi:10.1016/j.compchemeng.2011.05.014.
- Benyahia, B., Latifi, M. A., Fonteix, C., Pla, F., 2011b. Modeling of a batch emulsion copolymerization reactor in the presence of a chain transfer agent: Estimability analysis, parameters identification and experimental validation. *Computer Aided Chemical Engineering* 29, 126-130. doi.org/10.1016/B978-0-444-63234-0.50121-4
- Benyahia, B., Latifi, M. A., Fonteix, C., Pla, F., 2013. Emulsion copolymerization of styrene and butyl acrylate in the presence of a chain transfer agent. Part 2: Parameters estimability and confidence regions. *Chemical Engineering Science*, 90, 110–118. doi: 10.1016/j.ces.2012.12.013.
- Berkovitch-Yellin, Z., Addadi, L., Idelson, M., Lahav, M., Leiserowitz, L., 1982. Controlled Modification of Crystal Habit by “Tailor-Made” Impurities: Application to Benzamide. *Angewandte Chemie International Edition in English* 21, 631–632. doi:10.1002/anie.198206311.
- Berthoud, A., 1912. Theorie de la formation des faces d'un crystal. *Journal de Chimique Physique* 10, 624–635.
- Besenhard, M. O., Chaudhury, A., Vetter, T., Ramachandran, R., & Khinast, J. G., 2015. Evaluation of Parameter Estimation Methods for Crystallization Processes Modeled via Population Balance Equations. *Chemical Engineering Research and Design*, 94, 275–289. doi.org/10.1016/j.cherd.2014.08.004.
-

- Bhat, S.A., Huang, B., 2009. Preferential crystallization: Multi-objective optimization framework. *AIChE Journal* 55, 383–395. doi:10.1002/aic.11691.
- Bogacz, W., Al-Rashed, M.H., Lemanowicz, M., Wójcik, J., 2016. A Simple Densimetric Method to Determine Saturation Temperature of Aqueous Potassium Chloride Solution. *Journal of Solution Chemistry* 45, 1071–1076. doi:10.1007/s10953-016-0492-8.
- Bonvin, D., Georgakis, C., Pantelides, C.C., Barolo, M., Grover, M.A., Rodrigues, D., Schneider, R., Dochain, D., 2016. Linking Models and Experiments. *Industrial and Engineering Chemistry Research*. doi:10.1021/acs.iecr.5b04801..
- Borsos, A., Majumder, A., & Nagy, Z. K., 2016. Multi-impurity Adsorption model for modeling crystal purity and shape evolution during crystallization processes in impure media. *Crystal Growth & Design*, 16(2), 555–568. doi: 10.1021/acs.cgd.5b00320.
- Borsos, A., 2016b. Modelling and control of crystal purity, size and shape distributions in crystallization processes. Doctoral thesis, Loughborough University, Loughborough, UK.
- Borsos, Á., & Lakatos, B. G., 2014. Investigation and simulation of crystallization of high aspect ratio crystals with fragmentation. *Chemical Engineering Research and Design*, 92(6), 1133-1141. doi: 10.1016/j.cherd.2013.08.020.
- Borsos, Á., Szilágyi, B., Agachi, P.Ş., Nagy, Z.K., 2017. Real-Time Image Processing Based Online Feedback Control System for Cooling Batch Crystallization. *Organic Process Research & Development* 21, 511–519. doi:10.1021/acs.oprd.6b00242.
- Braatz, R.D., Nagy, Z.K., 2003. Robust nonlinear model predictive control of batch processes. *Aiche J.* 49, 1776–1786. doi:10.1002/aic.690490715.
- Bravi, M., Di Cave, S., Mazzarotta, B., Verdone, N., 2003. Relating the attrition behaviour of crystals in a stirred vessel to their mechanical properties. *Chemical Engineering Journal* 94, 223–229. doi:10.1016/S1385-8947(03)00053-6.
- Briesen, H., 2009. Two-dimensional population balance modeling for shape dependent crystal attrition. *Chemical Engineering Science* 64, 661–672. doi:10.1016/j.ces.2008.05.002.
- Briggs, N.E.B., Schacht, U., Raval, V., McGlone, T., Sefcik, J., Florence, A.J., 2015. Seeded Crystallization of β -L-Glutamic Acid in a Continuous Oscillatory Baffled Crystallizer. *Organic Process Research and Development* 19, 1903–1911. doi:10.1021/acs.oprd.5b00206.

-
- Brown, C.J., Adalakun, J.A., Ni, X. wei, 2015. Characterization and modelling of antisolvent crystallization of salicylic acid in a continuous oscillatory baffled crystallizer. *Chemical Engineering and Processing: Process Intensification* 97, 180–186. doi:10.1016/j.cep.2015.04.012.
- Brown, C.J., McGlone, T., Yerdelen, S., Srirambhatla, V., Mabbott, F., Gurung, R., L. Briuglia, M., Ahmed, B., Polyzois, H., McGinty, J., Perciballi, F., Fysikopoulos, D., MacFhionnghaile, P., Siddique, H., Raval, V., Harrington, T.S., Vassileiou, A.D., Robertson, M., Prasad, E., Johnston, A., Johnston, B., Nordon, A., Srari, J.S., Halbert, G., ter Horst, J.H., Price, C.J., Rielly, C.D., Sefcik, J., Florence, A.J., 2018. Enabling precision manufacturing of active pharmaceutical ingredients: workflow for seeded cooling continuous crystallisations. *Molecular Systems Design & Engineering*. doi:10.1039/C7ME00096K.
- Brunsteiner, M., Jones, A.G., Pratola, F., Price, S.L., Simons, S.J.R., 2005. Toward a molecular understanding of crystal agglomeration. *Crystal Growth and Design*. doi:10.1021/cg049837m.
- Brun, R., Kühni, M., Siegrist, H., Gujer, W., & Reichert, P., 2002. Practical identifiability of ASM2d parameters-systematic selection and tuning of parameter subsets. *Water Research*, 36(16), 4113–4127. doi:10.1016/s0043-1354(02)00104-5.
- Cao, Y., Acevedo, D., Nagy, Z.K., Laird, C.D., 2017. Real-time feasible multi-objective optimization based nonlinear model predictive control of particle size and shape in a batch crystallization process. *Control Engineering Practice* 69, 1–8. doi:10.1016/j.conengprac.2017.08.008.
- Cao, Y., Kariwala, V., & Nagy, Z. K., 2012. Parameter Estimation for Crystallization Processes using Taylor Method. *IFAC Proceedings Volumes*, 45(15), 880-885. doi:10.3182/20120710-4-sg-2026.00079.
- Chen, B. H., Bermingham, S., Neumann, A. H., Kramer, H. J., & Asprey, S. P., 2004. On the Design of Optimally Informative Experiments for Dynamic Crystallization Process Modeling. *Industrial & Engineering Chemistry Research*, 43(16), 4889-4902. doi:10.1021/ie030649n.
- Chen, J., Sarma, B., Evans, J.M.B., Myerson, A.S., 2011. Pharmaceutical crystallization. *Crystal Growth and Design* 11, 887–895. doi:10.1021/cg101556s.
-

- Chu, Y., Hahn, J., 2011. Generalization of a parameter set selection procedure based on orthogonal projections and the D-optimality criterion. *AIChE Journal*, 58(7), 2085–2096. doi:10.1002/aic.12727.
- Chianese, A., Kramer, H.J.M., 2012. Industrial Crystallization Process Monitoring and Control. *Industrial Crystallization Process Monitoring and Control*. doi:10.1002/9783527645206.
- Chung, S.H., Ma, D.L., Braatz, R.D., 1999. Optimal seeding in batch crystallization. *Canadian Journal of Chemical Engineering* 77, 590–596. doi:10.1002/cjce.5450770322.
- Cogoni, G., Frawley, P.J., 2015. Particle Size Distribution Reconstruction Using a Finite Number of Its Moments through Artificial Neural Networks: A Practical Application. *Crystal Growth & Design* 15, 239–246. doi:10.1021/cg501288z.
- Costa, C.B.B., MacIel Filho, R., 2005. Evaluation of optimization techniques and control variable formulations for a batch cooling crystallization process. *Chemical Engineering Science* 60, 5312–5322. doi:10.1016/j.ces.2005.04.068.
- Czapla, F., Haida, H., Elsner, M., Lorenz, H., & Seidel-Morgenstern, A., 2009. Parameterization of population balance models for polythermal auto seeded preferential crystallization of enantiomers. *Chemical Engineering Science*, 64(4), 753–763. doi: 10.1016/j.ces.2008.05.008.
- Davey, R.J., 1976. The effect of impurity adsorption on the kinetics of crystal growth from solution. *Journal of Crystal Growth* 34, 109–119. doi:10.1016/0022-0248(76)90268-2
- Davey, R.J., Garside, J., 2000. *From molecules to crystallizers: An Introduction to Crystallization*, 1st edition, Oxford University Press Inc., UK.
- Davey, R.J., Schroeder, S.L.M., ter Horst, J.H., 2013. Nucleation of Organic Crystals-A Molecular Perspective. *Angewandte Chemie International Edition* 52, 2166–2179. doi:10.1002/anie.201204824.
- David, R., Marchal, P., Marcant, B., 1995. Modelling of agglomeration in industrial crystallization from solution. *Chemical Engineering & Technology* 18, 302–309. doi:10.1002/ceat.270180503.
- Deb, K., 2001. Multi-objective optimization. *Multi-objective optimization using evolutionary algorithms* 13–46. doi:10.1007/978-1-4614-6940-7_15.

-
- Degenring, D., Froemel, C., Dikta, G., & Takors, R., 2004. Sensitivity analysis for the reduction of complex metabolism models. *Journal of Process Control*, 14(7), 729–745. doi: 10.1016/j.jprocont.2003.12.008.
- DiMasi, J.A., Hansen, R.W., Grabowski, H.G., 2003. The price of innovation: New estimates of drug development costs. *Journal of Health Economics* 22, 151–185. doi:10.1016/S0167-6296(02)00126-1.
- Dowling, R., Davey, R.J., Curtis, R.A., Han, G., Poornachary, S.K., Chow, P.S., Tan, R.B.H., 2010. Acceleration of crystal growth rates: an unexpected effect of tailor-made additives. *Chemical Communications* 46, 5924. doi:10.1039/c0cc00336k.
- Eghtesadi, Z., & McAuley, K. B., 2014. Mean square error based method for parameter ranking and selection to obtain accurate predictions at specified operating conditions. *Industrial & Engineering Chemistry Research*, 53(14), 6033–6046. doi:10.1021/ie5002444.
- Eisenschmidt, H., Bajcinca, N., Sundmacher, K., 2016. Optimal Control of Crystal Shapes in Batch Crystallization Experiments by Growth-Dissolution Cycles. *Crystal Growth and Design* 16, 3297–3306. doi: 10.1021/acs.cgd.6b00288.
- Epstein, M. A., 1982. Nucleation, growth, and impurity effects in crystallization process engineering. New York, NY: American Institute of Chemical Engineers.
- FDA, 2006. Guidance for Industry: Q8 Pharmaceutical Development, Guidance for Industry. doi:10.1016/j.ijpharm.2010.02.031.
- Feinberg, M., Hildebrandt, D., 1997. Optimal reactor design from geometric viewpoint- I. Universal properties of the attainable region. *Chemical Engineering Science* 52, 1637–1665. doi:10.1016/S0009-2509(96)00471-X.
- Ferguson, S., 2012. Application of Continuous Processing to Pharmaceutical Crystallization, Doctoral dissertation, University College Dublin, Dublin.
- Févotte, F., Févotte, G., 2010. A method of characteristics for solving population balance equations (PBE) describing the adsorption of impurities during crystallization processes. *Chemical Engineering Science* 65, 3191–3198. doi:10.1016/j.ces.2010.02.009.
- Fujiwara, M., Chow, P.S., Ma, D.L., Braatz, R.D., 2002a. Paracetamol Crystallization Using Laser Backscattering and ATR-FTIR Spectroscopy: Metastability, Agglomeration, and Control. *Crystal Growth and Design* 2, 363–370. doi:10.1021/cg0200098.

- Fujiwara, M., Ma, D. L., Togkalidou, T., Tafti, D. K., & Braatz, R. D., 2002b. Identification of pharmaceutical crystallization processes. *IFAC Proceedings Volumes*, 35(1), 253–258. doi:10.3182/20020721-6-es-1901.01351.
- Fujiwara, M., Nagy, Z.K., Chew, J.W., Braatz, R.D., 2005. First-principles and direct design approaches for the control of pharmaceutical crystallization. *Journal of Process Control*. doi:10.1016/j.jprocont.2004.08.003.
- Garside, J., Gibilaro, L.G., Tavare, N.S., 1982. Evaluation of crystal growth kinetics from a desupersaturation curve using initial derivatives. *Chemical Engineering Science* 37, 1625–1628. doi:10.1016/0009-2509(82)80031-6.
- Gerstlauer, A., Mitrovic, A., Motz, S., Gilles, E.D., 2001. A population model for crystallization processes using two independent particle properties. *Chemical Engineering Science* 56, 2553–2565. doi:10.1016/S0009-2509(00)00448-6.
- Gibbs, J.W., 1876. *Trans. Connect. Acad. Sci.*, 3, 108-248.
- Gibbs, J.W., 1878. *Trans. Connect. Acad. Sci.*, 16, 343-524.
- Gimbin, J., Liew, S.Y., Nagy, Z.K., Rielly, C.D., 2016. Three-Way Coupling Simulation of a Gas-Liquid Stirred Tank using a Multi-Compartment Population Balance Model. *Chemical Product and Process Modeling* 11, 205–216. doi:10.1515/cppm-2015-0076.
- Glasser, D., Hildebrandt, D., Crowe, C., 1987. A Geometric Approach to Steady Flow Reactors: The Attainable Region and Optimization in Concentration Space. *Industrial and Engineering Chemistry Research* 26, 1803–1810. doi:10.1021/ie00069a014.
- Gonnissen, Y., Gonçalves, S.I.V., De Geest, B.G., Remon, J.P., Vervaet, C., 2008. Process design applied to optimise a directly compressible powder produced via a continuous manufacturing process. *European Journal of Pharmaceutics and Biopharmaceutics* 68, 760–770 doi:10.1016/j.ejpb.2007.09.007.
- Gunawan, R., Fusman, I., Braatz, R.D., 2004. High resolution algorithms for multidimensional population balance equations. *AIChE Journal* 50, 2738–2749. doi:10.1002/aic.10228.
- Gu, T., Tsai, G. J, Tsao, G.T., 1991. Multicomponent adsorption and chromatography with uneven saturation capacities. *AIChE Journal* 37, 1333–1340. doi:10.1002/aic.690370906.

-
- Hemalatha, K., Rani, K. Y., 2016. Sensitivity analysis of Pareto solution sets of multiobjective optimization for a batch cooling crystallization process. *Proceeding Of Indian Control Conference (ICC) IEEE*, 493–498. doi: 10.1109/INDIANCC.2016.7441180.
- Hemalatha, K., Rani, K.Y., 2017. Multiobjective Optimization of Unseeded and Seeded Batch Cooling Crystallization Processes. *Industrial and Engineering Chemistry Research* 56, 6012–6021. doi:10.1021/acs.iecr.7b00586.
- Hildebrandt, D., Glasser, D., Crowe, C.M., 1990. Geometry of the Attainable Region Generated by Reaction and Mixing: With and without Constraints. *Industrial and Engineering Chemistry Research* 29, 49–58. doi:10.1021/ie00097a009.
- Horn, F.J.M., 1964. Attainable and non-attainable regions in chemical reaction technique. *Proceeding of the third European Symposium on Chemical Reaction Engineering*, Pergamon Press, London, UK.
- Hulburt, H.M., Katz, S., 1964. Some problems in particle technology. *Chemical Engineering Science* 19, 555–574. doi:10.1016/0009-2509(64)85047-8.
- ICH, 2006. ICH Q9: Quality Risk Management. CDER Advisory Committee for Pharmaceutical Science and Clinical Pharmacology 23.
- Janaideh, M. A., Rakheja, S., & Su, C. Y., 2008. Modelling rate-dependent symmetric and asymmetric hysteresis loops of smart actuators. *IJAMECHS International Journal of Advanced Mechatronic Systems*, 1(1), 32. doi:10.1504/ijamechs.2008.020836.
- Jayasankar, B. R., Ben-Zvi, A., & Huang, B., 2009. Identifiability and estimability study for a dynamic solid oxide fuel cell model. *Computers & Chemical Engineering*, 33(2), 484–492. doi: 10.1016/j.compchemeng.2008.11.005.
- Jiang, M., Zhu, X., Molaro, M.C., Rasche, M.L., Zhang, H., Chadwick, K., Raimondo, D.M., Kim, K.K.K., Zhou, L., Zhu, Z., Wong, M.H., O’Grady, D., Hebrault, D., Tedesco, J., Braatz, R.D., 2014. Modification of crystal shape through deep temperature cycling. *Industrial and Engineering Chemistry Research* 53, 5325–5336. doi:10.1021/ie400859d.
- Jolliffe, I. T., 1972. Discarding variables in a principal component analysis. I: Artificial data. *Applied Statistics*, 21(2), 160. doi:10.2307/2346488.
- Jones, A.G., 2002. *Crystallization Process Systems*. Butterworth-Heinemann, Oxford. doi:10.1016/B978-075065520-0/50009-2.
-

- Jones, A.G., Mullin, J.W., 1974. Programmed cooling crystallization of potassium sulphate solutions. *Chemical Engineering Science* 29, 105–118. doi:10.1016/0009-2509(74)85036-0.
- Kadam, S.S., Kramer, H.J.M., Ter Horst, J.H., 2011. Combination of a single primary nucleation event and secondary nucleation in crystallization processes. *Crystal Growth and Design* 11, 1271–1277. doi:10.1021/cg101504c.
- Kadam, S.S., Kulkarni, S.A., Coloma Ribera, R., Stankiewicz, A.I., ter Horst, J.H., Kramer, H.J.M., 2012. A new view on the metastable zone width during cooling crystallization. *Chemical Engineering Science* 72, 10–19. doi:10.1016/j.ces.2012.01.002.
- Kariwala, V., Cao, Y., Nagy, Z.K., 2012. Automatic differentiation-based quadrature method of moments for solving population balance equations. *AIChE Journal* 58, 842–854. doi:10.1002/aic.12613.
- Karpinski, P.H., Wey, J.S., 2002. Handbook of Industrial Crystallization, Handbook of Industrial Crystallization. doi:10.1016/B978-075067012-8/50008-2.
- Karthika, S., Radhakrishnan, T.K., Kalaichelvi, P., 2016. A Review of Classical and Nonclassical Nucleation Theories. *Crystal Growth and Design* 16, 6663–6681. doi:10.1021/acs.cgd.6b00794.
- Kendall, M., Keith, J., & Stuart, A., 1977. *The advanced theory of statistics*. London: Griffin and Company.
- Kessel, M., 2011. The problems with today's pharmaceutical business-an outsider's view. *Nature Biotechnology*. doi:10.1038/nbt.1748.
- Kestur, U.S., Taylor, L.S., 2013. Evaluation of the crystal growth rate of felodipine polymorphs in the presence and absence of additives as a function of temperature. *Crystal Growth and Design* 13, 4349–4354. doi:10.1021/cg400708p.
- Kougoulos, E., Jones, A.G., Wood-Kaczmar, M.W., 2006. A hybrid CFD compartmentalization modeling framework for the scaleup of batch cooling crystallization processes. *Chemical Engineering Communications* 193, 1008–1023. doi:10.1080/00986440500352022.
- Koswara, A., Nagy, Z.K., 2015. Anti-fouling control of plug-flow crystallization via heating and cooling cycle, in: *IFAC-PapersOnLine*. pp. 193–198. doi:10.1016/j.ifacol.2015.08.180.

-
- Kou, B., McAuley, K. B., Hsu, C. C., Bacon, D. W., & Yao, K. Z., 2005. Mathematical model and parameter estimation for gas-phase ethylene homopolymerization with supported metallocene catalyst. *Industrial & Engineering Chemistry Research*, 44(8), 2428–2442. doi:10.1021/ie048957o.
- Kramer, H.J.M., Dijkstra, J.W., Verheijen, P.J.T., Van Rosmalen, G.M., 2000. Modeling of industrial crystallizers for control and design purposes. *Powder Technology* 108, 185–191. doi:10.1016/S0032-5910(99)00219-3.
- Kramer, H.J.M., Jansens, P.J., 2003. Tools for Design and Control of Industrial Crystallizers - State of Art and Future Needs. *Chemical Engineering & Technology* 26, 247–255. doi:10.1002/ceat.200390036.
- Kravaris, C., Hahn, J., & Chu, Y., 2013. Advances and selected recent developments in state and parameter estimation. *Computers & Chemical Engineering*, 51, 111–123. doi: 10.1016/j.compchemeng.2012.06.001.
- Kubota, N., Mullin, J.W., 1995. A kinetic model for crystal growth from aqueous solution in the presence of impurity. *Journal of Crystal Growth* 152, 203–208. doi:10.1016/0022-0248(95)00128-X.
- Kubota, N., Sasaki, S., Doki, N., Minamikawa, N., Yokota, M., 2004. Adsorption of an Al (III) impurity onto the (100) face of a growing KDP crystal in supersaturated solution. *Crystal Growth and Design* 4, 533–537. doi:10.1021/cg034254i.
- Kubota, N., Doki, N., Yokota, M., Sato, A., 2001a. Seeding policy in batch cooling crystallization, in: *Powder Technology*. pp. 31–38. doi:10.1016/S0032-5910(01)00371-0.
- Kubota, N., 2001b. Effect of impurities on the growth kinetics of crystals, in: *Crystal Research and Technology*. pp. 749–769. doi:10.1002/1521-4079(200110).
- Kumar, J., Peglow, M., Warnecke, G., & Heinrich, S., 2008. The cell average technique for solving multi-dimensional aggregation population balance equations. *Computers & Chemical Engineering*, 32(8), 1810-1830. doi: 10.1016/j.compchemeng.2007.10.001.
- Kwon, J. S., Nayhouse, M., Orkoulas, G., Ni, D., & Christofides, P. D., 2015. Run-to-Run-Based Model Predictive Control of Protein Crystal Shape in Batch Crystallization. *Industrial & Engineering Chemistry Research Ind. Eng. Chem. Res.*, 54(16), 4293-4302. doi:10.1021/ie502377a.
-

- Lakatos, B.G., 1992. Influence of nucleation mechanisms on the multiplicity of steady states in isothermal CMSMPR crystallizers. *Reaction Kinetics & Catalysis Letters* 47, 305–310. doi:10.1007/BF02137665.
- Lakatos, B.G., 1996. Uniqueness and Multiplicity in Isothermal CMSMPR Crystallizers. *AIChE Journal* 42, 285–289.
- Lakatos, 2007. Population balance modelling of crystallization processes. *Hungarian Journal of Industrial Chemistry* 35, 7-17.
- Lakatos, B.G., Sapundzhiev, T.J., Garside, J., 2007b. Stability and dynamics of isothermal CMSMPR crystallizers. *Chemical Engineering Science* 62, 4348–4364. doi:10.1016/j.ces.2007.04.028.
- Lakerveld, R., Benyahia, B., Braatz, R. D. and Barton, P. I., 2013. Model-based design of a plant-wide control strategy for a continuous pharmaceutical plant. *AIChE J.*, 59, 3671–3685. doi:10.1002/aic.14107.
- Lang, Y. d, Cervantes, A.M., Biegler, L.T., 1999. Dynamic Optimization of a Batch Cooling Crystallization Process. *Industrial & Engineering Chemistry Research* 38, 1469–1477. doi:10.1021/ie980585u.
- Larsen, P.A., Patience, D.B., Rawlings, J.B., 2006. Industrial crystallization process control. *IEEE Control Systems Magazine* 26, 70–80.
- Lawton, S., Steele, G., Shering, P., Zhao, L., Laird, I., Ni, X.W., 2009. Continuous crystallization of pharmaceuticals using a continuous oscillatory baffled crystallizer. *Organic Process Research and Development* 13, 1357–1363. doi:10.1021/op900237x.
- LeVeque, R.J., 2002. *Finite Volume Methods for Hyperbolic Problems*. Cambridge University Press 54, 258. doi:10.1017/CBO9780511791253.
- Lim, B.G., Ching, C.B., Tan, R.B.H., 1995. Determination of competitive adsorption isotherms of enantiomers on a dual-site adsorbent. *Separations Technology* 5, 213–228. doi:10.1016/0956-9618(95)00126-3.
- Lindenberg, C., Krättli, M., Cornel, J., Mazzotti, M., Brozio, J., 2009. Design and Optimization of a Combined Cooling/Antisolvent Crystallization Process. *Crystal Growth & Design* 9, 1124–1136. doi:10.1021/cg800934h.

-
- Li, L., Lechuga-Ballesteros, D., Szkudlarek, B.A., Rodriguez-Hornedo, N., 1994. The Effect of Additives on Glycine Crystal Growth Kinetics. *J. Colloid Interface Sci.* 168, 8–14. doi: 10.1006/jcis.1994.1387.
- Liu, J., Rasmuson, Å.C., 2013. Influence of agitation and fluid shear on primary nucleation in solution. *Crystal Growth and Design* 13, 4385–4394. doi:10.1021/cg4007636.
- Lovette, M.A., Muratore, M., Doherty, M.F., 2012. Crystal shape modification through cycles of dissolution and growth: Attainable regions and experimental validation. *AIChE Journal* 58, 1465–1474. doi:10.1002/aic.12707.
- Lund, B. F., & Foss, B. A., 2008. Parameter ranking by orthogonalization—applied to nonlinear mechanistic models. *Automatica*, 44(1), 278–281. doi: 10.1016/j.automatica.2007.04.006.
- Ma, D.L., Braatz, R.D., 2003. Robust identification and control of batch processes, in: *Computers and Chemical Engineering*. pp. 1175–1184. doi:10.1016/S0098-1354(03)00045-0.
- Maggioni, G.M., Mazzotti, M., 2015. Modelling the stochastic behaviour of primary nucleation. *Faraday Discuss.* 179, 359–382. doi:10.1039/C4FD00255E.
- Mahoney, A.W., Ramkrishna, D., 2002. Efficient solution of population balance equations with discontinuities by finite elements. *Chemical Engineering Science* 57. doi:10.1016/S0009-2509(01)00427-4.
- Majumder, A., Kariwala, V., Ansumali, S., Rajendran, A., 2010. Fast high-resolution method for solving multidimensional population balances in crystallization. *Industrial and Engineering Chemistry Research* 49, 3862–3872. doi:10.1021/ie9016946.
- Majumder, A., Kariwala, V., Ansumali, S., Rajendran, A., 2012a. Lattice Boltzmann method for population balance equations with simultaneous growth, nucleation, aggregation and breakage. *Chemical Engineering Science* 69, 316–328. doi:10.1016/j.ces.2011.10.051.
- Majumder, A., Kariwala, V., Ansumali, S., Rajendran, A., 2012b. Lattice Boltzmann method for multi-dimensional population balance models in crystallization. *Chemical Engineering Science* 70. doi:10.1016/j.ces.2011.04.041.
- Majumder, A., Nagy, Z.K., 2013a. Fines removal in a continuous plug flow crystallizer by optimal spatial temperature profiles with controlled dissolution. *AIChE Journal* 59, 4582–4594. doi:10.1002/aic.14196.
-

- Majumder, A., Nagy, Z.K., 2013b. Prediction and control of crystal shape distribution in the presence of crystal growth modifiers. *Chemical Engineering Science* 101, 593–602. doi:10.1016/j.ces.2013.07.017.
- Majumder, A., Nagy, Z.K., 2015. Dynamic modeling of encrust formation and mitigation strategy in a continuous plug flow crystallizer. *Crystal Growth and Design* 15, 1129–1140. doi:10.1021/cg501431c.
- Mangin, D., Puel, F., Veessler, S., 2009. Polymorphism in processes of crystallization in solution: A practical review. *Organic Process Research and Development*. doi:10.1021/op900168f.
- Mascia, S., Heider, P. L., Zhang, H., Lakerveld, R., Benyahia, B., Barton, P. I., Trout, B. L., 2013. End-to-End Continuous Manufacturing of Pharmaceuticals: Integrated Synthesis, Purification, and Final Dosage Formation. *Angewandte Chemie*, 125(47), 12585-12589. doi:10.1002/ange.201305429.
- Mazzarotta, B., Di Cave, S., Bonifazi, G., 1996. Influence of Time on Crystal Attrition in a Stirred Vessel. *AIChE Journal* 42, 3554–3558. doi:10.1002/aic.690421226.
- McGraw, R., 1997. Description of aerosol dynamics by the quadrature method of moments. *Aerosol Science and Technology* 27, 255–265. doi:10.1080/02786829708965471.
- McLean, K. A. P., & McAuley, K. B., 2011. Mathematical modelling of chemical processes-obtaining the best model predictions and parameter estimates using identifiability and estimability procedures. *The Canadian Journal of Chemical Engineering*, 90(2), 351–366. doi:10.1002/cjce.20660.
- Mersmann, A., 1988. Design of Crystallizers. *Chemical Engineering and Processing* 23, 213–228. doi:10.1016/0255-2701(88)85014-1.
- Mersmann, A., 2001. *Crystallization Technology Handbook - Second Edition Revised and Expanded*, Marcel Dekker Inc.
- Mesbah, A., Huesman, A.E.M., Kramer, H.J.M., Nagy, Z.K., Van den Hof, P.M.J., 2011. Real-time control of a semi-industrial fed-batch evaporative crystallizer using different direct optimization strategies. *AIChE Journal* 57, 1557–1569. doi:10.1002/aic.12366.
- Mesbah, A., Landlust, J., Huesman, A.E.M., Kramer, H.J.M., Jansens, P.J., Van den Hof, P.M.J., 2010. A model-based control framework for industrial batch crystallization

-
- processes. *Chemical Engineering Research and Design* 88, 1223–1233. doi:10.1016/j.cherd.2009.09.010.
- Mesbah, A., Nagy, Z. K., Huesman, A. E., Kramer, H. J., & P. M. J. Van Den Hof, 2012. Nonlinear Model-Based Control of a Semi-Industrial Batch Crystallizer Using a Population Balance Modeling Framework. *IEEE Transactions on Control Systems Technology* IEEE Trans. Contr. Syst. Technol., 20(5), 1188-1201. doi:10.1109/tcst.2011.2160945.
- Mesbah, A., Paulson, J.A., Lakerveld, R., Braatz, R.D., 2017. Model Predictive Control of an Integrated Continuous Pharmaceutical Manufacturing Pilot Plant. *Organic Process Research & Development* 21, 844–854. doi:10.1021/acs.oprd.7b00058.
- Miettinen, K., 1999. “Concepts,” *Nonlinear MultiObjective Optimization, Nonlinear MultiObjective Optimization*. Springer Science & Business Media.
- Ming, D., Glasser, D., Hildebrandt, D., 2013. Application of attainable region theory to batch reactors. *Chemical Engineering Science* 99, 203–214. doi:10.1016/j.ces.2013.06.001.
- Ming, D., Glasser, D., Hildebrandt, D., Metzger, M., Glasser, B., 2016. *Attainable Region Theory: An Introduction to Choosing an Optimal Reactor*. Hoboken, New Jersey: John Wiley & Sons.
- Miyasaka, E., Ebihara, S., Hirasawa, I., 2006. Investigation of primary nucleation phenomena of acetylsalicylic acid crystals induced by ultrasonic irradiation-ultrasonic energy needed to activate primary nucleation. *Journal of Crystal Growth* 295, 97–101. doi:10.1016/j.jcrysgro.2006.07.020.
- Mullin, J.J.W., 2001. *Crystallization, Crystallization*. Elsevier. doi:10.1016/B978-075064833-2/50000-0.
- Myerson, A., 2002. *Handbook of Industrial Crystallization*. Butterworth-Heinemann, Oxford. doi:10.1016/B978-075067012-8/50007-0.
- Nagy, Z.K., Chew, J.W., Fujiwara, M., Braatz, R.D., 2008. Comparative performance of concentration and temperature controlled batch crystallizations. *Journal of Process Control* 18, 399–407. doi:10.1016/j.jprocont.2007.10.006.
- Nagy, Z.K., 2009. Model based robust control approach for batch crystallization product design. *Computers & Chemical Engineering* 33, 1685–1691. doi:10.1016/j.compchemeng.2009.04.012.
-

- Nagy, Z.K., Fevotte, G., Kramer, H., Simon, L.L., 2013. Recent advances in the monitoring, modelling and control of crystallization systems. *Chemical Engineering Research and Design* 91, 1903–1922. doi:10.1016/j.cherd.2013.07.018.
- Nichols, G., Byard, S., Bloxham, M.J., Botterill, J., Dawson, N.J., Dennis, A., Diart, V., North, N.C., Sherwood, J.D., 2002. A review of the terms agglomerate and aggregate with a recommendation for nomenclature used in powder and particle characterization. *Journal of Pharmaceutical Sciences*. doi:10.1002/jps.10191.
- Nicmanis, M., Hounslow, M.J., 1998. Finite-element methods for steady-state population balance equations. *AIChE Journal* 44, 2258–2272. doi:10.1002/aic.690441015.
- Nisoli, A., Malone, M. F. and Doherty, M. F., 1997. Attainable regions for reaction with separation. *AIChE J.*, 43: 374–387. doi:10.1002/aic.690430211.
- Noyes, A.A., Whitney, W.R., 1897. The rate of solution of solid substances in their own solutions. *Journal of the American Chemical Society* 19, 930–934. doi:10.1021/ja02086a003.
- Nýlvlt, J., 1994. Design of agitated crystallizers. *Crystal Research and Technology* 29, 895–899. doi:10.1002/crat.2170290622.
- Omar, H.M., Rohani, S., 2017. Crystal Population Balance Formulation and Solution Methods: A Review. *Crystal Growth & Design* 17, 4028–4041. doi:10.1021/acs.cgd.7b00645.
- Palwe, B.G., Chivate, M.R., Tavare, N.S., 1985. Growth Kinetics of Ammonium Nitrate Crystals in a Draft Tube Baffled Agitated Batch Crystallizer. *Industrial and Engineering Chemistry Process Design and Development* 24, 914–919. doi:10.1021/i200031a004.
- Park, K., Kim, D.Y., Yang, D.R., 2016. Operating Strategy for Continuous Multistage Mixed Suspension and Mixed Product Removal (MSMPR) Crystallization Processes Depending on Crystallization Kinetic Parameters. *Industrial and Engineering Chemistry Research* 55, 7142–7153. doi:10.1021/acs.iecr.6b01386.
- Paroli, F., 2012. Industrial Crystallizers Design and Control, in: *Industrial Crystallization Process Monitoring and Control*. Wiley-VCH, pp. 203–224. doi:10.1002/9783527645206.ch17.

-
- Patil, D.P., Andrews, J.R.G., 1998. An analytical solution to continuous population balance model describing floc coalescence and breakage - A special case. *Chemical Engineering Science* 53, 599–601. doi:10.1016/S0009-2509(97)00314-X.
- Peña, R., Oliva, J.A., Burcham, C.L., Jarmer, D.J., Nagy, Z.K., 2017a. Process Intensification through Continuous Spherical Crystallization Using an Oscillatory Flow Baffled Crystallizer. *Crystal Growth & Design* acs.cgd.7b00731. doi:10.1021/acs.cgd.7b00731.
- Peña, R., Burcham, C.L., Jarmer, D.J., Ramkrishna, D., Nagy, Z.K., 2017b. Modelling and optimization of spherical agglomeration in suspension through a coupled population balance model. *Chemical Engineering Science* 167, 66–77. doi:10.1016/j.ces.2017.03.055.
- Peña, R., Nagy, Z.K., 2015. Process Intensification through Continuous Spherical Crystallization Using a Two-Stage Mixed Suspension Mixed Product Removal (MSMPR) System. *Crystal Growth and Design* 15, 4225–4236. doi:10.1021/acs.cgd.5b00479.
- Perregaard, J., 1993. Model simplification and reduction for simulation and optimization of chemical processes. *Computers & Chemical Engineering*, 17(5-6), 465–483. doi:10.1016/0098-1354(93)80037.
- Pogány, J., 2008. ICH pharmaceutical quality system Q10. WHO Drug Information. doi:EMA/CHMP/ICH/214732/2007.
- Polakowski, C., Sochan, A., Bieganowski, A., Ryzak, M., Földényi, R., Tóth, J., 2014. Influence of the sand particle shape on particle size distribution measured by laser diffraction method. *International Agrophysics* 28, 195–200. doi:10.2478/intag-20014-0008.
- Powell, K., 2017. Improving continuous crystallisation using process analytical technologies: design of a novel periodic flow process (Ph.D.). Loughborough University.
- Price, W., 2014. Making Do in Making Drugs: Innovation Policy and Pharmaceutical Manufacturing. *Boston College Law Review* 55, 491. doi:10.2139/ssrn.2311682.
- Qamar, S., Elsner, M.P., Angelov, I.A., Warnecke, G., Seidel-Morgenstern, A., 2006. A comparative study of high resolution schemes for solving population balances in crystallization. *Computers and Chemical Engineering* 30, 1119–1131. doi:10.1016/j.compchemeng.2006.02.012.

- Qamar, S., Warnecke, G., 2007. Numerical solution of population balance equations for nucleation, growth and aggregation processes. *Computers and Chemical Engineering* 31, 1576–1589. doi:10.1016/j.compchemeng.2007.01.006.
- Quaiser, T., & Mönnigmann, M., 2009. Systematic identifiability testing for unambiguous mechanistic modeling – application to JAK-STAT, MAP kinase, and NF- κ B signaling pathway models. *BMC Systems Biology BMC Syst Biol*, 3(1), 50. doi:10.1186/1752-0509-3-50.
- Rabe, M., Verdes, D., Seeger, S., 2011. Understanding protein adsorption phenomena at solid surfaces. *Advances in Colloid and Interface Science* 162, 87–106. doi:10.1016/j.cis.2010.12.007.
- Ramkrishna, D., 1981. Analysis of population balance-IV. The precise connection between Monte Carlo simulation and population balances. *Chemical Engineering Science* 36, 1203–1209. doi:10.1016/0009-2509(81)85068-3.
- Ramkrishna, D., 2000. The Framework of Population Balance, in: *Population Balances: Theory and Applications to Particulate Systems in Engineering*. Academic Press, pp. 7–45. doi:http://dx.doi.org/10.1016/B978-012576970-9/50003-5.
- Randolph, A.D., 1964. A population balance for countable entities. *Canadian Journal of Chemical Engineering* 42, 280-281.
- Randolph, A.D., Larson, M.A., 1988. *Particulate Processes: Analysis and Techniques of Continuous Crystallization, Theory of Particulate Processes*. doi:10.1016/B978-0-12-579652-1.50001-6.
- Rane, C.V., Ganguli, A.A., Kalekudithi, E., Patil, R.N., Joshi, J.B., Ramkrishna, D., 2014. CFD simulation and comparison of industrial crystallizers. *Canadian Journal of Chemical Engineering* 92, 2138–2156. doi:10.1002/cjce.22078.
- Rathore, A.S., Mhatre, R., 2008. *Quality by Design for Biopharmaceuticals: Principles and Case Studies*, *Quality by Design for Biopharmaceuticals: Principles and Case Studies*. John Wiley and Sons. doi:10.1002/9780470466315.
- Rawlings, J.B., Miller, S.M., Witkowski, W.R., 1993. Model Identification and Control of Solution Crystallization Processes - a Review. *Industrial & Engineering Chemistry Research* 32, 1275–1296. doi:10.1021/ie00019a002.

-
- Ridder, B.J., Majumder, A., Nagy, Z.K., 2014. Population Balance Model Based Multi-Objective Optimization of a Multi-Segment Multi-Addition (MSMA) Continuous Plug Flow Antisolvent Crystallizer. *Industrial and Engineering Chemistry Research* 53, 4387–4397. doi:10.1021/ie402806n.
- Ridder, B.J., Majumder, A., Nagy, Z.K., 2016. Parametric, Optimization-Based Study on the Feasibility of a Multi-segment Antisolvent Crystallizer for in Situ Fines Removal and Matching of Target Size Distribution. *Industrial and Engineering Chemistry Research* 55, 2371–2380. doi:10.1021/acs.iecr.5b03024.
- Rielly, C.D., 2013. Transfer Processes, lecture notes distributed for Chemical Engineering module Transfer Processes, Loughborough University, UK.
- Rigopoulos, S., Jones, A.G., 2003. Finite-element scheme for solution of the dynamic population balance equation. *AIChE Journal*. doi:10.1002/aic.690490507.
- Rippin, D.W.T., 1988. Statistical methods for experimental planning in chemical engineering. *Computers & Chemical Engineering* 12, 109–116. doi:10.1016/0098-1354(88)85012-9.
- Rosolem, R., Gupta, H. V., Shuttleworth, W. J., Zeng, X., & Gonçalves, L. G., 2012. A fully multiple-criteria implementation of the Sobol' method for parameter sensitivity analysis. *Journal of Geophysical Research: Atmospheres*, 117(D7). doi:10.1029/2011jd016355.
- Saleemi, A., Onyemelukwe, I.I., Nagy, Z., 2013. Effects of a structurally related substance on the crystallization of paracetamol. *Frontiers of Chemical Science and Engineering* 7, 79–87. doi:10.1007/s11705-013-1308-7.
- Saltelli, A., Ratto, M., Andres, T., Campolongo, F., Cariboni, J., Gatelli, D., Saisana, M., Tarantola, S., 2008. Introduction to sensitivity analysis. *Global Sensitivity Analysis. The Primer* 1–51. doi:10.1002/9780470725184.ch1.
- Saltelli, A., Ratto, M., Tarantola, S., & Campolongo, F., 2005. Sensitivity analysis for chemical models. *ChemInform*, 36(42). doi:10.1002/chin.200542290.
- Saltelli, A., Tarantola, S., Campolongo, F., Saltelli, S. T., & Ratto, M., 2004. Sensitivity analysis in practice: A guide to assessing scientific models. United Kingdom: Wiley, John & Sons.

- Salvatori, F., Mazzotti, M., 2017. Manipulation of Particle Morphology by Crystallization, Milling, and Heating Cycles—A Mathematical Modeling Approach. *Industrial & Engineering Chemistry Research* acs.iecr.7b02070. doi:10.1021/acs.iecr.7b02070.
- Samad, N. A., Sin, G., Gernaey, K. V., & Gani, R., 2013. Introducing uncertainty analysis of nucleation and crystal growth models in Process Analytical Technology (PAT) system design of crystallization processes. *European Journal of Pharmaceutics and Biopharmaceutics*, 85(3), 911-929. doi: 10.1016/j.ejpb.2013.05.016.
- Samad, N. A., Sin, G., Gernaey, K. V., & Gani, R., 2013. A systematic framework for design of process monitoring and control (PAT) systems for crystallization processes. *Computers & Chemical Engineering*, 54, 8-23. doi: 10.1016/j.compchemeng.2013.03.003.
- Sarkar, D., Rohani, S., Jutan, A., 2006. Multi-objective optimization of seeded batch crystallization processes. *Chemical Engineering Science* 61, 5282–5295. doi:10.1016/j.ces.2006.03.055.
- Sato, K., Nagai, H., Hasegawa, K., Tomori, K., Kramer, H.J.M., Jansens, P.J., 2008. Two-dimensional population balance model with breakage of high aspect ratio crystals for batch crystallization. *Chemical Engineering Science* 63, 3271–3278. doi:10.1016/j.ces.2008.03.013.
- Schenkendorf, R., Kremling, A., Mangold, M., 2009. Optimal experimental design with the sigma point method. *IET systems biology* 3, 10–23. doi:10.1049/iet-syb:20080094.
- Schittkowski, K., 2007. Experimental design tools for ordinary and algebraic differential equations, *Industrial & Engineering Chemistry Research*, 46(26), pp. 9137–9147. doi: 10.1021/ie0703742.
- Schwartz, A.M., 2002. Handbook of Industrial Crystallization - Chapter 01 - Solutions and solution properties, *Handbook of Industrial Crystallization*. doi:10.1016/B978-075067012-8/50003-3.
- Sear, R.P., 2014. Quantitative studies of crystal nucleation at constant supersaturation: experimental data and models. *CrystEngComm* 16, 6506–6522. doi:10.1039/C4CE00344F.
- Sen, M., Rogers, A., Singh, R., Chaudhury, A., John, J., Ierapetritou, M.G., Ramachandran, R., 2013. Flowsheet optimization of an integrated continuous purification-processing

-
- pharmaceutical manufacturing operation. *Chemical Engineering Science* 102, 56–66. doi:10.1016/j.ces.2013.07.035.
- Shampine, L. F. and M. W. Reichelt, 1997. The MATLAB ODE Suite. *SIAM Journal on Scientific Computing*, 18, pp. 1–22.
- Sharma, S., Rangaiah, G.P., 2013. Multi-Objective Optimization in Chemical Engineering, Multi-Objective Optimization in Chemical Engineering: Developments and Applications. John Wiley & Sons Ltd, Oxford, UK. doi:10.1002/9781118341704.
- Sherwin, M.B., Shinnar, R., Katz, S., 1967. Dynamic behavior of the well-mixed isothermal crystallizer. *AIChE Journal* 13, 1141–1154. doi:10.1002/aic.690130621.
- Simone, E., 2015. Application of process analytical technology (PAT) tools for the better understanding and control of the crystallization of polymorphic and impure systems. Doctoral thesis, Loughborough University, Loughborough, UK.
- Simon, L., Myerson, A.S., 2011. Continuous antisolvent plug-flow crystallization of a fast-growing API. *International Symposium on Industrial Crystallization* 3–6.
- Sin, G., Gernaey, K. V., & Lantz, A. E., 2009. Good modeling practice for PAT applications: Propagation of input uncertainty and sensitivity analysis. *Biotechnology Progress*, 25(4), 1043–1053. doi:10.1002/btpr.166.
- Sin, G., Meyer, A. S., & Gernaey, K. V., 2010. Assessing reliability of cellulose hydrolysis models to support biofuel process design—Identifiability and uncertainty analysis. *Computers & Chemical Engineering*, 34(9), 1385–1392. doi:10.1016/j.compchemeng.2010.02.012.
- Sivanandam, S.N., Deepa, S.N., 2008. Introduction to genetic algorithms, Introduction to Genetic Algorithms. Springer Berlin Heidelberg. doi:10.1007/978-3-540-73190-0.
- Sizemore, J.P., Doherty, M.F., 2009. A new model for the effect of molecular imposters on the shape of faceted molecular crystals. *Crystal Growth and Design* 9, 2637–2645. doi:10.1021/cg8011124.
- Smith, R., 2005. Chemical Process Design and Integration, Chemical Engineering. doi:10.1017/CBO9781107415324.004.
- Sohnel, O., Garside, J., 1992. Precipitation. Butterworth-Heinemann, Oxford, UK.

- Sobol', I. M., 2001. Global sensitivity indices for nonlinear mathematical models and their Monte Carlo estimates. *Mathematics and Computers in Simulation*, 55(1-3), 271-280. doi:10.1016/s0378-4754(00)00270-6.
- Steendam, R. R. E., Keshavarz, L., Blijlevens, M. A. R., De Souza, B., Croker, D. M., & Frawley, P. J., 2018. Effects of Scale-Up on the Mechanism and Kinetics of Crystal Nucleation. *Crystal Growth and Design*, 18(9), 5547–5555. <https://doi.org/10.1021/acs.cgd.8b00857>.
- Stewart, T., Bandte, O., Braun, H., Chakraborti, N., Ehrgott, M., Göbelt, M., Jin, Y., Nakayama, H., Poles, S., Di Stefano, D., 2008. *Multiobjective Optimization, Multiobjective Optimization*. Springer Berlin Heidelberg, Berlin, Heidelberg. doi:10.1007/978-3-540-88908-3.
- Smith, M., Matsoukas, T., 1998. Constant-number Monte Carlo simulation of population balances. *Chemical Engineering Science* 53, 1777–1786. doi:10.1016/S0009-2509(98)00045-1.
- Snyder, R.C., Studener, S., Doherty, M.F., 2007. Manipulation of crystal shape by cycles of growth and dissolution. *AIChE Journal* 53, 1510–1517. doi:10.1002/aic.11174.
- Sun, X., Garetz, B.A., Myerson, A.S., 2008. Polarization switching of crystal structure in the nonphotochemical laser-induced nucleation of supersaturated aqueous l-histidine. *Crystal Growth and Design* 8, 1720–1722. doi:10.1021/cg800028v.
- Suresh, P., Basu, P.K., 2008. Improving pharmaceutical product development and manufacturing: Impact on cost of drug development and cost of goods sold of pharmaceuticals. *Journal of Pharmaceutical Innovation*. doi:10.1007/s12247-008-9043-1.
- Su, J., Gu, Z., Xu, X.Y., 2009. Advances in numerical methods for the solution of population balance equations for disperse phase systems. *Science in China, Series B: Chemistry* 52. doi:10.1007/s11426-009-0164-2.
- Su, Q., Hermanto, M. W., Braatz, R. D., & Chiu, M., 2016. Just-in-Time-Learning based Extended Prediction Self-Adaptive Control for batch processes. *Journal of Process Control*, 43, 1-9. doi: 10.1016/j.jprocont.2016.04.009.
- Su, Q., Nagy, Z. K., & Rielly, C. D., 2015. Pharmaceutical crystallisation processes from batch to continuous operation using MSMPR stages: Modelling, design, and control. *Chemical*

-
- Engineering and Processing: Process Intensification, 89, 41-53. doi: 10.1016/j.cep.2015.01.001.
- Surisetty, K., Hoz Siegler, H. D. la, McCaffrey, W. C., & Ben-Zvi, A., 2010. Model re-parameterization and output prediction for a bioreactor system. *Chemical Engineering Science*, 65(16), 4535–4547. doi: 10.1016/j.ces.2010.04.024.
- Szilágyi, B., Agachi, P.Ş., Lakatos, B.G., 2015. Numerical analysis of crystallization of high aspect ratio crystals with breakage. *Powder Technology* 283, 152–162. doi:10.1016/j.powtec.2015.05.029.
- Szilágyi, B., Nagy, Z.K., 2016. Graphical processing unit (GPU) acceleration for numerical solution of population balance models using high resolution finite volume algorithm. *Computers & Chemical Engineering* 91, 167–181. doi:10.1016/j.compchemeng.2016.03.023.
- Tai, C.Y., McCabe, W.L., Rousseau, R.W., 1975. Contact nucleation of various crystal types. *AIChE Journal* 21, 351–358. doi:10.1002/aic.690210217.
- Thompson, D.E., McAuley, K.B. and McLellan, P.J., 2009. Parameter estimation in a simplified MWD model for HDPE produced by a Ziegler-Natta catalyst, *Macromolecular Reaction Engineering*, 3(4), pp. 160–177. doi: 10.1002/mren.200800052.
- Togkalidou, T., Fujiwara, M., Patel, S., Braatz, R.D., 2001. Solute concentration prediction using chemometrics and ATR-FTIR spectroscopy. *Journal of Crystal Growth* 231, 534–543. doi:10.1016/S0022-0248(01)01518-4.
- Trasi, N.S., Taylor, L.S., 2012. Effect of additives on crystal growth and nucleation of amorphous flutamide. *Crystal Growth and Design* 12, 3221–3230. doi:10.1021/cg300370q.
- Tung, H.H., Paul, E.L., Midler, M., McCauley, J.A., 2008. *Crystallization of Organic Compounds: An Industrial Perspective*, *Crystallization of Organic Compounds: An Industrial Perspective*. John Wiley and Sons. doi:10.1002/9780470447796.
- Valeton, J.J.P., 1924. Wachstum und Auflösung der Kristalle. *Zeitschrift für Kristallographie*, 59, 483.
- Vajda, S., Rabitz, H., Walter, E., and Lecourtier, Y., 1989. Qualitative and quantitative identifiability analysis of nonlinear chemical kinetic models, *Chemical Engineering Communications*, 83(1), pp. 191–219. doi: 10.1080/00986448908940662.
-

- Van Leer, B., 1985. Upwind-difference methods for aerodynamic problems governed by the Euler equations, in: *Large-Scale Computations in Fluid Mechanics; Proceedings of the Fifteenth Summer Seminar on Applied Mathematics*. pp. 327–336.
- Varma, A., Morbidelli, M., Hua, W., & Wu, H., 2005. *Parametric sensitivity in chemical systems*. United Kingdom: Cambridge University Press.
- Vekilov, P.G., 2010. The two-step mechanism of nucleation of crystals in solution. *Nanoscale*, 2, 11, 2040-3364. <http://dx.doi.org/10.1039/C0NR00628A>
- Velez-Reys, M., Verghese, G.C., 1995. Subset selection in identification, and application to speed and parameter estimation for induction machines. *Proceedings of the 4th IEEE conference on Control Applications*, 991-997. doi: 10.1109/CCA.1995.555890.
- Vetter, T., Burcham, C.L., Doherty, M.F., 2014. Regions of attainable particle sizes in continuous and batch crystallization processes. *Chemical Engineering Science* 106, 167–180. doi:10.1016/j.ces.2013.11.008.
- Vetter, T., Burcham, C.L., Doherty, M.F., 2015. Designing Robust Crystallization Processes in the Presence of Parameter Uncertainty Using Attainable Regions. *Industrial and Engineering Chemistry Research* 54, 10350–10363. doi:10.1021/acs.iecr.5b00693.
- Virone, C., Kramer, H.J.M., van Rosmalen, G.M., Stoop, A.H., Bakker, T.W., 2006. Primary nucleation induced by ultrasonic cavitation. *Journal of Crystal Growth* 294, 9–15. doi:10.1016/j.jcrysgr.2006.05.025.
- Volmer, M., 1939. *Kinetik der Phasenbildung*, Steinkopf, Dresden.
- Walter, E., & Pronzato, L., 1997. *Identification of parametric models from experimental data*. Berlin: Springer.
- Wang, J., Lakerveld, R., 2017. Continuous Membrane-Assisted Crystallization to Increase the Attainable Product Quality of Pharmaceuticals and Design Space for Operation. *Industrial and Engineering Chemistry Research* 56, 5705–5714. doi:10.1021/acs.iecr.7b00514.
- Wang, T., Lu, H., Wang, J., Xiao, Y., Zhou, Y., Bao, Y., Hao, H., 2017. Recent progress of continuous crystallization. *Journal of Industrial and Engineering Chemistry*. doi:10.1016/j.jiec.2017.06.009.

-
- Wang, F.S., Wu, W.H., 2013. Multi-Objective Optimization in Chemical Engineering, Multi-Objective Optimization in Chemical Engineering: Developments and Applications. John Wiley & Sons Ltd, Oxford, UK. doi:10.1002/9781118341704.
- Ward, M.R., Alexander, A.J., 2012. Nonphotochemical laser-induced nucleation of potassium halides: Effects of wavelength and temperature. *Crystal Growth and Design* 12, 4554–4561. doi:10.1021/cg300750c.
- Ward, J.D., Mellichamp, D.A., Doherty, M.F., 2006. Choosing an operating policy for seeded batch crystallization. *AIChE Journal* 52, 2046–2054. doi:10.1002/aic.10808.
- Wibowo, C., Ng, K.M., 2001. Operational issues in solids processing plants: Systems view. *AIChE Journal* 47, 107–125. doi:10.1002/aic.690470112.
- Wohlgemuth, K., & Schembecker, G., 2013. Modeling induced nucleation processes during batch cooling crystallization: A sequential parameter determination procedure. *Computers & Chemical Engineering*, 52, 216–229. doi: 10.1016/j.compchemeng.2012.12.001.
- Wong, S.Y., Cui, Y., Myerson, A.S., 2013. Contact secondary nucleation as a means of creating seeds for continuous tubular crystallizers. *Crystal Growth and Design* 13, 2514–2521. doi:10.1021/cg4002303.
- Wu, Z., Yang, S., Wu, W., 2016. Application of temperature cycling for crystal quality control during crystallization. *CrystEngComm* 18, 2222–2238. doi:10.1039/C5CE02522B.
- Xie, S., Poornachary, S.K., Chow, P.S., Tan, R.B.H., 2010. Direct precipitation of micron-size salbutamol sulfate: New insights into the action of surfactants and polymeric additives. *Crystal Growth and Design* 10, 3363–3371. doi:10.1021/cg901270x.
- Yang, G., Kubota, N., Sha, Z., Louhi-Kultanen, M., Wang, J., 2006. Crystal shape control by manipulating supersaturation in batch cooling crystallization. *Crystal Growth and Design* 6, 2799–2803. doi:10.1021/cg0603873.
- Yang, Y., Nagy, Z.K., 2014. Model-based systematic design and analysis approach for unseeded combined cooling and antisolvent crystallization (CCAC) systems. *Crystal Growth and Design* 14, 687–698. doi:10.1021/cg401562t.
- Yang, Y. and Nagy, Z., 2015a. Combined Cooling and Antisolvent Crystallization in Continuous Mixed Suspension, Mixed Product Removal Cascade Crystallizers: Steady-

- State and Startup Optimization. *Industrial & Engineering Chemistry Research*, 54(21), pp.5673-5682.
- Yang, Y., Nagy, Z.K., 2015b. Advanced control approaches for combined cooling/antisolvent crystallization in continuous mixed suspension mixed product removal cascade crystallizers. *Chemical Engineering Science* 127, 362–373. doi:10.1016/j.ces.2015.01.060.
- Yang, Y., Pal, K., Koswara, A., Sun, Q., Zhang, Y., Quon, J., McKeown, R., Goss, C., Nagy, Z.K., 2017. Application of feedback control and in situ milling to improve particle size and shape in the crystallization of a slow growing needle-like active pharmaceutical ingredient. *International Journal of Pharmaceutics* 533, 49–61. doi:10.1016/j.ijpharm.2017.09.050.
- Yang, Y., Song, L., Zhang, Y., Nagy, Z.K., 2016. Application of wet milling-based automated direct nucleation control in continuous cooling crystallization processes. *Industrial and Engineering Chemistry Research* 55, 4987–4996. doi:10.1021/acs.iecr.5b04956.
- Yao, K.Z., Shaw, B.M., Kou, B., McAuley, K.B. and Bacon, D.W., 2003. Modeling ethylene/Butene Copolymerization with Multi-site catalysts: Parameter Estimability and experimental design, *Polymer Reaction Engineering*, 11(3), pp. 563–588. doi: 10.1081/pre-120024426.
- Yekeler, M., 2007. Particle Breakage, *Handbook of Powder Technology*. Elsevier. doi:10.1016/S0167-3785(07)12012-1.
- Yu, L., 2004. Applications of process analytical technology to crystallization processes. *Advanced Drug Delivery Reviews*, 56(3), 349-369. doi: 10.1016/j.addr.2003.10.012.
- Yu, X., Hounslow, M.J., Reynolds, G.K., 2015. Accuracy and optimal sampling in Monte Carlo solution of population balance equations. *AIChE Journal* 61, 2394–2402. doi:10.1002/aic.14837.
- Yu, Z.Q., Tan, R.B.H., Chow, P.S., 2005. Effects of operating conditions on agglomeration and habit of paracetamol crystals in anti-solvent crystallization. *Journal of Crystal Growth* 279, 477–488. doi:10.1016/j.jcrysgro.2005.02.050.

8 APPENDIX A: PUBLICATIONS

International journal publications

1. **Fysikopoulos, D.**, Benyahia, B., Borsos, A., Nagy, Z.K., Rielly, C.D., **2017**. Model Reliability and Estimability Analysis of a Multi-Impurity Population Balance Model for Crystallization Processes. *Computers and Chemical Engineering* (**Accepted**).
2. Brown, C.J., McGlone, T., Yerdelen, S., Srirambhatla, V., Mabbott, F., Gurung, R., L. Briuglia, M., Ahmed, B., Polyzois, H., McGinty, J., Perciballi, F., **Fysikopoulos, D.**, MacFhionnghaile, P., Siddique, H., Raval, V., Harrington, T.S., Vassileiou, A.D., Robertson, M., Prasad, E., Johnston, A., Johnston, B., Nordon, A., Srai, J.S., Halbert, G., ter Horst, J.H., Price, C.J., Rielly, C.D., Sefcik, J., Florence, A.J., **2018**. Enabling precision manufacturing of active pharmaceutical ingredients: workflow for seeded cooling continuous crystallisations. *Molecular Systems Design & Engineering*. doi:10.1039/C7ME00096K.

Publications in proceeding of international conferences

1. **Fysikopoulos, D.**, Borsos, A., Li, W., Onyemelukwe, I., Benyahia, B., Nagy, Z.K., Rielly, C.D., **2017**. Local vs Global Estimability Analysis of Population Balance Models for Crystallization Processes, *Computer Aided Chemical Engineering*, Elsevier, Volume 40, Pages 55-60, ISSN 1570-7946, ISBN 9780444639653, <https://doi.org/10.1016/B978-0-444-63965-3.50011-8>.

Abstracts

1. **D. Fysikopoulos**, A. Borsos, W. Li, I. Onyemelukwe, B. Benyahia, Z.K. Nagy, C.D. Rielly, Model Reliability and Practical Identifiability Analysis of Population Balance Models for Crystallization Processes, In *5th Quality by Design Symposium*, Leicester, UK, March, 2017.
2. **D. Fysikopoulos**, A. Borsos, W. Li, I. Onyemelukwe, B. Benyahia, Z.K. Nagy, C.D. Rielly, Model Reliability and Practical Identifiability Analysis of Population Balance Models for Crystallization Processes, In *CMAC Open Day 2017*, University of Strathclyde, Glasgow, UK, March, 2017.
3. **D. Fysikopoulos**, A. Borsos, B. Benyahia, Z.K. Nagy, C.D. Rielly, Model Reliability of multi-dimensional Population Balance Models for Crystallization, In *PSE@ResearchDayUK*, Imperial College, London, UK, July, 2016.
4. **D. Fysikopoulos**, A. Borsos, B. Benyahia, Z.K. Nagy, C.D. Rielly, Parameter Identification, Reliability and Model Discrimination of Population Balance Models for Crystallization, In *12th International Workshop of the Crystal Growth of Organic Material and 47th Annual British Association of Crystal Growth Conference (BACG) Joint Conference*, University of Leeds, Leeds, UK, June, 2016.
5. **D. Fysikopoulos**, Q. Su, A. Trybala, B. Benyahia, Z.K. Nagy, C.D. Rielly, Population Balance Modelling of Continuous Crystallization Processes, In *4th Quality by Design Symposium*, Leicester, UK, March, 2016.

Awards

1. Best poster presentation award (3rd place), 5th Quality by Design Symposium, De Montfort University, 2017
2. Best poster presentation award (2nd place), 4th Quality by Design Symposium, De Montfort University, 2016.

